System Theoretical Analyses of Voltage Stability in Power Electronics-Dominated Hybrid Power Systems

A thesis approved for the academic degree of

Doktor der Ingenieurwissenschaften (Dr.-Ing.)

at the

Faculty of Electrical Engineering and Information Technology

TU Dortmund University

by

Sebastian Liemann, M.Sc.

Supervisor: Univ.-Prof. Dr.-Ing. Christian Rehtanz, TU Dortmund University
Co-Advisor: Univ.-Prof. Dr.-Ing. Christian Becker, Hamburg University of Technology

Day of Oral Examination: 19.11.2024

Abstract

The massive integration of power electronic devices at the load and generation side is changing the dynamics and stability of power systems. In particular, power electronic loads can threaten voltage stability in the event of major disturbances, such as short circuits, due to their low voltage sensitivity. In addition, the ancillary services of decommissioned conventional power plants have to be taken over by grid-forming converters at the transmission level. Since power electronic converters and loads can discretely change their dynamics during disturbances, e.g. by current limitation or disconnection with zero power consumption, additional challenges for voltage stability arise. Therefore, in this thesis, hybrid system theory is used as a modelling basis to explicitly analyse the complex interactions between continuous and discrete dynamics in such events. It is examined how the theory of hybrid systems can extend the system theory of voltage stability and how it can support its assessment in the short and long term. Furthermore, since there is only a small overlap between conventional voltage stability dynamics and power electronics dynamics, it is not clear whether phasor or electromagnetic transient models should be used. Phasor models have the advantage of simulating large systems in a reasonable period of time, while electromagnetic transient models cover more high-frequency dynamics. Therefore, both types are used to model grid-forming converters and power electronic loads. The results show that the current limitation of grid-forming converters can lead to voltage instability in the short and long term. However, by applying stability-enhancing control methods, the instability induced by the converter can be avoided. The disconnection of power electronic loads during short circuits can initially stabilise the system due to the reduced power consumption. However, their potential fast power recovery during the fault can lead to instability or delayed voltage recovery afterwards. The combined simulation of grid-forming converters and power electronic loads showed that the simultaneous occurrence of current limitation and fast power recovery is a serious threat to short- and long-term voltage stability. For this reason, the maximum current of the converter is considered to be the most important parameter in this context. For the loads, an early disconnection during the fault and a slow power recovery could also improve stability if the loads were designed accordingly. Finally, the simulation results showed that phasor models may still be suitable for grid-forming converters, while electromagnetic transient models are needed for power electronic loads.

Kurzfassung

Die umfangreiche Integration von leistungselektronischen Betriebsmitteln auf der Last- und Erzeugungsseite verändert die Dynamik und Stabilität von elektrischen Energiesystemen. Zum einen können leistungselektronische Lasten bei großen Störungen wie Kurzschlüssen die Spannungsstabilität gefährden, da ihre Leistung nur eine geringe Spannungsempfindlichkeit aufweist. Zum anderen müssen netzbildende Umrichter zukünftig die erbrachten Systemdienstleistungen von stillgelegten Kraftwerken übernehmen. Da derartige Umrichter und Lasten ihre Dynamik bei Störungen diskret ändern können, z.B. durch Strombegrenzung, ergeben sich zusätzliche Herausforderungen für die Spannungsstabilität. Daher wird in dieser Arbeit die Theorie hybrider Systeme als Modellierungsgrundlage verwendet, um die Wechselwirkungen zwischen kontinuierlichen und diskreten Dynamiken explizit zu analysieren. Es wird untersucht, wie hybride Systeme die Systemtheorie der Spannungsstabilität erweitern können und wie sie deren Analyse unterstützen. Da zudem die Dynamiken zwischen konventioneller Spannungsstabilität und der von leistungselektronischen Betriebsmittel sich nur geringfügig überschneiden, ist es zudem nicht eindeutig, ob Zeigermodelle oder Modelle für transiente elektromagnetische Vorgänge verwendet werden sollten. Erstere haben den Vorteil, dass sie große Systeme in angemessener Zeit simulieren können, während Letztere mehr hochfrequente Dynamiken berücksichtigen. Daher werden beide Modellarten in dieser Arbeit untersucht und verglichen. Allgemein zeigen die Ergebnisse, dass die Strombegrenzung der Umrichter im Kurz- und Langzeitbereich zu Spannungsinstabilitäten führen kann. Durch die Anwendung zusätzlich stabilisierender Regelungsmethoden kann die durch den Umrichter verursachte Instabilität jedoch vermieden werden. Die Abschaltung der Lasten während der Kurzschlüsse kann das System zunächst durch die verringerte Leistungsaufnahme stabilisieren. Ihre schnelle Leistungswiederherstellung während des Fehlers kann jedoch zu Instabilität oder einer verzögerten Spannungserholung nach dem Fehler führen. Die gemeinsame Simulation von netzbildenden Umrichtern und Lasten hat gezeigt, dass das gleichzeitige Auftreten von Strombegrenzung und schneller Leistungswiederkehr eine ernsthafte Gefahr für die Spannungsstabilität im Kurz- und Langzeitbereich darstellt. Daher wird in dieser Arbeit für den Umrichter der maximale Umrichterstrom als dessen wichtigster Modellparameter angesehen. Bei den Lasten könnten bei einer entsprechenden Auslegung eine frühzeitige Abschaltung während des Fehlers und eine langsamere Leistungswiederherstellung die Stabilität ebenfalls verbessern. Abschließend zeigen die Simulationsergebnisse, dass für netzbildende Umrichter Zeigermodelle weiterhin geeignet sein können, während für leistungselektronische Lasten Modelle für transiente elektromagnetische Vorgänge erforderlich sind.

Danksagung

Die vorliegende Doktorarbeit ist während meiner Tätigkeit als wissenschaftlicher Mitarbeiter am Institut für Energiesysteme, Energieeffizienz und Energiewirtschaft (ie³) der Technischen Universität Dortmund entstanden.

Mein besonderer Dank gilt meinem Doktorvater Prof. Dr.-Ing. Christian Rehtanz für die stets hervorragende fachliche Unterstützung und Zusammenarbeit sowie die ausgezeichneten wissenschaftlichen und persönlichen Entwicklungsmöglichkeiten am ie³. Für die freundliche Übernahme des Korreferats bedanke mich bei Herrn Prof. Dr.-Ing. Christian Becker.

Mein Dank gilt auch allen Kolleginnen und Kollegen am ie³, die durch ihre stets kollegiale und freundliche Art zu einer außergewöhnlichen Arbeitsatmosphäre beigetragen haben. In diesem Zusammenhang möchte mich auch insbesondere bei der Themengruppe *Power System Stability and Operation* bedanken, deren Teil ich lange sein durfte und mit der stets ein exzellenter fachlicher und persönlicher Austausch stattgefunden hat. Mein persönlicher Dank gilt auch dem Research Team EMoCoSy des DFG SPP 1984, wodurch ich nicht nur fachliche Expertise, sondern auch neue Freundinnen und Freunde in ganz Deutschland gewinnen durfte. Darüber hinaus danke ich allen Studierenden, die mich im Rahmen von Abschlussarbeiten oder als wissenschaftliche Hilfskräfte tatkräftig unterstützt haben. Für die Durchsicht und konstruktive Kritik des Manuskriptes bedanke ich mich auch bei Marcel Klaes, Ismael Jaramillo-Cajica, Felix Goeke, Sebastian Raczka, Oliver Pohl und Madeleine Jendernalik.

Meine Eltern Margot und Michael sowie meine Schwester Vera möchte ich dabei an dieser Stelle besonders hervorheben, da sie mich mein ganzes Leben lang bedingungslos unterstützt und gefördert haben. Dafür danke ich euch außerordentlich. Mein größter Dank gilt meiner lieben Frau Lara, die mir während all der Zeit, insbesondere während des Schreibens, stets den Rücken freigehalten und mich motiviert hat, was somit erst zum Gelingen der Arbeit geführt hat.

Dortmund, April 2024

Sebastian Liemann

Contents

Abstract / Kurzfassung **III**

Danksagung **VII**

Table of contents **IX**

1 Introduction **1**
- 1.1 Research questions 4
- 1.2 Structure of the thesis 5

2 Voltage stability and its assessment methods **9**
- 2.1 Power system stability classification 9
- 2.2 System theory of voltage stability 12
- 2.3 State of the art of voltage stability assessment 17
  - 2.3.1 Assessment methods for short-term voltage stability 19
  - 2.3.2 Assessment methods for long-term voltage stability 22
- 2.4 Current practice of modelling power electronics for voltage stability analysis 25
- 2.5 Conclusion and derivation of methodical approach 29

3 Hybrid system theory in the context of power systems **31**
- 3.1 Literature review: Application of hybrid system theory to power systems . . 32
- 3.2 Formal modelling of hybrid systems 36
  - 3.2.1 Hybrid automaton 36
  - 3.2.2 Switched Systems 38
  - 3.2.3 Differential-algebraic-discrete system 39
- 3.3 Dynamical phenomena and stability of hybrid systems 40
  - 3.3.1 Hybrid dynamical phenomena 41
  - 3.3.2 Stability theory of continuous and hybrid systems 43
- 3.4 Application of hybrid system theory: Trajectory sensitivity with discontinuities 49
- 3.5 Conclusion of the chapter 55

4 Modelling of grid-forming converters with current limitation **57**
- 4.1 Converter model, AC filter and DC circuit 57

4.2 Outer loop: power synchronisation and voltage control 60
4.2.1 Droop control 61
4.2.2 Matching control 62
4.2.3 Dispatchable virtual oscillator control 63
4.2.4 Virtual synchronous machine 63
4.3 Inner loop: cascaded control and current limitation 64
4.3.1 Cascaded voltage and current control 64
4.3.2 Current limitation and anti-windup method 66
4.4 Stability-enhancing control methods 68
4.4.1 SECM-1: Active and reactive power reference adaptation based on limited current reference 68
4.4.2 SECM-2: Active power reference adaptation based on PCC voltage magnitude 73
4.4.3 SECM-3: Stability-enhancing component based on q-axis component of PCC voltage 73
4.4.4 SECM-4: Active power reference adaptation based on converter current 74
4.5 Droop-based grid-forming converter as hybrid system 75
4.6 Conclusion of the chapter 81

5 Measurement and modelling of power electronics-interfaced loads 83
5.1 General structure of power electronic loads and power response in case of voltage drops 83
5.2 Development of a power electronic load model for phasor simulations . . . 87
5.3 Measurement of real power electronic loads and derivation of EMT models 95
5.3.1 Laboratory setup 95
5.3.2 Measured power response 96
5.3.3 Derivation of EMT models for power electronic loads 100
5.4 Power electronic load as hybrid system 105
5.5 Conclusion of the chapter 108

6 Analyses of voltage stability of power electronics-dominated grids 109
6.1 Aggregated Nordic power system and simulation environment 110
6.2 Scenario setup and simulation environment 113
6.2.1 Scenario Setup 113
6.2.2 Simulation environment 116

6.3 Analysis of short-term voltage stability . . . 118
6.3.1 Impact of grid-forming converters with current limitation . . . 119
6.3.2 Impact of power electronic loads . . . 124
6.3.3 Mutual impact of grid-forming converters and power electronic loads 130
6.3.4 Summary and conclusion . . . 131
6.4 Analysis of long-term voltage stability . . . 133
6.4.1 Impact of grid-forming converters with current limitation . . . 133
6.4.2 Impact of power electronic loads . . . 138
6.4.3 Mutual impact of grid-forming converters and power electronic loads 145
6.4.4 Summary and conclusion . . . 148

7 Summary, conclusion and outlook 151
7.1 Summary . . . 151
7.2 Conclusion . . . 153
7.3 Outlook . . . 158

Bibliography 161

Journal publications 180

List of acronyms 183

List of symbols and indices 185

A Additional information about the modelling of GFM converters 191
A.1 Parameters of GFM controls and SECM . . . 191
A.2 DADS model of droop-based GFM converter in an islanded microgrid . . . 193
A.3 Eigenvalue analysis of DADS model with SECM-1 . . . 198

B Additional information about the modelling of power electronic loads 199
B.1 Inclusion of the phasor power electronic load model into transient stability programs . . . 199
B.1.1 Function for calculating the switch-on time with Cardano's formula 201
B.2 Laboratory: Load data and additional measurements . . . 203
B.2.1 Load and transformer data . . . 203
B.2.2 Distortion of power amplifier voltage due to current limitation . . . 205
B.2.3 Determination of grid impedance values for power response measurements . . . 206

B.2.4 Impact of high grid impedance on power response 207
B.2.5 Impact of EMI filter on power response 209
B.2.6 Component design of power electronic loads 209

C Parameters of the aggregated Nordic system 213

1 Introduction

"All models are wrong, but some are useful."

George E. P. Box, 1979[1]

Power systems around the world are changing due to the increasing installation of power electronics. On the generation side, wind turbines and photovoltaic systems are increasingly replacing conventional generation units such as synchronous generators. On the load side, a sharp increase in the number of power electronics-interfaced loads such as consumer electronics, light-emitting diodes (LEDs), information and communication technologies and electric vehicle charging stations can be observed. As a result, most load and generation units will be connected to the grid via power electronic interfaces. Since the stability and overall dynamics of a power system are highly dependent on these units, it is inevitable that stability and dynamics are changing and will continue to change. In particular, this new load composition presents challenges in terms of voltage stability, as it has completely different voltage sensitivities and dynamics. In addition, some of the new generation units are located far from load centres, such as offshore wind farms, requiring the energy to be transported over long distances, e.g. by high-voltage direct current (HVDC) links. As the decommissioning of synchronous generators means that their ancillary services will no longer be available, they have to be provided by other units. For this purpose, the large converters of HVDC links could be used, which could provide virtual inertia, e.g. through a grid-forming (GFM) control approach. As voltage stability is also largely determined by the grid structure, such changes in power transmission would also have a significant impact. This means that the changes on the load, generation and grid side will significantly alter the voltage dynamics and hence the stability. Therefore, the impact of these power electronic devices on voltage stability needs to be analysed and evaluated.

In the past, voltage stability has often been assessed by static analyses such as steady-state power flows or the calculation of $P(V)$-curves. However, power systems are highly non-linear systems that exhibit a variety of complex dynamics near the stability limit and under disturbances, especially for voltage phenomena [1]. For this reason, the mechanisms of voltage instability were first described by the bifurcation theory of non-linear dynamics [2].

[1] Box, G.E.P, "Robustness in the strategy of scientific model building", MRC Technical Summary Report no. 1954, May 1979

For non-linear dynamic systems, bifurcation describes a qualitatively sudden change in the system dynamics under variation of a parameter. However, this previous system theory of voltage stability was carried out for power systems based on synchronous machines and conventional loads and not for power electronics-dominated systems. A new challenge is that power electronic devices can discretely change their dynamics. In the case of power converters, discrete dynamics can arise, for example, by current limitation leading from a grid-forming to a grid-following mode [3]. This change in control and partial loss of flexibility can significantly alter voltage dynamics and threaten stability. In the case of power electronic loads, an abrupt switch-off with zero power consumption during a voltage drop and a rapid power recovery in the meantime is also observed [4]. This discontinuous response is also of a discrete nature. Based on this, power electronic devices cannot only be described by continuous states (e.g. voltages or currents) but also by discrete states and events. Therefore, they can be modelled by hybrid system theory instead as a system of pure differential-algebraic equations (DAEs) [5]. Note that in this thesis a hybrid system means a mathematical model consisting of continuous and discrete states. Since the discrete dynamics mentioned above occur especially in the case of large disturbances, linearisation as in the case of bifurcation theory is often not appropriate. Therefore, hybrid system theory can help to address these new challenges and thus extend the modelling and stability analysis methods alongside the conventional ones. This could help to specifically analyse the impact of the emerging discrete dynamics on voltage stability.

In [6] two new stability classes are introduced to cover the effects of an increasing number of power electronic devices. It also highlights the importance of hybrid system theory and its differences in stability from pure continuous systems. It is also pointed out that due to the fast response of power electronic devices, these two new stability classes need to be analysed using electromagnetic transient (EMT) models. At the same time, however, it is stated that all the dynamic phenomena considered in conventional power systems can be modelled by phasor models to investigate voltage stability. This raises the question of which modelling approach should be used to analyse voltage stability in a power system dominated by power electronics. On the one hand, EMT models can always lead to greater modelling detail and thus cover more dynamic phenomena. On the other hand, phasor models can lead to reduced complexity and larger simulation step sizes, which can increase the simulation speed by one or two orders of magnitude [7]. For this reason, the suitability of EMT models for low-frequency dynamics is very low. In addition, the analysis of phasor models can be much simpler than the waveforms of an EMT model, and the parameter space is likely to be larger. Fig. 1.1 illustrates the suitability of EMT and phasor models

for power converters. It also highlights the short- and long-term voltage dynamics that can occur in conventional power systems in addition to the converter dynamics, which are mainly based on its control and the model of the converter. It can be seen that some of the dynamics overlap, but there are regions such as the long-term voltage dynamics and the fast converter controls that do not intersect. Especially within the overlapping region, the suitability varies between the model types. In general, the simulation model used should capture all the dynamics required for accurate stability analysis. However, models that are too complex can lead to high computational costs and a difficult stability analysis. In summary, it is not clear which type of simulation model should be used to investigate short- and long-term voltage stability in a power electronics-dominated system, as both have advantages and disadvantages.

It can be concluded that the massive integration of power electronics into the power system raises a number of challenges. On the one hand, it turns out that the basic theory of voltage stability may not be sufficient to describe all relevant dynamic stability phenomena. On the other hand, it is not clear what the main dynamics are and what type of model is suitable for modelling them accurately but efficiently. Finally, there is of course the question of what the specific impact of the power electronic devices is on short- and long-term stability.

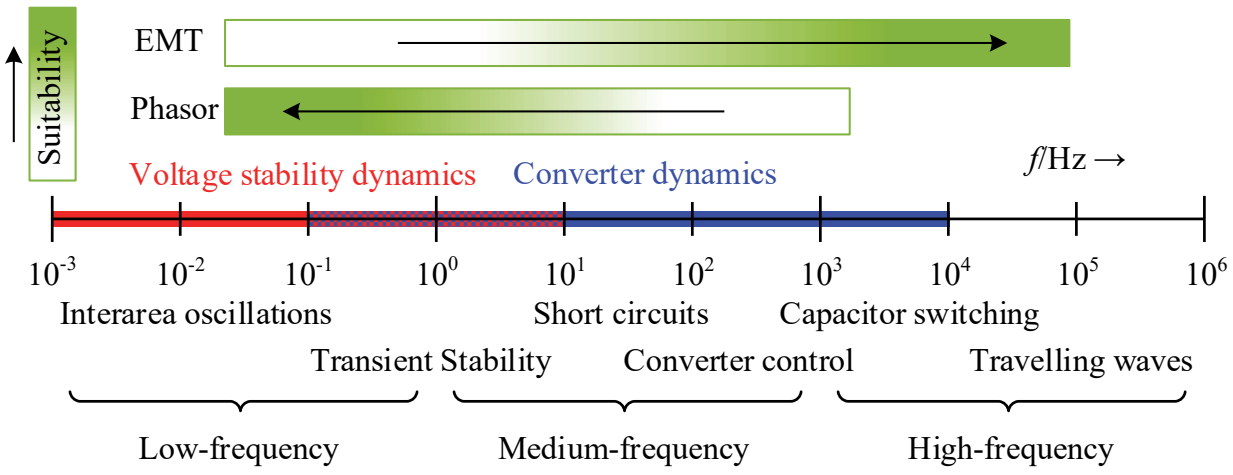

Figure 1.1: Suitability of EMT and phasor models of power converters based on [7] with highlighted time scales of voltage stability [6] and converter [8] dynamics.

1.1 Research questions

Voltage stability is a major concern at the transmission system level due to the high power that needs to be transmitted over long distances and the resulting high load on the lines at certain times of the year. Therefore, this thesis will mainly deal with stability aspects at the transmission system level. The focus is on current-limited GFM converters, as they are required to take over some of the ancillary services from synchronous generators, e.g. by HVDC converters. In the case of the power electronic loads, different types will be investigated, as there is a wide variety. As the previous introduction has shown, there are several open research questions in the field of power electronics and voltage stability. In particular, their discrete dynamics in the presence of large disturbances pose new challenges that need to be analysed in the short and long term. To address this issue, the main research question for this thesis is as follows:

Research question 1:

How do grid-forming converters and power electronic loads influence short- and long-term voltage stability and associated dynamics?

To answer this question, the theory of hybrid systems is used as a theoretical modelling basis. However, due to the increased complexity, it is not clear what benefits can be achieved by explicitly modelling the power system as a hybrid system. In addition, as there are several methods to analyse hybrid systems, it is an open question of which methods are helpful to assess voltage stability. To investigate this, the second research question is formulated as follows:

Research question 2:

How can hybrid system theory extend the modelling of dynamic power systems and support the assessment of voltage stability?

As the theory of hybrid systems only provides a general modelling basis, it is not able to recommend how the individual power electronic devices should be modelled in detail. Therefore, the suitability of EMT or phasor models must be individually assessed and compared. As the suitability mainly depends on an accurate representation of the required dynamics, the third research question is formulated as follows:

Research question 3:

How should grid-forming converters and power electronic loads be modelled and what are their main continuous and discrete dynamics?

As power electronic devices represent a promising solution to decarbonise the energy system, it is also important to ensure that its massive integration into the power system is robust and does not create new problems. As each device has several model and control parameters, all of which can affect the stability of the system, it is necessary to analyse which are the most important parameters. In addition, it may be helpful to have recommendations on how these parameters should be designed. This leads to the fourth and last research question:

Research question 4:

What are the key parameters of grid-forming converters and power electronic loads that affect short- and long-term voltage stability and how could they be designed for a robust integration of these devices?

The above research questions therefore aim to provide a structured analysis of how power electronic devices affect voltage stability and how the theory of hybrid systems can support this. In addition, it should be clarified what modelling basis is necessary and what the main dynamics are. Finally, the relevant modelling parameters that have a major influence on the stability of a robust integration of power electronics are identified.

1.2 Structure of the thesis

In order to answer the research questions systematically, the structure of this thesis is presented next. Its graphical representation is given in Fig. 1.2. After the introduction, a summary of the fundamentals of voltage stability and its assessment methods is given in Chapter 2. First, the classification of power system stability is outlined, with an emphasis on the differences and similarities between voltage stability and the other stability classes. Second, the system theory of voltage stability, mainly based on bifurcation theory, is presented to examine the extent to which it applies to power electronics-dominated systems. State-of-the-art voltage stability assessment methods for short- and long-term voltage

stability are then presented. The applicability of these methods to large-signal stability and power systems with a high proportion of power electronics is considered. In addition, the current practice of modelling power system components such as converters and loads for voltage stability analysis is described. It also reviews the extent to which the impact of GFM converters and power electronic loads on voltage stability has been analysed so far. The chapter closes with a conclusion and derivation of the methodical procedure.

In Chapter 3, firstly, a literature review is given on recent applications of hybrid system theory to power systems and the benefits that have been obtained. Secondly, different formal modelling approaches of hybrid systems are presented in order to analyse which approach is best suited for the given research questions. The dynamic phenomena that are unique to hybrid systems are described afterwards. The stability theory of hybrid systems and its difference from pure continuous systems is also highlighted. In the next step, the method of trajectory sensitivity with discontinuities is presented, which can be particularly helpful when investigating the stability of complex hybrid power systems. Finally, a conclusion is drawn on how hybrid system theory can support the modelling of power electronics and the analysis of voltage stability.

Chapter 4 deals with the modelling of GFM converters with current limitation. The first step is to outline the general converter model, including the AC filter and the DC energy model. In the second step, an overview of different GFM control approaches is given, consisting of the power synchronisation and voltage control loop. Emphasis is placed on how the control loops need to be modified if they are to be modelled for EMT or phasor simulations. This is followed by a description of how to model the cascaded internal control loops and the current limitation. This is followed by a proposal for a stability-enhancing control method (SECM) capable of stabilising the converter during current limitation. Other SECMs are also presented for comparison in later simulations. The chapter concludes with the explicit modelling of a droop-based GFM converter as a hybrid system. The aim is to analyse its characteristics as a hybrid system and how it can later be used to investigate voltage stability.

Similarly, in Chapter 5, the general structure of power electronic loads is presented first. The next step is to derive an analytical phasor model of a power electronic load for later simulations as nothing comparable was found in the literature. The power response of real power electronic loads to voltage drops is then measured in the laboratory. Based on the measurements, EMT load models are derived. In the final step, the phasor power electronic load model is explicitly modelled as a hybrid system and its characteristics are analysed.

In Chapter 6 the time-domain simulations are performed to finally analyse the voltage stability in power electronics-dominated grids. For this purpose, an aggregated version of the Nordic test system is proposed, which is much more computationally efficient but reflects the main short- and long-term voltage dynamics. The scenario setup and the simulation environment for the time-domain simulations are then presented. The analysis starts with short-term voltage stability, where the individual impact of GFM converters and power electronic loads is examined before they are combined. The same procedure is then followed for long-term voltage stability. Within these analyses, the comparison between the EMT and phasor models is also carried out, as well as the parameter study through the trajectory sensitivity calculation. Finally, in Chapter 7, a summary and a conclusion of the stated research questions are given, as well as an outlook on further research.

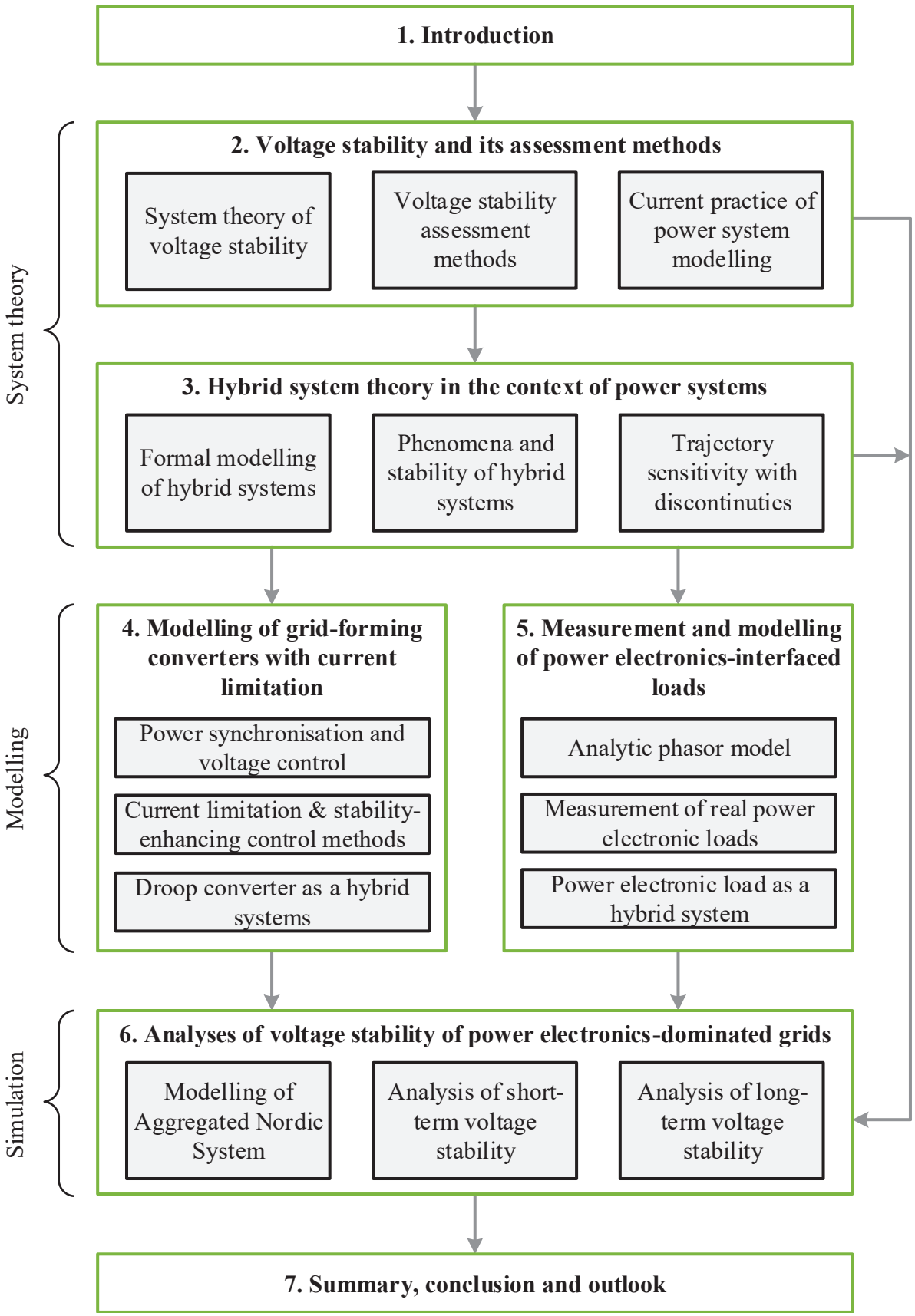

Figure 1.2: Graphical representation of the thesis structure

2 Voltage stability and its assessment methods

This chapter summarises the theoretical background of voltage stability, its assessment methods and current modelling practices. For this, an introduction to power system stability classification is given in Section 2.1. Here, special attention is given to voltage stability and its similarities and differences to other stability classes. Also, the differentiation of voltage stability into short- and long-term dynamics is specified. In Section 2.2, the system theory of voltage stability and dynamic phenomena are presented. Based on this, state-of-the-art voltage stability assessment methods are reviewed in Section 2.3. This section is further divided into short-term (Section 2.3.1) and long-term (Section 2.3.2) assessment methods. Afterwards, the current practice of modelling power electronics for voltage stability is presented in Section 2.4. In Section 2.5, the chapter closes with a summary and derivation of the subsequent methodical procedure, especially for the modelling and assessment of power electronics-dominated power systems.

2.1 Power system stability classification

In general, the stability of a (physical) dynamical system means that it can withstand certain disturbances where its states return to an equilibrium point after a transient phase. For power systems, a formal definition of stability is given in [6]:

"Power system stability is the ability of an electric power system, for a given initial operating condition, to regain a state of operating equilibrium after being subjected to a physical disturbance, with most system variables bounded so that practically the entire system remains intact."

By this definition, it is initially irrelevant what type of disturbance occurs and which states of the system are affected. Also, this definition considers the power system as a whole and not on a component level. This means that some subsystems may become unstable, but the majority of the power system remains intact after a disturbance. The definition also incorporates that only technically feasible operating points are defined as stable and not, for example, a state in which all voltages are equal to zero, although it is an equilibrium. This aspect is important for the distinction between a system-theoretical and a practical view

of stability. Fig. 2.1 illustrates the concept of power system stability, dividing the state-space into a region of attraction and a feasible operating region, e.g. by operational limits. All trajectories starting within the region of attraction will converge to the equilibrium. In contrast, the feasible operating region is a subset of the state space, which if trajectories leave this region could lead to undesirable or unsafe behaviour, like e.g. triggering a circuit breaker. The intersection of both regions is called *restricted stability region*, which takes into account the constraints that would lead to a structural change of the system and the region of attraction. [9] This means, that if a disturbance occurs, the states leave the

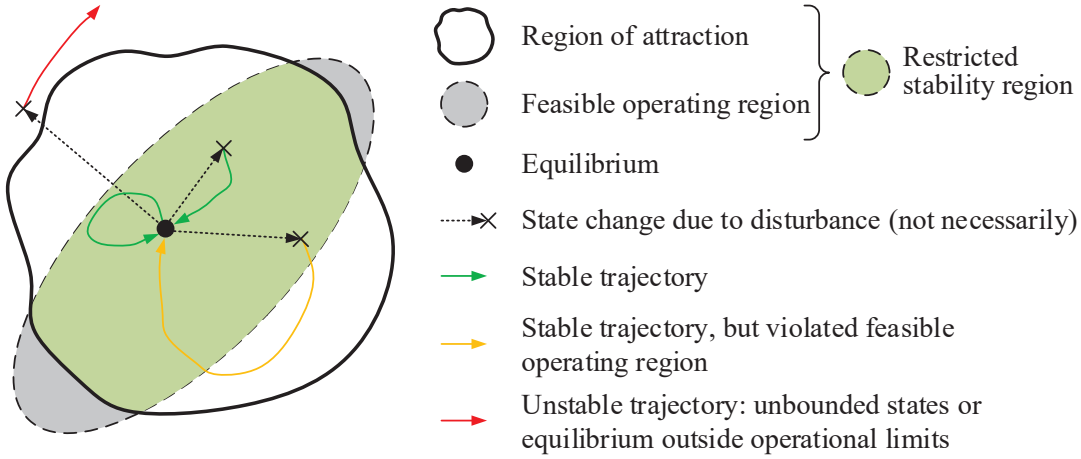

Figure 2.1: Visualization of power system stability concerning operational limits leading to a restricted stability region

equilibrium, perhaps undergoing a discrete change, and enter a transient phase. Based on the nature and size of the disturbance, the states either return to the equilibrium (green and yellow trajectory), become unbounded or reach another equilibrium which is maybe outside the operational limits (red trajectory). In case the operating limits have been violated during the transient phase (yellow trajectory), a reliable statement about system stability can only be made if e.g. the corresponding protection devices are taken into account. Since power systems are large, non-linear, complex and hybrid, their stability is usually evaluated by mathematical models and numerical calculations [10]. Therefore, if protection equipment or other structural changing assets are not considered in a model-based study, no exact statement about the stability can be made, as the confidence region of the model has been left. In addition, to determine if the system is stable, it depends on whether a short-term violation of operational limits is allowed or has to be endured. The difference between steady-state voltage limits and the fault ride-through curve serves as an example here [11].

As a consequence, for a numerical evaluation of power system stability, it is crucial to take the different operational limits into account.

Fig. 2.2 illustrates the revised stability classification. A distinction is made between the five stability classes. The three stability classes voltage, rotor angle and frequency stability have been introduced in [12], while the two new classes (resonance and converter-driven stability) have been added in [6], motivated by the increasing share of power electronics. As can be seen in Fig. 2.2, different models should be used depending on the stability class according to [6]. The reason for this is that for the new stability classes EMT models should be used due to the high-frequency dynamics of power electronics. At the same time, it is stated that conventional voltage stability can be analysed by using phasor models. This shows that it is not clear which modelling detail (i.e. EMT or phasor type) is needed when analysing voltage stability in power electronics-dominated grids. Next, the definition of voltage stability is given and how it is divided into short- and long-term stability.

Definition of Voltage Stability [6]: *"Voltage stability refers to the ability of a power system to maintain steady voltages at all buses in the system after being subjected to a disturbance. It depends on the ability of the combined generation and transmission systems to provide the power requested by loads. This ability is constrained by the maximum power transfer to a specific set of buses and linked to the voltage drop that occurs when active and/or reactive power flows through inductive reactances of the transmission network."*

The driving force behind voltage instability is the active and reactive power demanded by loads. If the requested power exceeds the transport capacity of the grid, a voltage collapse will occur. Voltage stability therefore always depends on the structure of the grid and the resulting voltage drop across lines and transformers. For this reason, the basic structure of the power system must always be preserved when investigating voltage stability. This is in contrast to frequency stability, where the grid structure can be neglected sometimes. Since the size of the disturbance influences the method of analysis, it is divided into *large and small disturbances*. For the former, it is usually necessary to carry out time-domain simulations, since the non-linearities of the grid and the dynamics of the grid components must be taken into account. The period of interest may be in the *short or long term*. Short-term stability is mainly analysed for large disturbances such as short circuits and the resulting load dynamics. Since short circuits are also the main disturbance in the case of rotor angle transient stability, the distinction between these types is not always clear [14]. In contrast, long-term voltage stability deals with slower dynamics such as on-load tap changer (OLTC) tap changes or over excitation limitation (OEL) activation of synchronous generators [1].

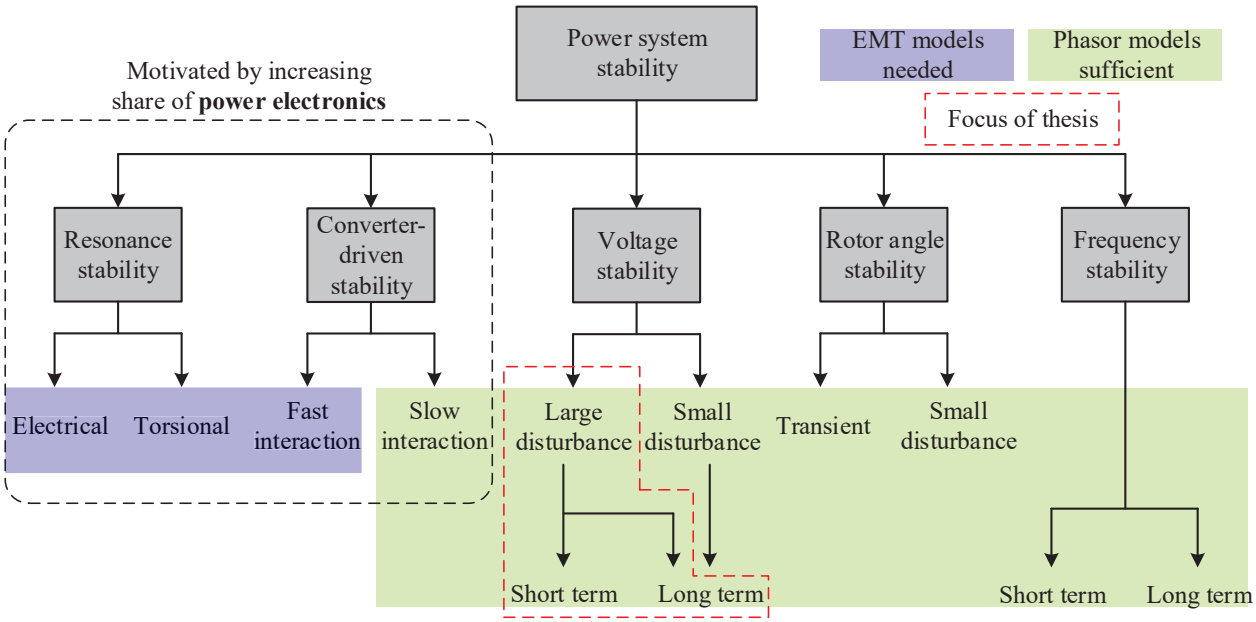

Figure 2.2: Power system classification, suitability of simulation models and focus of the thesis (own representation, based on [13])

As shown in Fig. 2.2, long-term voltage stability can be initiated by large disturbances like short circuits or by small disturbances, e.g. a slight increase in power consumption. For *small disturbances*, the system equations are linearised and the dynamics are set to zero due to the small incremental change in load. This allows a more analytical investigation such as bifurcation theory (see Section 2.2). As small load changes are usually associated with a slow growth rate, they consider long-term phenomena only. However, the focus of this thesis is on large disturbances, as these evoke the complex interactions between continuous and discrete dynamics, making linearisation infeasible. A more detailed look at the theory of voltage stability is given in the next subsection.

2.2 System theory of voltage stability

In the last decades, the theory of voltage stability has been mainly described by the bifurcation theory of differential and algebraic equations [15]. Bifurcation theory describes how a system qualitatively changes by slowly varying a parameter of the investigated system. Thus, a bifurcation point represents a strong change in the system characteristics by a comparatively small change of a parameter. By assuming that the power system is a non-linear

autonomous dynamical system with a parameter γ, it can be described by

$$\dot{\mathbf{x}} = f(\mathbf{x}, \gamma), \tag{2.1}$$

where the system has an equilibrium point at $\mathbf{x}_0$ if $f(\mathbf{x}_0, \gamma) = \mathbf{0}$. Depending on the bifurcation, the number and type (stable or unstable) of equilibrium points can change. This means that the phase portrait (geometric presentation of the trajectories regarding the solution) of the system significantly changes in the state space. Examples of bifurcations are saddle-node bifurcation, Hopf bifurcation, transcritical bifurcation and pitchfork bifurcation. However, it should be noted that this list is not complete (see e.g. [16]). This subchapter will concentrate on saddle-node and Hopf bifurcation as they have the most practical relevance [17]. With regard to voltage stability, the load power p_L is used as the parameter γ and the load voltage v_L as a state x to track the change in equilibrium points here.

Saddle-node bifurcation

In general, saddle-node bifurcation theory is applied to characterise the phenomenon of voltage collapse in a power system with increasing load demand. At a saddle-node bifurcation, the former stable equilibrium $\mathbf{x}_\mathrm{s}$ (respectively $\mathbf{x}_0$) collided with an unstable equilibrium $\mathbf{x}_\mathrm{u}$ to one saddle-node point $\mathbf{x}_\mathrm{SNB}$. It should be noted that $\mathbf{x}_\mathrm{SNB}$ is an equilibrium, but unstable. Consequently, any load change would result in a voltage collapse [2]. Fig. 2.3 visualises the collision of the two equilibrium points at a saddle-node bifurcation for an increasing load demand by an exemplary $P(V)$-curve. As the power flow equations have a quadratic dependency on the voltage, two solutions, one stable and one unstable, exist. To analyse a saddle-node bifurcation, the power system in (2.1) can be linearised by calculating its Jacobian matrix J_sys

$$\frac{\mathrm{d}f(\mathbf{x}, \gamma)}{\mathrm{d}\mathbf{x}} = J_\mathrm{sys}(\mathbf{x}, \gamma). \tag{2.2}$$

At the saddle-node bifurcation, the system reaches its maximum load $p_\mathrm{Lmax} = \gamma_\mathrm{SNB}$ and is at an unstable equilibrium point. At this point, the determinant of the Jacobian and one

eigenvalue λ_1 become zero, whereas the other eigenvalues are non-zero [2]

$$0 = f(\mathbf{x}_{\mathrm{SNB}}, \gamma_{\mathrm{SNB}}), \tag{2.3}$$

$$0 = \det\left(J_{\mathrm{sys}}(\mathbf{x}_{\mathrm{SNB}}, \gamma_{\mathrm{SNB}})\right), \tag{2.4}$$

$$0 = \det\left(J_{\mathrm{sys}}(\mathbf{x}_{\mathrm{SNB}}, \gamma_{\mathrm{SNB}}) - \lambda \cdot \mathbf{I}\right), \tag{2.5}$$

$$\lambda_i \begin{cases} = 0 & \text{for } i = 1, \\ \neq 0 & \text{else}, \end{cases} \tag{2.6}$$

where $\mathbf{I}$ is the identity matrix. This means that by analysing the eigenvalues of a system by slowly varying the load power, the critical point of the $P(V)$-curve can be detected. In addition, (2.3) and (2.4) can be taken to directly calculate the bifurcation point [18]. Due to the high number of loads in a power system, one bifurcation point for each bus can be determined. Also, the variation of the loads does not have to be independent and can be combined, which further increases the complexity of finding a reasonable loadability margin. Here, loadability margin means the distance from the current operation point to the maximum loading p_{Lmax}. In addition, depending on the modelling of the power system, the Jacobian can be either calculated by a static or dynamic model. However, it should be noted that the result may differ if e.g. excitation limitations of synchronous generators are not included in the static model [19]. Overall, saddle-node bifurcation explains the phenomenon of voltage collapse for a slow load increase very precisely and can be analysed by linearizing the static or dynamic power system equations.

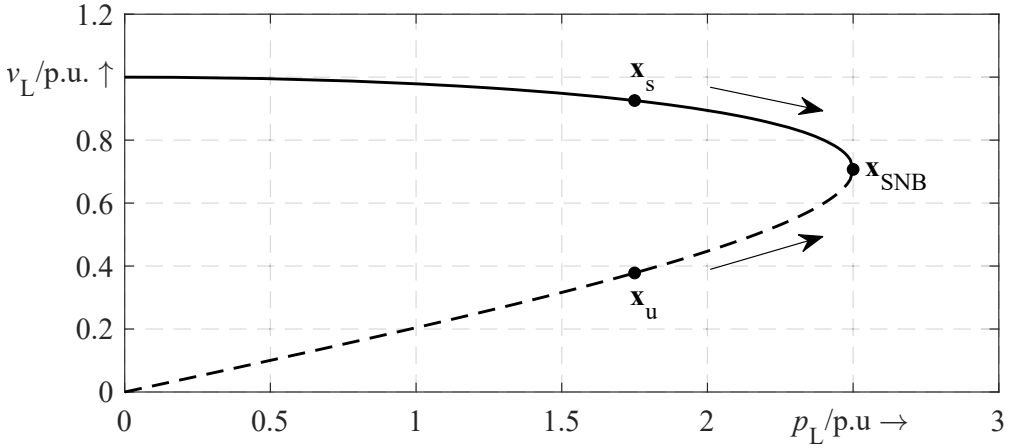

Figure 2.3: Example of a saddle-node bifurcation represented by a $P(V)$-curve

Hopf bifurcation

If there was previously a choice between static and dynamic modelling, dynamic equations must be used for Hopf bifurcation analyses [20]. In general, Hopf bifurcation is used to describe the phenomenon of voltage oscillations in a power system on a theoretical level. In the past, Hopf bifurcation theory has been applied to study voltage oscillations, e.g. in case of historical disturbances or by their occurrence due to automatic voltage regulators (AVRs) of synchronous generators [14, 21–23]. As already pointed out, for saddle-node bifurcation two equilibrium points collide into one equilibrium point. In the case of Hopf bifurcation, one equilibrium turns into a limit cycle with a periodic solution [24]. This means that the states are oscillating, which can either increase decay or stay in a stable periodic orbit. If a stable equilibrium changes to a stable limit cycle with an unstable equilibrium point this Hopf bifurcation is called supercritical. In contrast, if an unstable limit cycle with a stable equilibrium point changes to an unstable equilibrium point it is called subcritical [16]. Fig. 2.4 illustrates these two types of Hopf bifurcation.

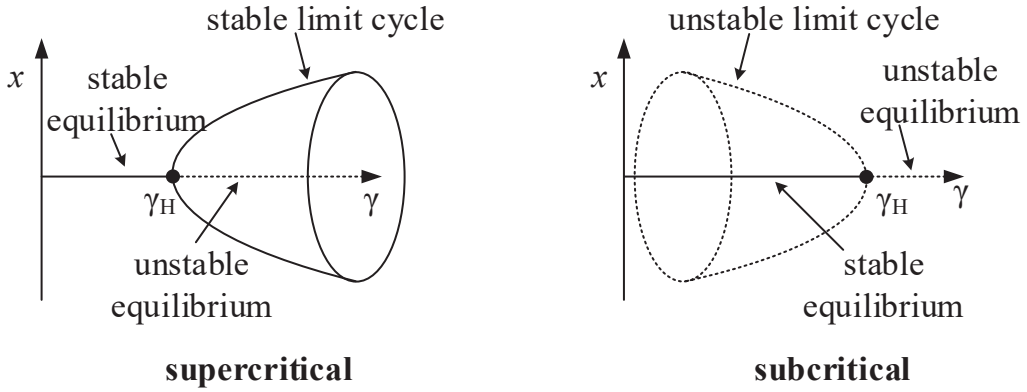

Figure 2.4: Illustration of super- and subcritical Hopf bifurcation (own representation, inspired by [25])

Hopf bifurcations occur if the system is at an equilibrium point and the Jacobian from (2.2) has a pair of purely imaginary eigenvalues [26]

$$\begin{aligned} & f(\mathbf{x}_{\mathrm{H}}, \gamma_{\mathrm{H}}) = 0, \\ & \det\left(J_{\mathrm{sys}}(\mathbf{x}_{\mathrm{H}}, \gamma_{\mathrm{H}}) - \lambda \cdot \mathbf{I}\right) = 0, \\ & \lambda_{1,2}(\gamma_{\mathrm{H}}) = \pm j\omega_{\mathrm{H}}. \end{aligned} \tag{2.7}$$

Here, γ_{H} is the varied parameter and $\mathbf{x}_{\mathrm{H}}$ is the corresponding state vector at Hopf bifurcation. In addition to the upper requirements the pair of complex eigenvalues have to cross the imaginary axes transversal, which is ensured if the the following expression is satisfied [26]

$$\frac{\mathrm{d}\Re\left\{\lambda_{1,2}(\gamma_{\mathrm{H}})\right\}}{\mathrm{d}\gamma} \neq 0. \tag{2.8}$$

The sign of the left-hand side in (2.8) determines if a birth or death of a limit cycle takes place. To analyse the stability of the periodic solution the eigenvalues of the monodromy matrix can be calculated [17, 26]. To get this matrix, the trajectories $\varphi\left(t, \mathbf{x}(t, \gamma)\right)$, which are the solutions of the states $\mathbf{x}(t, \gamma)$, have to be considered. If these trajectories are periodic, the following equation holds

$$\varphi\left(t, \mathbf{x}_0\right) = \varphi\left(t + T, \mathbf{x}_0\right), \tag{2.9}$$

where T is the period time and $\mathbf{x}_0$ are the initial states of the periodic solution. If the system is perturbed with $\mathbf{x}_0$+$\mathbf{d}_0$ a trajectory evolves in a distance $\mathbf{d}(t)$ to the periodic solution [26]

$$\mathbf{d}(t) = \varphi\left(t, \mathbf{x}_0 + \mathbf{d}_0\right) - \varphi\left(t, \mathbf{x}_0\right). \tag{2.10}$$

This distance is evaluated after one period T

$$\mathbf{d}(T) = \varphi\left(T, \mathbf{x}_0 + \mathbf{d}_0\right) - \varphi\left(T, \mathbf{x}_0\right), \tag{2.11}$$

and is linearised by its first Taylor expansion

$$\mathbf{d}(T) \approx \frac{\mathrm{d}\varphi\left(T, \mathbf{x}_0\right)}{\mathrm{d}\mathbf{x}}\mathbf{d}_0, \tag{2.12}$$

where

$$\frac{\mathrm{d}\varphi\left(T, \mathbf{x}_0\right)}{\mathrm{d}\mathbf{x}} = \mathbf{M}(\mathbf{x}_0, \gamma) \tag{2.13}$$

is the monodromy matrix $\mathbf{M}(\mathbf{x}_0, \gamma)$. In [26] a detailed explanation is given of how to get the monodromy matrix and the corresponding periodic solution by a boundary value problem. For the stability assessment of the limit cycles, the eigenvalues λ_{M} or Floquet multipliers of $\mathbf{M}(\mathbf{x}_0, \gamma)$ have to be calculated, where one eigenvalue lies on the unit circle. The periodic orbit is stable if the absolute value of all other eigenvalues is smaller than one. In contrast, the periodic solution is unstable if the absolute value of one eigenvalue is greater than one. Here, it has to be noted that the information about the stability is only for one particular periodic orbit for a given bifurcation parameter γ.

In summary, bifurcation theory describes the stability of a system by assuming a slow parameter change. This is important because in this case system equations can be linearised which simplifies the assessment. Differential and/or algebraic equations are typically used to model the system. Pure static models, containing only algebraic equations (usually power flow equations), have the advantage of smaller computational costs compared to dynamic models. However, static models may neglect important aspects of the system e.g. current limitation of power converters, fast power restoration of loads or OLTC tap changes. If these limits and discrete changes are taken into account, the system can also be interpreted as a hybrid system as the system equations change. As pointed out, bifurcation theory is used to describe phenomena of dynamic systems at stability boundaries, by linearised equations. However, to assess voltage stability not only for a slow parameter change but also for large disturbances, like e.g. short-circuits, non-linearities have to be taken into account, e.g. by time-domain simulations [13]. Bifurcation theory thus provides the fundamental system theoretical description of voltage stability, which helps to understand the underlying phenomena but does not cover the complete area of voltage stability assessment. Hence, bifurcation theory and hybrid system theory for non-linear phenomena could complement each other.

2.3 State of the art of voltage stability assessment

This subsection is mainly a summary of the literature review made in the Cigré and IEEE joint working group C4/C2.58/IEEE, where the author of this thesis has also participated in [27]. If available, the original references are given in this thesis, otherwise, reference is made to the technical brochure.

Besides the definition and fundamental principles of voltage stability, also its assessment methods are important for stability studies. In practical applications, the assessment method and its underlying stability threshold often determine if a system state is labelled stable or not. This subsection deals with state-of-the-art voltage stability assessment methods, with a focus on methods that can be applied in power electronics-dominated power systems. In general, transmission system operators evaluate voltage stability during long-term planning and operational studies as well as in real-time operation. In the case of long-term planning (2-10 years in advance), it is assessed if the power system has to be expanded due to identified voltage-related problems in the future. In the operational studies (2 years until one day before operation) it is assessed if the planned system will be in a safe condition, e.g.

in case of planned outages of power plants or transmission lines. For real-time assessment, the focus is set to possible contingencies or operating point changes that could endanger voltage stability. Also, it is assessed if the current system state is secure, based on the results of the state estimation. [27]

In all planning and operational phases different aspects of voltage stability are analysed by various assessment methods. On the one hand, short- or long-term voltage stability can be assessed. On the other hand, different methods can be applied to static or dynamic models or they take measurement results as input, in case of real-time operation. In Fig. 2.5 a taxonomy of voltage stability assessment methods with a selection of such methods is illustrated. As can be seen, methods applied to long-term studies are further classified into model, hybrid or measurement-based. For example, for a load flow or a $P(V)$-curve analysis a detailed power system model is needed, whereas some voltage stability indices only need voltage measurements to calculate the specific index. Therefore, some methods do not need a power system model to evaluate voltage stability, which is called *model-free* [28]. In the case of short-term assessment, no further classification is made, because nearly all methods only take the voltage magnitude as an input. Hence, the origin of the voltage value (from simulation or measurement) is of secondary importance, as most methods can be applied to both domains [27]. Next, a selection of voltage stability assessment methods is presented. The methods have been selected according to whether they can be used in power electronics-dominated power systems and if they can be applied to dynamic models. For a complete overview, the reader is referred to [27].

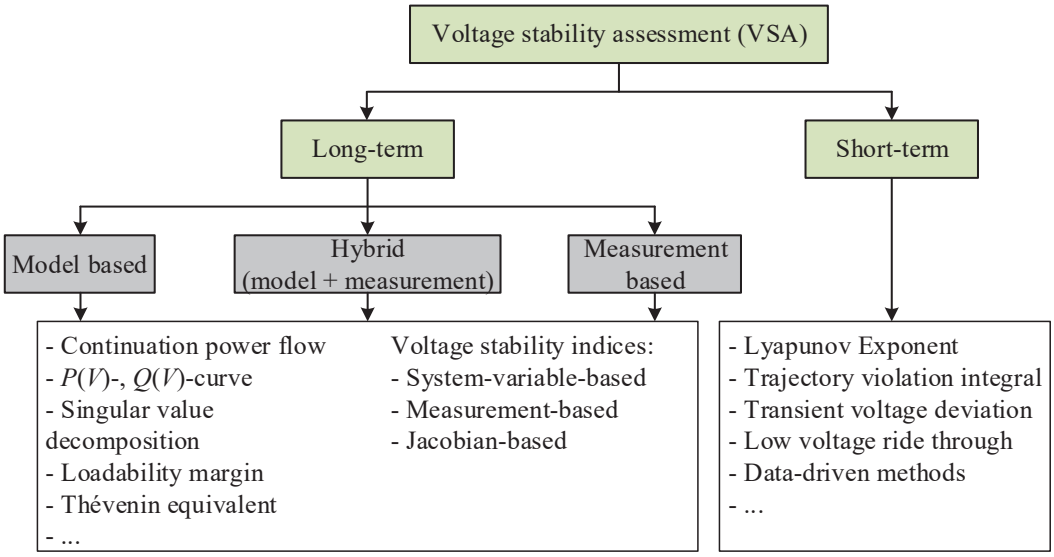

Figure 2.5: Taxonomy of voltage stability assessment (own illustration, inspired by [27])

2.3.1 Assessment methods for short-term voltage stability

Short-term voltage stability phenomena are fast and therefore their assessment has to be fast too, especially in real-time operation. Therefore, such evaluation methods are rated if they are real-time applicable with low computational costs. In addition, these methods should detect different phenomena of instability, like fault-induced delayed voltage recovery (FIDVR) or converter-driven slow interaction instability [28]. Since the focus of this thesis is to evaluate power systems with many power electronic devices, but not during real-time applications, the computational costs of these methods are of minor importance, but their applicability to various short-term phenomena is of high interest. Next, several assessment methods are reviewed by these requirements.

Low voltage ride-through curve

A basic assessment method for determining short-term voltage stability of power electronic generation is to check if they fulfil the low voltage ride-through (LVRT) requirements during a fault. These requirements are normally specified by grid codes of the power system operators and vary according to the type of generation and voltage level, e.g. in Germany by [11, 29–31], in North America by [32] and by European transmission system operators [33, 34]. In Fig. 2.6 an overview of different LVRT requirements for power electronic generation units (e.g. HVDC converters) at transmission level for different countries is given. Above the curves, the generators are not allowed to trip and shall stay connected to the grid. Note that it has to be kept in mind that there are also high voltage

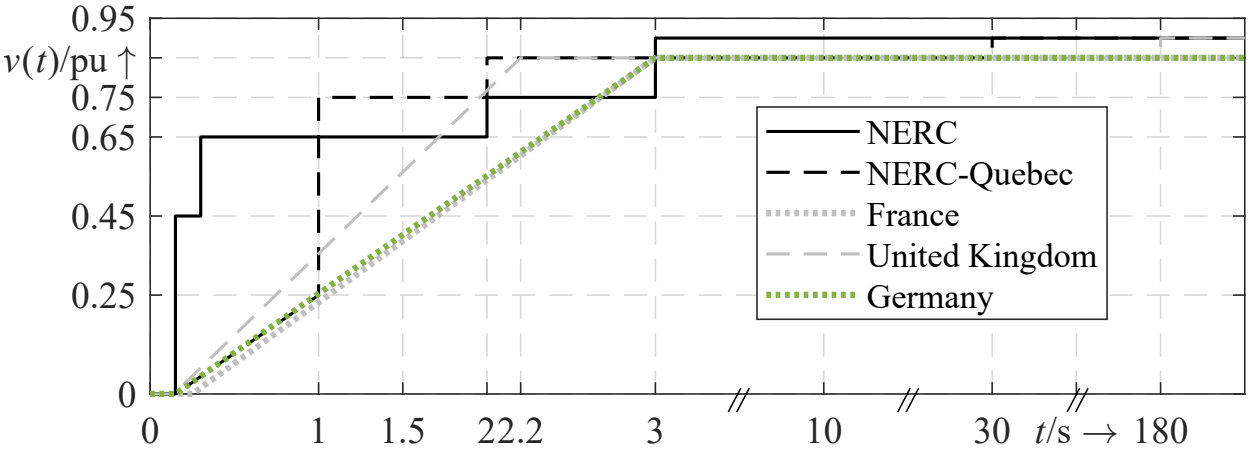

Figure 2.6: Low voltage ride-through requirements of different countries for power electronic generation at transmission level (based on [29, 32–34])

ride-through (HVRT) requirements to protect the devices and their insulation against high voltages, but these are not shown here. Below the LVRT curve, the generators can disconnect, but they do not have to. As can be seen in the figure, most grid codes demand a connection at zero voltage for 150 ms, which shall cover the time during the fault. After the fault, different requirements are made, based on the system operator's specifications.

In general, the advantages are the independence from a particular model and its explicit design for dynamic phenomena. In addition, the LVRT requirements in Fig. 2.6 are applied in real operation for power electronic generation. An advantage of this approach is that the confidence region of the model is taken more seriously and the result is just a binary output. The reason is that no dedicated protection equipment is modelled in this thesis. Therefore, any violation of the LVRT requirement could be assessed as unstable, like in [SL6].

Lyapunov Exponent

Since short- and long-term voltage stability contain non-linear dynamic phenomena, linearisation is often not possible. A fundamental method to estimate the stability or extent of chaos of a dynamic system is the Lyapunov exponent [35]. In illustrative terms, the Lyapunov exponent Γ indicates whether the trajectories of a dynamic system converge (negative exponent) or diverge (positive exponent) against each other over time (see Fig.2.7). For this, the distance $\delta(t)$ of the trajectories against each other is compared to some initial distance δ_0. This means that the Lyapunov exponent represents the exponential sensitivity to the initial condition [36]. The exponents are especially used when only measurements (i.e. sampled trajectories) and not the system equations are available. A first attempt to calculate Lyapunov exponents from time series data is made in [37] and has been further developed for more practical use in [35, 38]. In both papers, the focus lies on calculating the largest exponent of the system as this exponent ultimately determines if the trajectories converge to a stable equilibrium point. As this characteristic is important for stability assessment, many

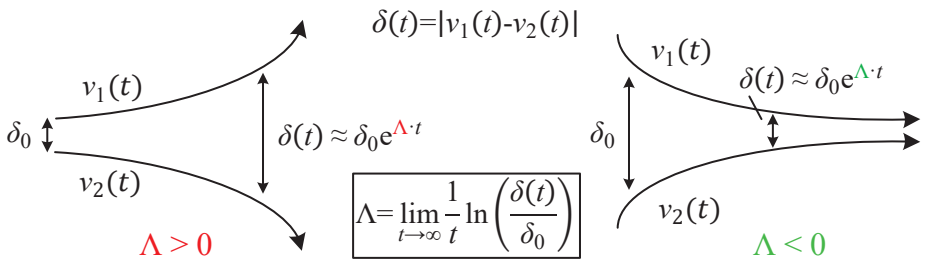

Figure 2.7: Concept of Lyapunov exponent (own presentation, based on [39])

works concentrate on the maximum Lyapunov exponent for power systems [40–43]. In [40, 42] an algorithm is proposed to calculate the largest exponent from voltage time series to assess short-term voltage stability using phase measurement unit (PMU) devices. Besides the maximum exponent, it is also possible to calculate an exponent for every bus and thus determine their contribution to the overall stability [42]. In general, the advantages of this assessment method are that it is model-free and capable of real-time monitoring based on PMU voltage measurement [40, 42]. In addition, it can be used in grids with a high share of power electronic components as it is suitable for various short-time phenomena [28]. As Lyapunov exponents can be calculated continuously, they can help to evaluate the stability of unknown phenomena and dynamics. In contrast to that, challenges lie in the measurement itself regarding noise, delay and too short measurement windows. An explanation of how Lyapunov exponents are calculated is given in [40].

Trajectory violation integral

While the previous methods focused more on the direct determination of stability, the trajectory violation integral (TVI) offers a greater quantitative comparability of voltage trajectories [28, 44]. The TVI requires upper and lower voltage limits, which can be set freely, but should be within or equal to the LVRT or HVRT requirements to be meaningful. The result of the TVI is a number that expresses how much the voltage trajectory violates the boundaries over a given period of time. In general, determination of the TVI begins after the fault. Also, the upper and lower boundaries decline exponentially over time to a stationary value, near the nominal voltage [44]. By this, it is taken into account that larger voltage deviations are tolerated more at the beginning, but that voltages should get back to nominal values after some time. Details of how to calculate the TVI are given in [44]. In Fig. 2.8 the TVI concept and corresponding values of exemplary voltage trajectories are represented. As can be seen, the TVI values rise for lower voltages. Yet, the TVI of the red trajectory is smaller compared to the yellow case, since the trajectory ends around $t = 3.1$ s, leading to a smaller integral value. Similar to the methods above, the advantages of the TVI concept are its model-freeness and usage in power electrics-dominated power systems [28]. The trajectories can also be better compared quantitatively. However, its quantitative nature is also the biggest disadvantage as no clear statement about the stability limit is given. In summary, this means that the biggest benefit of the TVI would be during the planning phase of a power system to compare different scenarios and optimise the trajectories after the general stability assessment.

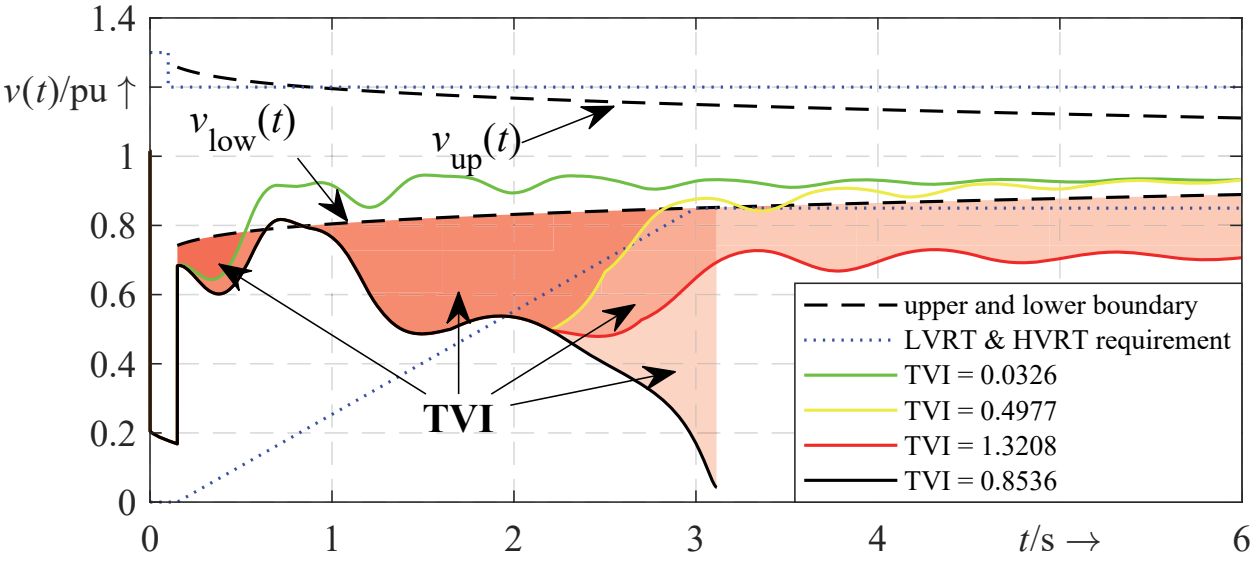

Figure 2.8: TVI values for different voltage trajectories ($t_f = 0.15\,\text{s}$, $t_{\text{end}} = 6.0\,\text{s}$, $v_{\text{st}} = 0.90\,\text{pu}$ and $\beta = 0.04$, see [44] for more information)

2.3.2 Assessment methods for long-term voltage stability

Dynamics of long-term voltage stability phenomena are mostly on a time scale from tens of seconds to several minutes, making them much slower compared to short-term effects. Therefore, in many voltage stability studies, the assessment of static models is widely used for this stability category [27, 45]. One of the reasons is that the actual transients are of minor importance, rather than their influence on steady-state voltages. In addition, even a static power flow calculation can include some sort of dynamics, such as OLTCs tapping. However, some aspects of long-term voltage stability can only be assessed by differential equations, like the point in time of the OEL of synchronous generators [1] or reactive power control of an active distribution network [46–48]. This implies that methods for assessing long-term voltage stability can be divided into static and dynamic. Next, a selection of the most applied assessment methods are described.

$P(V)$-curve and continuation power flow (CPF)

$P(V)$-curves are widely used for assessing long-term voltage stability [49]. To calculate such a curve, a sequence of power flows is calculated, increasing the power consumption of one or more loads after each calculation to determine the maximum power at which the system becomes unstable. In Section 2.2 the $P(V)$-curve has been used to visualise the concept of the collision of a stable and unstable operating point to a saddle-node bifurcation. In practical assessments often only the upper part of the $P(V)$-curve is calculated,

as only this part is inside the operational limits. Depending on the power flow algorithm, the tapping of OLTCs and reactive power limits of synchronous generators can be incorporated, leading to a non-smooth $P(V)$-curve. In the vicinity of the maximum load, numerical problems may occur in the power flow calculation due to the Jacobian matrix approaching singularity. To overcome this issue, the CPF can be used which guarantees that the Jacobian does not get singular near the maximum load. Details of how to implement it are given in [50]. The advantages of the CPF are that there are no convergence problems near the maximum load and that sensitivity information can be obtained, e.g. to identify the weakest bus. Also, the algorithm can be extended to include discrete events like reactive power limits [51] or to include unbalanced phases [52]. Next to this, there is also the concept of $Q(V)$-curve to determine the critical reactive power [53]. In summary, several methods exist to compute accurately the $P(V)$-curve with almost no convergence problems and incorporating discrete events such as reactive power limits. However, they can only deal with static models.

Voltage Stability Indices

Other methods for the assessment of voltage stability are voltage stability indices (VSIs). Their main purpose is to predict voltage instability, either in online or offline studies [15]. The index should have a clear stability threshold like one or zero so that the distance of the current operation point to voltage instability can be quantified. As noted in [15, 27], most indices are based on power flow equations and do not explicitly include dynamics for fast computation. A vast number of static indices exist in the literature. They can be classified differently, based on the focus of the analyses [54–56]. In Fig. 2.9 an overview of one possible classification of VSIs is illustrated. The VSIs in the first category, system-variable-

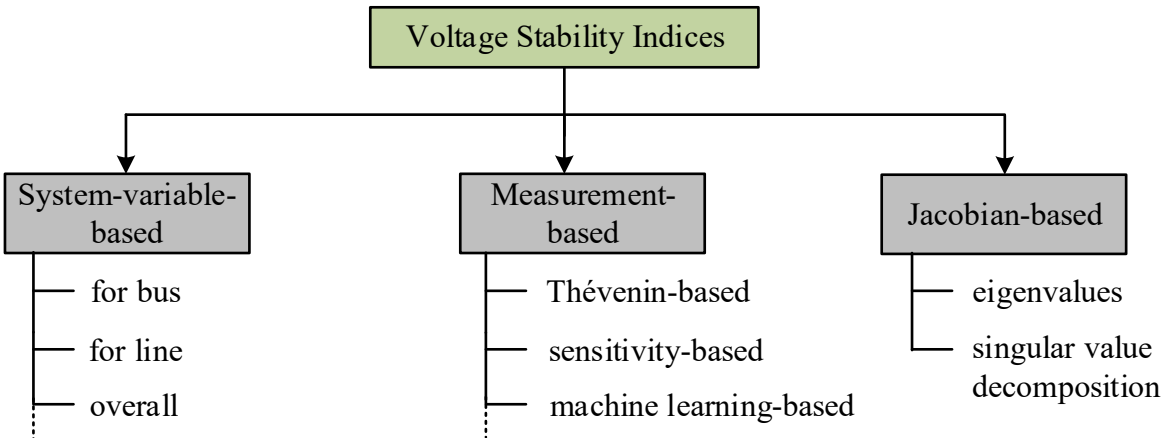

Figure 2.9: Composite classification of VSIs, based on the classifications in [54–56]

based, are calculated either for a bus, a line or for the whole system. For a bus, mainly its voltage magnitude value and the injected current are used to assess voltage stability at that particular bus [54]. In contrast, line VSIs are more used in the identification of weak connections between two buses. In general, the VSIs of multiple buses and lines can be determined to identify vulnerable grid zones. Jacobian-based VSIs can be roughly divided into eigenvalue and singular value decomposition indices. Both approaches can be applied either to the power flow equations or the full set of differential and algebraic equations. The last category is about measurement-based VSIs. One approach is to use the measurements to calculate a Thévenin equivalent of the system and to compare it to a Thévenin equivalent of the load under study. Overall, VSIs can be used for online or offline studies and mostly assess static or long-term voltage stability at specific buses and lines or for the whole system.

Evaluation of long-term voltage stability by time-domain simulations

Although long-term voltage stability is evaluated often by static assessment methods, time-domain simulations are needed, if multiple time-dependent assets are involved [13]. Thus, by dynamic simulations, these temporal dependencies can be represented accurately. In addition, the dynamic simulations can reveal if the timing of control actions leads to stability or how long it takes until the system becomes unstable. In contrast to LVRT limits for short-term effects, no additional thresholds are defined for long-term phenomena, despite the general voltage limits for steady-state and quasi-steady state conditions [11]. In the German grid code for the extra-high voltage level, all voltages shall always be between 1.05 pu and 0.90 pu. Also, the generation units shall stay connected if the voltage is between 0.85 pu and 0.90 pu, but only for 60 minutes. These static thresholds can be taken as the main indicators in assessment methods, e.g. in [46] for evaluating long-term voltage stability. On the one hand, it is assessed if post-disturbance voltages stay above this limit and on the other hand, if the system becomes unstable and the voltages collapse. In this context, in [48], the impact of active distribution networks on emergency controls for long-term voltage stability is analysed, where the possible final system state is classified by traffic light colours. A different approach, called local identification of voltage emergency situations (LIVES), is proposed in [57], where the voltage deviation within two OLTC time delays is measured and if they are both negative, an alarm is raised for subsequent emergency control actions. Although this method is similar to other indices described previously, its main difference is that it takes into account the temporal dependencies of OLTCs, which is why dynamic simulations are necessary. A generalisation of this method is done in [58] to the new LIVES index (NLI). The concept is that the tapping of the OLTC is seen as a change in the con-

ductance ΔG of the load admittance on the primary side of the transformer. Besides, in [59] the LIVES method has been further extended (eLIVES) to account for different OLTC time delays and other events that affect the voltage during the measurement. For this, it uses a linear regression model with a recursive least square method to identify the overall voltage slope, while only requiring a small set of measurements. The authors in [60] take this method and incorporate it into a multi-agent system, where the agents notice the OLTC tapping and raise a warning if the voltage slope is negative. In summary, most of the described time-domain methods aim at predicting long-term voltage stability and may initiate corrective measures to stabilise the system. A disadvantage is that, due to the complexity of non-linear dynamic systems, they often do not have a clear stability threshold. Nevertheless, if linearisation is not feasible for specific disturbances, like short circuits, time-domain simulations are the main choice.

2.4 Current practice of modelling power electronics for voltage stability analysis

In this section, the current practice of power system modelling for voltage stability in industry and research is outlined. Emphasis is placed on the modelling of power electronic components for short- and long-term voltage stability studies.

Modelling of grid-forming and grid-following converters

Next, an overview is given of current practice in modelling power electronic converters for voltage stability studies, e.g. photovoltaic (PV), wind turbine or HVDC systems. Here, only dynamic models are considered, as static models are normally simple injections and are not in the scope of this thesis.

The literature review reveals that in most references about long-term voltage stability, the focus lies on grid-following converters within the phasor domain [46–48, 61–63, SL8, SL5]. Here, the references mostly concentrate on representing the outer power control loop and not the fast inner current control loop. However, the current limitation is considered in all references but differs in the prioritisation of reactive or active current in the case of low voltages. In addition, self-developed models are used in most references. In contrast, in [46] the control is based on the Western Electricity Coordinating Council generic control of PV systems [64], whereas in [47] the respective generic wind turbine models from [65] are used.

For short-term voltage stability, the modelling and simulation of grid-following converters are also mainly conducted in the phasor domain [28, 66–69], while only a few are analysed in the EMT domain [70, 71]. A comparison of both simulation domains is done in [72], where it is stated that the critical clearing times are similar in both domains, but differ regarding some voltage dynamics. In all cases, a strong focus is set on accurate modelling of the current limitation and its active or reactive current prioritisation. In contrast to long-term voltage stability studies, the inner current control is considered in most studies [28, 67, 68, 72], but not in [66, 69]. This shows that for short-term voltage stability studies the modelling complexity tends to increase and that both simulation domains are used, unlike long-term voltage stability.

In case of GFM converters (see a more detailed explanation in Chapter 4) the common research focus clearly lies in short-term dynamics [73–85]. In all these studies, the EMT domain has been chosen, except in [85]. In all references, the converter control structure is modelled with a high degree of detail. Yet, the converter itself is represented by an average model, as in the above references on grid-following converters. Moreover, some of these detailed models are also used to investigate small-signal in terms of converter-driven stability [86]. In general, many references focus on the stability of post-fault synchronisation with the grid, as this is a known challenge for GFM converters [73–76]. Since the principles of power synchronisation of GFM converters are similar to those of synchronous generators, some references classify these dynamics as transient (rotor angle) stability [77–80]. Besides, frequency stability is also an important research field concerning GFM converters, as they could replace the inertia of synchronous generators in future power systems [81–83, 87, 88]. In contrast, voltage stability phenomena have received little attention so far, e.g. in [84] for short-term voltage stability. This emphasises the research gap in terms of GFM converters and voltage stability.

Load Modelling

As stated in Section 2.1, voltage instability is mainly driven by loads. Therefore, load dynamics play an important role, as they have a decisive influence on the course of the voltage [1]. A survey in [89] identified the various load models (constant power, current, impedance,...) that are mainly used for dynamic power system studies. A comprehensive overview of static and dynamic load models can be found in [90], which also describes the two main approaches that are used to select and parametrise the load models. The first approach is component-based, which means the load model mainly consists of the physical and electrical representation of the actual load device. In contrast, in the measurement-

based approach, measured data are used to configure a model to fit this data. Both approaches have advantages and disadvantages. On the one hand, the component-based approach is suitable for a very close representation of the real load dynamics. On the other hand, it can be too cumbersome and computationally expensive for large-scale grid simulations. In contrast, the measurement-based approach has its advantages in this regard, as it can capture different load characteristics in one or a composition of generic models. A disadvantage is, that the measured data is only valid for a specific location, time and type of disturbance. [90]

For power system stability analyses in the phasor domain, the above-mentioned load models have been extensively used in the past [1, 49, 91]. However, some of these models cannot be used directly in the EMT domain, especially for the so-called *static* load models, e.g. constant power, constant current and exponential model. This is because they assume a well-defined voltage magnitude and angle at all time steps. For example, the voltage dependency of an exponential load model can be expressed by

$$P(V) = P_0 \left(\frac{|\underline{V}|}{V_0} \right)^{\alpha}, \tag{2.14}$$

where P_0 is the base active power, V_0 the base voltage magnitude, α the degree of voltage dependency and $|\underline{V}|$ the magnitude of the complex load voltage. In a phasor simulation, (2.14) can be used directly, as the real and imaginary parts of the voltage are normally states and thus the magnitude of the voltage can be easily calculated. However, in an EMT simulation, the magnitude has to be calculated separately by a Fourier- or a dq-transformation. Therefore, such load models need to be given special treatment (see Section 6.1 for the inclusion of a constant current load in an EMT environment).

As constant power loads in phasor simulations are often motivated by representing power electronic loads, the above-mentioned modelling differences are also of great importance for this load type. In general, power electronic loads can be categorised into

- switch-mode power supplies (SMPS)-based, e.g. information and communication technology (ICT) devices or consumer electronics like televisions
- lighting loads, e.g. LEDs or compact fluorescent lamps
- adjustable or variable speed drives, e.g. pumps

as they all contain power electronic components [4, 92]. Although this is not considered in detail in this work, it is pointed out that sector coupling, e.g. to the gas or heating

network, adds new electrical consumers that are also connected via power electronics and can endanger voltage stability [93]. Due to their complex and non-linear behaviour, many different static and dynamic power electronic load models have been developed in recent research [4, 94–101]. In detail, the authors in [92, 95–97] derive generic equivalent circuits from detailed circuits of adjustable speed drives from which they determine steady-state ZIP and exponential load models. However, these loads do not act like constant power loads, especially in the case of large voltage fluctuations [94]. In contrast to this, in [99–101] different types of power electronic loads like LED, electrical vehicle chargers and SMPS are measured and equivalent circuits for the EMT domain are developed to match the measurements. Similarly, in [4] an approach is presented in which detailed EMT models are compared to laboratory measurements. State-space averaging of power electronic loads within a hybrid systems context is carried out in [98] to derive models for small signal stability. In [94], the composite power response of multiple power electronic loads during and after a voltage sag is derived for phasor simulations. However, the derived model is difficult to handle, as the power response is a time-domain function and detailed information about the fault duration and shape of the voltage sag have to be known before. In contrast to this, an actual transient stability load model is developed in [102], which covers the fundamental power response of an induction motor with speed control. Similarly, in [103], a part of the composite load model consists of an electronic part for phasor simulations, where different voltage thresholds are included to incorporate the disconnection of these loads at low voltages.

In summary, this literature review reveals a wide variety of static and dynamic power electronic load models. However, detailed examinations of voltage stability for this load type are still missing. It is therefore necessary to first analyse what level of modelling detail is required and how this load type can be represented in the phasor and EMT domain. As there exists a large number of different power electronic load types, the focus in this thesis is on SMPS-based loads, as they represent one of the main types. Following this, their impact on short- and long-term voltage stability must be thoroughly investigated.

2.5 Conclusion and derivation of methodical approach

Next, a summary of this chapter is given to derive the subsequent methodical procedure of this thesis. The repetition of the definition of voltage stability showed its generality, allowing it to be applied even to a system that is dominated by power electronics. Although many power systems are undergoing a significant change, the fundamental requirements for system stability based on power equilibrium and technical operating limits do not change. What is changing, however, is how voltages and currents (and thus the power) of the grid are affected by the power electronic generators and loads. Since the converter is the central interface to the power system, its physical connection and its control can evoke new grid dynamics, especially through discrete events. For this reason, the main focus of this thesis is to determine how to model the continuous and discrete dynamics of power electronic devices properly and what their impact on voltage stability is.

From a system theory perspective, voltage stability can be described by bifurcation theory. In general, it is good for describing the theory of small-signal stability. However, it reaches its limits for large-signal stability due to its linearisation. Especially for short-term effects like short-circuits the non-linearities and discontinuities have to be considered for an accurate stability analysis. Therefore, this thesis concentrates on dynamic stability analyses based on hybrid system theory. In Chapter 3 it is more elaborated on which methods can help to assess voltage stability.

As shown in this chapter, several assessment methods for short- and long-term voltage stability can be used for power electronics-dominated systems. Most of these methods can be used with measurement and simulation data as they are model-free and mainly take voltage magnitudes as input. As the LVRT and HVRT requirements provide a clear stability threshold compared to the Lyapunov exponent or TVI, these requirements are used as an assessment method for short-term voltage stability. Therefore, for this thesis, the LVRT and HVRT requirements of the German grid codes are taken for three-phase faults [29]. Similarly, as static approaches like $P(V)$-curves, CPF and voltage stability indices are not suitable for dynamic phenomena, time-domain simulations are used to analyse long-term phenomena in this thesis. Especially due to the rapid increase in today's computer system performance, the costs for dynamic simulations have become low, making it easy to supplement static analyses. In addition, as the focus is not on predicting instability during the simulation, methods such as the new LIVES index are also not considered here. Instead, the voltage trajectories of the time-domain simulations are used to compare whether the

system has reached an equilibrium and whether the voltages are in a safe operating region. In this way, the results can be analysed more flexibly.

The literature review revealed contradictional practices exist between conventional voltage stability and power electronics analysis. Phasor simulations are mostly used for voltage stability analyses, whereas the current practice lies in the EMT domain of modelling power electronics. Therefore, both domains are analysed to determine their impact on stability and differences in power system dynamics in this thesis. As it is shown that there is a research gap in terms of GFM converters and voltage stability, the focus of this thesis is on this topic. Special attention is given to the current limitation of GFM converters as it changes their dynamics discretely. Similarly, power electronic loads can change their dynamics discretely, e.g. at low voltages, leading to fluctuating power consumption or even disconnection from the grid. Therefore, the voltage stability of this type of load is also investigated, which leads to the second focus of this thesis. As GFM converters and power electronic loads include discrete dynamics, their modelling approach can be motivated by a hybrid system approach with continuous and discrete dynamics. As hybrid systems differ in terms of their formal modelling, their dynamic phenomena and stability properties are discussed in more detail in the next chapter.

3 Hybrid system theory in the context of power systems

In this chapter, the hybrid system modelling approach in the context of power systems is outlined. In general, a hybrid dynamical system (hereafter referred to as *hybrid system*) consists of continuous and discrete states. The continuous states can be described by differential and algebraic equations, whereas the discrete states are determined by events, including switching dynamics and jump phenomena (see Section 3.2). In this context, *switching* means that the differential and algebraic equations change after an event. *Jumping* describes the discrete change of a state after an event. This means that a discrete state only changes if an event condition is satisfied (e.g. time or state-based) and is thus constant between these events. These two event characteristics are the main difference to pure continuous systems. They can take place together or alone during an event. If the modelling approach of hybrid systems is now transferred to power systems, the continuous states would be represented by voltages, currents or powers and behave according to the physical laws given by differential and algebraic equations. The discrete states could represent controller limits (e.g. the current limitation of a converter), operation modes, protection equipment or assets with discrete characteristics like OLTC or power electronics. Especially for the latter, the hybrid system modelling approach is chosen in this thesis, as power electronic assets like converters and loads can have a variety of switching dynamics and jump phenomena as will be shown in Chapter 4 and 5. In general, modelling the power system as a hybrid system is just a logical extension, as all power system components can be described by this approach. If the discrete states are neglected, the classic power system modelling approach is obtained as a differential and algebraic system. However, in such a case not all relevant dynamics are maybe present to accurately investigate the stability of the system.

The remainder of the chapter is organised as follows. First, as a motivation, a literature review of how hybrid system theory has been applied to power systems is given in Section 3.1. Second, multiple formal and mathematical descriptions of hybrid dynamical systems are given in Section 3.2. In Section 3.3.1, the dynamic phenomena and stability properties of hybrid systems and their differences from continuous systems are outlined. Afterwards, a specific application of the hybrid system theory to the analysis of hybrid power systems by trajectory sensitivities is given in Section 3.4. In the end, Section 3.5 concludes how the hybrid system theory will be applied in this thesis to analyse the impact of power electronics on voltage stability.

3.1 Literature review: Application of hybrid system theory to power systems

Over the last two to three decades, interest in considering power systems as hybrid systems has increased significantly. As outlined in [104], especially for large-disturbance analysis of power systems, the hybrid system approach can be advantageous, as complex behaviour can result from the interaction of continuous and discrete dynamics. However, in the past, stability analyses were often divided into only three different stages, such as *pre-disturbance, disturbance* and *post-disturbance* conditions [12]. In this way, the hybrid nature is only implicitly taken into account when disturbances affect power systems. As the system was considered not explicitly as a hybrid system, the special characteristics regarding stability and hybrid phenomena (cf. Section 3.3) may have been missed. This raises the question of whether a power system must always be modelled and analysed as a hybrid system. For many large disturbance stability analyses, the hybrid system approach is not explicitly considered, although they contain discrete dynamics (see e.g. [28, 46–48, 61, 62, 66, 68]). One reason for this could be that advanced simulation software removes the need for users to think about implementing discontinuities or changes in the dynamic equations. This raises the question of what additional value can be obtained if the power system is explicitly considered a hybrid system. To address this question, a literature review is carried out to determine the additional value. In order to systematically identify how hybrid system theory is used in a power system context, the review will focus sequentially on

- the origin of the discrete dynamics and discontinuities,
- the formal modelling approach (e.g. hybrid automaton, switched system, etc.),
- techniques and methods for analysing hybrid power systems and their added value.

The first key point serves to determine the reasons for modelling the power system as a hybrid system. The second key point is to find out on which mathematical basis the modelling is carried out, whereby the most common approaches are to be identified. These findings are also used as an input for Section 3.2. Finally, through the third key point, the advantages arising from the explicit use of the hybrid modelling approach are presented. It should be noted that only references that explicitly consider the hybrid systems approach are used. The reason for this is that many references include discrete dynamics or discontinuities in their analyses, but do not consider them from a hybrid systems perspective. Therefore, no statements can be made for them.

Origin of discrete dynamics and discontinuities

In general, the origin of discrete dynamics can be categorised into three modelling layers of a power system: physical layer, control layer and communication layer. The physical layer represents the actual grid devices such as power lines, transformers, loads and generators. Here the failure of power lines, generators, loads or short-circuits are identified as a source of discontinuity [105–108]. Also the discrete tap changes of OLTCs [104, 109–111] or switching capacitors [112] introduce switching dynamics. At the control layer, the switching of different control modes in case of changing conditions at the physical layer is also a source of discrete or switching dynamics, as described in [113–115]. Similarly, a hybrid controller for different grid conditions can be derived based on the connected and active generators and storage devices [116]. Also, discontinuities within a controller, such as a limited PI controller with anti-windup, can lead to hybrid phenomena as in [117, 118]. Discrete states can also occur at the communication layer as shown in [119]. The discrete states represent different modes in the communication network and power system states (e.g. normal, alert or emergency). Overall, this shows that the origin of discrete dynamics and discontinuities is highly variable and depends on the domain of interest.

Hybrid system modelling approach

Next, an overview of formal modelling approaches based on discrete dynamics is given. The hybrid automaton approach is particularly chosen for modelling different control modes as shown in [113, 115, 116]. It is also used to represent the status of a cyber-physical energy system using the discrete states as performance indicators [119]. It is also used to represent the time-varying generation and load mix in interconnected microgrids and the emerging disturbances in [108]. This small collection demonstrates the general applicability of hybrid automata to a wide range of applications. A piecewise affine (PWA) or switching ordinary differential equation (ODE) approach is taken in [114] to enable power converters to switch among different control algorithms. The same approach is used in [117] to model a PI controller with anti-windup. Similarly, switching DAE is used in [106] to account for the changing algebraic network equations in the case of line tripping. To capture the discrete dynamics in a power system, e.g. by tap changes of OLTC, the differential-algebraic-discrete system (DADS) model has been introduced in [104, 109]. This model is extended to the differential-algebraic impulsive switched system (DAIS) model to capture the impulsive behaviour of the continuous states, which is used in [105, 110–112]. Moreover, the DAIS approach is also chosen for modelling PI controllers with anti-windup [118]. As the DAIS is quite general, similar to hybrid automata, it can be used for a variety of applica-

tions. In contrast to the previous references, for the static analysis of component failures, such as line tripping, the discrete-event system is used in [107]. Here each discrete state represents the status of the component and an event triggers a switch to disconnect or connect the component. Overall, the formal modelling approaches can be grouped into hybrid automata, switched systems, PWA, DADS/DAIS and discrete-event systems. The review also reveals that the same discrete dynamics, e.g. PI controller with anti-windup, can be modelled by different approaches. The reasons for choosing a hybrid modelling approach therefore do not necessarily lie in the discrete dynamics per se, but rather in the analysis methods subsequently applied, which are described next.

Techniques and methods for analysing hybrid power systems

In the case of hybrid automata, reachability analysis is one of the most relevant analysis methods for determining the state-space region that can be reached from an initial state [108, 115, 116]. As a result, it is possible to reduce the possibly unbounded state space to a subspace that consists of the reachable subsets. This can be used to check whether undesirable states are avoided or whether a target region is reachable from a given location. In the context of power system operation, this allows it to analyse the mode transition management of a virtual power plant [116]. Similarly, reachable dynamics for different types of disturbances in microgrids can be determined [108]. Furthermore, it is also possible to detect false data injection in a cyber-physical energy system by comparing the actual invariants of the system with candidate invariants [115].

For the discrete-event system, which can be regarded as a subclass of hybrid automata, the technique of parallel composition of automata is used in [107]. The idea is that two or more separate automata can be combined into a single automaton if some properties are the same. Through this common automaton, the individual subsystems can be analysed as a whole, e.g. by reachability analysis. In [107], individual automata of generators, loads and lines are combined to obtain a complete model, which is subsequently used to identify cascading failures and design a supervisory control to initiate countermeasures.

In [114] a dwell-time stability analysis method for switched ODE is used. The aim of this method is to derive sufficient stability conditions where the dwell time declares the minimum waiting time between two successive switches. Also for switched ODE, in [117] Filippov theory for anti-windup PI controllers is used to avoid chattering and deadlock situations (see Section 3.3.1 for more information). The theory helps to define sufficient transition conditions to prevent the PI controller from chattering by creating a new state

where the trajectory can evolve smoothly (or slide) along the discontinuous surface. By this, numerical problems are avoided.

In the case of DADS, the trajectory sensitivity analysis with discontinuities has been developed in [109]. The work extends the sensitivity calculations from continuous systems (see e.g. [120]) by giving instructions on how to calculate time-dependent sensitivities also for switching equations and impulsive behaviour in hybrid systems. In general, trajectory sensitivities describe how a trajectory would change over time for small changes in initial conditions or parameters. This can be used, for example, to determine the degree of influence of certain control parameters on a trajectory. Furthermore, this method can be applied to non-linear systems and new trajectories can be approximated for small parameter changes without the need for additional time-domain simulation. These sensitivities are also used in [110, 111]. Here, inverse problems (parameter estimation of a model to fit the measurements of its real counterpart) are of interest to tune power system models and to determine uncertainties in trajectories by worst-case parameter scenarios. Based on these sensitivities, there is also the shooting method for grazing phenomena, used in [105, 112]. Here, the trajectory sensitivities are applied to determine a set of parameters where the surface of a triggering condition in the state space is only tangentially touched (or grazed). As a result, parameter regions can be identified where an event or discontinuity will or will not be triggered. In this way, overvoltage phenomena [105] or non-linear limit cycles [105] can be mitigated.

In summary, the methods and techniques described above show that additional value can be added to power system analysis when it is considered as a hybrid system. In some cases, this is even necessary, e.g. for calculating trajectory sensitivities. Since detailed dynamic power system models almost always contain discontinuities (e.g. from power electronics, switching control modes, constraints, outages, protection devices and communication technologies), it should be natural to consider them from a hybrid system perspective. Specifically, by knowing the origin of discontinuities and other discrete dynamics within a power system model, an appropriate modelling approach can be chosen. Based on this, appropriate analysis methods for stability assessment or other types of investigations can be selected. In this way, added value can be created when power systems are explicitly considered as hybrid systems. Next, in Section 3.2, the formal modelling of hybrid systems is described using some of the approaches mentioned above.

3.2 Formal modelling of hybrid systems

In the following section, an introduction to the formal modelling of hybrid systems is given. Some common approaches are presented like hybrid automata and switched systems and DADS. In this context, it should be noted that some of the modelling approaches are strongly related or encompass each other [5, 121]. Thus, by providing various descriptions of hybrid system approaches, similarities and differences can be pointed out.

3.2.1 Hybrid automaton

A hybrid automaton combines the DAEs of a dynamic continuous system with a finite state machine or transition system, which are known from theoretical computer science [5]. In general, a hybrid automaton H can be described by an 8-tuple [5]

$$H = (\mathbf{q}, \mathbf{x}, \boldsymbol{f}, \mathit{Init}, \mathit{Inv}, \Theta, \mathcal{G}, \mathcal{R}), \tag{3.1}$$

where

- $\mathbf{q} = [q_1, ..., q_k]^{\mathrm{T}}$ is a vector with k discrete states,
- $\mathbf{x} = [x_1, ..., x_n]^{\mathrm{T}}$ is a vector with n continuous states (differential and algebraic),
- $\boldsymbol{f} = \mathbf{q} \times \mathbb{R}^n \rightarrow \mathbb{R}^n$ is an activity function or set of vector fields $\dot{\mathbf{x}} = \boldsymbol{f}(\mathbf{q}, \mathbf{x})$,
- $\mathit{Init} \subset \mathbf{q} \times \mathbb{R}^n$ is the set of initial states $(\mathbf{q}_{,0}, \boldsymbol{x}_0)$,
- $\mathit{Inv} : \mathbf{q} \times 2^{\mathbb{R}^n}$ describe the invariants at the discrete states or *locations*,
- $\Theta \subseteq \mathbf{q} \times \mathbf{q}$ is a set of transition relations,
- $\mathcal{G} : \Theta \rightarrow 2^{\mathbb{R}^n}$ is a set of guard conditions,
- $\mathcal{R} : \Theta \rightarrow 2^{\mathbb{R}^n} \times 2^{\mathbb{R}^n}$ is the reset map.

The discrete states of a hybrid automaton are also called *locations*. This means that a specific set of discrete states $\mathbf{q}_1$ form a location in which one vector field $\dot{\mathbf{x}} = f_{\mathbf{q}_1}(\mathbf{x})$ is active, where the continuous states evolve. For each location, there exists a set of invariants that define the domain of the active vector field $f_{\mathbf{q}_1}$ and determine the admissible state-space of the continuous states. A discrete state change can be initiated if a guard condition becomes

true. In addition, if a continuous state violates a condition of the invariants then also a discrete transition occurs. In this context, invariants and guard conditions play complementary roles by defining when a discrete state change happens. For general hybrid automata, guard conditions describe that a transition may occur, whereas invariants describe that a transition must take place. Which transition takes place in a hybrid automaton is described by the set of transition relations Θ. Based on this set, a guard condition is constructed for every relation that determines when a transition happens. Furthermore, if a transition causes a state jump, the reset map $\mathcal{R}$ defines how the current states $\mathbf{x}^-$ (before the transition) jumps to the new values $\mathbf{x}^+$ (after the transition) before they evolve according to the new active vector field. However, as not every discrete state change leads to state jumps the reset map of a transition can also be $\mathbf{x}^+ = \mathbf{x}^-$. [5]

Fig. 3.1 shows a schematic hybrid automaton to illustrate the formal mathematical description. Within this figure, each discrete state is represented by a circle, whereas each transition is displayed by a directed edge. The discrete states are completed by showing the corresponding active vector field and its invariants. For the transition of a discrete state, a guard function and its reset map are given for each edge. This also applies to *loops*, which are transitions where the starting and finishing discrete states are identical. The initial conditions are given by $(q_0, \mathbf{x}_0)$ together with an arrow pointing to the first state.

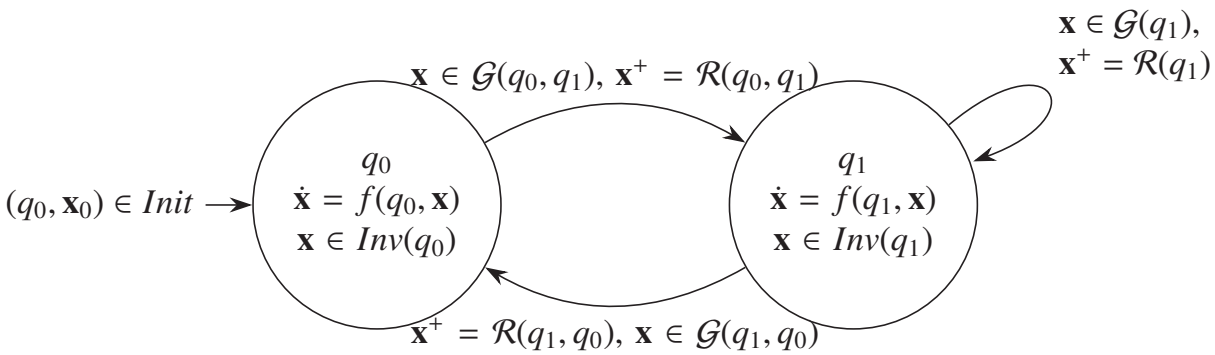

Figure 3.1: Schematic illustration of a hybrid automaton with two discrete states and three transitions (own representation, inspired by [5])

3.2.2 Switched Systems

A switched system is a hybrid system that consists of several subsystems with differential (and algebraic) equations where an internal logic determines which set of equations are active. An illustration of an exemplary switched system is given in Fig. 3.2. In general, a non-linear switched system can be described by [5]

$$\begin{aligned} \dot{\mathbf{x}} &= \boldsymbol{f}(\mathbf{x}, \mathbf{y}, \mathbf{q}, \mathbf{u}), \\ \mathbf{0} &= \boldsymbol{g}(\mathbf{x}, \mathbf{y}, \mathbf{q}, \mathbf{u}), \end{aligned} \tag{3.2}$$

where

- $\mathbf{x} = [x_1, .., x_n]^{\mathrm{T}}$ is a vector with n differential states,
- $\mathbf{y} = [y_1, .., y_m]^{\mathrm{T}}$ is a vector with m algebraic states,
- $\mathbf{q} = [q_1, .., q_k]^{\mathrm{T}}$ is a vector with k discrete states,
- $\mathbf{u} = [u_1, .., u_l]^{\mathrm{T}}$ is a vector with l input signals,
- $\boldsymbol{f} = \left\{ f_{\mathbf{q}_1}(\mathbf{x}, \mathbf{y}, \mathbf{u}), ..., f_{\mathbf{q}_p}(\mathbf{x}, \mathbf{y}, \mathbf{u}) \right\}$ is a set of vector fields,
- $\boldsymbol{g} = \left\{ g_{\mathbf{q}_1}(\mathbf{x}, \mathbf{y}, \mathbf{u}), ..., g_{\mathbf{q}_p}(\mathbf{x}, \mathbf{y}, \mathbf{u}) \right\}$ a set of algebraic equations.

A big difference between hybrid automata and switched systems is, that for the continuous states of the switched system, the rest map $\mathcal{R}$ is the identity map, leading to no state jumps after a switch [121, 122]. Therefore, only the discrete states are allowed to jump, which are determined by the switching logic (see Fig 3.2). In the case of a switched differential-algebraic system, state jumps of differential and/or algebraic states can occur (see the example in Fig. 3.5) [123]. The handling of these jumps is not trivial, as it can be interpreted that no solution exists or that Dirac impulses arise so that a solution exists. Depending on the inputs of the switching logic, the switching events can be classified into [123]

- state-dependent or time-dependent,
- autonomous (uncontrolled) or controlled.

This means that for a state-dependent event, the decision of which subsystem is being activated depends on the states $\mathbf{x}$ and/or $\mathbf{y}$, whereas for a time-dependent event only the time t is taken into account (see Fig. 3.2). In case of controlled events, the switching can be initiated from outer control signals $\mathbf{u}$. If the events are not triggered by the inputs,

they are defined as autonomous. However, it has to be noted that differentiating between these event types is not trivial [123]. For example, if a failure in a power system (e.g. short-circuit) happens this would be normally considered as *autonomous*, whereas the subsequent automatic initiated countermeasure (e.g. line tripping by protection equipment) would be defined as an *controlled* switching.

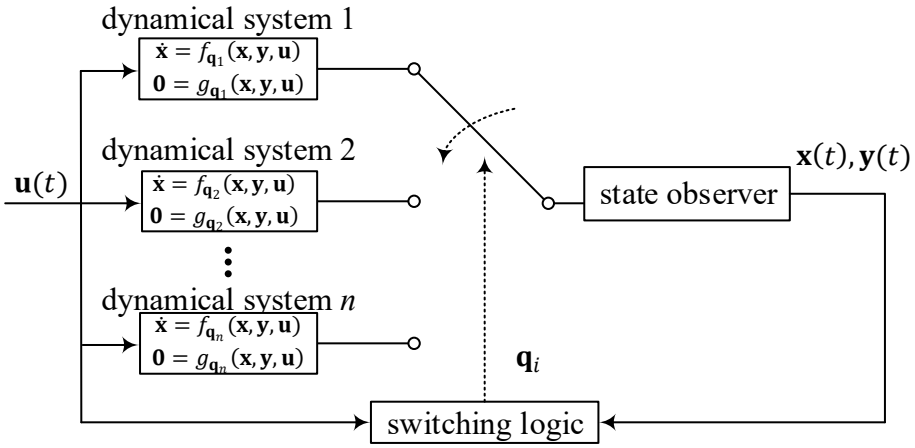

Figure 3.2: Illustration of a switched system with a switching logic determining the active dynamical system (own illustration, inspired by [123]

3.2.3 Differential-algebraic-discrete system

The DADS is intended explicitly for power systems, in contrast to previous modelling approaches [110]. In general, the DADS approach is based on switched systems with a special focus on state resets of discrete states and switching algebraic equations. According to [110], an advantage of the approach is its modularity, as single components can be modelled as a DADS and then coupled via algebraic equations to a bigger system. In detail, a DADS can be described as

$$\dot{\mathbf{x}} = f(\mathbf{x}, \mathbf{y}, \mathbf{q}, \mathbf{p}), \tag{3.3}$$

$$\mathbf{0} = g(\mathbf{x}, \mathbf{y}, \mathbf{q}, \mathbf{p}) = \begin{cases} g_i^-(\mathbf{x}, \mathbf{y}, \mathbf{q}, \mathbf{p}), & s_i(\mathbf{x}, \mathbf{y}, \mathbf{q}, \mathbf{p}) < 0, \\ g_i^+(\mathbf{x}, \mathbf{y}, \mathbf{q}, \mathbf{p}), & s_i(\mathbf{x}, \mathbf{y}, \mathbf{q}, \mathbf{p}) > 0, \end{cases} \tag{3.4}$$

$$\mathbf{q}^+ = h_i(\mathbf{x}^-, \mathbf{y}^-, \mathbf{q}^-, \mathbf{p}^-) \quad \text{when } s_i(\mathbf{x}, \mathbf{y}, \mathbf{q}, \mathbf{p}) = 0, \tag{3.5}$$

where $\mathbf{x}$ are differential states, $\mathbf{y}$ algebraic states, $\mathbf{q}$ discrete states and $\mathbf{p}$ parameters. The superscript "−" means before and "+" after a switching event. The triggering surface $s_i(\cdot)$, which can be any arbitrary condition, determines when a switch of the algebraic equations or the triggering of a reset function occurs. As a DADS can contain multiple subsystems, the index i denotes here one of them. A special aspect of the DADS is that only discrete states can be reset, which is different from hybrid automata. The state reset function $h(\mathbf{x}^-, \mathbf{y}^-)$ specifies the new value of $\mathbf{q}^+$ after the event. Yet, not every switching leads to a state jump so that $\mathbf{q}^+ = \mathbf{q}^-$ can result. Although only discrete states change after an event, the algebraic states must also be initialised and thus jump, so that the constraint $\mathbf{0} = g_i^+(\mathbf{x}, \mathbf{y}, \mathbf{q}, \mathbf{p})$ is satisfied. By introducing the following notation

$$\overline{\mathbf{x}} = \begin{pmatrix} \mathbf{x} \\ \mathbf{q} \\ \mathbf{p} \end{pmatrix}, \quad \overline{f} = \begin{pmatrix} f \\ \mathbf{0} \\ \mathbf{0} \end{pmatrix}, \quad \overline{h}_i = \begin{pmatrix} \mathbf{x} \\ h_i \\ \mathbf{p} \end{pmatrix}, \tag{3.6}$$

a compact form of the DADS is given by

$$\dot{\overline{\mathbf{x}}} = \overline{f}(\overline{\mathbf{x}}, \mathbf{y}), \tag{3.7}$$

$$\mathbf{0} = \begin{cases} g_i^-(\overline{\mathbf{x}}, \mathbf{y}), & s_i(\overline{\mathbf{x}}, \mathbf{y}) < 0, \\ g_i^+(\overline{\mathbf{x}}, \mathbf{y}), & s_i(\overline{\mathbf{x}}, \mathbf{y}) > 0, \end{cases} \tag{3.8}$$

$$\overline{\mathbf{x}}^+ = \overline{h}_i(\overline{\mathbf{x}}^-, \mathbf{y}^-) \quad \text{when } s_i(\overline{\mathbf{x}}, \mathbf{y}) = 0, \tag{3.9}$$

which is used for introducing the concept of trajectory sensitivity in Section 3.4. Note that the differential equations for the discrete states and parameters in (3.7) are zero.

3.3 Dynamical phenomena and stability of hybrid systems

In this subsection, an introduction to hybrid dynamical phenomena and stability properties of hybrid systems is given. At first, it is outlined which dynamic phenomena can only occur in hybrid systems compared to continuous systems. Subsequently, the stability theory of continuous and hybrid systems is summarised to highlight their similarities and differences.

3.3.1 Hybrid dynamical phenomena

In order to introduce the phenomena of hybrid systems, an exemplary trajectory is presented first and given in Fig. 3.3. The trajectory starts at given initial conditions with $\mathbf{x}(t_0)$ for the continuous states and q_1 for the discrete state. Subsequently, the continuous states evolve according to the local vector field $f(q_1, \mathbf{x})$ (light blue area). If the guard condition $\mathcal{G}(q1, \mathbf{x})$ is satisfied, an event is triggered. At the event, mainly two things happen. On the one hand, the post-event states $\mathbf{x}^+$ are reset by the reset map $\mathcal{R}(q1, \mathbf{x}^-)$. On the other hand, a switch of the dynamics to a new vector field is made, represented by the light yellow area. After the event, the continuous states evolve according to the new vector field and the whole process starts again. If several invariants or guard conditions are satisfied at the same time, a sequence of ordered events can take place [124]. However, dealing with multiple events is not trivial.

A known dynamical phenomenon of hybrid systems, especially for switched systems, is *chattering* [5]. This can happen if the vector fields between a switching surface $\mathcal{S}$ point to each other (see Fig. 3.4 (a)). Here, the term switching surface means the boundary between two or more vector fields in the state space. If a trajectory $\mathbf{x}(t)$ crosses this surface, the vector field pushes the states back, but the other vector field also points back. As a result, the states chatter and "slide" over the switching surface which can lead to infinite fast switching. In [124] this is called *livelock*, where a discrete state switches between different

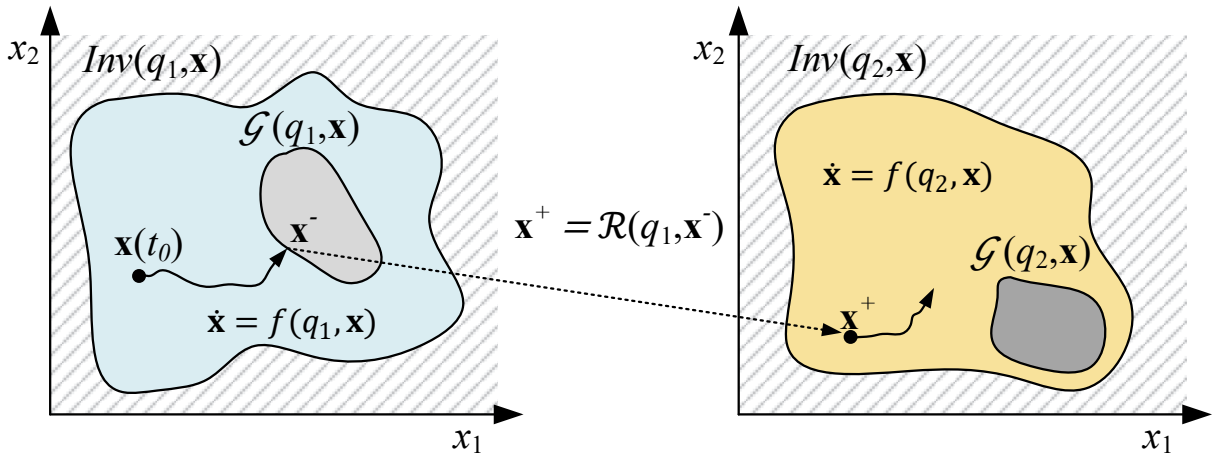

Figure 3.3: Schematic illustration of a hybrid trajectory with switching dynamics and state jump (own illustration, inspired by [5])

locations, but does not proceed in time. In contrast to this, a *deadlock* situation arises, if the system ends up in a state where the continuous states can not evolve further and no other possible jump to another location [124, 125]. A similar phenomenon to chattering is *hysteresis switching* [123]. The trajectory is bounded between two switching surfaces but without chattering (see Fig. 3.4 (b)). In this example, the grey area represents that either the vector field $f(q_1, \mathbf{x})$ or $f(q_2, \mathbf{x})$ is active, based on the last switching surface. For example, if the trajectory hits $\mathcal{S}_1$, then $f(q_1, \mathbf{x})$ is active and if $\mathcal{S}_2$ is hit, then the states evolve according to $f(q_2, \mathbf{x})$. This means that the vector field and trajectory $\mathbf{x}(t)$ does not only depend on the current state, and thus to describe the complete dynamics of the system a discrete state is necessary [123].

When an infinite number of events occur in a finite time interval, this phenomenon is called *Zeno* behaviour [5, 123, 124]. As long as the hybrid trajectory converges to a unique value, Zeno behaviour does not automatically lead to instability. However, in the case of a numerical simulation, problems can arise due to approximation errors, which can lead to a non-deterministic or incorrect trajectory [5]. In general, Zeno behaviour is a modelling artefact and does not occur in real applications. Therefore, a hybrid model should be checked to see if Zeno trajectories can occur and either be avoided by implementation or by including a detection and mitigation strategy. Like continuous non-linear systems, hybrid systems can also be sensitive to initial conditions, which is also referred to as *chaotic* behaviour [5, 124]. This means that a small deviation from the initial conditions can lead to trajectories that deviate from the original trajectories. To detect such sensitivity, the Lyapunov exponents described in Subsection 2.3.1 can be used. Note that chaotic does not mean non-deterministic. In fact, given the same initial conditions, the same trajectory will evolve. Undefined behaviour can occur when the vector field is tangent to a switching surface or when two switching surfaces overlap [5].

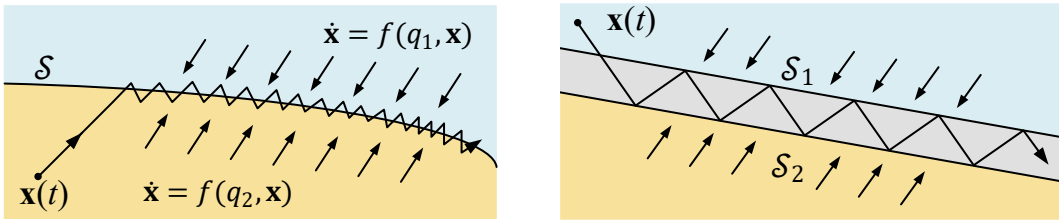

Figure 3.4: Schematic illustration of (a) chattering (b) hysteresis switching (own illustration, based on [5] and [123])

3.3.2 Stability theory of continuous and hybrid systems

Next, a brief introduction to the stability theory of dynamical systems is given. For introductory reasons, the subsection starts with the stability theory of pure continuous systems in order to highlight the differences to hybrid systems later on. It is also distinguished whether the system consists entirely of ODEs or also has algebraic equations and whether these equations are linear or non-linear. The following topic is mostly based on Lyapunov's stability theory, which is about the stability of equilibrium points [120]. The main two statements of this theory can be summarised as follows:

- An equilibrium is stable if all nearby trajectories remain close to it when starting from a specific neighbourhood around that equilibrium.
- An equilibrium is asymptotically stable if the trajectories converge to that equilibrium over time when starting from that neighbourhood.

In this context, neighbourhood means a region in the state space around that equilibrium which is used as initial conditions. However, Lyapunov's theory only gives sufficient conditions but does not give information about whether they are necessary. This means that if these conditions are met, the system is stable. If they are not, it cannot be concluded that the system is unstable. Although an attempt is made to give a comprehensive picture of the subject, it should be noted that not all mathematical details and conditions are reproduced here. The reader is referred to the original references for full details. Also, unless otherwise stated, the following theorems are only valid for autonomous systems that do not depend directly on the independent variable, which in this case is time t. Overall, this subsection aims to give an overview of the main differences in stability conditions between continuous and hybrid systems and how modelling assumptions (e.g. linear or non-linear) affect them.

Continuous non-linear ODE

The general idea of Lyapunov stability theory is to find a function $V(\mathbf{x}) : \mathbb{R}^n \to \mathbb{R}$, which can be interpreted as a function for the energy of the non-linear ODE system

$$\dot{\mathbf{x}}(t) = f(\mathbf{x}(t)). \tag{3.10}$$

If this function fulfils certain requirements, then the system is stable. The first requirement is that the function has to be continuously differentiable and positive definite, where the

latter is expressed by [120]

$$\begin{aligned} &V(\mathbf{x}(t)) > 0 \text{ for all } \mathbf{x}(t) \neq \mathbf{0}, \\ &V(\mathbf{0}) = 0 \text{ for } \mathbf{x}(t) = \mathbf{0}, \end{aligned} \tag{3.11}$$

where $\mathbf{x}(t) = \mathbf{0}$ is an equilibrium of the system. The second requirement is that its derivative $\dot{V}(\mathbf{x})$ shall always decrease along its time-domain solution $\phi(t, \mathbf{x}(t))$

$$\dot{V}(\mathbf{x}) = \frac{\mathrm{d}}{\mathrm{d}t} V\left(\phi(t, \mathbf{x}(t))\right) < 0 \text{ for all } \mathbf{x} \neq \mathbf{0}. \tag{3.12}$$

In case the solution is not known, the following expression is also valid

$$\dot{V}(\mathbf{x}) = \frac{\mathrm{d}V}{\mathrm{d}\mathbf{x}} f(\mathbf{x}) < 0 \text{ for all } \mathbf{x} \neq \mathbf{0}. \tag{3.13}$$

If $V(\mathbf{x})$ fulfills these conditions, then the equilibrium in $\mathbf{x} = \mathbf{0}$ is asymptotically stable. The challenge is to construct such a function and to prove the above requirements, especially in the non-linear case.

Continuous non-linear DAEs

As dynamic power systems are usually described by DAEs, this type of system is of particular interest. The reason for this is that there are some major differences in the notion of stability compared to pure ODE systems. In general, non-linear DAE systems can be described by [126]

$$\mathbf{E}(\mathbf{x})\dot{\mathbf{x}}(t) = f(\mathbf{x}(t)), \tag{3.14}$$

where $\mathbf{E(x)} \in \mathbb{R}^{n \times n}$ is a quadratic matrix connecting the differential and algebraic equations. For example, if a row in $\mathbf{E(x)}$ only consists of zeros, this would indicate that the corresponding derivative is also zero and hence an algebraic equation. In contrast to conventional power system descriptions, the states $\mathbf{x}$ here describe differential and algebraic states. Similar to continuous non-linear ODEs, the system in (3.14) is asymptotically stable, if there exists a continuously differentiable non-negative function $V(\mathbf{x}(t))$ [126]

$$\begin{aligned} &V(\mathbf{x}(t)) > 0 \text{ for all } \mathbf{x}(t) \neq \mathbf{0}, \\ &V(\mathbf{0}) = 0 \text{ for } \mathbf{x}(t) = \mathbf{0}, \end{aligned} \tag{3.15}$$

with its derivative

$$\frac{\mathrm{d}}{\mathrm{d}t} V(\mathbf{x}) = \dot{V}(\mathbf{x}(t)) = \nabla V\left(\mathbf{x}(t)\right) \dot{\mathbf{x}}(t) < 0. \tag{3.16}$$

The challenge is to find such a function, as there are no general procedures. Further information and remarks on the stability of non-linear DAE systems can be found in [126].

Continuous linear DAEs

Next, linear DAE systems of the form

$$\mathbf{E}\dot{\mathbf{x}}(t) = \mathbf{A}\mathbf{x}(t), \tag{3.17}$$

are considered, where $\mathbf{A}$ is a square matrix. For a stable system, the matrix pair (**E,A**) must be regular (for details see [127]). Then, a quadratic Lyapunov function can be defined by [126]

$$V(\mathbf{x}(t)) = (\mathbf{E}\mathbf{x})^{\mathrm{T}}\mathbf{P}\mathbf{E}\mathbf{x}, \tag{3.18}$$

where $\mathbf{P} = \mathbf{P}^{\mathrm{T}}$ is a square and positive definite matrix. To find $\mathbf{P}$ the following equation has to be solved

$$\mathbf{A}^{\mathrm{T}}\mathbf{P}\mathbf{E} + \mathbf{E}^{\mathrm{T}}\mathbf{P}\mathbf{A} = -\mathbf{Q}, \tag{3.19}$$

where $\mathbf{Q} = \mathbf{Q}^{\mathrm{T}}$ can be any positive definite matrix (e.g. the identity matrix $\mathbf{I}$ if valid). The derivative of $V(\mathbf{x})$ is then given by

$$\dot{V}(\mathbf{x}) = \mathbf{x}^{\mathrm{T}}(\mathbf{A}^{\mathrm{T}}\mathbf{P}\mathbf{E} + \mathbf{E}^{\mathrm{T}}\mathbf{P}\mathbf{A})\mathbf{x} = -\mathbf{x}^{\mathrm{T}}\mathbf{Q}\mathbf{x} < 0. \tag{3.20}$$

In case the DAE in (3.17) is of index one (meaning the number of times the equations of the DAE system have to be differentiated by the independent variable, e.g. the time t, to get a pure ODE system) (3.19) changes to

$$\begin{aligned} \mathbf{A}^{\mathrm{T}}\mathbf{P} + \mathbf{P}^{\mathrm{T}}\mathbf{A} &= -\mathbf{Q}, \\ \mathbf{P}^{\mathrm{T}}\mathbf{E} = \mathbf{E}^{\mathrm{T}}\mathbf{P} &\geq \mathbf{0}, \end{aligned} \tag{3.21}$$

for any positive definite $\mathbf{Q}$ [126]. Then a quadratic Lyapunov function can be constructed by

$$V(\mathbf{x}) = (\mathbf{E}\mathbf{x})^{\mathrm{T}}\mathbf{P}\mathbf{x}, \tag{3.22}$$

where its derivative simplifies to

$$\dot{V}(\mathbf{x}) = \mathbf{x}^{\mathrm{T}}(\mathbf{A}^{\mathrm{T}}\mathbf{P} + \mathbf{P}^{\mathrm{T}}\mathbf{A})\mathbf{x} = -\mathbf{x}^{\mathrm{T}}\mathbf{Q}\mathbf{x} < 0. \tag{3.23}$$

Switched linear DAE

Now the hybrid case for switched linear DAE is considered, which are of the form [128]

$$\mathbf{E}_{\sigma(t)}\dot{\mathbf{x}}(t) = \mathbf{A}_{\sigma(t)}\mathbf{x}(t), \tag{3.24}$$

where $\sigma(t) \in \{1, ..., N\}$ is the switching signal and each matrix pair $(\mathbf{E}_\sigma, \mathbf{A}_\sigma)$ is regular as in the continuous case. In this context, regular means that for consistent initial conditions, there are always unique solutions. This assumption is important because there are some major differences between switched ODE and switched DAE systems. It should be noted that for the following paragraphs most of the statements are taken from [128] and [126].

As shown in Section 3.2.1, state jumps are defined by the invariants and the reset map of a hybrid automaton. In the case of a switched linear DAE, however, the jumps are already implicitly defined between the jumps of the matrix pairs $(\mathbf{E}_\sigma, \mathbf{A}_\sigma)$. The reason for this is that each subsystem has its own consistency space $\Omega_{(\mathbf{E}_\sigma, \mathbf{A}_\sigma)} \subset \mathbb{R}^n$ which is restricted by the algebraic constraints. Therefore, when a switch occurs, there may be jumps in the differential and algebraic states, depending on the new subsystem. In addition to jumps, impulsive behaviour can also arise, leading to Dirac impulses in the solution [129].

To illustrate this, an example of an electrical circuit is given in Fig. 3.5. The circuit consists only of a DC voltage source, a switch and an inductance, all of which are ideal elements. First, the switch S1 is closed and a current i_L flows into the inductance L. At $t = t_\mathrm{s}$ the switch is opened and the equation of the system changes. At this point, there are potentially two ways to proceed [129]. The first option is that there is no solution in the *open* subsystem, since the ideal switch forces $i_\mathrm{L} = 0$, but the current cannot jump to zero due to the inductance, as there is no derivative of a jump. However, as motivated in,[129], if the *space of distributions* from mathematical analysis is taken into account, then there would be a Dirac impulse δ in the solution, which has a well-defined derivative in this space. In this example, the inductance voltage v_L would contain a Dirac impulse δ_ts at $t = t_\mathrm{s}$ with the magnitude $-i_\mathrm{ts}$, so that the current is zero afterwards. As there are no ideal elements in reality, a spark could be observed at the inductance, which would discharge it. The occurrence of such a Dirac pulse in a model can therefore be an indication of undesirable behaviour in reality. Therefore, for stability analysis, it is assumed that no impulsive behaviour occurs. Note that *jumps* can still occur (see Fig. 3.5 for the difference).

To check for impulsive behaviour is present in a system, the concept of a consistency projector Π is introduced, which maps inconsistent initial values from the previous subsystem

to the consistency space of the activated subsystem

$$\mathbf{x}(t+) = \Pi_\sigma \mathbf{x}(t-), \tag{3.25}$$

where $t-$ stands for the time just before the switch and $t+$ for the time just after the switch. With the help of these consistency projectors, it is now possible that state values that are not suitable for the new subsystem, here $\mathbf{x}(t-)$, are transformed so that they fulfil the new constraints. However, as seen in Fig. 3.5 this can lead to impulsive and therefore unstable behaviour. Therefore, the consistency projectors can be used to check for impulsive behaviour, as they contain state space mapping information.

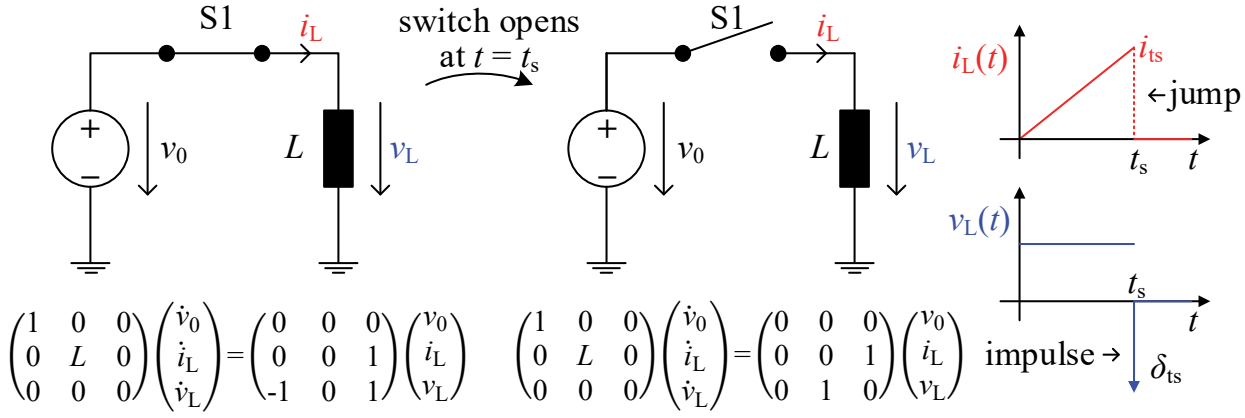

Figure 3.5: Exemplary jump and impulsive phenomena in a switched linear DAE system (taken from [129], see chapter 3.1.2)

Suppose p and q denote subsystems with matrix pairs $(\mathbf{E}_p, \mathbf{A}_p), (\mathbf{E}_q, \mathbf{A}_q)$ and a switch from p to q takes place. The switch is impulse-free if the following condition is true,[129]

$$\mathbf{E}_p(I - \Pi_p)\Pi_q = \mathbf{0}, \tag{3.26}$$

where I is the identity matrix. The above equation can also be simplified to check that there are no jumps in the states[130]

$$(I - \Pi_p)\Pi_q = \mathbf{0}. \tag{3.27}$$

For a detailed description of how to calculate these consistency projectors, the reader is referred to [129, 130]. If impulsive behaviour is excluded, the stability of the switched linear DAE can be further investigated by Lyapunov functions. For each subsystem, a Lyapunov function $V_\sigma(\mathbf{x}) = (\mathbf{E}_\sigma \mathbf{x})^T \mathbf{P}_\sigma \mathbf{E}_\sigma \mathbf{x}$ has to be determined by solving the linear

matrix inequality

$$\mathbf{A}_\sigma^{\mathrm{T}}\mathbf{P}_\sigma\mathbf{E}_\sigma + \mathbf{E}_\sigma^{\mathrm{T}}\mathbf{P}_\sigma\mathbf{A}_\sigma = -\mathbf{Q}_\sigma, \tag{3.28}$$

where $\mathbf{P}_\sigma$ and $\mathbf{Q}_\sigma$ have to be positive definite. In addition, the inequality

$$V_q(\Pi_q\mathbf{x}) \leq V_p(\mathbf{x}), \tag{3.29}$$

has to be fulfilled, demonstrating the need for consistency projectors for stability analysis.

Non-linear switched DAE

In the end, the stability of non-linear switched DAE of the form

$$\mathbf{E}_{\sigma(t)}(\mathbf{x})\dot{\mathbf{x}}(t) = f_{\sigma(t)}(\mathbf{x}), \tag{3.30}$$

are considered. In general, the concept of stability is similar to that of switched linear DAE. First, the switches between the subsystems must be impulse-free by finding suitable consistency projectors. Second, for each subsystem a Lyapunov function $V_\sigma(\mathbf{x})$ must be found and the condition (3.29) must be satisfied and the functions must coincide at their intersection. In such a case, the non-linear switched DAE is also asymptotically stable under arbitrary switching. However, as already seen for the other non-linear cases, the big challenge is to find suitable Lyapunov functions, since there is no general procedure. A further challenge is to find suitable consistency projectors that also satisfy (3.29). More information about how to set up these consistency projectors can be found in [131].

As seen by the above introduction to the stability theory of hybrid systems, the formal stability proof comes with great challenges. Therefore, analytical investigations become more complex and are often only possible with great simplifications. It should be noted that these disadvantages do not arise from the hybrid system approach itself, but from the discontinuities present in the model. Therefore, if discontinuities are present in a system under study, a hybrid system approach should be considered to take into account the unique characteristics of the system. Whether or not simplifications are possible depends heavily on the model and scenario at hand. Since the present work mainly uses detailed models, most of which contain non-linearities, a formal stability assessment is not pursued. Instead, the stability region of the models is to be analysed using various scenarios in the time domain. However, to narrow down the solution domain, the trajectory sensitivity analysis is used to efficiently determine the qualitative influence of different model parameters, which is described next.

3.4 Application of hybrid system theory: Trajectory sensitivity with discontinuities

This subsection mainly summarises the work of [109], where conditions are derived to calculate trajectory sensitivities at discontinuities. In general, trajectory sensitivities determine the influence of a small change in initial states $\mathbf{x}_0$ or parameters $\mathbf{p}$ on the trajectories obtained by a time-domain simulation. For this, the system is considered as a DADS as described in (3.7)-(3.9). For convenience, the notation for the state vector, differential equations and reset function given in (3.6) is repeated here

$$\overline{\mathbf{x}} = \begin{pmatrix} \mathbf{x} \\ \mathbf{q} \\ \mathbf{p} \end{pmatrix}, \quad \overline{f} = \begin{pmatrix} f \\ \mathbf{0} \\ \mathbf{0} \end{pmatrix}, \quad \overline{h}_i = \begin{pmatrix} \mathbf{x} \\ h_i \\ \mathbf{p} \end{pmatrix}. \tag{3.31}$$

For the compact DADS in (3.7)-(3.9), the time-domain solution or *flow* Φ is given by

$$\overline{\mathbf{x}}(t) = \Phi_{\overline{\mathbf{x}}}(\overline{\mathbf{x}}_0, \mathbf{y}_0, t), \tag{3.32}$$

$$\mathbf{y}(t) = \Phi_{\mathbf{y}}(\overline{\mathbf{x}}_0, \mathbf{y}_0, t). \tag{3.33}$$

To determine the change in the trajectories in case of slightly changed initial conditions $\overline{\mathbf{x}}_0$, the flow in (3.32)-(3.33) is expressed by a Taylor series, where only the first term is kept (same for $\Delta\mathbf{y}(t)$) [109]

$$\begin{aligned} \Delta\overline{\mathbf{x}}(t) = \Delta\Phi_{\overline{\mathbf{x}}}(\overline{\mathbf{x}}_0, \mathbf{y}_0, t) &= \frac{\mathrm{d}\Phi_{\overline{\mathbf{x}}}(\overline{\mathbf{x}}_0, \mathbf{y}_0, t)}{\mathrm{d}\overline{\mathbf{x}}_0}\Delta\overline{\mathbf{x}}_0 + \text{higher order terms}, \\ &\approx \frac{\mathrm{d}\Phi_{\overline{\mathbf{x}}}(\overline{\mathbf{x}}_0, \mathbf{y}_0, t)}{\mathrm{d}\overline{\mathbf{x}}_0}\Delta\overline{\mathbf{x}}_0 = \overline{\mathbf{x}}_{\overline{\mathbf{x}}_0}(t) \cdot \Delta\overline{\mathbf{x}}_0. \end{aligned} \tag{3.34}$$

Then, $\overline{\mathbf{x}}_{\overline{\mathbf{x}}_0}(t)$ (same for $\mathbf{y}_{\overline{\mathbf{x}}_0}(t)$) represents the trajectory sensitivities with respect to the initial conditions $\overline{\mathbf{x}}_0$. Note that the sensitivities are calculated for continuous and discrete states as well as parameters, as the initial conditions $\overline{\mathbf{x}}_0$ contain all of them.

Trajectory sensitivity between two consecutive events

Next, it is described how these sensitivities are calculated between two consecutive events. For this, a smooth DAE system with no change in $g(\overline{\mathbf{x}}, \mathbf{y})$ or state resets is considered. First,

the system is differentiated by the initial conditions $\overline{\mathbf{x}}_0$

$$\dot{\overline{\mathbf{x}}}_{\overline{\mathbf{x}}_0} = \overline{f}_{\overline{\mathbf{x}}}(t)\overline{\mathbf{x}}_{\overline{\mathbf{x}}_0} + \overline{f}_{\mathbf{y}}(t)\mathbf{y}_{\overline{\mathbf{x}}_0}, \tag{3.35}$$

$$\mathbf{0} = g_{\overline{\mathbf{x}}}(t)\overline{\mathbf{x}}_{\overline{\mathbf{x}}_0} + g_{\mathbf{y}}(t)\mathbf{y}_{\overline{\mathbf{x}}_0}. \tag{3.36}$$

Second, to calculate $\overline{\mathbf{x}}_{\overline{\mathbf{x}}_0}(t)$ and $\mathbf{y}_{\overline{\mathbf{x}}_0}(t)$, an implicit numerical method has to be used to get the corresponding Jacobian matrix. Then, the Jacobian matrix contains the information on how sensitive the trajectories are for each state or parameter. For example, according to [109], the implicit Trapezoid rule could be applied. The Trapezoidal is of the form

$$\begin{aligned} \overline{\mathbf{x}}^{k+1} &= \overline{\mathbf{x}}^{k} + \frac{\Delta t}{2}\left(\overline{f}\left(\overline{\mathbf{x}}^{k}, \mathbf{y}^{k}\right) + \overline{f}\left(\overline{\mathbf{x}}^{k+1}, \mathbf{y}^{k+1}\right)\right), \\ \mathbf{0} &= g\left(\overline{\mathbf{x}}^{k+1}, \mathbf{y}^{k+1}\right), \end{aligned} \tag{3.37}$$

where the superscript k means the time instant at t_k and $k+1$ for the next time instant at t_{k+1}. The difference $t_k - t_{k+1}$ is the integration time step Δt. By applying the Trapezoidal rule to (3.35)-(3.36) and rearranging the sensitivities according to the time instant, the following equation is obtained

$$\begin{bmatrix} \frac{\Delta t}{2}\overline{f}_{\overline{\mathbf{x}}}^{k+1} - \mathbf{I} & \frac{\Delta t}{2}\overline{f}_{\mathbf{y}}^{k+1} \\ g_{\overline{\mathbf{x}}}^{k+1} & g_{\mathbf{y}}^{k+1} \end{bmatrix} \begin{bmatrix} \overline{\mathbf{x}}_{\overline{\mathbf{x}}_0}^{k+1} \\ \mathbf{y}_{\overline{\mathbf{x}}_0}^{k+1} \end{bmatrix} = \begin{bmatrix} -\overline{\mathbf{x}}_{\overline{\mathbf{x}}_0}^{k} - \frac{\Delta t}{2}\left(\overline{f}_{\overline{\mathbf{x}}}^{k} \cdot \overline{\mathbf{x}}_{\overline{\mathbf{x}}_0}^{k} + \overline{f}_{\mathbf{y}}^{k} \cdot \mathbf{y}_{\overline{\mathbf{x}}_0}^{k}\right) \\ \mathbf{0} \end{bmatrix}, \tag{3.38}$$

which has to be solved every time-step (detailed derivation of (3.38) in [109]). The matrices $\overline{f}_{\overline{\mathbf{x}}}, \overline{f}_{\mathbf{x}}, g_{\overline{\mathbf{x}}}, g_{\mathbf{y}}$ are the time-dependent factorised Jacobian matrix and $\mathbf{I}$ is the identity matrix. As a result, the sensitivities can be calculated by solving the above equation after the states $\overline{\mathbf{x}}^{k+1}$ and $\mathbf{y}^{k+1}$ of the regular numerical integration have been obtained. The initial sensitivities are given by [109]

$$\overline{\mathbf{x}}_{\overline{\mathbf{x}}_0}(t_0) = \mathbf{I}, \tag{3.39}$$

$$\mathbf{y}_{\overline{\mathbf{x}}_0}(t_0) = \left(g_{\mathbf{y}}(t_0)\right)^{-1} \cdot g_{\overline{\mathbf{x}}}(t_0) \cdot \overline{\mathbf{x}}_{\overline{\mathbf{x}}_0}(t_0). \tag{3.40}$$

Note that (3.38) can only be used to calculate sensitivities away from events. They need to be treated specifically at discontinuities, which are described next.

Trajectory sensitivity at the time of events

In this section, it is assumed that no multiple events occur at the same time. This means that there are no two switching conditions $s(\overline{\mathbf{x}}, \mathbf{y})$ that become zero at the same time. It is also assumed that the trajectories cross the triggering surfaces and do not touch them

tangentially. Otherwise, the sensitivities would become infinite with respect to the initial conditions. The time at which the event is triggered is called the junction time τ. The superscript " − " is defined as the limit of the time t as it approaches a junction time τ from the left and is denoted as τ^-. Similarly, the superscript " + " is defined as the limit of the time t as it approaches a junction time τ from the right and is denoted as τ^+.

The sensitivity of the junction time to the initial conditions can be determined by the following equation [109]

$$\tau_{\overline{\mathbf{x}}_0} = \frac{\left(s_{\overline{\mathbf{x}}} - s_{\mathbf{y}} \left(g_{\mathbf{y}}^-\right)^{-1} g_{\overline{\mathbf{x}}}^-\right)\Big|_{\tau^-} \overline{\mathbf{x}}_{\overline{\mathbf{x}}_0}(\tau^-)}{\left(s_{\overline{\mathbf{x}}} - s_{\mathbf{y}} \left(g_{\mathbf{y}}^-\right)^{-1} g_{\overline{\mathbf{x}}}^-\right)\Big|_{\tau^-} \cdot \overline{f}\Big|_{\tau^-}}, \tag{3.41}$$

where $s_{\overline{\mathbf{x}}}$ and $s_{\mathbf{y}}$ are the partial derivatives of the switching conditions. Also, the term $\overline{f}\Big|_{\tau^-} = \overline{f}(\overline{\mathbf{x}}(\tau^-), \mathbf{y}(\tau^-))$ in (3.41) represents the differential equations and is evaluated just before the event. With this, the trajectory sensitivities just after the event can be calculated by (detailed derivation in [109])

$$\overline{\mathbf{x}}_{\overline{\mathbf{x}}_0}(\tau^+) = \overline{h}_{\overline{\mathbf{x}}}^* \cdot \overline{\mathbf{x}}_{\overline{\mathbf{x}}_0}(\tau^-) - \left(\overline{f}\Big|_{\tau^+} - \overline{h}_{\overline{\mathbf{x}}}^* \, \overline{f}\Big|_{\tau^-}\right) \tau_{\overline{\mathbf{x}}_0}, \tag{3.42}$$

$$\mathbf{y}_{\overline{\mathbf{x}}_0}(\tau^+) = \left(\left(g_{\mathbf{y}}^+\right)^{-1} g_{\overline{\mathbf{x}}}^+\right)\Big|_{\tau^+} \overline{\mathbf{x}}_{\overline{\mathbf{x}}_0}(\tau^+), \tag{3.43}$$

with

$$\overline{h}_{\overline{\mathbf{x}}}^* = \left(\overline{h}_{\overline{\mathbf{x}}} - \overline{h}_{\mathbf{y}} \left(g_{\mathbf{y}}^-\right)^{-1} g_{\overline{\mathbf{x}}}^-\right)\Big|_{\tau^-}. \tag{3.44}$$

Note that $\overline{h}_{\overline{\mathbf{x}}}$ and $\overline{h}_{\mathbf{y}}$ are the partial derivatives of the reset function $\overline{h}$. From (3.44) and (3.41) it is clear that both the triggering conditions and the state reset functions have an impact on the sensitivities and thus need to be considered. Overall, with the continuous sensitivities in (3.38) and the initial conditions in (3.39)-(3.40), the trajectory sensitivities can now be calculated for hybrid systems. An example of the trajectory sensitivities is given next.

Example: ideal single-phase rectifier

To demonstrate the concept of trajectory sensitivities for a hybrid system, a simple single-phase rectifier with an ideal diode as a power electronic load is used. The circuit diagram and component values are shown in Fig. 3.6 along with its time-domain response for 190 ms after start-up.

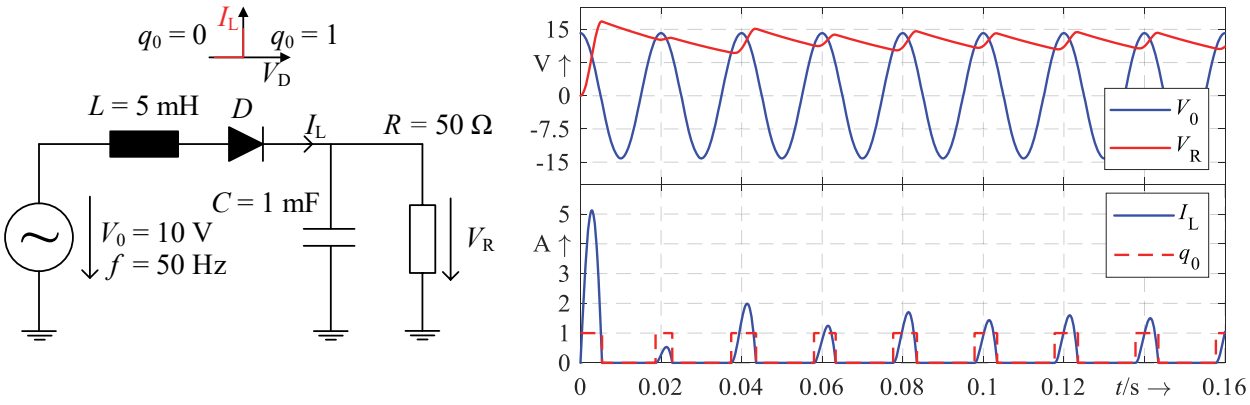

Figure 3.6: Rectifier circuit with an ideal diode as hybrid system example for trajectory sensitivity analysis

The considered system can be described as a DADS by the following equations

$$\dot{I}_\mathrm{L} = \frac{V_0 - V_\mathrm{R}}{L} \cdot q_0, \tag{3.45a}$$

$$\dot{V}_\mathrm{R} = \frac{I_\mathrm{L} - \frac{V_\mathrm{R}}{R}}{C}, \tag{3.45b}$$

$$\dot{q}_0 = 0, \tag{3.45c}$$

$$0 = V_0 - \hat{V}_0 \cdot \cos(\omega t), \tag{3.45d}$$

where V_0 is the grid voltage, I_L the load current, V_R the rectified voltage, R the load resistance and C the capacitance to smoot the voltage. The first two equations (3.45a)-(3.45b) describe the current and voltage dynamics of the inductance and capacitance. To mimic the ideal diode, the discrete state q_0 is introduced with a dummy derivative to include it as a fictional differential state. The last equation (3.45d) is an implicit algebraic equation to define a constant AC voltage source, where $\hat{V}_0$ is the peak voltage and ω is the fundamental angular frequency of the grid. The rectifier is able to adopt two operation modes, denoted by $q_0 = 0$ for the blocking mode and $q_0 = 1$ for the charging mode. Both operation conditions can be expressed by a triggering condition $s(\overline{\mathbf{x}}, \mathbf{y})$ and a reset function $h(\overline{\mathbf{x}}, \mathbf{y})$. The rectifier switches to a blocking mode ($q_0 = 0$) when the current I_L becomes zero, which is described by the triggering condition $s_1(\overline{\mathbf{x}}, \mathbf{y})$ in (3.46). Also, q_0 is set to zero by the reset function $h_1(\overline{\mathbf{x}}, \mathbf{y})$ so that the current I_L remains zero

$$s_1(\overline{\mathbf{x}}, \mathbf{y}) = I_\mathrm{L} = 0, \qquad \mathbf{h}_1(\overline{\mathbf{x}}, \mathbf{y}) = \begin{pmatrix} I_\mathrm{L}^+ \\ V_\mathrm{R}^+ \\ q_0^+ \end{pmatrix} = \begin{pmatrix} I_\mathrm{L}^- \\ V_\mathrm{R}^- \\ 0 \end{pmatrix}. \tag{3.46}$$

The charging mode ($q_0 = 1$) is enabled, if the voltage V_R falls below V_0. Then, the discrete state q_0 is set to one, allowing a current to flow. For this mode, the triggering condition and reset function are given by

$$s_2(\overline{\mathbf{x}}, \mathbf{y}) = V_0 - V_\mathrm{R} + q_0 = 0, \qquad \mathbf{h}_2(\overline{\mathbf{x}}, \mathbf{y}) = \begin{pmatrix} I_\mathrm{L}^+ \\ V_\mathrm{R}^+ \\ q_0^+ \end{pmatrix} = \begin{pmatrix} I_\mathrm{L}^- \\ V_\mathrm{R}^- \\ 1.0 \end{pmatrix}. \tag{3.47}$$

Note that for triggering condition $s_2(\overline{\mathbf{x}}, \mathbf{y})$, the discrete state q_0 is also included, which ensures that the charging mode is only enabled from a blocking mode, mainly for implementation and numerical reasons. As seen in Fig. 3.6 the discrete state q_0 changes depending on whether the rectifier is in a blocking or charging mode. Based on this formulation, the trajectory sensitivities of the capacitance C and the inductance L are calculated.

Fig. 3.7 shows the sensitivity $X_{\mathrm{VR,C}}$ of the rectified voltage V_R with respect to C and the sensitivity $X_{\mathrm{IL,L}}$ of the current I_L with respect to the inductance L. Before going into detail, the concept of relative trajectory sensitivity is introduced and developed for this thesis. As the sensitivities are calculated by a linear approximation for each point of the trajectory, their validity is also limited around a small change of initial condition or parameter. As can be seen in Fig. 3.7, the sensitivity $X_{\mathrm{VR,C}}$ is approximately between $-9000\frac{V}{F}$ and $2500\frac{V}{F}$, which can be considered as high numbers compared to other state and component values. In general, this sensitivity *could* be interpreted as meaning that a change in the capacitance C of $\Delta C = 1F$ would change the change in the voltage trajectory around $-9000\,\mathrm{V}$ and $2500\,\mathrm{V}$. It is clear that these changes are not realistic for this example. However, such

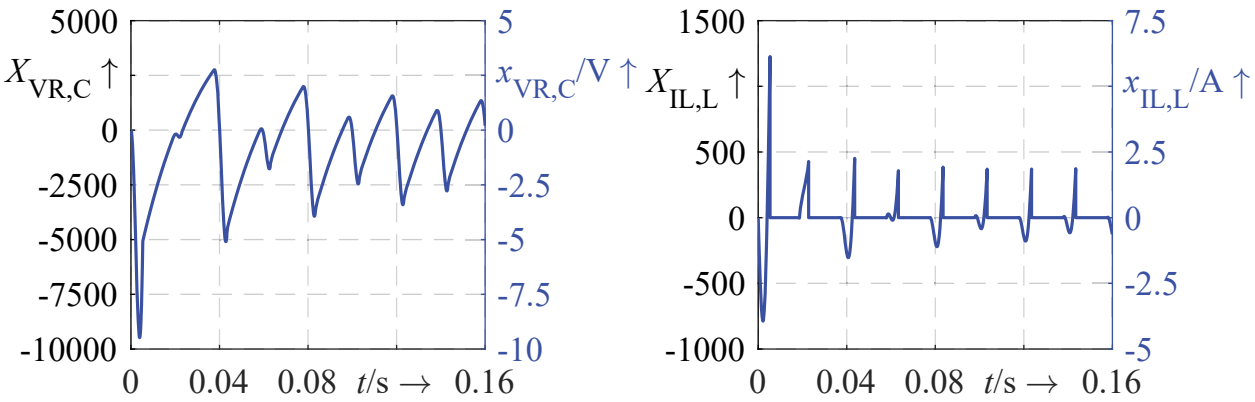

Figure 3.7: Trajectory sensitivities of C and L regarding the voltage V_R and current I_L

values arise from the fact that a change in the capacity of 1 F would also be very extreme. Therefore, the sensitivities should be qualified with respect to the underlying values of the initial conditions and parameters. In this example, the value of the capacity is $C = 10^{-3}\,F$. By multiplying the sensitivity $X_{\mathrm{VR,C}}$ by C one obtains the relative trajectory sensitivity $x_{\mathrm{VR,c}}$

$$x_{\mathrm{VR,c}} = X_{\mathrm{VR,c}} \cdot C. \tag{3.48}$$

This relative sensitivity $x_{\mathrm{VR,c}}$ means that if C is increased by its nominal value (or doubled), the change in voltage trajectory would be between −9 V and 2.5 V (blue axis in Fig. 3.7). The advantage is that the values of the sensitivities are now in a more realistic and meaningful numerical range, as their validity is limited by linearisation. This allows a quicker interpretation of the sensitivities obtained, as they are not overestimated. Note that this relationship also works in the opposite direction for parameters with high nominal values (>> 1). This also ensures that sensitivities are not underestimated. A closer look at Fig. 3.7 shows that increasing the capacitance has a smoothing effect on the rectified voltage, as the sensitivity is negative during charging and mostly positive during blocking. This fits well with the general design principles of such a circuit. Similarly, the inductance initially has a damping effect on the current but becomes positive as the inductance holds the current longer at higher values during charging. Especially at the beginning of the simulation, when the capacitor is charged, it has its highest negative sensitivity. It should be noted that these sensitivities also provide information if the capacitance or inductance is reduced. In this case, the sensitivities can be considered as having been multiplied by minus one.

The sensitivities can also be used to construct a first-order approximation of a trajectory for a parameter change without the need for a new time-domain simulation [109]. This is done by adding to the initial trajectory, e.g. the voltage $V_{\mathrm{R}}(t)$, the product of its parameter sensitivity $X_{\mathrm{VR,C}}$ and the parameter change ΔC

$$V_{\mathrm{R,appr}}(t) = V_{\mathrm{R}}(t) + X_{\mathrm{VR,C}}(t) \cdot \Delta C. \tag{3.49}$$

It should be noted that such an approximation does not take into account the possible change in the event junction times that could result from the parameter change. To counteract this, a method is presented in [109], which uses the sensitivities of the junction times from (3.41) to construct refined approximated trajectories. Generally, the accuracy of the approximated trajectory decreases with the size of the parameter change.

In Fig. 3.8 approximated trajectories of V_{R} and I_{L} are shown along with their original and actual perturbed trajectories (based on a new simulation with the changed parameter). For

the sake of clarity, only the first 100 ms are shown. It can be seen that in both cases the approximated trajectory agrees well with the perturbed trajectory. It is also shown that the sensitivities can be used for negative (Fig. 3.8 (a)) and positive (Fig. 3.8 (b)) parameter changes. Although not shown, the former statements are also valid for a change in the initial conditions of the differential states.

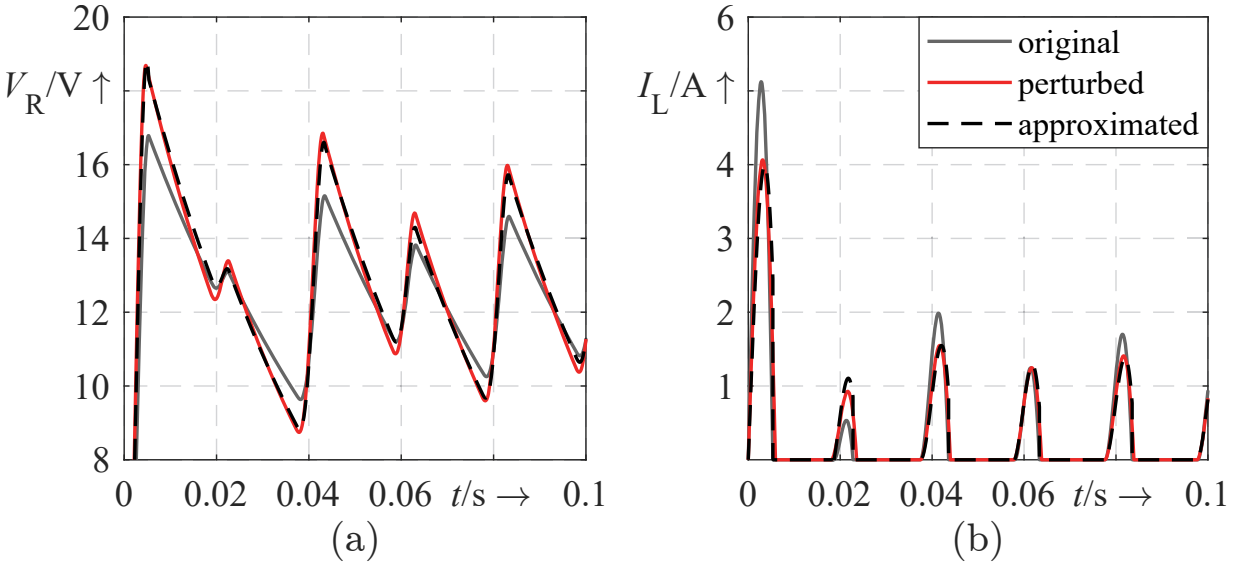

Figure 3.8: Exemplary trajectory approximation for different parameter changes
(a) $\Delta C = -3 \cdot 10^{-4}\text{F}\,(-30\%)$ (b) $\Delta L = +2 \cdot 10^{-4}\text{H}\,(+40\%)$

3.5 Conclusion of the chapter

This chapter discussed the theory of hybrid systems in the context of power systems. On the one hand, the literature review has shown that the origin of discrete dynamics can be at the component, control or communication level. On the other hand, several formal modelling approaches exist for hybrid systems. Here, the hybrid automaton can be considered as the most general case for modelling a hybrid system. Although switching systems are very similar, the main difference is that only the discrete states are allowed to jump in this case. For power systems, the DADS has been developed, which is quite similar to switching systems, which is assumed to be sufficient for this work. Therefore, the DADS approach is chosen for this thesis as it is explicitly designed for power systems at either the component or system level.

Because hybrid systems contain discrete dynamics, they can exhibit special hybrid dynamical phenomena such as sliding modes, infinitely fast switching, Zeno or chaotic behaviour. Therefore, when analysing hybrid systems, special attention must be paid to these phenomena. Furthermore, the stability of hybrid systems differs from that of pure continuous systems. In this chapter, different stability requirements for switched ODE and DAE systems are presented, based on Lyapunov's stability theory. It is shown that for linear switched ODE and DAE systems there are procedures to formally prove stability, although they can be difficult to compute. In addition, concepts such as the consistency projector can help to analyse linear hybrid systems in more detail, as it can determine whether impulsive behaviour (which can be problematic in real applications) is present. For non-linear switching systems, sufficient stability conditions can be established, but there is no general method for determining them. For this reason, formal verification of the stability of a detailed power system (hybrid and non-linear) is usually not possible. Otherwise, too many simplifications would have to be made, with the result that the system would be far away from reality. For the present work, this means that a formal proof of stability is not pursued. Instead, individual components, such as grid-forming converters or power electronic loads, are analysed according to their hybrid system modelling approach and characteristics.

Notable methods for analysing hybrid systems are reachability analysis, dwell-time analysis, Filippov theory, trajectory sensitivity and shooting method for grazing phenomena. As the first three have their strength in linear systems, they are mainly suitable for small models. In contrast, trajectory sensitivity is well suited for large, non-linear models, as it provides insight into their time-domain behaviour for changes in parameters and initial conditions. Similarly, the shooting method (based on trajectory sensitivity) can determine when a triggering surface is hit. However, it is more computationally intensive compared to trajectory sensitivity. Therefore, in this thesis, trajectory sensitivity is taken as the main method for analysing hybrid non-linear power systems.

4 Modelling of grid-forming converters with current limitation

In this chapter, the modelling approach of grid-forming (GFM) converters for this thesis is presented. First, the converter model, the AC filter and the DC circuit are described in Section 4.1. Second, the outer loop control, which is responsible for power synchronisation and voltage control, is outlined in Section 4.2. In detail, four approaches for power synchronisation are presented (droop control, matching control, dispatchable virtual oscillator control (dVOC) and virtual synchronous machine (VSM)), which will be used later to study their impact on voltage stability. The inner loop control, consisting of cascaded voltage and current control along with current limitation, is presented in Section 4.3. This is followed by an introduction to certain stability-enhancing control methods (SECMs) that are used to stabilise the GFM in the case of current limitation. Afterwards, in Section 4.5 an analysis of an exemplary GFM converter as a hybrid system. Emphasis is placed on how to correctly model the converter as a hybrid system and analyse its characteristics. In the end, a conclusion of the chapter is given in Section 4.6.

4.1 Converter model, AC filter and DC circuit

According to their control strategy, power electronic converters can be mainly divided into GFM and grid-following (GFL) converters. A graphical illustration of both concepts is given in Fig. 4.1. In general, a GFM converter is controlled to behave like a voltage source.

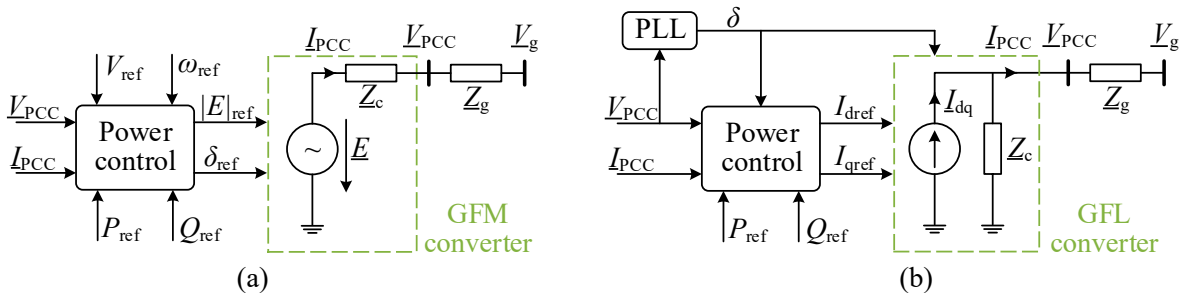

Figure 4.1: Simplified control concept of (a) grid-forming (GFM) converter (b) grid-following (GFL) converter (own illustration, based on [132] and [133])

This means that its active and reactive power reference P_{ref} and Q_{ref} are realised by controlling the magnitude and frequency of the voltage $\underline{V}_{\mathrm{PCC}}$ at the point of common coupling (PCC). In contrast to this, a GFL converter achieves its power references by adjusting the magnitude and phase of its current $\underline{I}_{\mathrm{PCC}}$. It thus behaves as a controllable current source and requires a synchronisation unit, such as a phase-locked loop (PLL). [133]

Most modern converters use insulated gate bipolar transistors (IGBTs) as power electronic switches. Depending on the harmonic requirements, voltage level and power rating, there are different converter configurations such as two-, three-level or multilevel converters. At the transmission system, modular multilevel converters are the most promising due to their scalability and low harmonics [134]. Since the frequency range of the dynamics of interest in this thesis is mainly about the fundamental frequency, an average model of the converter is used, consisting of controllable voltage sources, illustrated in Fig. 4.2. This is in line with current modelling guidelines for stability studies of power electronics [8, 135].

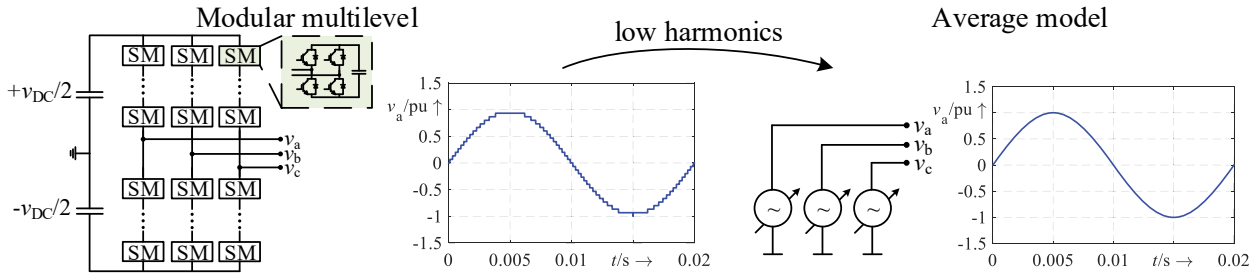

Figure 4.2: Simplification of the multilevel converter to an average model

The general design of the GFM converter model, AC filter and DC power source model in this thesis is mainly based on [81] and is illustrated in Fig. 4.3. The parameters of the converter and its control are given in Appendix A.1. Its three-phase filter dynamics in a dq reference frame are given by

$$c_{\mathrm{f}}\frac{\mathrm{d}}{\mathrm{d}t}v_{\mathrm{cd}} = i_{\mathrm{cd}} - i_{\mathrm{d}} + v_{\mathrm{cq}}c_{\mathrm{f}}\omega_0, \tag{4.1a}$$

$$c_{\mathrm{f}}\frac{\mathrm{d}}{\mathrm{d}t}v_{\mathrm{cq}} = i_{\mathrm{cq}} - i_{\mathrm{q}} - v_{\mathrm{cd}}c_{\mathrm{f}}\omega_0, \tag{4.1b}$$

$$l_{\mathrm{f}}\frac{\mathrm{d}}{\mathrm{d}t}i_{\mathrm{cd}} = v_{\mathrm{cd}} - i_{\mathrm{cd}}R_{\mathrm{f}} + i_{\mathrm{cq}}\omega_0 l_{\mathrm{f}} - v_{\mathrm{d}}, \tag{4.1c}$$

$$l_{\mathrm{f}}\frac{\mathrm{d}}{\mathrm{d}t}i_{\mathrm{cq}} = v_{\mathrm{cq}} - i_{\mathrm{cq}}R_{\mathrm{f}} - i_{\mathrm{d}}\omega_0 l_{\mathrm{f}} - v_{\mathrm{q}}, \tag{4.1d}$$

with l_f, c_f and r_f as the filter impedances, $\underline{v}_{cdq}$ as converter terminal voltage, $\underline{i}_{dcq}$ as the converter current, $\underline{v}_{dq}$ as the PCC voltage and $\underline{i}_{dq}$ as the PCC current. For independent control of active and reactive power, the coupling terms in (4.1a)-(4.1d) between the dq components must be compensated, which is described in more detail in Section 4.3.

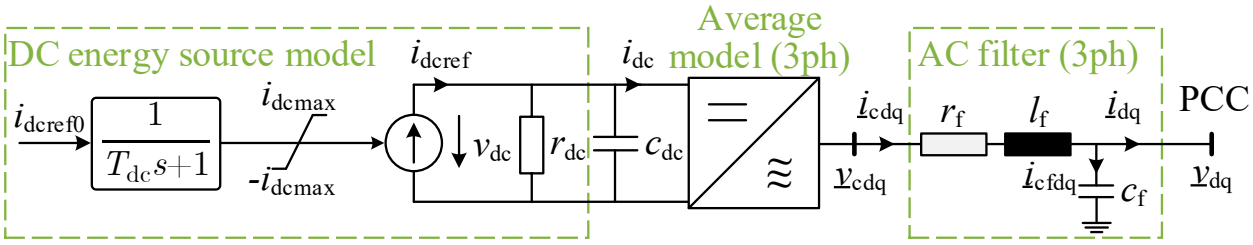

Figure 4.3: GFM converter model with DC energy source model and AC filter (own illustration, based on [81])

The DC circuit consists of a capacitance c_{dc}, a loss resistance r_{dc} and a controlled current source as an energy model. It is assumed that the energy source includes battery storage or represents a converter of an HVDC system. Thus, both configurations could provide a bi-directional power flow. The DC reference value i_{dcref0} is calculated as follows

$$i_{dcref0} = \frac{p_{ref}}{v^*_{dc}} + (v^*_{dc} - v_{dc})k_{dc} + \frac{v_{dc}}{r_{dc}} + \frac{\Delta p_{cf}}{v^*_{dc}}, \tag{4.2}$$

where p_{ref} is the active power reference, k_{dc} a droop parameter, v^*_{dc} the nominal and v_{dc} the actual dc voltage. Also, the AC-filter losses are included, which is represented by the active power difference Δp_c between the converter terminals and PCC

$$\Delta p_c = v_{cd} i_{cd} + v_{cq} i_{cq} - \left(v_d i_d + v_q i_q\right), \tag{4.3}$$

which is filtered via a first-order system

$$\Delta \dot{p}_{cf} = (\Delta p_c - \Delta p_{cf})\omega_f, \tag{4.4}$$

with ω_f as the filtering frequency. To model a finitely fast reacting energy source, an additional first-order system is introduced with the time constant T_{dc}

$$\dot{i}_{dcref\tau} = \frac{i_{dcref0} - i_{dcref\tau}}{T_{dc}}. \tag{4.5}$$

Because the DC power source can only deliver a certain amount of current, it is limited by

$$i_{\mathrm{dcref}} = \begin{cases} i_{\mathrm{dcref}\tau} & \text{if } i_{\mathrm{dcref}\tau} < i_{\mathrm{dcmax}}, \\ \mathrm{sgn}(i_{\mathrm{dcref}\tau}) i_{\mathrm{dcmax}} & \text{if } i_{\mathrm{dcref}\tau} >= i_{\mathrm{dcmax}}, \end{cases} \tag{4.6}$$

where i_{dcmax} is the maximum DC current and $\mathrm{sgn}(\cdot)$ is the sign function. Finally, the DC circuit is modelled by

$$\dot{v}_{\mathrm{dc}} = \frac{1}{c_{\mathrm{dc}}} \left(i_{\mathrm{dcref}} - \frac{v_{\mathrm{dc}}}{r_{\mathrm{dc}}} - i_{\mathrm{dc}} \right), \tag{4.7}$$

where the current i_{dc} is the power coupling between the DC and AC side given by

$$i_{\mathrm{dc}} = \frac{p_{\mathrm{c}}}{v_{\mathrm{dc}}} = \frac{\Re(\underline{v}_{\mathrm{cdq}} \cdot \bar{\underline{i}}_{\mathrm{cdq}})}{v_{\mathrm{dc}}} = \frac{v_{\mathrm{cd}} i_{\mathrm{cd}} + v_{\mathrm{cq}} i_{\mathrm{cq}}}{v_{\mathrm{dc}}}. \tag{4.8}$$

In addition, the terminal AC voltage $\underline{v}_{\mathrm{cdq}}$ is coupled with the DC voltage side by

$$\underline{v}_{\mathrm{cdq}} = \underline{v}_{\mathrm{cdqm}} \cdot \frac{v_{\mathrm{dc}}}{v_{\mathrm{dc}}^*}, \tag{4.9}$$

where $\underline{v}_{\mathrm{cdqm}}$ is the modulation voltage from the inner control (see Section 4.3).

For the phasor model, the DC circuit is modelled in such a way that only the DC voltage deviation Δv_{dc} from its nominal value is considered, which is important for matching control (see Section 4.2). This is similar to synchronous machines where only the speed deviation is considered. In cases where the real value of the DC voltage is required, e.g. in (4.9), the voltage deviation is increased by its nominal value. In this way, the EMT and the phasor converter are modelled similarly in balanced conditions. The main differences therefore arise in the modelling of the grid dynamics.

4.2 Outer loop: power synchronisation and voltage control

GFM controls have attracted a lot of interest in recent research due to their stabilising properties in power electronics-dominated systems, which is reflected in the number of different control approaches and their corresponding classification [132, 136, 137]. GFM controls can be classified into droop-based, synchronous machine based, and other approaches such

as virtual oscillators [132]. These approaches can be further classified according to their operating characteristics (e.g. grid-forming or grid-supporting), their control modes (e.g. $f(P)$ and $V(Q)$) and their grid connection (e.g. islanded or grid connected) [137]. To control active and reactive power independently, the GFM control is usually divided into a power synchronisation loop and a voltage control loop. Here, active power p is controlled by changing the frequency f of the converter (or its relative angle θ to the grid) and reactive power q by changing its voltage magnitude v. Unlike GFL converters, GFM converters do not require a dedicated synchronisation unit like a PLL. Instead, based on the mismatch between the active power reference p_{ref} and the measured active power p_{meas}, an acceleration or deceleration of the converter's terminal voltage angle θ_{c} takes place. Since the synchronisation of a GFL converter with a PLL is usually much faster than that of a GFM, the provided amount of inertia of a GFM converter is much higher [132]. However, the amount is limited by the energy source and its storage size. In addition, the current limitation of the converter also limits its inertia capacity. In the following, the GFM control approaches used in this thesis are described in more detail. Here, droop, matching, dVOC and VSM are used to analyse different types of GFM control. These controls thus cover a large part of the GFM classification.

4.2.1 Droop control

Due to its simplicity, droop control is a well-known GFM approach. As the control has a proportional characteristic, parallel operation of such converters is possible. Here a frequency-based droop control is used, shown in Fig. 4.4, where the measured power p_{meas} is used as input, which is filtered by a low-pass filter.

$$\dot{p}_{\text{f}} = (p_{\text{meas}} - p_{\text{f}})\omega_{\text{f}}, \tag{4.10}$$

where ω_{f} is the filter frequency and p_{f} is the filtered power. As noted in [138], the droop control is only able to provide inertia through the combination of filter time constant and droop gain, as this causes a delay in power synchronisation. The droop control law is given by

$$\dot{\theta} = \omega = \omega_{\text{ref}} + (p_{\text{ref}} - p_{\text{f}})k_{\text{d}}, \tag{4.11}$$

with k_{d} as the droop parameter, p_{ref} as the active power reference and ω_{ref} as the angular frequency reference. For a phasor model, ω_{ref} must be omitted as only the difference to the

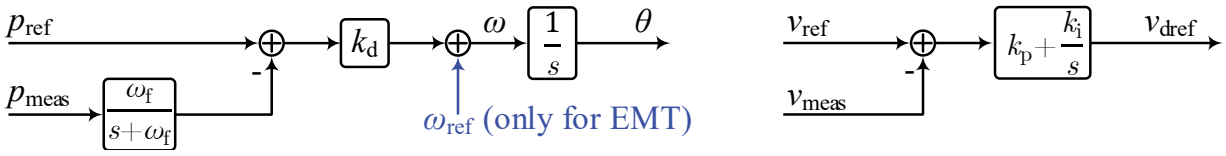

Figure 4.4: Block diagram of droop control (own illustration, based on [81])

fundamental frequency is required. For voltage control, a PI controller is used, given by

$$\dot{x}_v = (v_{ref} - v_{meas})k_i, \tag{4.12a}$$

$$v_{dref} = x_v + (v_{ref} - v_{meas})k_p, \tag{4.12b}$$

where k_p is the proportional and k_i is the integral gain.

4.2.2 Matching control

Matching control is based on the structural similarities of power balancing between the electromechanical part of a synchronous generator with its turbine and the DC circuit of a converter with its DC capacitance [81]. Here, an active power mismatch is detected, either as a speed deviation (synchronous machine) or as a DC voltage deviation (converter). Therefore, the DC voltage v_{dc} is used to determine the angle dynamics $\dot{\theta}$

$$\dot{\theta} = \omega = v_{dc}k_m, \tag{4.13}$$

where k_m is a parameter to match the desired angular frequency (see Fig. 4.5). For phasor simulations, only the DC voltage deviation Δv_{dc} is taken, as only the angular frequency deviation $\Delta\omega$ is needed. Like the droop control, the voltage control is implemented by a PI controller as in (4.12).

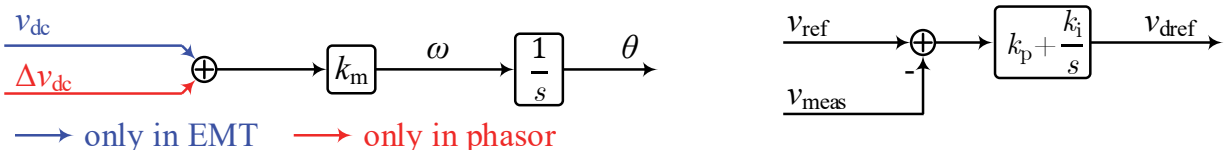

Figure 4.5: Block diagram of matching control (own illustration, based on [81])

4.2.3 Dispatchable virtual oscillator control

The dVOC is derived from the theory of coupled harmonic oscillators to operate in parallel with other converters [81]. The power synchronisation principle and angle dynamics $\dot{\theta}$ are given by

$$\dot{\theta} = \omega = \omega_{\text{ref}} + \eta \left(\frac{p_{\text{ref}}}{v_{\text{ref}}^2} - \frac{p_{\text{f}}}{v_{\text{dref}}^2} \right), \tag{4.14}$$

where η is a control parameter, v_{ref} the reference voltage and p_{f} the filtered active power (see Fig. 4.6). For phasor simulations, ω_{ref} is neglected. The reactive and voltage control dynamics are described by

$$\dot{v_{\text{dref}}} = v_{\text{dref}} \left(\eta \left(\frac{q_{\text{ref}}}{v_{\text{ref}}^2} - \frac{q_{\text{f}}}{v_{\text{dref}}^2} \right) + \beta \left(v_{\text{ref}}^2 - v_{\text{dref}}^2 \right) \right), \tag{4.15}$$

where $\beta = (\eta\alpha)/(v_{\text{ref}}^2)$ and α are control parameters and q_{f} is the filtered reactive power. To counteract a singularity at $v_{\text{dref}} = 0$ or $v_{\text{ref}} = 0$, a lower bound ϵ can be inserted (see Fig. 4.6). However, this does not represent a desired operating point and should be avoided.

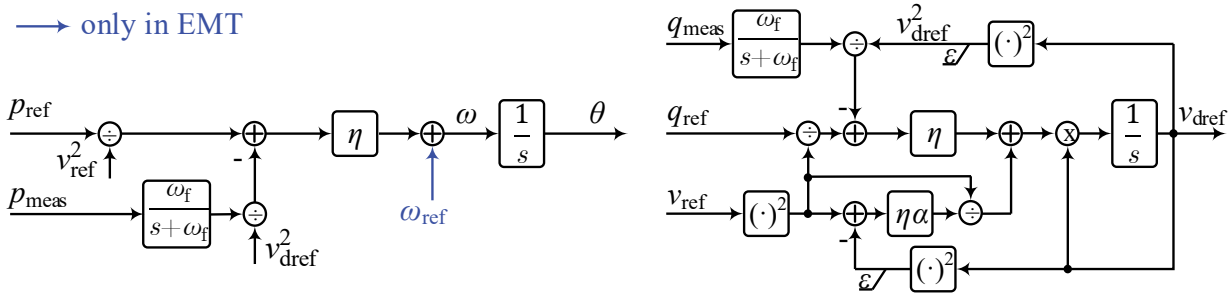

Figure 4.6: Block diagram of dVOC (own illustration, based on [81])

4.2.4 Virtual synchronous machine

While matching control is inspired only by the similarities of energy conservation in a synchronous generator, the VSM tries to emulate it by the well-known swing equation

$$\ddot{\theta} = \dot{\omega} = \frac{1}{J} \left(t_{\text{ref}} - t_{\text{f}} + D(\omega_{\text{ref}} - \omega) \right), \tag{4.16}$$

where J is the virtual inertia parameter and D is the damping factor (see Fig. 4.7). The power signals p_{ref} and p_{meas} are converted to their torque values t_{ref} and t_{f} by dividing by ω_{ref}. Similar to the droop and matching control, a PI-based controller is used for voltage control. The difference is that a virtual mutual impedance m_{fd} and the angular frequency ω are also used to emulate a AVR. This control loop is described by

$$\dot{x}_{\text{v}} = (v_{\text{ref}} - v_{\text{meas}})k_{\text{i}}, \tag{4.17a}$$

$$v_{\text{dref}} = \omega m_{\text{fd}} i_{\text{fd}}, \tag{4.17b}$$

$$= \omega m_{\text{fd}} \left(x_{\text{v}} + (v_{\text{ref}} - v_{\text{meas}})k_{\text{p}} \right), \tag{4.17c}$$

where i_{fd} is the virtual field current and k_{i} and k_{p} the respective PI gains.

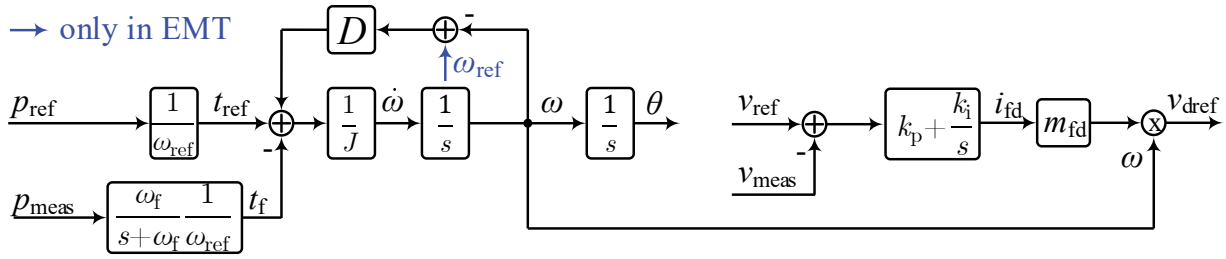

Figure 4.7: Block diagram of VSM control (own illustration, based on [81])

4.3 Inner loop: cascaded control and current limitation

Next, the low-level control, consisting of a cascaded voltage and current loop, and the current limitation are described. In general, the cascaded control mainly reflects the AC filter equations given in (4.1a)-(4.1d) and allows independent control of active and reactive power. The control structure and parameters are taken from [81].

4.3.1 Cascaded voltage and current control

The cascaded control is in a local dq-reference frame where all voltage and current measurements are transformed by the angle θ from the power synchronisation loop. The reference voltage is $\underline{v}_{\text{dq}}$ at the PCC. The transformation angle θ is used to align the voltage

$\underline{v}_{\mathrm{dq}}$ on the d-axis so that in steady state $v_{\mathrm{q}} = 0$ results. Unlike GFL converters, GFM converters have a voltage control loop between the power synchronisation loop and the inner current control. This converts the voltage references for the PCC into converter current references, which are then finally converted into converter terminal voltage references. These cascaded controls allow the insertion of a current limitation to protect the power electronic components from high overcurrents, which is described in the next section.

As shown in Fig. 4.8, the voltage control loop consists of two PI controllers and two decoupling terms, which can be described by

$$\begin{aligned} \dot{x}_{\mathrm{vd}} &= (v_{\mathrm{dref}} - v_{\mathrm{d}})k_{\mathrm{iv}}, \\ \dot{x}_{\mathrm{vq}} &= (v_{\mathrm{qref}} - v_{\mathrm{q}})k_{\mathrm{iv}}, \end{aligned} \tag{4.18}$$

where x_{vd} and x_{vq} are states and k_{iv} is the integral gain. The current reference value of the converter $\underline{i}_{\mathrm{cdqref}} = i_{\mathrm{cdref}} + \mathrm{j}i_{\mathrm{cqref}}$ is given by

$$\begin{aligned} i_{\mathrm{cdref}} &= i_{\mathrm{d}} + x_{\mathrm{vd}} + (v_{\mathrm{dref}} - v_{\mathrm{d}})k_{\mathrm{pv}} - \frac{v_{\mathrm{q}}}{x_{\mathrm{cf}}}, \\ i_{\mathrm{cqref}} &= i_{\mathrm{q}} + x_{\mathrm{vq}} + (v_{\mathrm{qref}} - v_{\mathrm{q}})k_{\mathrm{pv}} + \frac{v_{\mathrm{d}}}{x_{\mathrm{cf}}}, \end{aligned} \tag{4.19}$$

where v_{dref} and v_{qref} are inputs from the outer loop (with $v_{\mathrm{qref}} = 0$) and k_{pv} is the proportional gain. Adding $\frac{v_{\mathrm{q}}}{x_{\mathrm{cf}}}$ and $\frac{v_{\mathrm{d}}}{x_{\mathrm{cf}}}$ to the current reference values decouples the dq components (see (4.1a) and (4.1b)).

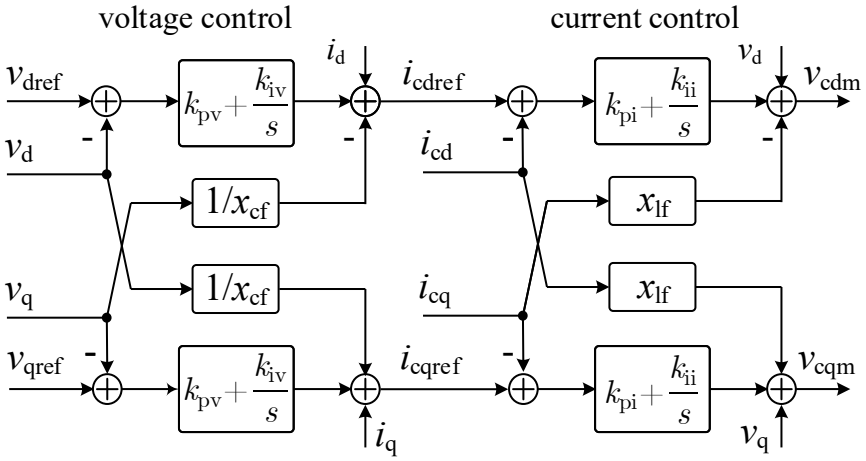

Figure 4.8: Cascaded voltage and current control (own illustration, based on [81])

These current reference values of the converter are then used as input to the current control, where the dynamics of the PI controllers are given by

$$\begin{aligned} \dot{x}_{\mathrm{id}} &= (i_{\mathrm{cdref}} - i_{\mathrm{cd}})k_{\mathrm{ii}}, \\ \dot{x}_{\mathrm{iq}} &= (i_{\mathrm{cqref}} - i_{\mathrm{cq}})k_{\mathrm{ii}}, \end{aligned} \tag{4.20}$$

where k_{ii} is the integral gain and x_{id} and x_{iq} are the integral controller states. Similarly to the voltage control loop, the filter dynamic equations are used to control the converter current

$$\begin{aligned} v_{\mathrm{cdm}} &= v_{\mathrm{d}} + x_{\mathrm{id}} + (i_{\mathrm{cdref}} - i_{\mathrm{cd}})k_{\mathrm{pi}} - i_{\mathrm{cq}}x_{\mathrm{lf}}, \\ v_{\mathrm{cqm}} &= v_{\mathrm{q}} + x_{\mathrm{iq}} + (i_{\mathrm{cqref}} - i_{\mathrm{cq}})k_{\mathrm{pi}} + i_{\mathrm{cd}}x_{\mathrm{lf}}, \end{aligned} \tag{4.21}$$

where k_{pi} is the proportional gain and x_{id} and x_{iq} are the integral controller states. The output is the modulation voltage $\underline{v}_{\mathrm{cdqm}}$ which is coupled to the DC voltage, see (4.9).

4.3.2 Current limitation and anti-windup method

There are several methods to protect a converter from overcurrents, such as virtual impedance or current saturation algorithms [3, 139]. All these approaches lead to a discrete change in the converter dynamics. This results in two conflicting control objectives. On the one hand, accurate current limitation is important to ensure that the converter is not damaged by overcurrents. On the other hand, the GFM capabilities should be maintained so that the converter remains synchronised with the grid, as the current limitation can decouple the outer and inner control loops. To achieve the first objective, in this thesis a circular current limitation is used, which is also known from GFL converters. For the second objective, an additional control is developed and implemented, which is called SECM in this thesis and introduced in Section 4.4.

If the absolute value of the converter current reference $|\underline{i}_{\mathrm{cdqref}}|$ exceeds its maximum value i_{cmax}, the current reference value is limited to $\underline{i}_{\mathrm{cdqlim}}$ to protect the converter (see Fig. 4.9). Here it is possible to choose whether the current is reduced without any axis prioritisation (also called circular current limitation [140] and the default case in this thesis)

$$\underline{i}_{\mathrm{cdqlim}} = \begin{cases} \underline{i}_{\mathrm{cdqref}} & \text{if } |\underline{i}_{\mathrm{cdqref}}| < i_{\mathrm{cmax}}, \\ \underline{i}_{\mathrm{cdqref}} \frac{i_{\mathrm{cmax}}}{|\underline{i}_{\mathrm{cdqref}}|} & \text{if } |\underline{i}_{\mathrm{cdqref}}| \geq i_{\mathrm{cmax}}, \end{cases} \tag{4.22}$$

or the q-axis current is prioritised

$$i_{\mathrm{cqlim}} = \begin{cases} i_{\mathrm{cqref}} & \text{if } |i_{\mathrm{cqref}}| < i_{\mathrm{cmax}}, \\ \mathrm{sgn}(i_{\mathrm{cqref}}) \cdot i_{\mathrm{cmax}} & \text{if } |i_{\mathrm{cqref}}| \geq i_{\mathrm{cmax}}, \end{cases} \tag{4.23}$$

$$i_{\mathrm{cdlim}} = \begin{cases} i_{\mathrm{cdref}} & \text{if } |i_{\mathrm{cdref}}| < \sqrt{i_{\mathrm{cmax}}^2 - i_{\mathrm{cqlim}}^2}, \\ \mathrm{sgn}(i_{\mathrm{cqref}}) \cdot \sqrt{i_{\mathrm{cmax}}^2 - i_{\mathrm{cqlim}}^2} & \text{if } |i_{\mathrm{cdref}}| \geq \sqrt{i_{\mathrm{cmax}}^2 - i_{\mathrm{cqlim}}^2}, \end{cases} \tag{4.24}$$

to inject more reactive power. The main advantage of this current limitation is that it effectively reduces the current to a specified level [139]. However, in a real application, i_{cmax} should be chosen below the thermal capacity of the power electronics to keep a certain distance. In addition, this current limitation can lead to large control errors in the preceding voltage control. To counteract this, an anti-windup method is implemented for this thesis (which is not part of the original implementation in [81]), which sets the derivatives of the integral controllers to zero in case of current limitation (cf. (4.18)):

$$\dot{x}_{\mathrm{vd}} = 0, \quad \dot{x}_{\mathrm{vq}} = 0. \tag{4.25}$$

This avoids large control errors during current limitation and keeps a residual amount of control in the proportional controller. The red lines in Fig. 4.9 indicate the signal of the anti-windup, where the line to the outer loop indicates that the signal is also used for the voltage PI controller in the outer loop, setting $\dot{x}_{\mathrm{v}}$ to zero. This multiple anti-windup is part of the developed SECM which is described in more detail in the next section.

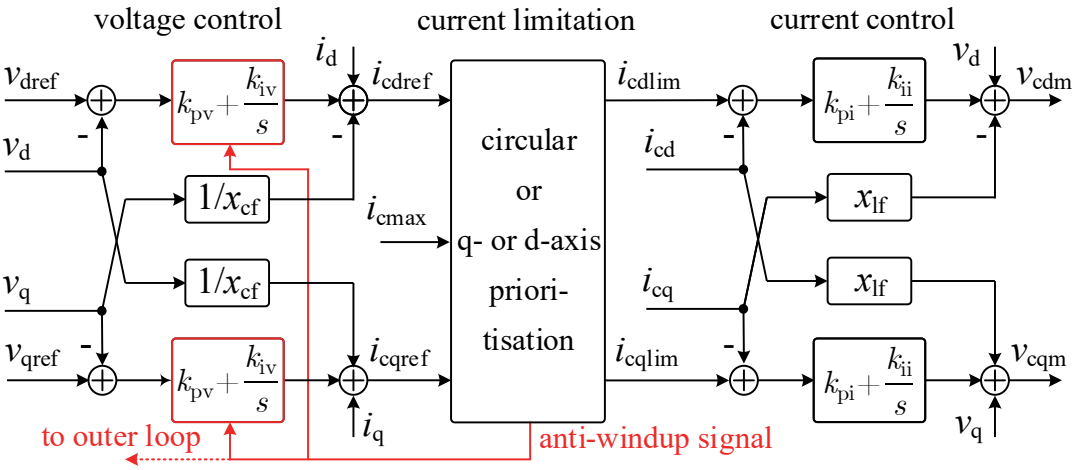

Figure 4.9: Cascaded voltage and current control with current limitation and anti-windup method (own illustration, based on [81])

4.4 Stability-enhancing control methods

In the event of major grid disturbances, such as short circuits, GFM converters may lose their stable operating point. Since the dynamics of GFM converters are similar to those of synchronous generators, they can exhibit a loss of synchronism such as transient instability. The main causes are either the absence of a stable equilibrium point after the fault or the overshoot of the unstable equilibrium point from the $P(\delta)$-curve during the fault. Several methods have been proposed to improve the transient stability of GFM converters, which can be divided into two categories

- adaptation of active and reactive power references,
- modification of control loops or parameters.

Methods of the first category try to reduce the power mismatch between reference and measured power to minimise the acceleration of the angle θ. Methods in the second category also attempt to achieve the same effect, by changing the virtual inertia or damping parameters, for example. The challenge here is to find suitable parameters for a variety of grid scenarios, as some approaches depend on the grid impedance. [3]

Throughout this thesis, all these methods will be referred to as SECMs for simplicity. The names of each method are followed by a number corresponding to the order in which they are presented, e.g. SECM-1 for the first method. To avoid algebraic loops within the later EMT models, the output of all SECMs are filtered by a first-order lag system with a time constant of 10^{-4} s. Also, they are limited by the maximum rated apparent power of the converter (except SECM-3). Next, the SECM developed for this thesis is described and its advantages over comparable methods are highlighted. The other methods are then presented.

4.4.1 SECM-1: Active and reactive power reference adaptation based on limited current reference

The proposed method belongs to the category that adapts the active and reactive power reference. Current limitation can occur for two main reasons. First, the power reference values are set above the rated power of the converter, which is unrealistic and should be avoided during normal operation. Second, the voltage $\underline{v}_{\mathrm{dq}}$ at the PCC is so low that the current that would have to be injected exceeds the capabilities of the converter. This means

that the maximum active and reactive power injected by the converter in the case of current limitation depends on the maximum converter current i_{cmax} and the PCC voltage $\underline{v}_{\mathrm{dq}}$. Thus, if the active power reference p_{ref} is greater than the maximum possible active power injection, the angle θ will increase continuously and the converter will lose synchronism with the grid. A similar control error results for the reactive power control loop due to the mismatch between the reference and the measured value.

The idea is to use the limited current reference $\underline{i}_{\mathrm{cdqlim}} = i_{\mathrm{cdlim}} + \mathrm{j}i_{\mathrm{cqlim}}$ in combination with the PCC voltage $\underline{v}_{\mathrm{dq}}$ to calculate new power reference values

$$p_{\mathrm{ref}} = \begin{cases} p_{\mathrm{ref0}} & \text{if } |\underline{i}_{\mathrm{cdqref}}| < i_{\mathrm{cmax}}, \\ v_{\mathrm{d}} \cdot i_{\mathrm{cdlim}} + v_{\mathrm{q}} \cdot i_{\mathrm{cqlim}} & \text{if } |\underline{i}_{\mathrm{cdqref}}| \geq i_{\mathrm{cmax}}, \end{cases} \tag{4.26}$$

$$q_{\mathrm{ref}} = \begin{cases} q_{\mathrm{ref0}} & \text{if } |\underline{i}_{\mathrm{cdqref}}| < i_{\mathrm{cmax}}, \\ v_{\mathrm{q}} \cdot i_{\mathrm{cdlim}} - v_{\mathrm{d}} \cdot i_{\mathrm{cqlim}} + \frac{|\underline{v}_{\mathrm{dq}}|^2}{x_{\mathrm{cf}}} & \text{if } |\underline{i}_{\mathrm{cdqref}}| \geq i_{\mathrm{cmax}}, \end{cases} \tag{4.27}$$

where p_{ref0} and q_{ref0} are the original power reference values. For the reactive power reference q_{ref} the reactive power injection $\frac{|\underline{v}_{\mathrm{dq}}|^2}{x_{\mathrm{cf}}}$ of the filter capacitance x_{cf} is included to get the total reactive power behind the PCC. By (4.26)-(4.27) the power references follow the output of the current limitation, whereas in normal operation the converter current follows the power references. The advantage of $\underline{i}_{\mathrm{cdqlim}}$ is that it is a control signal and therefore there is no measurement delay (except for $\underline{v}_{\mathrm{dq}}$). Next, a brief analysis of the SECM-1 for droop control is performed to show its stabilising effect in the case of current limitation.

For simplicity, the angle dynamics of the droop control are repeated here

$$\dot{\theta} = \omega_{\mathrm{ref}} + (p_{\mathrm{ref}} - p_{\mathrm{f}})k_{\mathrm{d}}. \tag{4.28}$$

Assuming that the filtered active power p_{f} is equal to the measured active power, (4.28) can be rewritten as

$$\dot{\theta} = \omega_{\mathrm{ref}} + (p_{\mathrm{ref}} - p_{\mathrm{meas}})k_{\mathrm{d}}. \tag{4.29}$$

The measured active power is given by $p_{\mathrm{meas}} = v_{\mathrm{d}}i_{\mathrm{d}} + v_{\mathrm{q}}i_{\mathrm{q}}$ which results in

$$\dot{\theta} = \omega_{\mathrm{ref}} + (p_{\mathrm{ref}} - v_{\mathrm{d}}i_{\mathrm{d}} - v_{\mathrm{q}}i_{\mathrm{q}})k_{\mathrm{d}}. \tag{4.30}$$

By inserting (4.26) in case of current limitation, (4.30) becomes

$$\dot{\theta} = \omega_{\mathrm{ref}} + (v_{\mathrm{d}} i_{\mathrm{cdlim}} + v_{\mathrm{q}} i_{\mathrm{cqlim}} - v_{\mathrm{d}} i_{\mathrm{d}} - v_{\mathrm{q}} i_{\mathrm{q}}) k_{\mathrm{d}}, \tag{4.31}$$

and rearranging gives

$$\dot{\theta} = \omega_{\mathrm{ref}} + \Big(v_{\mathrm{d}} (i_{\mathrm{cdlim}} - i_{\mathrm{d}}) + v_{\mathrm{q}} (i_{\mathrm{cqlim}} - i_{\mathrm{q}}) \Big) k_{\mathrm{d}}. \tag{4.32}$$

Eq. (4.32) shows that it is mainly the deviation between the limited current reference values and the actual currents that determines the acceleration or deceleration of θ with respect to ω_{ref}. For example, if i_{d} or i_{q} is greater than i_{cdlim} or i_{cqlim}, indicating that more active power is being injected as intended, θ will be decelerated. Assuming steady-state conditions, the current equation in Fig. 4.3 is given by

$$\underline{i}_{\mathrm{dq}} = \underline{i}_{\mathrm{cdq}} - \underline{i}_{\mathrm{cfdq}} = \underline{i}_{\mathrm{cdq}} - \frac{\underline{v}_{\mathrm{dq}}}{\underline{x}_{\mathrm{cf}}}, \tag{4.33}$$

with $\underline{x}_{\mathrm{cf}} = \frac{1}{\mathrm{j}\omega c_{\mathrm{f}}}$. Since the q-axis component of the PCC voltage is zero at steady state, $v_{\mathrm{q}} = 0$, (4.33) can be rewritten as

$$\underline{i}_{\mathrm{dq}} = \underline{i}_{\mathrm{cdq}} - \frac{v_{\mathrm{d}}}{\underline{x}_{\mathrm{cf}}}. \tag{4.34}$$

Separating the real and imaginary parts results in

$$i_{\mathrm{d}} = i_{\mathrm{cd}}, \tag{4.35a}$$

$$i_{\mathrm{q}} = i_{\mathrm{cq}} - v_{\mathrm{d}} \omega c_{\mathrm{f}}. \tag{4.35b}$$

This shows that at steady state the d-axis component of the converter i_{cd} is equal to the grid current i_{d}. Furthermore, steady state means that $i_{\mathrm{cd}} = i_{\mathrm{cdlim}}$ (same for q-axis) as the current control has reached its reference values. By considering these conditions in (4.32)

$$\dot{\theta} = \omega_{\mathrm{ref}} + \left(v_{\mathrm{d}} (\underbrace{i_{\mathrm{cdlim}} - i_{\mathrm{d}}}_{=0}) + \underbrace{v_{\mathrm{q}}}_{=0} (i_{\mathrm{cqlim}} - i_{\mathrm{q}}) \right) k_{\mathrm{d}} = \omega_{\mathrm{ref}}, \tag{4.36}$$

it is shown that the proposed SECM-1 not only stabilises the converter during transients but also during steady-state current limitation. This stabilising effect can also be shown for the VSM and dVOC as they have comparable power synchronisation principles. In order to show the effect on the matching control, the DC circuit must be taken into account.

Assuming that the DC reference current i_{dcref0} is not limited and the time constant of the energy model is negligible, the DC voltage dynamics from (4.7) can be stated as

$$\dot{v}_{\mathrm{dc}} = \frac{1}{c_{\mathrm{dc}}} \left(\underbrace{\frac{p_{\mathrm{ref}}}{v_{\mathrm{dc}}^*} + (v_{\mathrm{dc}}^* - v_{\mathrm{dc}}) k_{\mathrm{dc}} + \frac{v_{\mathrm{dc}}}{r_{\mathrm{dc}}} + \frac{\Delta p_{\mathrm{c}}}{v_{\mathrm{dc}}^*}}_{=i_{\mathrm{dcref0}}} - \frac{v_{\mathrm{dc}}}{r_{\mathrm{dc}}} - i_{\mathrm{dc}} \right). \tag{4.37}$$

Next, (4.26) for p_{ref} in the case of current limitation and (4.8) for i_{dc} are included and the DC losses are deleted as they cancel each other out, resulting in

$$\dot{v}_{\mathrm{dc}} = \frac{1}{c_{\mathrm{dc}}} \left((v_{\mathrm{dc}}^* - v_{\mathrm{dc}}) k_{\mathrm{dc}} + \frac{\Delta p_{\mathrm{c}}}{v_{\mathrm{dc}}^*} + \frac{\overbrace{v_{\mathrm{d}} \cdot i_{\mathrm{cdlim}} + v_{\mathrm{q}} \cdot i_{\mathrm{cqlim}}}^{p_{\mathrm{ref}}}}{v_{\mathrm{dc}}^*} - \underbrace{\frac{v_{\mathrm{cd}} i_{\mathrm{cd}} + v_{\mathrm{cq}} i_{\mathrm{cq}}}{v_{\mathrm{dc}}}}_{i_{\mathrm{dc}}} \right). \tag{4.38}$$

Assuming steady state conditions again, the DC reference voltage is equal to the actual DC voltage $v_{\mathrm{dc}}^* = v_{\mathrm{dc}}$ and the assumptions made above. Inserting Δp_{c} from (4.3) into (4.38) it can be rewritten as (assuming that v_{q} is zero)

$$\dot{v}_{\mathrm{dc}} = \frac{1}{c_{\mathrm{dc}}} \left(\frac{v_{\mathrm{cd}} i_{\mathrm{cd}} + v_{\mathrm{cq}} i_{\mathrm{cq}} - v_{\mathrm{d}} i_{\mathrm{d}}}{v_{\mathrm{dc}}^*} + \frac{v_{\mathrm{d}} \cdot i_{\mathrm{cdlim}}}{v_{\mathrm{dc}}^*} - \frac{v_{\mathrm{cd}} i_{\mathrm{cd}} + v_{\mathrm{cq}} i_{\mathrm{cq}}}{v_{\mathrm{dc}}} \right), \tag{4.39}$$

and rearranging results in

$$\dot{v}_{\mathrm{dc}} = \frac{1}{c_{\mathrm{dc}}} \left(\underbrace{\frac{v_{\mathrm{d}} \cdot i_{\mathrm{cdlim}}}{v_{\mathrm{dc}}^*} - \frac{v_{\mathrm{d}} i_{\mathrm{d}}}{v_{\mathrm{dc}}^*}}_{=0} + \underbrace{\frac{v_{\mathrm{cd}} i_{\mathrm{cd}} + v_{\mathrm{cq}} i_{\mathrm{cq}}}{v_{\mathrm{dc}}^*} - \frac{v_{\mathrm{cd}} i_{\mathrm{cd}} + v_{\mathrm{cq}} i_{\mathrm{cq}}}{v_{\mathrm{dc}}}}_{=0} \right) = 0, \tag{4.40}$$

which demonstrates that a balance can also be found for matching control in the case of current limitation. In addition, (4.40) also reveals that the DC circuit is also balanced in the case of a different GFM control with current limiting.

As q_{ref} only appears in the dVOC control for reactive power, the influence of SECM-1 is only analysed there. By inserting (4.27) into (4.15) the following expression is obtained

$$\dot{v_{\mathrm{dref}}} = v_{\mathrm{dref}} \left(\eta \left(\frac{v_{\mathrm{q}} \cdot i_{\mathrm{cdlim}} - v_{\mathrm{d}} \cdot i_{\mathrm{cqlim}} + \frac{|\underline{v}_{\mathrm{dq}}|^2}{x_{\mathrm{cf}}}}{v_{\mathrm{ref}}^2} - \frac{q_{\mathrm{f}}}{v_{\mathrm{dref}}^2} \right) + \beta \left(v_{\mathrm{ref}}^2 - v_{\mathrm{dref}}^2 \right) \right). \tag{4.41}$$

It is assumed that the filter delay for q_f is negligible and $q_\mathrm{f} = q_\mathrm{meas}$. The measured reactive power at the PCC is given by

$$\begin{aligned} q_\mathrm{meas} &= \Im\left(\underline{v}_\mathrm{dq}\left(\underline{i}^*_\mathrm{cdq} - \underline{i}^*_\mathrm{cfdq}\right)\right) \\ &= \Im\left(\left(v_\mathrm{d} + \mathrm{j}v_\mathrm{q}\right)\left(i_\mathrm{cd} - \mathrm{j}i_\mathrm{cq} - \frac{v_\mathrm{d} - \mathrm{j}v_\mathrm{q}}{\mathrm{j}x_\mathrm{cf}}\right)\right) \\ &= v_\mathrm{q} i_\mathrm{cd} - v_\mathrm{d} i_\mathrm{cq} + \frac{v_\mathrm{d}^2 + v_\mathrm{q}^2}{x_\mathrm{cf}}. \end{aligned} \tag{4.42}$$

By inserting q_meas from (4.42) into (4.41) and assuming that in steady state $v_\mathrm{ref} = v_\mathrm{dref}$ holds, the dVOC voltage control dynamics result in

$$\dot{v}_\mathrm{dref} = v_\mathrm{dref}\eta\left(\frac{v_\mathrm{q}\cdot i_\mathrm{cdlim} - v_\mathrm{d}\cdot i_\mathrm{cqlim} + \frac{|\underline{v}_\mathrm{dq}|^2}{x_\mathrm{cf}}}{v_\mathrm{ref}^2} - \frac{v_\mathrm{q} i_\mathrm{cd} - v_\mathrm{d} i_\mathrm{cq} + \frac{v_\mathrm{d}^2+v_\mathrm{q}^2}{x_\mathrm{cf}}}{v_\mathrm{dref}^2}\right). \tag{4.43}$$

Since $|\underline{v}_\mathrm{dq}|^2 = v_\mathrm{d}^2 + v_\mathrm{q}^2$, (4.43) can be rewritten to

$$\dot{v}_\mathrm{dref} = v_\mathrm{dref}\eta\left(\underbrace{\frac{v_\mathrm{q}\cdot i_\mathrm{cdlim}}{v_\mathrm{ref}^2} - \frac{v_\mathrm{q}\cdot i_\mathrm{cd}}{v_\mathrm{dref}^2}}_{=0} + \underbrace{\frac{v_\mathrm{d}\cdot i_\mathrm{cq}}{v_\mathrm{dref}^2} - \frac{v_\mathrm{d}\cdot i_\mathrm{cqlim}}{v_\mathrm{ref}^2}}_{=0} + \underbrace{\frac{v_\mathrm{d}^2 + v_\mathrm{q}^2}{v_\mathrm{ref}^2 x_\mathrm{cf}} - \frac{v_\mathrm{d}^2 + v_\mathrm{q}^2}{v_\mathrm{dref}^2 x_\mathrm{cf}}}_{=0}\right) = 0, \tag{4.44}$$

and results in an equilibrium for the voltage control loop of the dVOC.

Overall, the above analyses demonstrate that SECM-1 is capable of stabilising all the GFM controllers presented. SECM-1 is complemented by the described anti-windup method for both the inner and outer voltage PI controllers (see Section 4.3). Its main advantage is that it can find a stable equilibrium point for the converter in the case of current limitation, regardless of the current axis prioritisation. On the one hand, if the q-axis current is prioritised, p_ref will also decrease accordingly. On the other hand, p_ref will decrease less if the d-axis current is prioritised. As this SECM has no parameters, there is no need to tune them. Next, the other SECMs are presented to serve as benchmarks for later stability analysis.

4.4.2 SECM-2: Active power reference adaptation based on PCC voltage magnitude

In [141] a linear adaptation of the active power reference based on the per unit voltage $|\underline{v}_{\mathrm{dq}}|$ is presented and described by

$$p_{\mathrm{ref}} = \begin{cases} p_{\mathrm{ref}} & \text{if } |\underline{v}_{\mathrm{dq}}| \geq 0.9 \text{ pu}, \\ p_{\mathrm{ref}} \cdot |\underline{v}_{\mathrm{dq}}| & \text{if } |\underline{v}_{\mathrm{dq}}| < 0.9 \text{ pu}. \end{cases} \tag{4.45}$$

Thus, SECM-2 is only activated at a certain voltage threshold, regardless of whether the current is limited or not. Unlike SECM-1, there is no q_{ref} adjustment here. The next step is to analyse when the steady state conditions are fulfilled when SECM-2 is active. To do this (4.30) from the droop example is used. By inserting (4.45) the following expression is obtained

$$\begin{aligned} \dot{\theta} &= \omega_{\mathrm{ref}} + (p_{\mathrm{ref}}|\underline{v}_{\mathrm{dq}}| - v_{\mathrm{d}} i_{\mathrm{d}} - v_{\mathrm{q}} i_{\mathrm{q}}) k_{\mathrm{d}} \\ &= \omega_{\mathrm{ref}} + (p_{\mathrm{ref}} \sqrt{v_{\mathrm{d}}^2 + v_{\mathrm{q}}^2} - v_{\mathrm{d}} i_{\mathrm{d}} - v_{\mathrm{q}} i_{\mathrm{q}}) k_{\mathrm{d}}. \end{aligned} \tag{4.46}$$

Applying $v_{\mathrm{q}} = 0$ for steady state, (4.46) can be rewritten as

$$\begin{aligned} \dot{\theta} &= \omega_{\mathrm{ref}} + (p_{\mathrm{ref}} v_{\mathrm{d}} - v_{\mathrm{d}} i_{\mathrm{d}}) k_{\mathrm{d}} \\ &= \omega_{\mathrm{ref}} + v_{\mathrm{d}} \underbrace{(p_{\mathrm{ref}} - i_{\mathrm{d}})}_{\text{have to be equal}} k_{\mathrm{d}}. \end{aligned} \tag{4.47}$$

Eq. (4.47) indicates that an equilibrium is only possible if $p_{\mathrm{ref}} = i_{\mathrm{d}}$ (in per unit). Problems could arise if the q-axis current component is prioritised, as this significantly reduces i_{cdlim} (and thus i_{d}) and only a very low original power reference value could stabilise the converter. In contrast, current prioritisation on the d-axis should be advantageous for the SECM-2, as in this case equality should be mostly possible, if $p_{\mathrm{ref}} \leq 1.0\,\mathrm{pu}$ and $i_{\mathrm{cmax}} = 1.0\,\mathrm{pu}$.

4.4.3 SECM-3: Stability-enhancing component based on q-axis component of PCC voltage

In [78], a stability-enhancing component is introduced that adds a damping term $\Delta\omega$ to the angular frequency ω in the power synchronisation loop, consisting of the q-axis component

of $\underline{v}_{\mathrm{dq}}$ multiplied by the factor k_{q}

$$\Delta\omega = v_{\mathrm{q}} \cdot k_{\mathrm{q}}. \tag{4.48}$$

Since v_{q} is zero in steady state, it only dampens the acceleration of θ during transients. Originally designed for $P-f$ droop control, it can also be used for other GFM approaches by adding it to the angular frequency ω at the appropriate positions. As noted in [78], the stability-enhancing component is only effective when the grid voltage v_{g} is greater than (derived for a $P-f$ droop control in [78])

$$v_{\mathrm{g}} > \frac{p_{\mathrm{ref}} + k_{\mathrm{q}} \cdot x_{\Sigma} \cdot i_{\mathrm{max}}/k_{\mathrm{d}}}{\sqrt{i_{\mathrm{max}}^2 + \left(k_{\mathrm{q}}/k_{\mathrm{d}}\right)^2}}, \tag{4.49}$$

where x_{Σ} is the sum of filter, transformer and grid inductance and k_{d} is the droop parameter. Since p_{ref} and the grid impedance are not always known, k_{q} must be tuned accordingly to stabilise the converter in a wide range of grid scenarios. However, in most cases a higher value of k_{d} will result in a wider stable voltage range, as shown by (4.49).

4.4.4 SECM-4: Active power reference adaptation based on converter current

In [81] a SECM is presented where the active power reference is reduced by a droop characteristic of $\underline{i}_{\mathrm{cdq}}$ in case of current limitation

$$p_{\mathrm{ref}}^{*} = \begin{cases} p_{\mathrm{ref}} & \text{if } |\underline{i}_{\mathrm{cdq}}| < i_{\mathrm{thr}}, \\ p_{\mathrm{ref}} - \gamma(|\underline{i}_{\mathrm{cdq}}| - i_{\mathrm{thr}}) & \text{if } |\underline{i}_{\mathrm{cdq}}| \geq i_{\mathrm{thr}}, \end{cases} \tag{4.50}$$

where γ is a droop parameter and i_{thr} pu is the current threshold for activation, which should be less than the maximum converter current i_{cmax}. Next, the same analysis as for SECM-1 and SECM-2 is carried out to derive the conditions under which a steady-state equilibrium is possible in the case of current limitation. For this purpose (4.50) is included in (4.30).

$$\begin{aligned} \dot{\theta} &= \omega_{\mathrm{ref}} + (p_{\mathrm{ref}} - \gamma(|\underline{i}_{\mathrm{cdq}}| - i_{\mathrm{thr}}) - v_{\mathrm{d}} i_{\mathrm{d}} - v_{\mathrm{q}} i_{\mathrm{q}}) k_{\mathrm{d}} \\ &= \omega_{\mathrm{ref}} + (p_{\mathrm{ref}} - \gamma(\sqrt{i_{\mathrm{d}}^2 + i_{\mathrm{q}}^2} - i_{\mathrm{thr}}) - v_{\mathrm{d}} i_{\mathrm{d}} - v_{\mathrm{q}} i_{\mathrm{q}}) k_{\mathrm{d}}. \end{aligned} \tag{4.51}$$

Applying $v_q = 0$ for steady state, (4.51) can be rewritten as

$$\dot{\theta} = \omega_{ref} + \underbrace{(p_{ref} - \gamma(i_d - i_{thr}) - v_d i_d)}_{\text{has to be zero for steady-state}} k_d, \tag{4.52}$$

which means that no clear conditions for achieving an equilibrium can be derived, as the question arises of how to parameterise i_{thr} and γ. In [81] it is stated that the droop parameter can be chosen to be $\gamma = 2.3\frac{p_{base}}{i_{base}}$, where p_{base} is the base active power and i_{base} is the base current of the converter. Similar to SECM-2, the d-axis current prioritisation should be advantageous and the q-axis current prioritisation disadvantageous for the stability of the converter.

4.5 Droop-based grid-forming converter as hybrid system

In this subsection, a droop-based GFM converter is described as a DADS to explore its differential, algebraic and discrete states, as well as its properties as a hybrid system. The effect of current limitation and SECM-1 on the small-signal stability of the converter is also investigated. To simplify the analysis, the converter is placed in an islanded microgrid supplying a resistive-inductive load as shown in Fig. 4.10. Similar analyses could be carried out for the other GFM control approaches, but are not done in this thesis. In general, most of the differential and algebraic equations of the converter from Section 4.1 to 4.4 remain the same. The focus is on the description of the discrete dynamics and their translation into a DADS. A complete list of equations as DADS is given in the Appendix A.2.

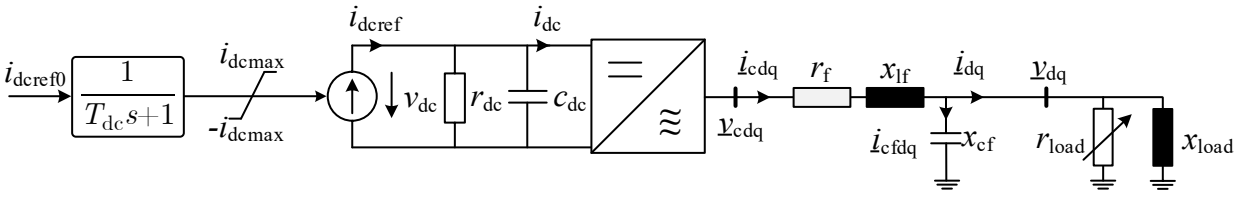

Figure 4.10: droop-based GFM converter in an islanded microgrid to describe it as a DADS (droop control not shown)

To explore its discrete dynamics, the circular current limitation of (4.22) is taken and repeated here for convenience, but only for the d-axis (same procedure for the q-axis)

$$i_{\mathrm{cdlim}} = \begin{cases} i_{\mathrm{cdref}} & \text{if } |\underline{i}_{\mathrm{cdqref}}| < i_{\mathrm{cmax}}, \\ i_{\mathrm{cdref}} \frac{i_{\mathrm{cmax}}}{|\underline{i}_{\mathrm{cdqref}}|} & \text{if } |\underline{i}_{\mathrm{cdqref}}| \geq i_{\mathrm{cmax}}. \end{cases} \tag{4.53}$$

As mentioned in the general DADS description in (3.7)-(3.9), a switch in the algebraic equation from $g_i^-(\overline{\mathbf{x}}, \mathbf{y})$ to $g_i^+(\overline{\mathbf{x}}, \mathbf{y})$, occurs if the switching condition $s_i(\overline{\mathbf{x}}, \mathbf{y})$ is greater or less than zero. Taking this into account, (4.53) can be rewritten as

$$0 = \begin{cases} g_{\mathrm{icdlim}}^-(\overline{\mathbf{x}}, \mathbf{y}) = i_{\mathrm{cdlim}} - i_{\mathrm{cdref}}, & s_{\mathrm{imax}}(\overline{\mathbf{x}}, \mathbf{y}) = |\underline{i}_{\mathrm{cdqref}}| - i_{\mathrm{cmax}} < 0, \\ g_{\mathrm{icdlim}}^+(\overline{\mathbf{x}}, \mathbf{y}) = i_{\mathrm{cdlim}} - i_{\mathrm{cdref}} \frac{i_{\mathrm{cmax}}}{|i_{\mathrm{cdref}}|}, & s_{\mathrm{imax}}(\overline{\mathbf{x}}, \mathbf{y}) = |\underline{i}_{\mathrm{cdqref}}| - i_{\mathrm{cmax}} > 0. \end{cases} \tag{4.54}$$

The main difference is that (4.53) is reformulated as an implicit algebraic equation, where i_{cdlim} becomes an algebraic state. For the switching condition $s_{\mathrm{imax}}(\overline{\mathbf{x}}, \mathbf{y})$, i_{cmax} is moved to the left-hand side to compare it with zero. Also, the inequality sign changes to a greater-than sign (>) instead of greater-than or equal to sign (≥). This can have an impact on the later implementation, which will be discussed in more detail in the rest of this chapter and in Section 6.1. The above procedure also applies to i_{cqlim}.

From a formal point of view, (4.54) is sufficient to describe the circular current limitation as a DADS, which involves only switching algebraic equations and no impulsive behaviour. However, from an implementation point of view, problems may arise for the numerical solver if the equations switch during the simulation, due to adaptive step sizes and internal caches which may not be updated to the new equations after a jump. Therefore, from the solver's point of view, it is advantageous if the equations remain static during the numerical integration. This topic is further elaborated in Section 6.1, where some requirements for the implementation and simulation of hybrid systems in the Julia programming language are pointed out. To obtain a static expression of (4.54), the discrete state q_{imax} is introduced, which can only have the values zero or one. Thus, (4.54) is expressed as

$$0 = i_{\mathrm{cdlim}} - \left(\underbrace{(1 - q_{\mathrm{imax}}) i_{\mathrm{cdref}}}_{\text{normal operation}} + \underbrace{q_{\mathrm{imax}} \frac{i_{\mathrm{cdref}} i_{\mathrm{cmax}}}{\sqrt{i_{\mathrm{cdref}}^2 + i_{\mathrm{cqref}}^2}}}_{\text{current limitation}} \right), \tag{4.55}$$

where the discrete state q_{imax} changes its value according to the reset function $h_{\mathrm{qimax}}(\overline{\mathbf{x}}^{-}, \mathbf{y}^{-})$ when the switching condition $s_{\mathrm{imax}}(\overline{\mathbf{x}}, \mathbf{y})$ is satisfied

$$q_{\mathrm{imax}}^{+} = h_{\mathrm{qimax}}(\overline{\mathbf{x}}^{-}, \mathbf{y}^{-}) = 1 - q_{\mathrm{imax}}^{-}, \qquad s_{\mathrm{imax}}(\overline{\mathbf{x}}, \mathbf{y}) = |\underline{i}_{\mathrm{cdqref}}| - i_{\mathrm{cmax}} = 0. \tag{4.56}$$

Here the reset function h_{qimax} (the entries for all other states are zero) is designed in a way that q_{imax} only jumps between one and zero. Changing q_{imax} "activates" and "deactivates" parts of (4.55) each time the condition in (4.56) is fulfilled. There is still a switch in the equation expression, but the solver has all the information it needs to evaluate the equations as both parts are already included. Furthermore, (4.55) and (4.56) are still in a DADS representation by inserting a discrete state with impulsive behaviour and implicitly switching algebraic equations.

In the next step, the anti-windup of the voltage control states is implemented by using the discrete state q_{imax}

$$\begin{aligned} \dot{x}_{\mathrm{vd}} &= (v_{\mathrm{dref}} - v_{\mathrm{d}}) k_{\mathrm{iv}} (1 - q_{\mathrm{imax}}), \\ \dot{x}_{\mathrm{vq}} &= (v_{\mathrm{qref}} - v_{\mathrm{q}}) k_{\mathrm{iv}} (1 - q_{\mathrm{imax}}), \end{aligned} \tag{4.57}$$

and the adaptation of the active power reference of the SECM-1 by an algebraic equation

$$0 = p_{\mathrm{ref}} - \left((1 - q_{\mathrm{imax}}) p_{\mathrm{ref0}} + q_{\mathrm{imax}} \left(i_{\mathrm{cdlim}} v_{\mathrm{d}} + i_{\mathrm{cqlim}} v_{\mathrm{q}} \right) \right), \tag{4.58}$$

where p_{ref} also becomes an algebraic state. This shows that with the appropriate choice of a discrete state, a compact description of the converter as a hybrid system is achieved. For a complete DADS model, a second discrete state q_{dcmax} is required to account for the DC current limit of the energy model (see (4.6)). This allows the GFM converter and the microgrid to be described by two discrete, ten differential and eight algebraic states. Here the algebraic states are divided into two states for the grid and six for the converter. The complete list of equations can be found in the Appendix A.2.

A general problem that can arise from the above implementation is the hybrid phenomenon of chattering or infinitely fast switching. This can happen, for example, if the converter reaches its maximum current i_{cmax} in a steady state and $|\underline{i}_{\mathrm{cdqref}}| - i_{\mathrm{cmax}} = 0$ is always satisfied. In this case, q_{imax} would (theoretically) switch between zero and one infinitely fast due to this condition. To avoid this, Filippov theory could be used to introduce a *sliding mode*, where the system trajectories slide along the surface of a switching condition [117, 142]. The dynamics of the system during sliding is then given by a combination of the dynamics before and after this surface. This highlights that it should be kept in mind that some

hybrid phenomena are highly dependent on how the hybrid system is implemented and are therefore based on modelling artefacts [5]. Another approach is to split the switching condition in (4.56) into two parts to counteract this phenomenon

$$q^{+}_{\mathrm{imax}} = h_{\mathrm{qimax},1}(\overline{\mathbf{x}}^{-}, \mathbf{y}^{-}) = 1, \qquad s_{\mathrm{imax},1}(\overline{\mathbf{x}}, \mathbf{y}) = |\underline{i}_{\mathrm{cdqref}}| - i_{\mathrm{cmax}} - k \cdot q_{\mathrm{imax}} \geq 0, \tag{4.59}$$

$$q^{+}_{\mathrm{imax}} = h_{\mathrm{qimax},0}(\overline{\mathbf{x}}^{-}, \mathbf{y}^{-}) = 0, \qquad s_{\mathrm{imax},0}(\overline{\mathbf{x}}, \mathbf{y}) = (|\underline{i}_{\mathrm{cdqref}}| - i_{\mathrm{cmax}}) \cdot q_{\mathrm{imax}} < 0. \tag{4.60}$$

This has several advantages. First, there is no chattering at steady state during current limitation because the switching condition $s_{\mathrm{imax},1}(\overline{\mathbf{x}}, \mathbf{y})$ is only activated once. The factor k is used (e.g. set to 10) to ensure that even if $|\underline{i}_{\mathrm{cdqref}}|$ would become very large (in per units) during current limitation, the total expression will remain below zero. Since q_{imax} is zero in normal operation, k has no effect on entering the current limiting mode. So the reset function is only called once. Second, when the converter switches from current limitation to normal operation, the multiplication with q_{imax} in $s_{\mathrm{imax},0}(\overline{\mathbf{x}}, \mathbf{y})$ ensures that the corresponding reset function is also called only once since it is zero afterwards.

On the one hand, changing the switching conditions from an equality constraint to an inequality constraint is much easier for later implementation. Because of the inequality, no root-finding methods are required to calculate the exact time at which the condition is satisfied. Instead, it is only necessary to check in each integration step whether the conditions are true or not. On the other hand, this change means that the system is no longer a pure DADS. However, if the time steps are small enough, the trajectory sensitivities can still be calculated, as shown in the later results. The above changes for the switching conditions of q_{dcmax} are also made, but not shown here (see Appendix A.2).

A graphical illustration of the GFM converter as a hybrid automaton is given in Fig. 4.11. As can be seen, the two discrete states lead to four discrete locations by their combination. Transitions from opposite states could also be possible (e.g. from *normal* to *DC & AC current limitation*) but are not drawn. The reasons for this are that it is very unlikely that both conditions are fulfilled at the same time, and it would lead to an overloaded automaton with less additional information. Also, consecutive transitions in an arbitrarily short time might be possible to overcome this problem. In general, the automaton shows that the two discrete states are mostly independent of each other. If the transitions from the opposite nodes are also considered, the automaton would represent a complete graph, where each state can be reached from any other state. Of course, further calculations can be made to

analyse the circumstances under which the DC and AC limits depend on each other.

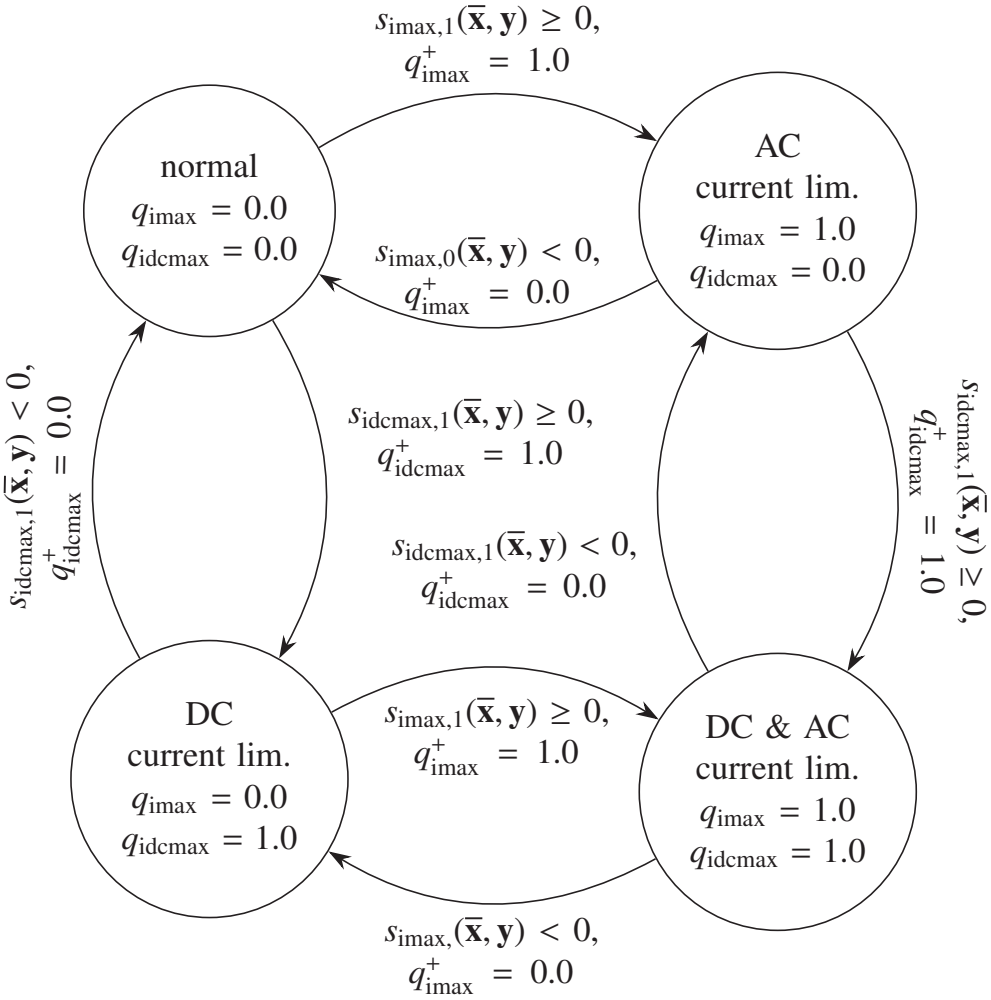

Figure 4.11: Hybrid automaton of a droop-based GFM converter with two discrete states and four locations

In general, it depends very much on whether the d- or q-axis current is prioritised within the AC current limitation, as the DC current is mainly coupled to the d-axis AC current. However, this is beyond the scope of this work.

To analyse and demonstrate the effectiveness of SECM-1 under AC current limitation, a time-domain simulation is carried out to demonstrate the stabilising properties of SECM-1. Within the simulation three positive load steps of r_{load} are performed with an additional power equivalent of 0.2 pu per step and one negative step of -0.6 pu at $t = 5$ s (see Fig. 4.12).

After the third step, the converter goes into current saturation ($q_{\mathrm{imax}} = 1.0$) and SECM-1 is activated. As the time-domain simulation results show, the SECM-1 limits the frequency decline during current limitation, resulting in a lower steady-state frequency deviation. It should be noted that the droop control was developed primarily for parallel operation of converters and not for islanding conditions. However, it does show how SECM-1 affects the frequency of the converter when the current is limited. Besides the frequency, the voltage peak after the third load step is also significantly reduced when SECM-1 is activated. In summary, it is shown that SECM-1 can keep the converter in a quasi-stationary state during current limitation, resulting in less frequency deviation and better synchronisation with the rest of the system after the current limitation. Also, an eigenvalue analysis is carried out to show its impact on small-signal stability. The eigenvalues and graphical illustration are given in Appendix A.3, showing its effectiveness also for steady-state conditions.

From the above theoretical DADS description and the graphical representation as a hybrid automaton, it can be concluded that two discrete states are sufficient to describe a state-of-the-art phasor GFM converter with current limitation. If considering a switching model of the converter, more discrete states are very likely necessary. It is shown that there are several approaches to describe a hybrid system, as there is no general procedure and it depends on the later implementation. However, it can be deduced that the hybrid phenomenon of chattering may be present if the switching conditions are not properly implemented. The time-domain simulation and eigenvalue analysis demonstrate that the SECM-1 can stabilise the converter during current limitation. However, the general impact of GFM converters and SECM on voltage stability requires further investigation, which will be done in chapter 6 after the modelling description of the power electronic loads.

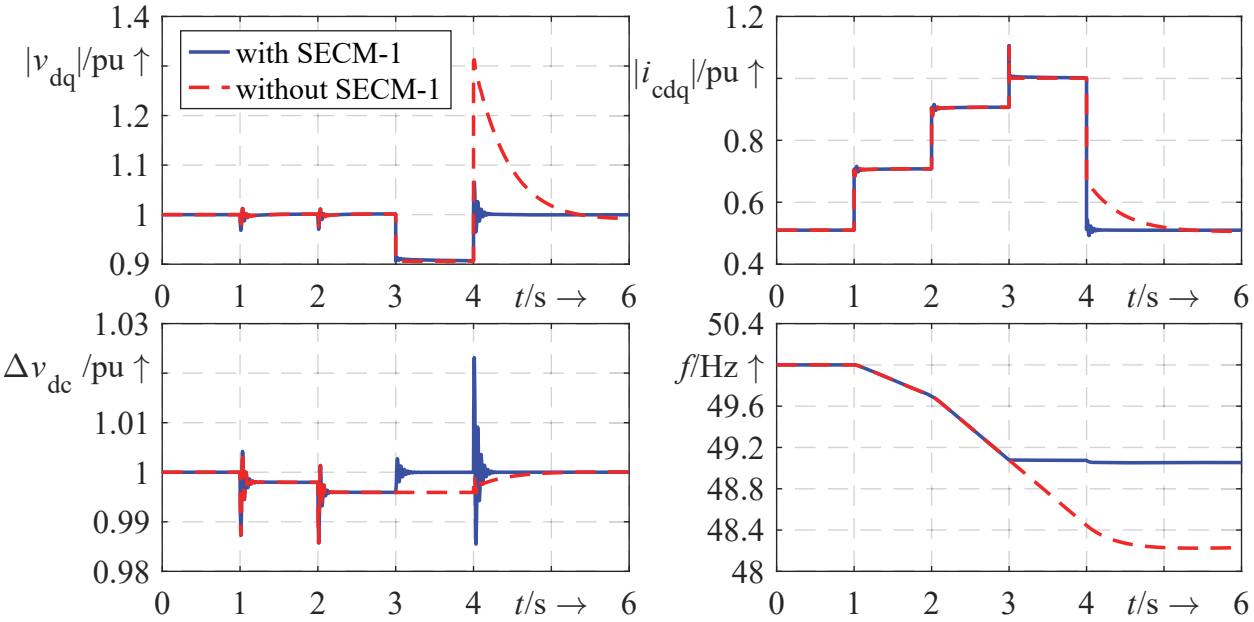

Figure 4.12: Evolution of selected states of droop-based GFM converter as DADS under three load steps of +0.2 pu and -0.6 pu (with and without SECM-1)

4.6 Conclusion of the chapter

In the preceding chapter, the modelling basis of the GFM converters with current limitations has been developed. First, the general structure of the converter model, the AC filter and the DC energy model were outlined. Second, different GFM control approaches for power synchronisation and the outer voltage control loop were presented. Emphasis was placed on the differences between their EMT and phasor implementations. The next step was to describe the inner cascaded control loop used and the current limitation with anti-windup. Subsequently, the parameter-free SECM-1 was proposed, and it was mathematically shown that it can stabilise all the presented GFM control approaches during current limitation. In addition, other SECMs were presented which will be used as benchmarks for the later voltage stability analyses. Finally, a droop-based GFM converter was used as an example to analyse its properties as a hybrid system. It was shown that the definitions of the reset functions and switching conditions to implement the current limitation need to be well-defined to obtain numerical stability and avoid hybrid phenomena such as chattering or infinitely fast switching. By the mathematical formulation of the GFM converter as DADS it can also be seen that the system is non-linear due to its power calculation and the dq-transformation using the angle state $\Delta\theta$ in the sine and cosine functions (see Appendix A.2 for the equations). This means that non-linear methods must be con-

sidered to determine the stability of this system. However, as described in Section 3.3.2, there is no general procedure for proving the stability of non-linear switched DAE systems. Therefore, stability will not be studied analytically, but for specific scenarios, mainly by time-domain simulations in Chapter 6. The focus will be on the various GFM control approaches as well as the different SECMs under current limitation, both for short-term and long-term voltage stability. The statements on stability will therefore relate primarily to the differences between the individual control approaches.

5 Measurement and modelling of power electronics-interfaced loads

The following chapter examines how power electronics-interfaced loads can be modelled for phasor and EMT simulations. To do this, the general structure of power electronic loads is first presented in Section 5.1, where parts of the literature review are based on the work in [T3]. It is also shown how this type of load responds to a voltage drop to demonstrate its non-linear and discrete dynamics. Section 5.2 describes how a generic power electronic load model can be modelled for phasor simulations. Then, in Section 5.3, EMT models of real power electronic loads are developed by measuring their power response to different voltage drops. Afterwards, a DADS model of the phasor load model is derived in Section 5.4 to analyse its properties as a hybrid system. In the end, a conclusion of the chapter is drawn in Section 5.5.

5.1 General structure of power electronic loads and power response in case of voltage drops

An overview of the general structure of power electronic loads with a SMPS is presented next. For this purpose, the power electronic load is described in terms of its main components, as shown in Fig. 5.1. Unless otherwise stated, the component descriptions are mainly based on the references in [92, 143]. This is followed by an outline of a generic equivalent power electronic load model and its power response to a voltage dip to demonstrate its non-linear dynamics.

As can be seen in Fig. 5.1, the interface between the load and the grid is an electromagnetic interference (EMI) filter. The main purpose of this filter is to reduce high-frequency emissions from the power electronic load into the grid. Sources of these emissions can come from the DC/DC converter or the active power factor correction (PFC) stage within the DC load [92, 144]. Here, the DC/DC converter can have switching frequencies between 65 kHz and 300 kHz [92], while a classical PFC has about 125 kHz [144]. Since the filter elements have small values compared to other elements of the power electronic load, the filter has only a small effect on the overall dynamics of the load [143]. This topic is discussed in more detail in Section 5.3 and Appendix B.2.5, where the influence of the EMI filter on the

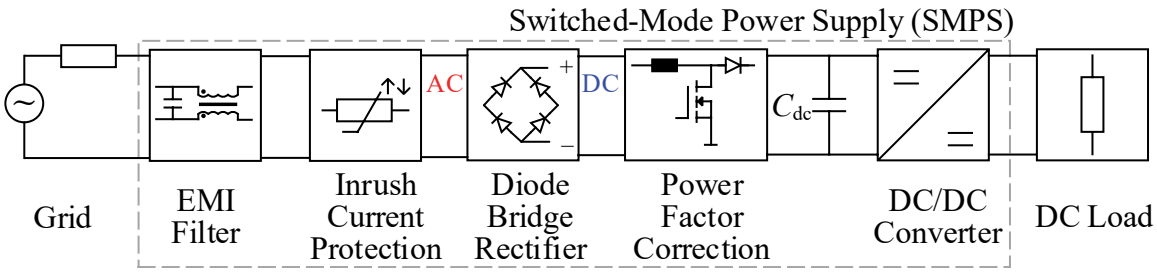

Figure 5.1: General structure of a power electronic load with SMPS (own visualisation, based on [143])

fundamental power response is measured. Inrush current protection is required because the DC-link capacitor C_{dc} has a low impedance when discharged, resulting in a high current at switch-on [143]. This inrush current can damage the load's internal components. There are several methods to counteract this. The simplest and most commonly used method is to use a resistor with a negative temperature coefficient, which has a high impedance when the load is connected from a cold start, but decreases over time during operation [143]. Other methods use active components, such as transistors, to slow down the voltage rise [145].

To convert the AC voltage to DC, most SMPS use an uncontrolled bridge rectifier. This consists of four diodes for single-phase applications and six diodes for three-phase applications. As the rectifier produces an impulsive DC voltage, a capacitor (in this case C_{dc}) is required to provide a smoothed voltage. The value of the capacitor is normally chosen according to the maximum voltage ripple and the required hold-up time. [143]. The selection of suitable capacitor values is discussed in more detail in Appendix B.2.6.

The uncontrolled rectifier causes a highly non-linear current that is drawn from the grid. As a result, the current contains many harmonics that can stress other components in the system. Based on the power rating of the power electronic load, specific harmonic limits must be met based on harmonic legislation. To meet these, there are several PFC techniques to reduce the harmonics of the grid current. The overall aim is to make the grid current more sinusoidal and in line with the grid voltage. In [101] and [146] it was found that almost all SMPS can be divided into three categories: without or no PFC (n-PFC), passive PFC (p-PFC) and active PFC (a-PFC). A more detailed description of these PFC techniques is given in Section 5.3.

As the DC link voltage contains voltage ripple and may not have the correct amplitude for the actual DC load, a DC/DC converter is placed in between. For this purpose, there are mainly two converter types: forward converter and flyback converter. The former is

mainly used for low-power applications, while the latter is used for loads with higher power due to its higher efficiency. In both cases, however, the aim is to have a tightly regulated DC voltage with low fluctuations to protect the DC load. For this, the output voltage is measured and feedback to the controller of the DC/DC converter. In some cases, if the DC link voltage is too low, the converter can also disconnect the DC load. This behaviour is especially relevant for modelling the dynamics of power electronic loads, as shown in Section 5.3.

In general, the output voltage of the SMPS can be used for a wide variety of DC load applications. Most commonly it is used for consumer electronics such as computers and televisions, but also for many ICT devices. In addition, the above general structure can also be used to power LEDs and single-phase electric vehicle chargers [143]. Next, the power response of a generic power electronic load to voltage drops is shown to demonstrate its non-linear and discrete dynamics.

Power response of a generic power electronic load in case of voltage drops

The dynamics of the power electronic load under consideration is shown in Fig. 5.2, which is a generic equivalent circuit for a wide range of power electronic devices [90, 94, 147]. It consists of an uncontrolled ideal diode-bridge rectifier (D1-D4) with a capacitor C_{dc} to smooth the DC voltage. The real DC load is represented by a constant load P_{dc}, which is modelled here as a controlled impedance. In most cases, this assumption is valid, as the subsequent DC/DC converter controls the actual DC load voltage very quickly, and thus constant power is achieved [148]. Overall, the power electronic load circuit in Fig. 5.2 can mainly represent a low-power, single-phase SMPS without power factor correction (n-PFC) [101] or a type II electric vehicle charger [100].

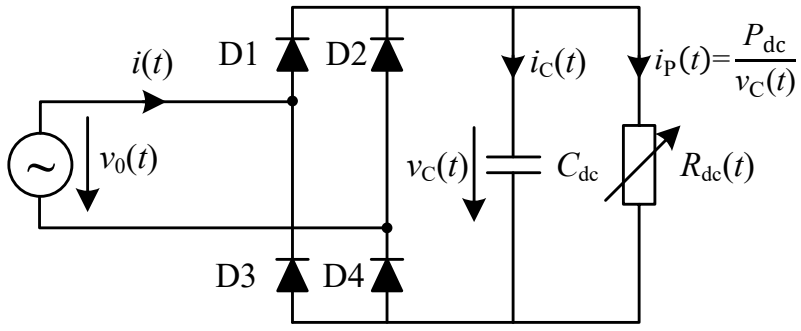

Figure 5.2: Generic equivalent power electronic load without PFC (own visualization, based on [143])

To understand how the power or current of the power electronic load responds, an exemplary 50 % voltage drop of the grid voltage $v_0(t)$ for three AC cycles (3·20 ms) is applied, as shown in Fig. 5.3. Initially, the power electronic load is in a periodic steady state. However, after the voltage drop at $t = 0.04$ s, no current is drawn from the grid, since the capacitor voltage $v_C(t)$ is greater than the grid voltage for a full cycle. When the discharge of the capacity causes the voltage $v_C(t)$ to drop low enough to reach the grid voltage $v_0(t)$, current is drawn again, as can be seen for the half-cycle at $t = 0.06$ s. For the next three half-cycles, it can be seen that the amplitude of the current becomes larger than before. This can be explained by the constant load model because the load current $i_P(t)$ increases as the capacitor voltage $v_C(t)$ decreases (see Fig. 5.2). At $t = 0.1$ s both the grid voltage and the capacitor voltage $v_C(t)$ are restored to their pre-fault values. This charging process is accompanied by a high inrush current due to the discharged capacitor. The power electronic load then returns to a periodic steady state.

Overall, this example demonstrates the highly non-linear dynamics of a power electronic load. If the voltage drop is large enough, the power electronic load will "disconnect" and initially draw no power from the grid. However, it will reconnect if the DC voltage drop is large enough. In this case, the load will draw a higher current from the grid and consume full power again. After the voltage drop, a high current is observed which charges the capacitor in half a cycle. The power electronic load then returns to a periodic steady state. It should be noted that whether no power is drawn or how long it takes depends on the drop of the grid voltage, the capacitor C_{dc} and the constant load P_{dc}. This also applies to the inrush current when the voltage recovers.

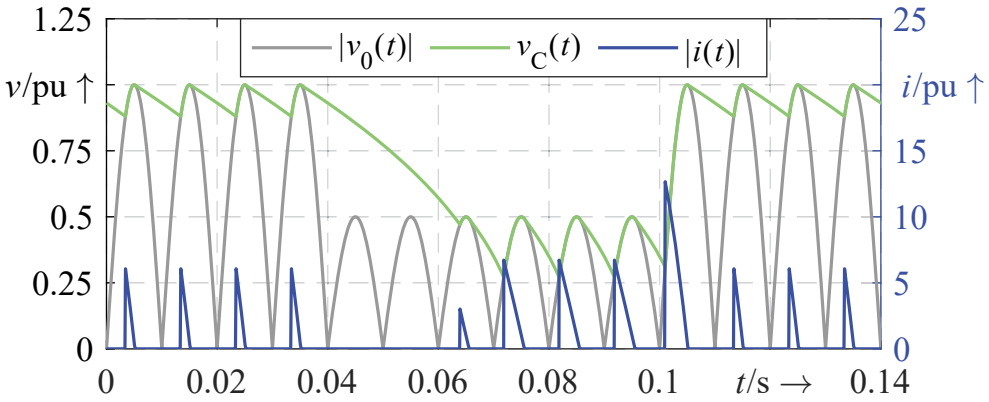

Figure 5.3: Exemplary 50 % grid voltage drop for 60 ms with power electronic load current response

5.2 Development of a power electronic load model for phasor simulations

In the following, the modelling approach of the power electronic load model for transient stability simulations is presented. The subsequent results are mainly based on the work done in [SL5].

As previously shown, the power response of the power electronic load mainly depends on the current $i(t)$ drawn from the grid. To analyse this current, the dynamics of the power electronic load can be divided into two discrete states. In the charging state, the capacitor voltage $v_C(t)$ is equal to the grid voltage $v_0(t)$ and a current flows into the load. In the discharge state, the capacitor voltage $v_C(t)$ is greater than the grid voltage $v_0(t)$ and no current flows into the load. As can be seen in Fig. 5.3, the current $i(t)$ contains many harmonics. However, in a phasor simulation, only the fundamental component is of interest. Therefore, the general idea is to develop a phasor model that calculates only the fundamental component of this current at each time step. To obtain the fundamental component, the transition times from one state to the other must first be determined. Second, based on these times, Fourier components can be calculated to mathematically determine the fundamental current wave that flows during a cycle.

This is done by first determining the transition time t_{off}, which represents the end of the charge state when the current $i(t)$ becomes zero (see Fig. 5.4). Secondly, the transition time when the current starts to flow again, here t_{on}, is calculated. Finally, these time values are used to determine the fundamental wave of the current by calculating its corresponding Fourier components, from which root mean square (RMS) values are derived. In summary, the steps are

- Calculating the switch-off time t_{off} of the current
- Calculating the switch-on time t_{on} of the current
- Calculating the fundamental wave of $i(t)$ with t_{on} and t_{off} and derive RMS values

These steps are described in more detail below. Appendix B.1 outlines how the phasor model can be included in a transient stability program. The subsection ends with a comparison of the power response between the phasor and an EMT model of the load.

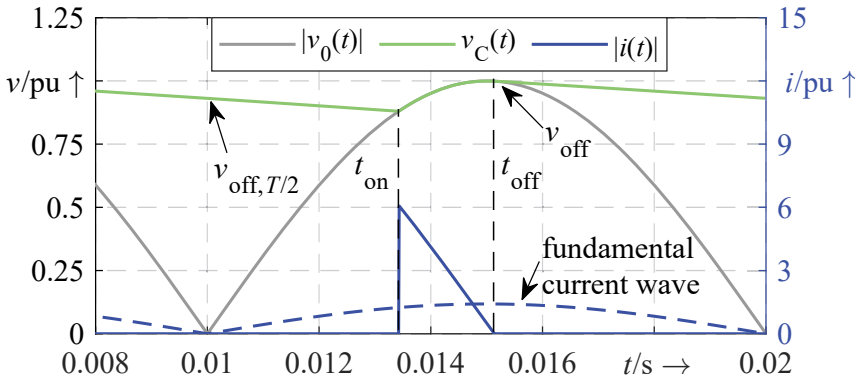

Figure 5.4: Exemplary illustration of the transition times t_{on}, t_{off} and the fundamental wave of the current $i(t)$

Calculating the switch-off time t_{off} of the current

As shown in Fig. 5.2, the current $i(t)$ flowing from the grid to the power electronic load during the charging state consists of the capacitor current $i_C(t)$ and the load current $i_P(t)$

$$i(t) = i_C(t) + i_P(t). \tag{5.1}$$

Assuming that the grid voltage $v_0(t)$ is purely sinusoidal

$$v_0(t) = \hat{V}_0 \cdot \sin(\omega_0 t), \tag{5.2}$$

where $\hat{V}_0$ is the peak value of grid voltage, (5.1) can be rewritten and set to zero to determine the switch-off time t_{off}

$$\begin{aligned} i(t) &= C_{dc}\frac{\mathrm{d}\, v_0(t)}{\mathrm{d}t} + \frac{P_{dc}}{v_0(t)} \\ &= C_{dc} \cdot \omega_0 \cdot \hat{V}_0 \cdot \cos(\omega_0 t) + \frac{P_{dc}}{\hat{V}_0 \cdot \sin(\omega_0 t)} = 0. \end{aligned} \tag{5.3}$$

Using the trigonometric identity $\sin(x) \cdot \cos(x) = \frac{1}{2}\sin(2x)$, (5.3), the time t can be resolved to

$$t = \frac{\arcsin\left(\frac{-2 \cdot P_{dc}}{\omega_0 \cdot C_{dc} \cdot \hat{V}_0^2}\right)}{2 \cdot \omega_0}. \tag{5.4}$$

One problem is that (5.4) only gives negative times because the parameters in the argument of the inverse sine function are always positive. The way to solve this is to look at the time intervals when the current goes to zero. The time interval starts at the peak voltage of $t = \frac{\pi}{2 \cdot \omega_0}$ $(\sin(\omega_0 t) = 1)$ until the voltage goes to zero at $t = \frac{\pi}{\omega_0}$ $(\sin(\omega_0 t) = 0)$. As the range

of the inverse sine function is normally defined between $[\frac{-\pi}{2}, \frac{\pi}{2}]$ (i.e. a sine function from -1 to 1), it can be seen that the inverse sine function has to be multiplied by -1 so that its range starts from 1 (i.e. the peak voltage) to -1. This gives positive values for the switch-off time. However, this is only one part of getting the correct switch-off times. Consider the following example, if P_{dc} would be zero, (5.4) would also be zero. However, the point at which the current becomes zero would be at the peak voltage at $t = \frac{\pi}{2 \cdot \omega_0}$ and not at $t = 0$. Therefore an offset of $\frac{\pi}{2 \cdot \omega_0}$ has to be added for the switch-off time. The real switch-off time t_{off} can then be calculated as follows

$$t_{\mathrm{off}}(\hat{V}_0) = \frac{\pi}{2 \cdot \omega_0} + \frac{\arcsin\left(\frac{2 \cdot P_{\mathrm{dc}}}{\omega_0 \cdot C_{\mathrm{dc}} \cdot \hat{V}_0^2}\right)}{2 \cdot \omega_0}. \tag{5.5}$$

As can be seen from (5.5), the switch-off time only depends on the variable peak voltage $\hat{V}_0$, since all other parameters are assumed to be constant, including the frequency.

Calculating the switch-on time t_{on} of the current

To calculate the switch-on time t_{on}, the circuit in Fig. 5.2 is reduced to the capacitor and the constant load, as the diodes D1-D4 disconnect the load from the grid. The criterion for the grid current $i(t)$ to start flowing is that the capacitor voltage $v_{\mathrm{C}}(t)$ is equal to the grid voltage $v_0(t)$. Here the discharge state can be described by the differential equation

$$C_{\mathrm{dc}} \frac{\mathrm{d}\, v_{\mathrm{C}}(t)}{\mathrm{d}t} = \frac{P_{\mathrm{dc}}}{v_{\mathrm{C}}(t)}. \tag{5.6}$$

The time-domain solution of (5.6) is [94]

$$v_{\mathrm{C}}(t) = \sqrt{{v_{\mathrm{off}}}^2 - \frac{2 \cdot P_{\mathrm{dc}} \cdot t}{C_{\mathrm{dc}}}}. \tag{5.7}$$

Here, (5.7) already contains the initial condition v_{off}

$$v_{\mathrm{off}} = v_{\mathrm{C}}(t = 0) = v_0(t = t_{\mathrm{off}}) = \hat{V}_0 \cdot \sin(\omega_0 t_{\mathrm{off}}). \tag{5.8}$$

This means that at the start of the discharge state, the value of the capacitor voltage $v_{\mathrm{C}}(t)$ is equal to the grid voltage at the switch-off time. So the switch-off time t_{off} is needed to determine the switch-on time t_{on}, which has to be considered for later implementation. Since the criterion for the switch-on time t_{on} is that the capacitor voltage must drop to the

grid voltage, the next step is to equate (5.7) and (5.2) and square both sides

$$(v_{\text{off}})^2 - \frac{2 \cdot P_{\text{dc}} \cdot t}{C_{\text{dc}}} = \hat{V}_0^2 \cdot \sin^2(\omega_0 t). \tag{5.9}$$

However, (5.9) shows that the time t cannot be analytically rearranged to one side of the equation, due to the sine squared function. Therefore, the sine squared function is approximated by a cubic function, but only for the first quarter of the cycle

$$\sin^2(t) \approx x_1 + x_2 \cdot t + x_3 \cdot t^2 + x_4 \cdot t^3, \;\; t \in \left[0, \frac{\pi}{2}\right]. \tag{5.10}$$

Here x_1 to x_4 are free parameters that can be used to approximate the sine function as needed. Note that the angular frequency ω_0 can be neglected for the approximation, but will be used later to adjust the frequency. Next, a cost function is set up to determine the parameters x_1 to x_4 in a subsequent minimisation

$$\int_0^{\frac{\pi}{2}} \left[\sin^2(t) - \left(x_1 + x_2 \cdot t + x_3 \cdot t^2 + x_4 \cdot t^3\right)\right]^2 \, \mathrm{d}t. \tag{5.11}$$

The cost function in (5.11) is constructed as follows. First, the original function and the approximation are subtracted from each other. Second, the subtraction is squared to obtain only positive values. Finally, the integral is formed over the first quarter cycle, because it is only in this range that the voltage of the capacitor can meet the grid voltage, so only this part is of interest (see Fig. 5.4). This means that if the capacitor voltage $v_{\text{C}}(t)$ is greater than the grid peak value $\hat{V}_0$ at the time of the peak ($t = \frac{\pi}{2\omega_0}$), the two voltages will not coincide in this half-cycle and therefore no current or power will be drawn from the grid. Eq. (5.11) can be solved symbolically using the *Symbolic Math Toolbox* in MATLAB. The resulting expression is then minimised in MATLAB using the function *fmincon*[2]. A graphical comparison between the original function and its approximation is shown in Fig. B2 in Appendix B.1.1. Overall, the maximum deviation is 0.45 %, which is a sufficiently good approximation.

Before using the approximation, the initial condition v_{off} of the left side of (5.9) has to be modified to $v_{\text{off},T/2}$ to match the domain $[0, \frac{\pi}{2}]$ of (5.10) (cf. Fig. 5.4)

$$v_{\text{off},T/2} = \sqrt{v_{\text{off}}^2 - \frac{2 \cdot P_{\text{dc}} \cdot (T/2 - t_{\text{off}})}{C_{\text{dc}}}}. \tag{5.12}$$

[2]Result: $x_1 = 0.004517042542168$, $x_2 = -0.084973441092720$, $x_3 = 1.367157627046003$, $x_4 = -0.580239811988436$

With (5.12) the decrease of the capacitor voltage from t_{off} to the beginning of the new half-cycle is calculated (which would be at $t = 0.01\,\text{s}$ in Fig. 5.4), with $\frac{T}{2} = 0.01\,\text{s}$. The next step is to insert the approximation of (5.10) in (5.9) by considering (5.12) and rearranging it to a polynomial with t_{on} as unknown and set to zero

$$\begin{aligned} f(t = t_{\text{on}}) = & t_{\text{on}}^3 \left(\hat{V}_0^2 {\omega_0}^3 x_4 \right) + t_{\text{on}}^2 \left(\hat{V}_0^2 {\omega_0}^2 x_3 \right) \\ & + t_{\text{on}} \left(\hat{V}_0^2 \, \omega_0 x_2 + \frac{2P_{\text{dc}}}{C_{\text{D}}} \right) + \hat{V}_0^2 x_1 - \left(v_{\text{off},T/2} \right)^2 \\ = & t_{\text{on}}^3 \cdot A + t_{\text{on}}^2 \cdot B + t_{\text{on}} \cdot C + D = 0. \end{aligned} \tag{5.13}$$

For a clearer presentation of (5.13), the parameters A, B, C and D are introduced, which consist only of constants and the variables t_{off} and $\hat{V}_0$. In the last step, t_{on} is calculated from (5.13) using Cardano's formulas to solve the cubic equation. This has two advantages for the later implementation. First, Cardano's formulas provide an analytic solution for the above function and are computationally efficient. Second, the solution for t_{on} becomes negative if there is no coincidence of the capacitor voltage and the grid voltage, and is therefore easy to check. Cardano's formulas for solving cubic equations can be found in [149] and in Appendix B.1.1.

Calculating the fundamental current wave with t_{on} and t_{off}

To determine the fundamental current $i_1(t)$ of the grid current $i(t)$, the Fourier components of its Fourier series must be calculated. In general, the current $i(t)$ can be described by its Fourier series by

$$i(t) = \frac{a_0}{2} + \sum_{n=1}^{\infty} \left[a_n \cdot \cos(n\omega_0 t) + b_n \cdot \sin(n\omega_0 t) \right]. \tag{5.14}$$

In this case, $\frac{a_0}{2}$ corresponds to the DC component, which is zero here, while a_n and b_n are the n^{th} Fourier components of the current. These components can be calculated as

$$a_n = \frac{2}{T} \int_{-T/2}^{-T/2} i(t) \cdot \cos(n\omega_0 t) \, \mathrm{d}t, \tag{5.15}$$

$$b_n = \frac{2}{T} \int_{-T/2}^{-T/2} i(t) \cdot \sin(n\omega_0 t) \, \mathrm{d}t, \tag{5.16}$$

where $i(t)$ from (5.3) is used here. For $n = 1$ the fundamental components are calculated, where a_1 is the fundamental reactive and b_1 is the fundamental active part of the grid

current. Using t_{on} and t_{off}, b_1 is calculated by (similarly for a_1 with $\cos(\omega_0 t)$)

$$\begin{aligned} b_1 &= \frac{4}{T}\int_{t_{\mathrm{on}}}^{t_{\mathrm{off}}} i(t)\cdot\sin(\omega_0 t)\,\mathrm{d}t \\ &= \frac{4}{T}\int_{t_{\mathrm{on}}}^{t_{\mathrm{off}}} \left(C_{\mathrm{dc}}\cdot\omega_0\cdot\hat{V}_0\cdot\cos(\omega_0 t)+\frac{P_{\mathrm{dc}}}{\hat{V}_0\cdot\sin(\omega_0 t)}\right)\sin(\omega_0 t)\,\mathrm{d}t \\ &= \frac{4}{T}\left[-C_{\mathrm{dc}}\cdot\hat{V}_0\cdot\frac{\cos(2\omega_0 t)}{4}+\frac{P_{\mathrm{dc}}t}{\hat{V}_0}\right]_{t_{\mathrm{on}}}^{t_{\mathrm{off}}} \\ &= \frac{4}{T}\left[C_{\mathrm{dc}}\cdot\hat{V}_0\cdot\frac{\cos(2\omega_0 t_{\mathrm{on}})-\cos(2\omega_0 t_{\mathrm{off}})}{4}+\frac{P_{\mathrm{dc}}(t_{\mathrm{off}}-t_{\mathrm{on}})}{\hat{V}_0}\right]. \end{aligned} \tag{5.17}$$

Since the Fourier components are usually calculated over one cycle, (5.17) is doubled, since t_{on} and t_{off} only cover half a cycle. However, this calculation also indicates that the general determination of the Fourier components is strongly dependent on the current $i(t)$ in (5.3). If its description would be different, e.g. including inductance derivatives, an analytical calculation may no longer be possible. Using the same procedure, a_1 can be calculated (result only)

$$\begin{aligned} a_1 = \frac{4}{T}\Bigg[&\frac{\hat{V}_0}{4}C_{\mathrm{dc}}\left(2\omega_0(t_{\mathrm{off}}-t_{\mathrm{on}})+\sin(2\omega_0 t_{\mathrm{off}})-\mathrm{sind}(2\omega_0 t_{\mathrm{on}})\right) \\ &+\frac{P_{\mathrm{dc}}}{\hat{V}_0\omega_0}\left(\ln\left(\sin(2\omega_0 t_{\mathrm{off}})\right)-\ln\left(\sin(2\omega_0 t_{\mathrm{on}})\right)\right)\Bigg]. \end{aligned} \tag{5.18}$$

As a result, the fundamental Fourier components in (5.17) and (5.18) depend only on $\hat{V}_0$, t_{on}, t_{off} and other constant parameters. Thus, they can be determined at each time step of a phasor simulation. Finally, the fundamental current $i_1(t)$ is given by

$$i_1(t) = a_1\cdot\cos(\omega_0 t)+b_1\cdot\sin(\omega_0 t)=\hat{I}_1\cdot\sin(\omega_0 t+\varphi), \tag{5.19}$$

where $\hat{I}_1 = \sqrt{a_1^2+b_1^2}$ is the amplitude of the current and $\varphi = \arctan(\frac{a_1}{b_1})$ is the phase angle. The Fourier components can thus be used for the inclusion in a phasor or transient stability program. A detailed explanation of how to include this model in such a program, e.g. to deal with different simulation step sizes, is given in Appendix B.1.

Next, a simulation-based comparison is made of the power response between the developed phasor load model and the EMT circuit in Fig. 5.2. For this example, P_{DC} is 1 kW, $\hat{V}_0 = 230\sqrt{2}\,\mathrm{V}$ and $C_{\mathrm{dc}} = 700\,\mu\mathrm{F}$, giving a capacitive power factor of $\cos(\varphi) = -0.951$. The detailed circuit of Fig. 5.2 is simulated in MATLAB Simulink with a fixed simulation

step size of 1 μs, while the phasor load model is simulated in PowerDynamics.jl (adaptive step sizes, but with a maximum step size of 1 ms, see Section 6.1 for more information). To determine the fundamental values of the grid voltage and current and to calculate the corresponding fundamental active power p and reactive power q, a Fourier transformation with a running average window (RAW) of one cycle length is used in Simulink. The simulation results are given in Fig. 5.5. In a periodic steady state, both loads consume the same active and reactive power. When the voltage drops at $t = 0.04$ s, the power consumption of the phasor load model goes directly to zero. This is due to the implementation of the load, as it is immediately determined that the capacitor voltage v_C will not coincide with the grid voltage within this cycle. In contrast, the power output of the RAW of the EMT model takes about half a cycle to go to zero, as it also uses past values to calculate the power. This difference can also be seen in the voltage recovery, where the higher power consumption of the RAW lasts for one cycle, but the high current only lasts for half a cycle. The power response of such a phasor model therefore reflects the instantaneous power rather than the average power over one period. However, as this does not necessarily reflect the character-

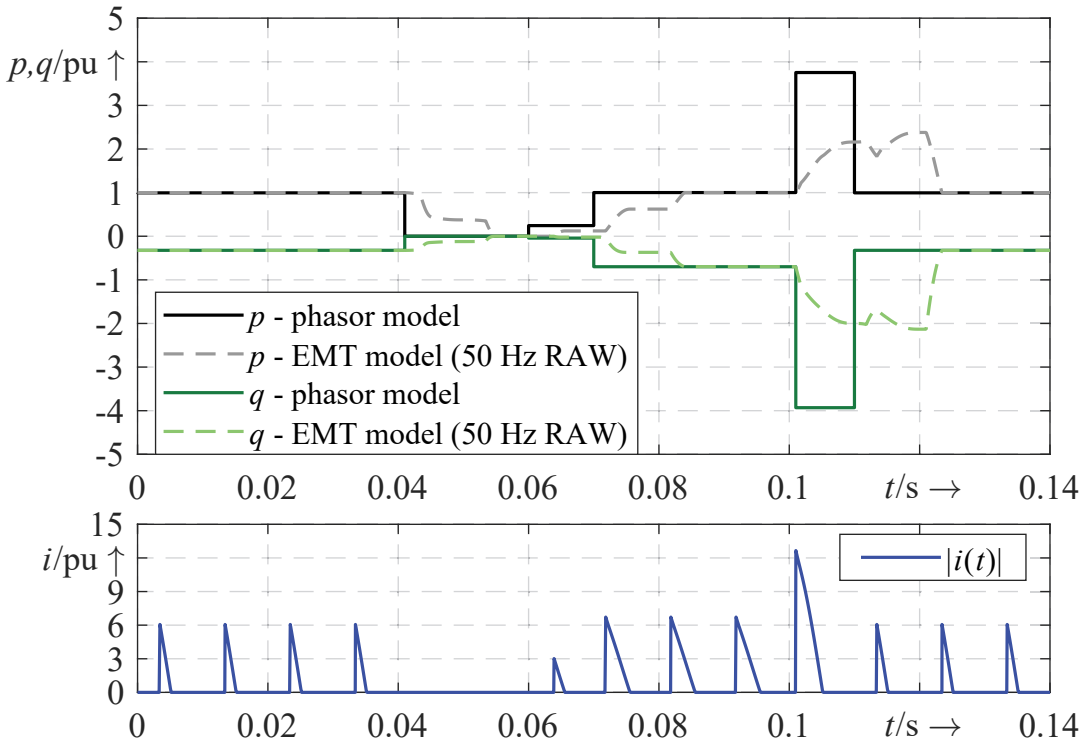

Figure 5.5: Comparison of the power response between the phasor power electronic load model and its EMT equivalent

istics of a phasor model, the active and reactive power is filtered by a first-order lag element to achieve a smoother and more averaged power. The time constant is set to the period of a half-wave (10 ms) to account for the fast response. The comparison is shown in Fig. 5.6. The result shows that the trajectories are now much closer, which better reproduces the response of the EMT model. Therefore, this filtered active and reactive power is used in later simulations.

Overall, the comparison shows that the phasor load model is capable of calculating the correct steady-state power values and represents the main power dynamics during transients. It should be noted, however, that the phasor load gives its most accurate results when the periods of the voltage dynamics are greater than one cycle and when the load current does not affect the input voltage (i.e. a very low grid impedance). In addition, if there is a not negligible grid inductance, the description of the current $i(t)$ from (5.1) would be non-linear. Then, most of the analytical calculations made would no longer be possible. In contrast, this demonstrates that power electronic loads with more complex circuits are very difficult to model for phasor simulations. Therefore, only this power electronic load model is considered for phasor simulations in this thesis. Yet, the extent to which this load model is also suitable for voltage stability analyses in more complex grid models has to be investigated, which is done in Chapter 6. In addition, due to its discrete characteristics, this power electronic load model is taken as a basis for modelling it as a hybrid system and analysing its characteristics in Section 5.4.

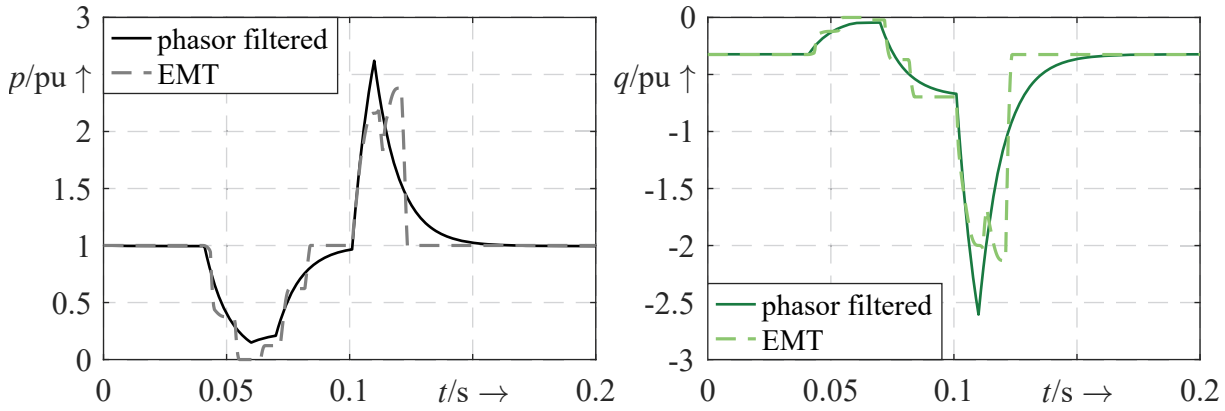

Figure 5.6: Comparison between the filtered power of the phasor power load model and the fundamental power of the EMT model by Fourier transformation and RAW

5.3 Measurement of real power electronic loads and derivation of EMT models

The results in this section are mainly based on the work done in [SL4]. Here, the power response of power electronic loads to voltage drops is measured in the laboratory and their dynamics are analysed. From this, dynamic EMT simulation models are derived which can be used for voltage stability studies. As there is a wide variety of power electronic loads, this subsection concentrates on four SMPS loads with different PFC techniques. In addition, the influence of the grid impedance and the EMI filter on the power response is measured and analysed in Appendix B. Based on the measurements, the simulation models are derived and described. The aim is to determine their main structure, but not their parameters. This is because a large number of loads would have to be measured in order to make general statements about their parameters. However, with the help of the literature, it is explained how the individual components could be designed if detailed information is not available (see Appendix B.2.6). It should also be noted that voltage stability is mostly related to the balance between fundamental reactive and active power. Therefore, this subsection is mainly about the fundamental component of power.

5.3.1 Laboratory setup

Fig. 5.7 represents the laboratory setup for measuring the power of single and three-phase power electronic loads at high resolution. A single-line diagram of the setup is shown in Fig. 5.7, which illustrates the main components. To generate the voltage drops, three power amplifiers (Rohrer PFL-2250-26-U/I-DC370) are used which act like a programmable voltage source where the desired voltage evolution can be specified (see (A) in Fig.5.7). Note that the power amplifiers are limited to a maximum current of 30 A (peak). They have internal current protection that reduces the output voltage if the current exceeds the maximum. In order to add a small impedance between the source and the load, a transformer with a voltage ratio of one is used, which can be either single-phase (B) or three-phase (C). Their electrical parameters can be found in the Table B2 in the Appendix B.2.1. Current and voltage sensors are installed in front of the power electronic load to calculate the active and reactive power of the fundamental components (D). The signal recorder has a resolution of 10^5 samples per second, which is sufficient for the experiments carried out. The device under test is then connected, which are the power electronic loads (E). At (F)

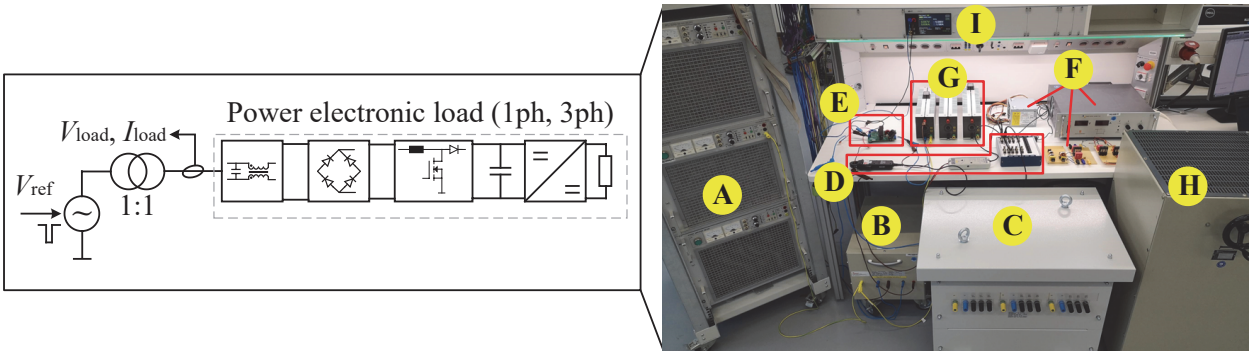

A: Three-phase power amplifier
B: Single-phase transformer
C: Three-phase transformer
D: Measurement devices
E: Device under test
F: SMPS & Filter
G: Single-phase load resistance
H: Three-phase load resistances
I: 12V DC auxillary power supply

Figure 5.7: Single line diagram and laboratory setup for measuring the power response of 1ph and 3ph power electronic loads for different voltage drops and periods

some of the power electronic loads and EMI filters can be seen. As the loads are intended to operate at rated power, several resistors can be connected in series or in parallel to achieve the desired value (G). For three-phase loads, there is also a variable resistor with a higher-rated current (H). A 12 V DC auxiliary power supply is also provided for the on-board controllers of a-PFC loads (I). In this work the following power electronic loads are analysed, labelled 'PEL' and a number for ease of reference:

- **PEL-1**: Coming Data Lithium Battery Charger C2920
- **PEL-2**: Fujitsu PC Power Supply NPS-230EB B
- **PEL-3**: PFC Evaluation Board UCC28180EVM-573
- **PEL-4**: DC Power Supply SM300-10D

These loads have been selected to provide a wide variety of SMPS loads with different PFC techniques and phases. This makes it possible to determine the different dynamics of each PFC circuit on the power response during voltage transients. In addition, these PFC circuits represent the most common ones used in mass-market devices [146]. Detailed information on each load can be found in Table B1 in Appendix B.2.1.

5.3.2 Measured power response

Next, the measurement results of the power electronic loads are presented. Only the fundamental component (50 Hz) of the active and reactive power is shown, which is deter-

mined by calculating the corresponding fundamental current and voltage components using a short-term Fourier transformation. The window length of the Fourier transformation is one period of the fundamental frequency. With a sampling frequency of 100 kHz, this corresponds to 2000 samples per period. For each new measurement point, a new Fourier transformation is calculated so that the windows of each transformation overlap.

Fig. 5.8 illustrates the power response of the PEL-1 load for different fault durations, where all voltage drops start at $t = 0.04\,\mathrm{s}$. Furthermore, the voltage drop starts at a level of $\Delta v = 0.2\,\mathrm{pu}$ and increases in steps of $\Delta v = 0.2\,\mathrm{pu}$ in the next measurement until zero voltage at $\Delta v = 1.0\,\mathrm{pu}$. Note that both active and reactive power are rated to the corresponding rated active power P_{dc} of each power electronic load from Table B1. This makes it easier to compare the power response of different loads. As can be seen in Fig. 5.8, the overall power response is very similar to the phasor load model in Section 5.2. The power consumption initially goes to zero but recovers during the fault. The recovery time is longer if the voltage drop is higher, as the capacitor voltage has to fall to the value of the grid voltage. Also, high power consumption can be observed during voltage recovery, followed by steady-state conditions. Comparing the power response between the different fault durations, it can be seen that the fault duration does not lead to a significant change in the curve. This is because the load recovers during the fault, leading to an intermediate quasi-steady state. For this reason, only a fault duration of 100 ms is considered in the following. However, as shown in Fig. 5.8 for $t_{\mathrm{fault}} = 160\,\mathrm{ms}$ and $\Delta u = 0.8\,\mathrm{pu}$, the load disconnects during the fault and does not recover its power consumption. Also, the load disconnects after recovery and reconnects after 1.4 s, which is not shown here. This is also the case for $\Delta u = 1.0\,\mathrm{pu}$. The reason for this behaviour is not known, but this observation shows that if the voltage drops are deep and long enough, loads can switch off during and after the fault. This effect is also partly measured for PEL-2 to PEL-4, but already for a fault duration of 100 ms, which are described next.

Fig. 5.9 presents the measurement results of the active and reactive power behaviour for PEL-2 to PEL-4 for a fault duration of 100 ms. The legend entries apply here per load. The measurements marked with an asterisk (*) mean that the power amplifiers had to reduce their voltage because the requested load current exceeded their maximum current. However, this only happens after the fault and during the high inrush current. Examples of measured distorted amplifier voltages can be seen in Fig. B4 in Appendix B.2.2. In addition, the degree of voltage distortion varies according to the load. Therefore, the measurement results of the high power consumption after voltage recovery may not reflect the actual load dynamics. However, the measurement results during the fault are not affected. In the

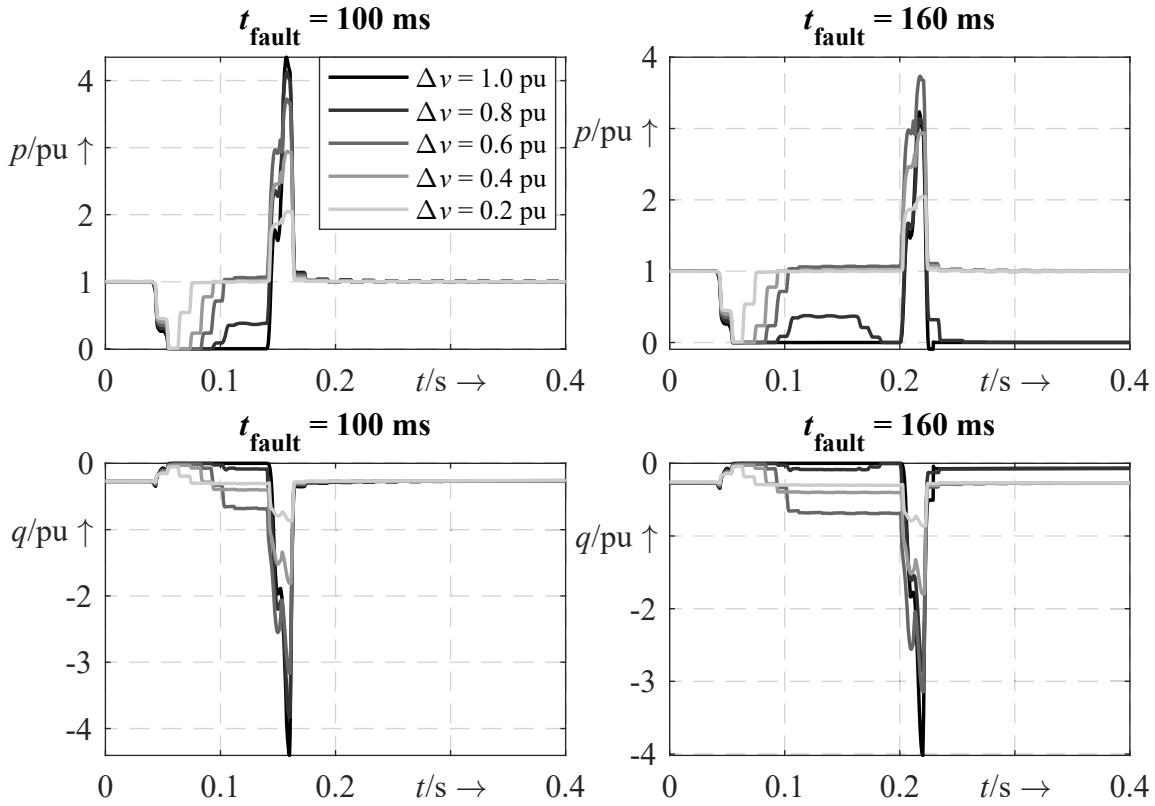

Figure 5.8: Measured active and reactive power response of PEL-1 for fault durations of 100 ms and 160 ms

case of ideal voltage recovery, higher power consumption can be expected. For PEL-2, the measurement results show that it switches off at a voltage drop of 0.4 pu. As a result of this disconnection, the power curve does not change significantly for higher voltage drops. In addition, there is a short period after the voltage recovers during which the power consumption decreases again. This is because, that after the peak voltage, a current still flows due to the filtering inductance. As a result, the rectified voltage is higher than the grid peak voltage and has to drop before a load current can flow again. Compared to PEL-1, the reactive power of PEL-2 is inductive, which can also be explained by the inductance for passive PFC. Although the peak current of the PEL-2 is only 3 A in normal operation, the load tries to draw a slightly higher current than 30 A when the voltage recovers (see Fig. B4). This is why the amplifier voltage is briefly reduced at this peak.

In contrast to that, PEL-3 does not reach the current limit, even though its rated power is higher. This is because its active PFC reduces the inrush current. Furthermore, as can be seen in Fig. 5.9, the internal control leads to a fast power recovery during the fault. For $\Delta v = 0.8$ pu it is assumed that the internal boost converter has reached its control limit, resulting in a reduced DC voltage and no full active power recovery. Compared to

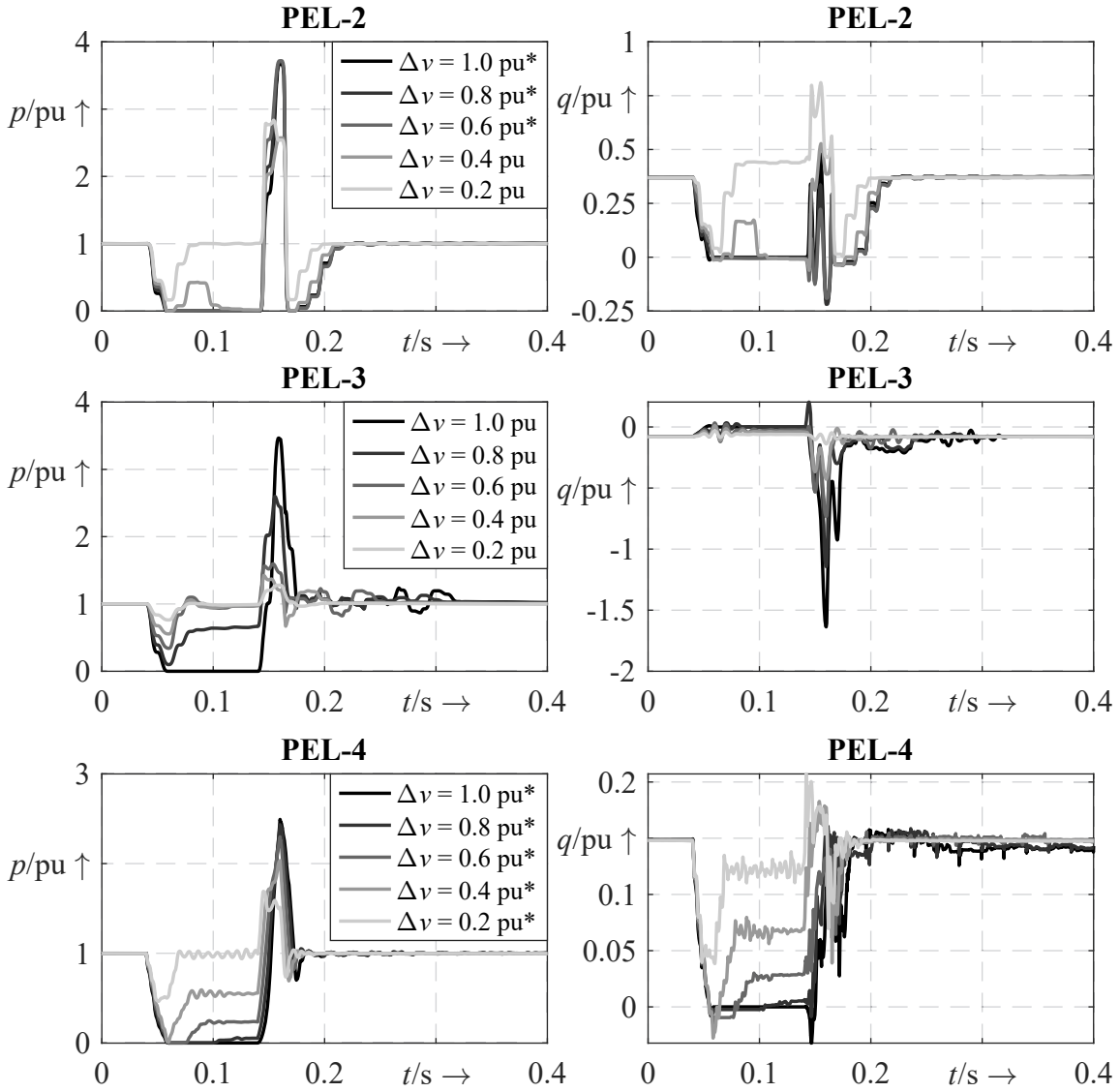

Figure 5.9: Measured active and reactive power response for PEL-2 to PEL-4 with a fault duration of 100 ms

all other power electronic loads, its reactive power consumption is very low before and during the voltage dip but rises sharply as the voltage recovers. Slight power oscillations can also be observed afterwards. In the case of PEL-4, all three power amplifiers reach their current limit during voltage recovery for all voltage drops (see Fig.B4 for one phase). The reason for this is that the power consumption of this load is generally high (3 kW) and the amplifiers already operate at full their power rating. Therefore, the PEL-4 post-fault power response must be treated with caution and probably does not reflect the real power consumption of the load. It should be noted that the active and reactive power of the PEL-4 in Fig. 5.9 is the sum over all three phases. However, during the fault, the amplifiers do not reach their limit, but the active power is reduced during normal operation,

as shown in Fig. 5.9. During this time, the active power of the PEL-4 has a quadratic voltage dependency like a purely resistive load. It is assumed that the internal DC/DC voltage regulator of the PEL-4 has reached its limit and cannot draw any more current.

The measurements demonstrate that all power electronic loads undergo a transient power response when there is a significant voltage drop and subsequent recovery. In general, the power response can be divided into three phases. The first phase is the power reduction as the load is effectively disconnected from the grid due to the blocking rectifier. The level of power restoration depends on the limits of the internal DC-DC converter, which determines the intermediate steady state. The last phase is during the voltage recovery, resulting in a short but high inrush current and correspondingly high power consumption, which can be four times as high. For PEL-2 (and partly for PEL-4) a subsequent power reduction is also observed, due to the inductance for passive PFC. As the active power dynamics are quite similar for all power electronic loads, the reactive power dynamics vary more. Here the implemented PFC determines whether the reactive power consumption is capacitive (PEL-1 and PEL-3) or inductive (PEL-2 and PEL-4). Based on these insights, the main components and other modelling aspects are derived to develop power electronic load models that can be used in power system stability studies.

5.3.3 Derivation of EMT models for power electronic loads

Next, it is described how the power electronic loads are modelled to emulate their main measured voltage dynamics. It should be noted that the structures of the loads are largely inspired by several references, such as [92, 94, 101, 147], which are ultimately based on their general PFC circuit design. For these models, their circuit element values are given in Table B3. However, these values should not be considered as general as they are only valid for these specific loads. For general values, a large number of loads should be measured to derive such values. An overview of how these elements are designed for different PFC techniques in general is given in Appendix B.2.6.

Fig. 5.10 illustrates the EMT load models for PEL-1 to PEL-4. In general, the circuit design is inspired by the general PFC design and a trial and error process to match the measurement. This matching process has been accompanied by finding suitable values for the circuit elements. The structure of the PEL-1 without PFC (n-PFC) is the same as for the phasor load model. For the loads with passive PFC (PEL-2 and PEL-4), an inductor is placed after the rectifier to smooth the load current. The main difference between the

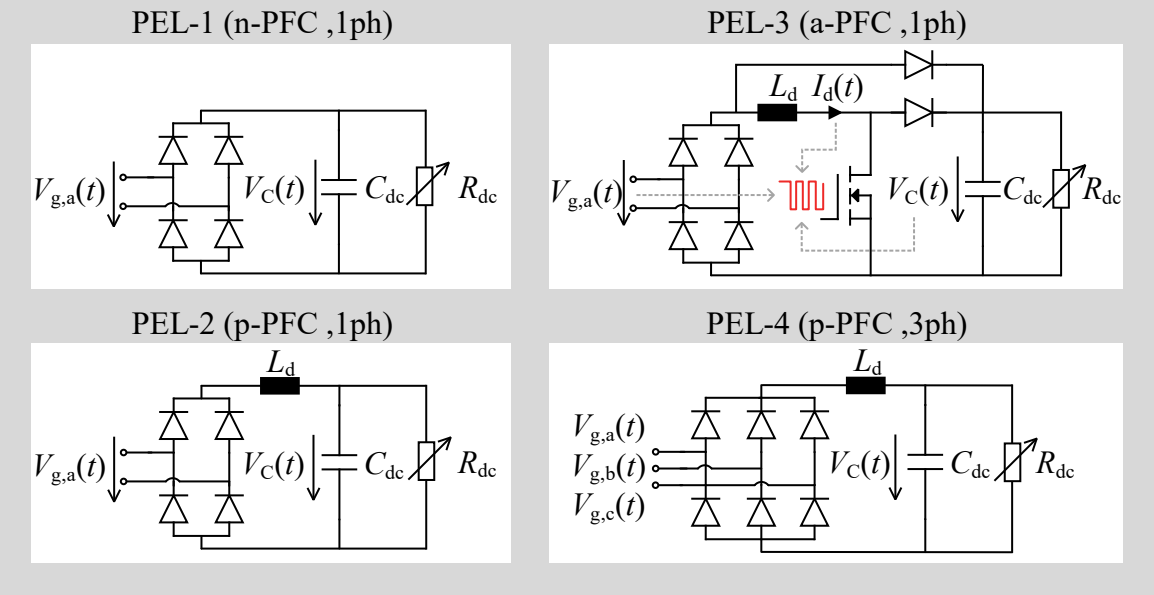

Figure 5.10: Overview of the derived EMT load models for PEL-1 to PEL-4 with different PFC techniques

single-phase and the three-phase p-PFC load is that the latter has six diodes instead of four. Unlike these loads, the PEL-3 has an additional boost converter stage after the rectifier to shape the load current $I_d(t)$ sinusoidally and to increase the DC voltage $V_C(t)$. The block diagram of the boost converter stage controller is shown in Fig. B3 in Appendix B.2.1. Its two main functions are to align the load current with the grid voltage and to transform the DC voltage to a specified reference voltage. In addition, the PEL-3 contains a so-called pre-charge diode which charges the C_{dc} capacitor when it is connected to the grid. Common to all loads is that the EMI filter is neglected, as it has almost no influence on the fundamental active and reactive power behaviour (see the analysis in Appendix B.2.5). Also, like the phasor load model, all EMT models have a variable resistor acting as a constant power load instead of the DC-DC converter. This assumption has also been made in other studies [92, 94, 147], as the DC-DC converter keeps the DC voltage at the load constant even under large disturbances. A major difference to the load models in the above references is that a simple approach is introduced to reproduce the disconnection of loads at low voltages. For this, the load resistance $R_{dc}(t)$ has two cases

$$R_{dc}(t) = \begin{cases} \frac{V_C^2(t)}{P_{dc}} & V_C(t) \geq V_{trip}, \\ \infty & \text{else}, \end{cases} \tag{5.20}$$

where V_{trip} is the tripping or switch-off voltage parameter. As before, the DC load resistance $R_{dc}(t)$ depends on the capacitor voltage $V_C(t)$, but if the voltage $V_C(t)$ falls below V_{trip},

the resistance becomes infinite and thus no power is drawn from the grid, resulting in a quasi-disconnection. This can emulate the observed disconnection of some loads at low voltages. In addition, there is a lower limit for the load resistance, which is 10 % of the base impedance, calculated from the DC power P_{dc} and its rated AC voltage. This avoids numerical problems near zero voltage and takes into account the limited capability of the internal DC/DC converter.

Next, a brief overview of the circuit element values used for the load models is given. Note that the values are chosen to match the fundamental power response and not the deformed power or total harmonic distortion (THD). The impedance values x_{Cdc} and x_{Ld} from C_{Cdc} and L_{d} are mostly chosen manually by trial and error. For PEL-3, the values are taken from its datasheet in [150]. The specific values can be found in Table B3 in Appendix B.2.1. Their DC power P_{dc} and rated AC voltage V_{base} are taken to convert them into per unit values. Based on these per unit values, they can be transformed for use at higher voltage levels or power ratings, which will be important for the later simulative analyses in Chapter 6. The parameter v_{trip} for disconnecting the load is based on the peak value of V_{base} which is $230\sqrt{2}$ V. They have been set to emulate the disconnection of loads from the measurements of Fig. 5.8 and 5.9. The asterisk symbol * in Table B3 means that instead of the trip voltage v_{trip} a certain minimum value for R_{dc} has been set. This is because PEL-4 shows a clear quadratic voltage dependence below a certain voltage, which could result from a constant resistance. Therefore the minimum value is set to 65 % of the base impedance, for which good results are obtained. Since the PEL-3 includes a boost converter stage for its PFC, a simple but sufficient PI controller is implemented for the transistor (here a Metal Oxide Semiconductor Field-Effect Transistor (MOSFET)). The control parameters are chosen manually to match the power response (given in Appendix B.2.1 in Fig. B3). It should be noted that it is more likely that the control parameters are normally chosen according to the desired power factor, harmonic distortion or response time in the case of load steps [151]. For the sake of completeness, it should be mentioned that there are other more sophisticated techniques for finding the exact load parameters, such as those presented in [4, 151, 152]. However, the main objective here is to match the measurement to be compared next.

Power response comparison between measurement and simulation results

Fig. 5.11 shows the comparison of the power response between measurement and simulation for all power electronic loads. A simple transformer model is used for the simulations, with only the winding resistance and leakage inductance of the laboratory transformer in-

cluded to account for their influence (see. Table B2). The simulations are performed in MATLAB Simulink. As can be seen, the simulation results for PEL-1 agree very well with the measurements. There are only small differences such as the maximum power consumption during voltage recovery or the active power consumption for $\Delta v = 0.8\,\text{pu}$ during the fault. For PEL-2, there are differences during voltage recovery, which are small for active power but larger for reactive power. A possible explanation for this could be the current limitation of the power amplifiers during the voltage recovery of the measurements (see Fig. B4). However, this can only be assumed, although it could explain why the largest differences occur at the time of current limiting. This conclusion is supported by the simulation results of PEL-3 since there is no current limitation and the match between active and reactive power is high. There is a slight discrepancy in the time of power restoration during the fault. Also, there are no small oscillations after the fault in the simulations. These discrepancies could be explained by the fact that the controller of the active PFC from Fig. B3 is not the same as the one used in [150]. For PEL-4, it can be seen that there is a greater mismatch during and shortly after voltage recovery. Since the distortion of the amplifier voltages is much greater compared to PEL-2, it is plausible that this is also reflected here (see Fig. B4). However, before voltage recovery, the match between simulation and measurement results is very high. It can therefore be concluded that the simulation results better describe how PEL-4 would react in the case of a less distorted voltage source.

The comparison reveals that the simulation models capture the main dynamics of the measured loads. However, due to the limitations of the laboratory equipment, there are larger discrepancies for PEL-2 and PEL-4. Another source of error could be the transformer model and also the accuracy of the transformer data from Tab. B2. In addition, laboratory cables and plugs contain additional impedances that have not been taken into account here. As the component and parameter values are selected manually, there may also be potential for better matching. Even if more appropriate parameters had been found, these values would not represent general values as they belong to specific loads. In summary, this means that some mismatch can be tolerated, as the aim of the simulation models is to represent the main power dynamics depending on the PFC, which has been achieved here.

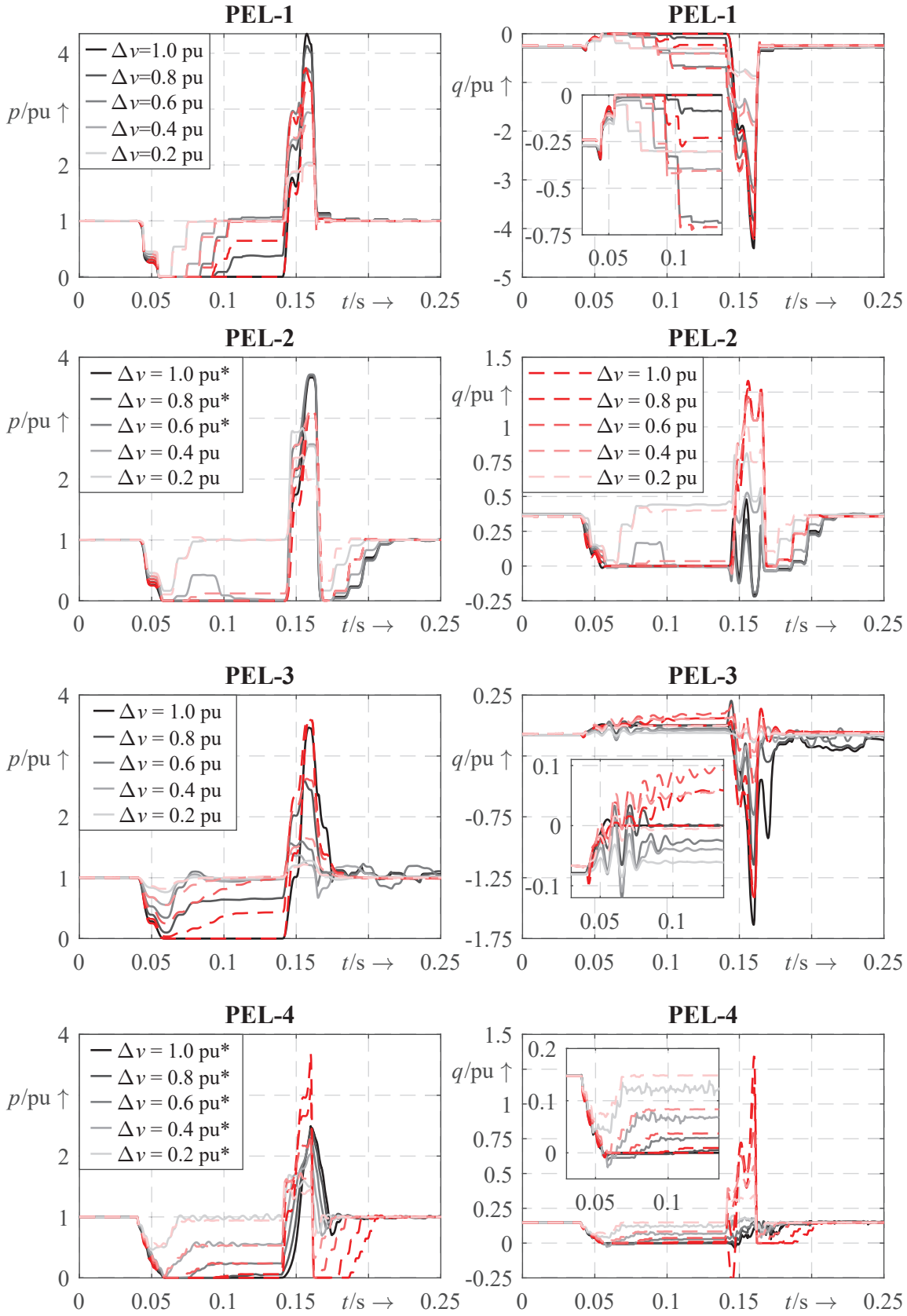

Figure 5.11: Comparison of active and reactive power response between measurement (grey solid lines) and simulation (red dashed lines) for all PE loads

5.4 Power electronic load as hybrid system

Similar to the droop-based GFM converter, in this subsection the phasor power electronic load from Section 5.2 is modelled as a hybrid system in order to analyse its properties. To do this, the DADS modelling approach and its hybrid automaton representation shown in Fig. 5.12 are used. The main parts of the DADS description are also given there. The load model consists of the following states and parameters

$$\dot{\mathbf{x}} = \frac{\mathrm{d}}{\mathrm{d}t}\begin{bmatrix} p_{\mathrm{flt}} \\ q_{\mathrm{flt}} \end{bmatrix}, \quad \mathbf{y} = \begin{bmatrix} \hat{v}_0 \\ p_1 \\ q_1 \end{bmatrix}, \quad \mathbf{p} = \begin{bmatrix} C_{\mathrm{dc}} \\ P_{\mathrm{dc}} \end{bmatrix}, \quad \dot{\mathbf{q}} = \frac{\mathrm{d}}{\mathrm{d}t}\begin{bmatrix} q_{\mathrm{on}} \\ t_{\mathrm{on}} \\ t_{\mathrm{off}} \\ v_{\mathrm{off,T/2}} \\ v_{\mathrm{off}} \end{bmatrix} = \mathbf{0}. \tag{5.21}$$

As can be seen, two differential states, two algebraic and five discrete states are used to model the load dynamics. The third algebraic state $\hat{v}_0$ results from the grid voltage which serves as the input for the load (see Fig. 5.2). The two discrete states represent the filtered active and reactive power and the output of the load

$$\dot{p}_{\mathrm{flt}} = \frac{p_1 - p_{\mathrm{flt}}}{T_{\mathrm{flt}}}, \qquad \dot{q}_{\mathrm{flt}} = \frac{q_1 - q_{\mathrm{flt}}}{T_{\mathrm{flt}}}, \tag{5.22}$$

where T_{flt} is the filter time constant, which is 10 ms. The fundamental active power p_1 and reactive power q_1 of the power electronic load are calculated by the algebraic equations

$$0 = p_1 - q_{\mathrm{on}} \cdot b_1 \frac{\hat{v}_0}{\sqrt{2}}, \qquad 0 = q_1 - q_{\mathrm{on}} \cdot a_1 \frac{\hat{v}_0}{\sqrt{2}}, \tag{5.23}$$

where a_1 and b_1 are fundamental active and reactive currents from (5.18)-(5.17) and q_{on} is a discrete boolean state to switch on or off the power electronic load. Depending on whether the switch-on time t_{on} is positive or negative, q_{on} is set to one or zero. The other discrete states are used to update the internal load states, which is almost done at every time step.

The four locations A, B, C and D of the hybrid automaton in Fig. 5.12 reflect the sequential steps during a time-domain simulation. To determine the current point in time of the voltage half-wave, the internal variable $t_{\mathrm{sum}} = \mathrm{mod}(t, T/2)$ is used, where $\mathrm{mod}(\cdot)$ is the modulo operation. The start of a simulation is always at the beginning of the half-wave at location A. Then, depending on the previous half-wave, $v_{\mathrm{off,T/2}}$ and t_{on} are updated. At the start of a simulation, t_{on} is assumed to be positive. Depending on the new value of t_{on}^{+}, the

states t_{off}, v_{off} and q_{on} are also updated before entering location B. In general, the switch-on time t_{on} greatly determines which discrete states are updated, as it also determines if the load consumes any power and if q_{on} is set to one or zero. At location B, depending on the sign of t_{on}, the Fourier components and the switch-on/off times at each time step are updated. If t_{sum} is greater than the switch-on time, the next location C is entered. The difference between location B and C is that in the latter, t_{on} is not updated because it is in the past within this half-wave. Similarly, when location D is reached, none of the switching times are updated. After location D, if the time has progressed, location A is entered again. Note here that it is assumed that a time-stepping method is used that hits every $t = k \cdot \frac{T}{2},\ k \in \mathbb{N}$ during the simulation. Also, the time step Δt should be small enough so that the locations are entered sequentially. However, this is not a necessary condition, as there could be additional transitions between the locations, which are not considered here. The hybrid automaton thus represents the simulation of the power electronic load during a time-domain simulation.

To complete the description of the power electronic load as a DADS, the reset functions f_{toff}, f_{ton}, f_{qon} and f_{voff} shown in Fig. 5.12 are explained in more detail. For the reset function f_{toff} (5.5) is used with $\hat{v}_0$ as input. Similarly, for f_{voff} the equations from (5.12) is used, where the time t and $v_{\text{last,off}}$ serve as an input

$$f_{\text{voff}}(t, v_{\text{last,off}}) = v^{+}_{\text{off,T/2}} = \sqrt{(v_{\text{last,off}})^2 - \frac{2 \cdot P_{\text{dc}} \cdot t}{C_{\text{dc}}}}. \tag{5.24}$$

Depending on whether t_{on} is positive or negative, either v^{-}_{off} or $v^{-}_{\text{off,T/2}}$ are used for $v_{\text{last,off}}$ to calculate the new value of $v^{+}_{\text{off,T/2}}$. As known from Section 5.2, t_{on} has to be found by Cardano's formulas. Therefore, the reset function f_{on} should not be considered as a mathematical function, but as a set of (programming) instructions that are evaluated during the numerical integration. These steps include the function from (5.13) so that it can be solved using Cardano's formulas. The code for the implementation of the function f_{on} is given in the Appendix B.1. As already mentioned, the discrete state q_{on} is a boolean variable and its reset function is given by

$$f_{\text{qon}}(t_{\text{on}}) = \begin{cases} 1.0 & t_{\text{on}} \geq 0, \\ 0.0 & t_{\text{on}} < 0. \end{cases} \tag{5.25}$$

Overall, the DADS modelling of the phasor power electronic load shows that its discrete dynamics are mainly determined by its internal states to determine the fundamental power.

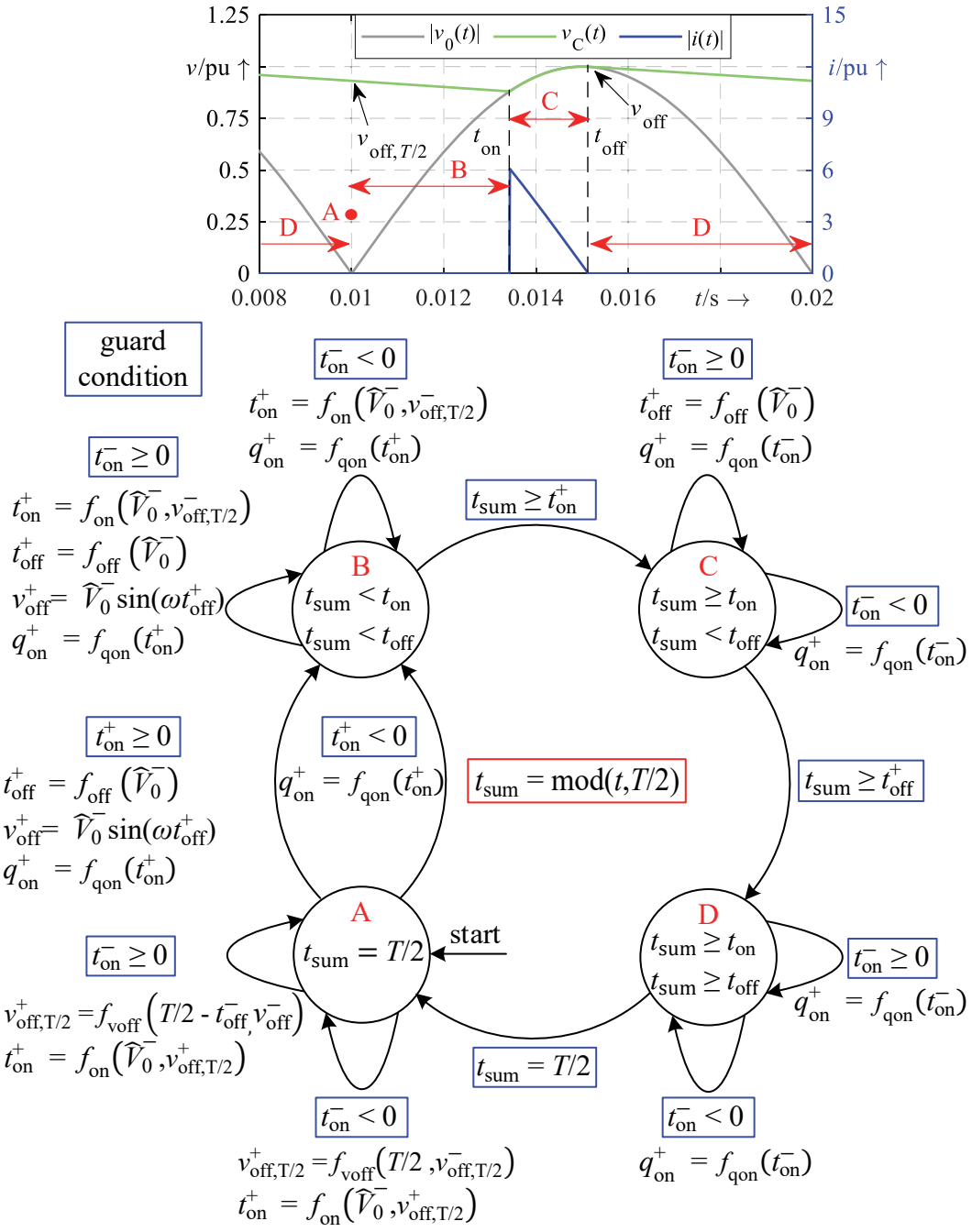

Figure 5.12: Hybrid automaton of phasor power electronic load model (n-PFC) with five discrete states and four locations

Based on this, the filtered power serves as an output for the grid. Similar to the DADS in Section 5.4, the switching conditions of the load model are mostly formulated by an inequality, meaning that the description is not a strict DADS. In addition, its hybrid automaton is strongly focused on the sequence of the time-domain simulation, where most of the reset functions of the discrete states are called at each time step. This means that the dis-

crete states are updated much more frequently compared to the GFM DADS. In contrast, the load DADS could be interpreted as a linear system, but since the dynamics are only trivial differential equations, linear stability analysis methods such as eigenvalues cannot be properly used here. Therefore, time-domain simulations are still required to investigate its impact on voltage stability. For the subsequent simulations, this phasor power electronic load model will be labelled as PEL-1a, as its general circuit structure is equal to PEL-1, but differs in the size of its circuit elements. They are given in Table B4 in Appendix B.2.1. The parameters are based on the standard parameters for a load without any PFC states from Section B.2.6.

5.5 Conclusion of the chapter

This chapter aimed to derive phasor and EMT models for power electronic loads and to analyse their dynamics. To do this, the general power response of such a load during a voltage drop and subsequent recovery is first shown. In general, the power response is divided into three phases. Firstly, the load disconnects from the grid as no current flows into the uncontrolled bridge rectifier. Secondly, the load recovers its power consumption during the fault if the DC voltage has fallen low enough. When the voltage recovers, there is a high current and power consumption due to the charging of the smoothing capacitor. Based on these insights, a phasor model based on a common n-PFC load is derived through detailed analytical calculations. Afterwards, real power electronic loads were measured in the laboratory, which verified the general power response but also highlighted its dependence on the PFC technique used. Although only outlined in Appendix B.2.4 and B.2.5, the influence of a high grid impedance and the EMI filter on the power response has been measured. It could be demonstrated that the fundamental power response is highly dependent on the grid impedance whereas the influence of the EMI filter is negligible. Detailed EMT models are then derived, which are used as a reference against the phasor model in later simulations. In general, the EMT models reflect the measured power response, but the accuracy varies between models, partly due to the limitations of the laboratory equipment. Finally, a DADS of the phasor load model is developed, showing that its discrete dynamics depend on its internal states to determine the fundamental power and also its dependence on the simulation sequence. Overall, the derived models provide a suitable basis for analysing their impact on voltage stability, but it must be pointed out that these loads only reflect a small part of this load category.

6 Analyses of voltage stability of power electronics-dominated grids

In the preceding chapters, the modelling basis for analysing GFM converters and power electronic loads has been derived. The discussion of the stability conditions of hybrid systems in Section 3.3.2 has shown that a formal stability analysis is hardly possible. Therefore, the voltage stability analyses are performed by time-domain simulations for the hybrid and non-linear models of the GFM converters and power electronic loads. This is carried out separately for short- and long-term voltage stability. As known from the stability classification from Chapter 2, large-signal disturbances like short circuits can lead to short- and long-term instability. As short-term voltage instability would occur first due to the time sequence of such a disturbance, its analysis is also started first in this chapter. In order to analyse the individual impact of GFM converters and power electronic loads on voltage stability, they are first simulated separately and then together. In addition, the differences between the phasor and EMT models for the power electronic components are examined. The investigations are completed by the calculation of trajectory sensitivities to determine the influence of different model parameters on the voltage evolution and thus the stability.

The rest of the chapter is organised as follows. In Section 6.1, the utilised grid model for investigating short- and long-term voltage stability is described, which is an aggregated version of the IEEE Nordic test system. Then, in Section 6.2, the scenario setup for investigating short- and long-term voltage stability is outlined. This is followed by a description of the simulation environment, with a focus on how hybrid systems can be implemented. Then in Section 6.3 the impact of power electronics on short-term voltage stability is analysed. First, the individual impact of GFM converters with current limitation is considered, followed by power electronic loads. Their combined effect on short-term voltage stability is then evaluated. The same procedure is used in Section 6.4 to analyse long-term voltage stability. A summary and conclusion of the voltage stability analysis is given at the end of this chapter.

6.1 Aggregated Nordic power system and simulation environment

The IEEE Nordic test system in [153] is a widely-used grid for investigating short-term [28, 66, 69] and long-term [46, 47, 60] voltage stability in the phasor domain. In order to derive a voltage stability test system that can also be easily used for long-term EMT simulations with small step sizes and large parameter sampling studies, the aggregated Nordic system (ANS) is proposed for this thesis. This reduces the computational complexity and preserves the essential voltage dynamics. Furthermore, by aggregating generation and load, conventional generators and loads can be easily replaced by GFM converters and power electronic loads. This makes it much easier to emulate a higher dominance of power electronic devices within a power system and to analyse their impact and voltage stability. Although the creation of ANS is mainly motivated by its EMT implementation, the reduction in computational complexity is also beneficial for phasor simulations. The grid parameters are given in Appendix C. Next, the aggregation procedure is outlined.

In general, a voltage-critical grid consists of a main load area (with a relatively low generation) and a main generation area which are connected by a long transmission corridor, resulting in highly-loaded transmission lines. This is also the case for the original Nordic test system, which consists of two main generation areas (External and North) and two load areas (Central and South) connected by several transmission lines. A key objective is to preserve this structure for the ANS, which is illustrated in Fig. 6.1. The first step in the modelling of the ANS is the aggregation of the main generation area (green area). As the voltages in this area remain close to nominal values, they are represented in the ANS by a constant voltage source with $\underline{v}_0$. However, to represent its limited short-circuit contribution in the event of a fault, a grid impedance $\underline{z}_\mathrm{g}$ is introduced. The voltage $\underline{v}_0$ and the grid impedance $\underline{z}_\mathrm{g}$ are chosen to match the sub-transient short-circuit power S''_k on bus 4031 in the Nordic test system. The magnitude of $\underline{v}_0$ is chosen in such a way that the pre-fault steady-state magnitude of $\underline{v}_1$ is close to that of bus 4031 in the original system. In the second step, the long transmission lines between the North and Central areas are connected in parallel and aggregated into one line, except for the line between bus 4032 and 4044. This line is modelled without any changes to emulate the original fault and its subsequent disconnection. As a result, the ANS is weakened exactly as in the original system. In addition, the fault impedance is $\underline{Z}_\mathrm{f} = R_\mathrm{f} + \mathrm{j}X_\mathrm{f} = 20 + \mathrm{j}20\,\Omega$ as in the original system, which is the base case in most simulations. To match the voltage drop in the load area during the short circuit, the fault location is at a distance of 10 % from bus 2 in the ANS.

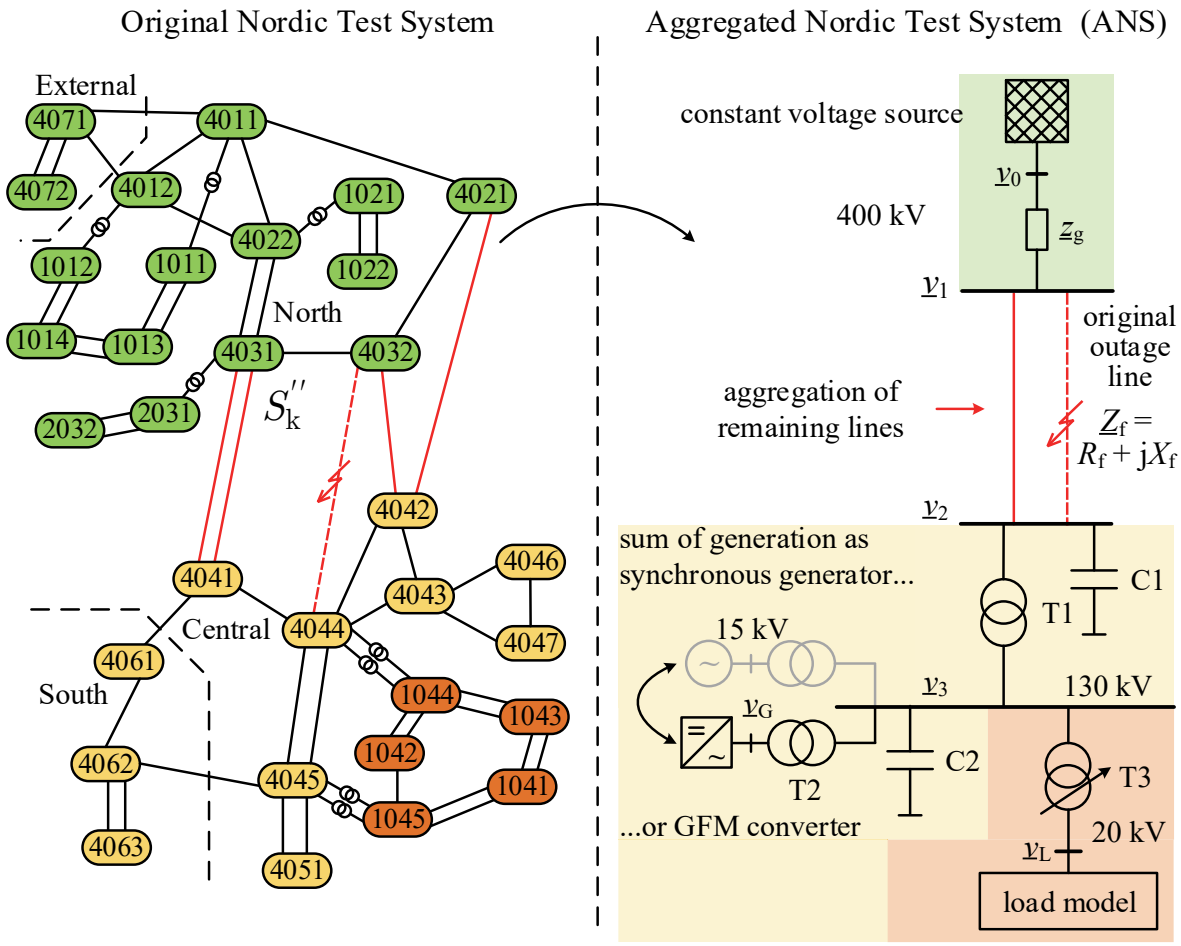

Figure 6.1: Aggregation procedure of the Nordic test system to the ANS

In the final step, the generation units and loads in the Central and South areas are aggregated and connected via the transformers T2 and T3 to the 130 kV level. For the aggregated generator the machine parameters of the generator G6 are taken from [153]. The generator is equipped with an automatic voltage regulator and an OEL. The EMT model of the generator includes also a power system stabiliser. Transformer T3 is equipped with an OLTC on the secondary side. In general, the transformer parameters are based on the typical parameters of the corresponding transformer of the original Nordic Test System. However, they are slightly adjusted to take into account the voltage drops across the transmission lines and transformers within the original Central area. The shunt capacitors are also aggregated, but separately for the 400 kV and 130 kV buses, in order to achieve better results without significantly increasing the complexity. A detailed illustration of the load model is given in Fig. 6.2. In general, it is split into the aggregated power of the Nordic test system, which is p_{aggr} for active and q_{aggr} for reactive power, and the power of the power electronic load (PEL) with p_{L} and q_{L}. To emulate the original voltage dependence

of the aggregated load in the EMT model (linear for active power and quadratic for reactive power), the active power part is modelled as a constant current source synchronised by a PLL in $\alpha\beta$-coordinates that follows the voltage angle of $\underline{v}_{\mathrm{L}}$. The PLL control parameters are taken from [154]. There is also an additional shunt reactance $\underline{x}_{\mathrm{shunt}}$ which is used later in the simulations to compensate for the reactive power of the power electronic load, which can be either capacitive or inductive. It should also be noted that when the shunt reactance is used, the reactive power q_{L} is the sum of the reactive power of the power electronic load and the shunt. As the EMT models PEL-1 to PEL-3 (and also PEL-1a) are single-phase loads, three loads are connected in a Delta connection.

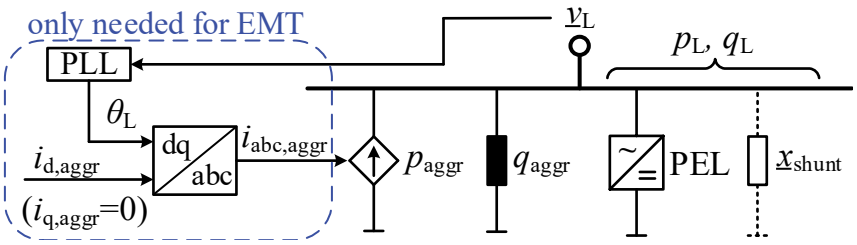

Figure 6.2: Load model of the aggregated Nordic System (ANS)

A comparison of the voltage dynamics of the original system and the ANS is shown in Fig. 6.3. Note that the focus is on the load region (yellow and orange trajectories) as this is where the power electronics are located in the following simulations. During the short circuit, a good match is derived in terms of the voltage drop. However, the subsequent voltage oscillations in the ANS are not as distinct as in the original system. In the case of the long-term voltage dynamics within the ANS, they are mainly determined by single, but larger events, such as the activation of the OEL and the tap changes of the OLTC. In the original system, a more continuous voltage drop can be observed. This is due to the larger number of dynamic devices with smaller event impacts. Yet, similar voltage collapse times are obtained for both test systems. This means that the voltage dynamics in the ANS are much more determined by the aggregated assets. Therefore, by replacing the aggregated generation and load with power electronic devices, their impact on the voltage dynamics should be amplified. This can be valuable when analysing power grids with a high proportion of power electronics, which is the main interest here. Finally, this aggregation procedure reduces the number of differential and algebraic states from about 400 of the original system (phasor model) to 23 of the ANS, which is a reduction of around 94%.

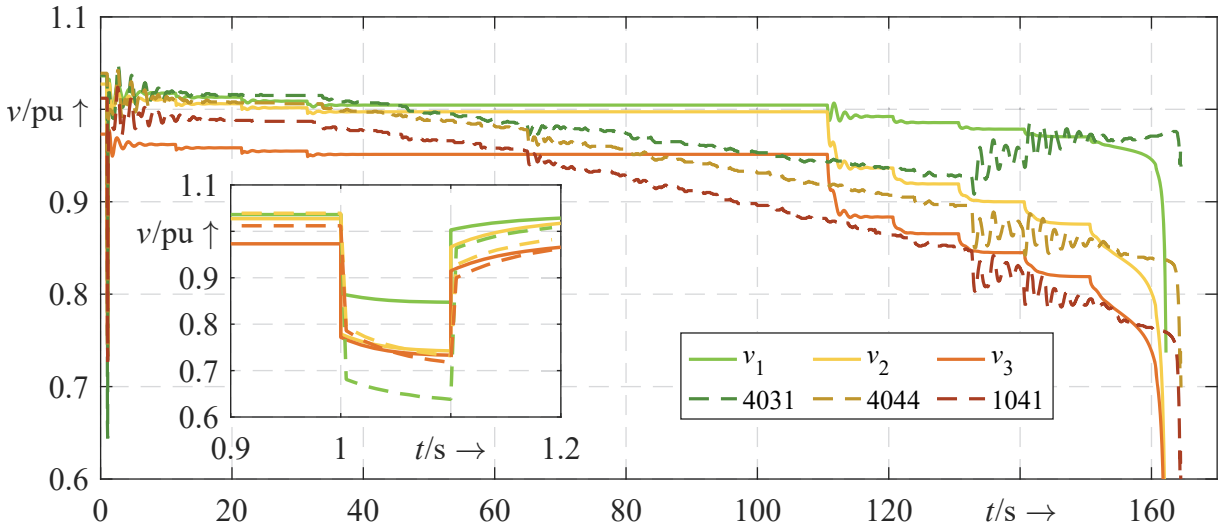

Figure 6.3: Comparison of voltage dynamics between the Nordic test system and ANS in a phasor simulation (for synchronous generators and no power electronic loads)

6.2 Scenario setup and simulation environment

In the following, the scenario setup and simulation environment are outlined. First, a description is given of which adjustments are made to the ANS in which scenario, to analyse the GFM converters and power electronic loads. In all scenarios, the former presented ANS serves as the basis for the simulations. This is followed by a presentation of the simulation environment in which the ANS is implemented. Furthermore, it is outlined how the events can be implemented for the modelling of hybrid systems.

6.2.1 Scenario Setup

In case the GFM converter is examined, the synchronous generator is completely replaced by it, but the transformer T2 is kept. When considering different GFM control approaches (i.e. droop, matching, dVOC and VSM), only the power synchronisation and the outer voltage control loop are exchanged. Unless otherwise stated, the circular current limitation

is assumed for the simulations. At the start of each simulation, the converter is operating at the same operating point as the aggregated synchronous generator with an active power injection of $P_{\mathrm{G}} = 4440\,\mathrm{MW}$ and controlling the voltage magnitude of $\underline{v}_{\mathrm{G}}$ to 1.0 pu. Unless otherwise stated, the rated apparent power of the converter is also equal to the synchronous generator with $S_{\mathrm{G}} = 5300\,\mathrm{MVA}$.

When power electronic loads are analysed, parts of the aggregated load are exchanged. Here, only the active power part p_{aggr} of the original load model is converted to the power electronic load. The reason for this is that the steady-state reactive power consumption of the power electronic loads can only be determined by iterative simulations, as it depends on the grid operating point. For example, if a power electronic load is modelled with a share of 30 % of the total load, the aggregated active power load is reduced by this amount (i.e. $P_{\mathrm{aggr}} = 7580\,\mathrm{MW} \cdot 0.7 = 5306\,\mathrm{MW}$). In addition, the DC power P_{dc} of the power electronic load is set to $7580\,\mathrm{MW} \cdot 0.3 = 2274\,\mathrm{MW}$, which is also used as its rated power to size its circuit elements. The aggregated reactive load q_{aggr} remains unchanged. Due to space reasons, the abbreviation PEL is used in simulation figures which means power electronic loads. For the following simulation figures, the variables p_{L} and q_{L} represent the active and reactive power consumption of the power electronic load and, if used, the shunt reactance. The power trajectories within the simulation figures are rated by the base active power, which is 7580 MW. In general, all of the above applies to both the EMT and phasor models. For the GFM converters, all four control approaches are investigated within the EMT and phasor simulation. As the EMT models are more detailed, most of the simulations for stability analysis are performed with them and are considered as benchmarks. The comparison with the phasor models will show whether they can represent the main dynamics and whether they are still suitable for voltage stability studies, especially in the case of a high proportion of power electronics.

The first half of the analysis starts with short-term voltage stability, as a large disturbance usually occurs before the slower dynamics become dominant. This also better reflects the natural course of a disturbance. In general, the main focus of the short-term voltage stability simulations is to investigate, what the dynamics of GFM converters and power electronic loads are in the event of a short-circuit and what their qualitative impact on stability is. An overview of the scenarios for investigating short-term voltage stability is given in Table 6.1. It lists the adaptations that are made to the ANS in each section and the focus of the analysis.

Table 6.1: Scenarios and ANS adaptations for analysing short-term voltage stability

Section	Focus of analysis	ANS Adaptations
6.3.1-i	comparison of voltage trajectories between EMT and phasor GFM model	GFM: droop, SECM-1
6.3.1-ii	comparison of short-term voltage stability between EMT and phasor model	GFM: droop, matching, dVOC, VSM, constant current load share
6.3.1-iii	impact of GFM control approach and SECM on short-term stability (EMT)	GFM: droop, matching, dVOC, VSM, SECM-1 to SECM-4, $\underline{Z}_{\mathrm{f}}$
6.3.1-iv	impact of current axis prioritisation in case of current limitation on short-term stability (EMT)	GFM: droop, SECM-1 to SECM-4, $\underline{Z}_{\mathrm{f}}$, current axis prioritisation
6.3.1-v	trajectory sensitivity analyses of selected GFM control parameters (phasor)	GFM: droop, SECM-1
6.3.2-i	comparison of voltage trajectories between EMT and phasor load model	PEL-1a with 30 % load share
6.3.2-ii	impact of different power electronic loads on short-term stability (EMT)	PEL-1 to PEL-4 with load shares from 30 % to 100 %
6.3.2-iii	trajectory sensitivity analysis of PEL-1a parameters (phasor)	PEL-1a with 30 % load share
6.3.3-i	mutual impact of GFM converters with different power electronic loads on short-term voltage stability (EMT)	GFM: droop with SECM-1, PEL-1 to PEL-4 with 15 % load share

At first, the impact of the GFM converters and the power electronic loads are analysed separately for different scenarios. Afterwards, their mutual impact is considered. The first two sections start with a comparison of the EMT with the phasor model. A trajectory sensitivity analysis is also performed in these cases. For better comparability of the GFM converters and the power electronic loads, the sensitivities and approximated voltage trajectories are always determined for the voltage magnitude of $|\underline{v}_3|$. Based on the scenario, an approximated trajectory is also compared with an actual perturbed trajectory (based on a new simulation) to check if the sensitivities are correct. The second half of the analysis focuses on the investigation of long-term voltage stability, which has a similar structure to the short-term analysis. An overview of the scenarios for the investigation of long-term voltage stability is given in Table 6.2.

Table 6.2: Scenarios and ANS adaptations for analysing long-term voltage stability

Section	Focus of analysis	ANS Adaptations
6.4.1-i	comparison of voltage trajectories between EMT and phasor model with GFM converter	GFM: droop, SECM-1, reduced S_G (-3 %)
6.4.1-ii	impact of GFM control approach and SECM on long-term stability (EMT)	GFM: droop, matching, dVOC, VSM, SECM-1 to SECM-4, reduced S_G (-3 %)
6.4.1-iii	trajectory sensitivity analyses of selected GFM control parameters (phasor)	GFM: droop, SECM-1, reduced S_G (-3 %)
6.4.1-iv	comparison of approximated and perturbed trajectories (phasor)	GFM: droop, SECM-1, reduced S_G (-3 %)
6.4.2-i	comparison of voltage trajectories between EMT and phasor model with power electronic load	PEL-1a with 30 % load share, shunt reactance
6.4.2-ii	impact of different power electronic loads on long-term stability (EMT)	PEL-1 to PEL-4 with load shares from 10 % to 50 %
6.4.2-iii	Trajectory sensitivity analyses of PEL-1a parameters (phasor)	PEL-1a with 30 % load share
6.4.2-iv	comparison of approximated and perturbed trajectories (phasor)	PEL-1a with 30 % load share
6.4.3-i	mutual impact of GFM converters with different power electronic loads on long-term voltage stability (EMT)	GFM: droop, matching, dVOC and VSM with SECM-1, PEL-1 to PEL-4 with 10 % and 30 % load share

6.2.2 Simulation environment

As important as the mathematical description of power system components is their implementation in a specific simulation environment or tool. This is because each tool offers only a limited set of modelling and analysis features. The choice of simulation environment should therefore be based on the requirements of the models to be developed. However, there is often no single tool that fits all requirements.

For the phasor simulations, the ANS is modelled with *PowerDynamics.jl*, which is an Open-Source package for modelling dynamic power systems within the Julia programming language [155]. The resulting hybrid DAE system is solved using *DifferentialEquations.jl*, which is also an Open-Soure package written in Julia that provides many numerical solvers for such systems [156]. This package also defines how the events of the corresponding hybrid system are modelled. This is done through so-called *callbacks*, which can be used

to create user-defined events to model switching events and impulsive behaviour. In general, two types of callbacks are supported. The first is the so-called *continuous callback*, which evaluates a user-defined function, including states and parameters, and checks when the function becomes zero. A root-finding method (and adaptive integration steps) is then used to find the exact time when the function becomes zero. This means that the integration algorithm steps back and forth in time until the evaluation of the root-finding method is within certain tolerances. This type of callback is of particular interest to ensure that an event should only occur at a very precise point in the state space. The second type of callback is the so-called *discrete callback*, which checks whether a given condition (or function) is true at the end of each integration step. This means that no additional root-finding method is used. An advantage is that inequality conditions can be used to trigger an event. However, the simulation step size should be set small enough that the event is triggered in a reasonable time after the condition becomes true. Then, regardless of whether the condition of a continuous or discrete callback becomes true, a so-called *affect function* is called, in which user-defined code can be placed to modify the dynamic system, e.g. by changing differential or discrete states or parameters. Through the combination of callbacks and affect function, the characteristic events of hybrid systems can be realised. In this thesis, the discrete callback type is mostly used because, as seen in Section 4.5 and 5.4, inequality conditions are mostly used. Also, to avoid numerical instability, it is important not to change the differential and algebraic equations. However, to get around this restriction, boolean discrete states can be used to enable or disable some parts of the equations, which is already considered in the DADS description in Section 4.5.

The EMT model of the ANS is implemented in MATLAB/Simulink [157]. As only the modelling environment is visible to the user here, no additional information can be given on how events are handled during the numerical simulations. Event modelling therefore takes place at a higher level of modelling, which means that the same results can be achieved without knowing the exact implementation.

The Julia package *SciMLSensitivity.jl* is used to compute trajectory sensitivities [158]. This package can be used to compute the sensitivities of hybrid DAE systems by automatic differentiation. Automatic differentiation is a technique for computing the derivatives of almost arbitrary functions in a numerically efficient way. The mathematical background of trajectory sensitivities given in Section 3.4 is still valid as the power system in this thesis is modelled as a DADS and is beneficial for calculating the correct sensitivities with the given package. However, it should be noted that a DADS representation is not a necessary requirement for the trajectory sensitivity calculation of this package.

6.3 Analysis of short-term voltage stability

Next, the simulation results are presented for analysing the impact of GFM converters with current limitation and power electronic loads on short-term voltage stability. For this, mainly two methods for evaluating stability are used. The first method is a time-domain comparison of the corresponding voltage and/or power trajectories. This is used in particular for the comparison between the phasor and EMT models. The second method takes the high-voltage (HV) and low-voltage (LV) thresholds of the fault ride-through requirements from [29]. The simulation is considered unstable if the thresholds are violated during a 5 s simulation time. The aim is to determine the stability region of the system by varying the short-circuit impedance $\underline{Z}_\mathrm{f} = R_\mathrm{f} + jX_\mathrm{f}$ with a fixed short-circuit duration of 100 ms. The resolution of the impedance sampling is given by $|\Delta X_\mathrm{f}|$ and $|\Delta R_\mathrm{f}|$ and depends on the given scenario.

Fig. 6.4 shows an example of the determination of a short-term voltage stability region and its corresponding stability limit by short-circuit impedance sampling. The voltage v_G at the generation terminal bus is used for the stability evaluation, since the voltage thresholds from [29] are fault ride-through requirements for power electronic generation units. For the sake of simplicity, only the stability limits are shown in the following results figures to describe the stability region. This means that the area between the stability boundary and the coordinate origin is always the unstable stability region.

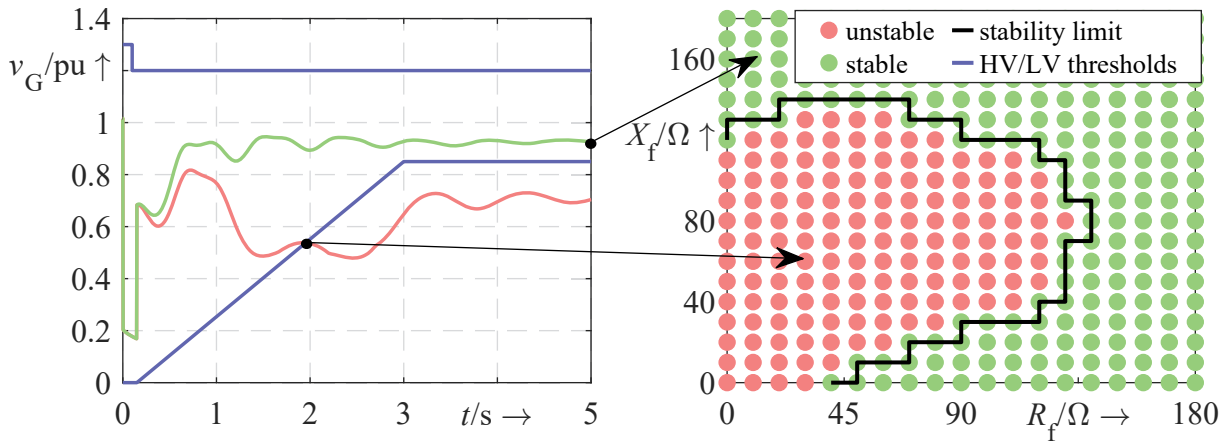

Figure 6.4: Exemplary determination of a short-term voltage stability region and limit by short-circuit impedance sampling ($|\Delta X_\mathrm{f}| = |\Delta R_\mathrm{f}| = 10\,\Omega$) and assessing high and low-voltage stability thresholds

6.3.1 Impact of grid-forming converters with current limitation

As the current limitation of GFM converters is changing their dynamics significantly it is analysed next how this affects short-term voltage stability in case of short circuits. For this, different GFM controls, SECMs and current axis prioritisation are taken into account. Parts of the results are based on the work in [SL1].

i) Comparison of voltage trajectories between EMT and phasor GFM model

Fig. 6.5 shows the comparison between the EMT and the phasor model of the ANS with droop converter for the base case. Without SECM-1 it can be seen that the system becomes unstable, resulting in decreasing voltages after the short circuit is cleared. The reason for this is that during the short-circuit there is an active power mismatch, which leads to an increasing angle θ of the converter. After the fault, the large angle difference leads to a loss of synchronism with the rest of the system. This process is partly comparable to the dynamics of transient stability of synchronous generators, which also originate from an active power mismatch. In contrast, the system is stable when the proposed SECM-1 is activated, resulting in a much better post-fault synchronisation. Comparing the EMT and phasor models, it can be seen that the main voltage dynamics are similar. Differences occur particularly at the start and end of the fault. In the phasor model, the voltages drop and rise instantaneously due to their algebraic equations. In the EMT model, the magnitude of the voltage is determined by calculating the root mean square through a running average window over one cycle, where also past values are used. However, it can be seen that the steady-state values at the end of the fault and simulation are close together.

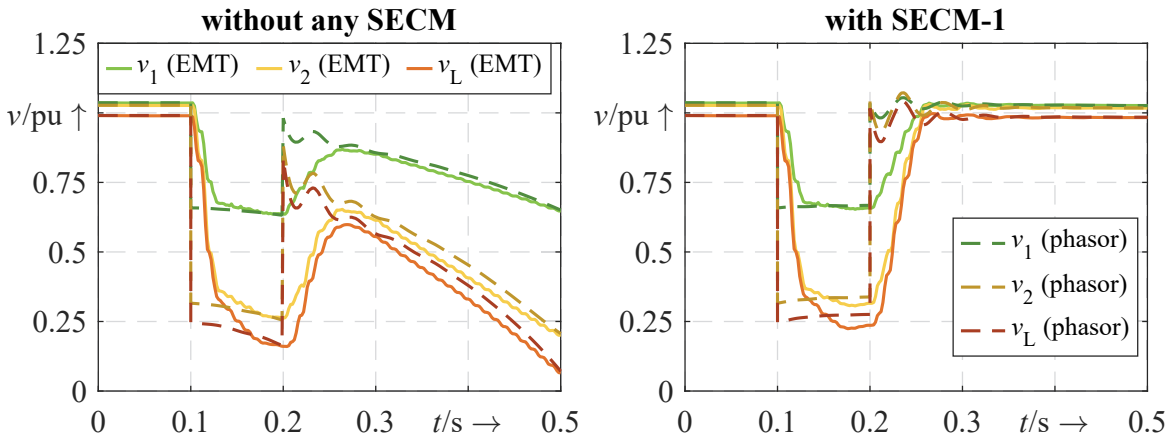

Figure 6.5: Comparison of voltage dynamics between EMT and phasor ANS model with droop converter for $\underline{Z}_{\mathrm{f}} = 20 + \mathrm{j}20\Omega$ as well as with and without SECM-1

ii) Comparison of short-term voltage stability between EMT and phasor GFM model

The next analysis looks at the differences in terms of their stability region and limit regarding the GFM controls. Since the active power load model is also very different between these models (phasor: algebraic equation, EMT: current source and PLL dynamics), its share is varied to investigate its influence on the stability region. Fig. 6.6 illustrates the different stability limits of the four different GFM converters with different load compositions and simulation types without any SECM. For example, $p_{\mathrm{L,I}} = 0.9$ means that 90 % of the active power of the load is modelled as constant current and 10 % as constant resistance. For $p_{\mathrm{L,I}} = 1.0$, the droop, dVOC and VSM controls are similar in terms of their stability region. In contrast, matching control has a larger unstable region. By reducing the proportion of active power by constant current, the stability region increases significantly due to the higher voltage dependence. However, most phasor models are slightly more optimistic

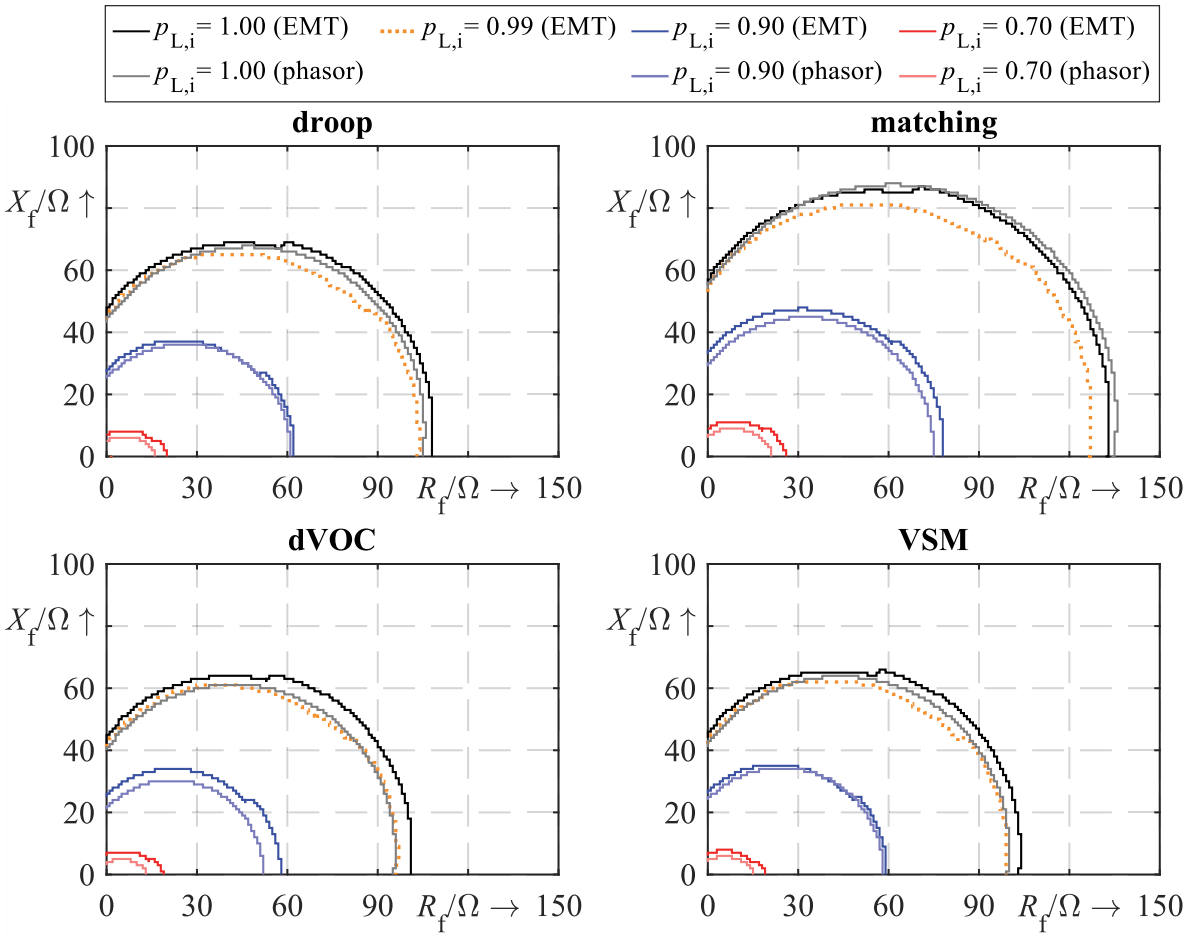

Figure 6.6: Short-term voltage stability limits of four different GFM converters for different load compositions and simulation models ($|\Delta X_{\mathrm{f}}| = |\Delta R_{\mathrm{f}}| = 1\,\Omega$)

about the stability region than the EMT models. Yet, a small 1 % decrease ($p_{\mathrm{L,I}} = 0.99$ only for EMT model) in the constant current load in the EMT model increases the stability region more than using a phasor model. This means that the stability region is highly sensitive to the load composition. For this reason, the choice of load composition in modelling should be considered more carefully than the type of model alone in this case.

iii) Impact of GFM control approach and SECM on short-term stability

Next, a comparison is made between the SECMs and GFM controls, see Fig. 6.7. This is only done in the EMT domain. As the results show, the proposed SECM-1 increases the stability region the most. Only for VSM, SECM-2 leads to a higher increase than SECM-1. In contrast, the effect of SECM-3 and SECM-4 varies more between the GFM controls, but SECM-3 has the least stabilising effect for all GFM controls. Comparing the GFM controls, it can be seen that droop and dVOC are similar in their stability limits, whereas matching and VSM vary more. In summary, all SECMs can significantly improve the stability region (see Fig.6.6 as a comparison), but SECM-1 and SECM-2 clearly stand out.

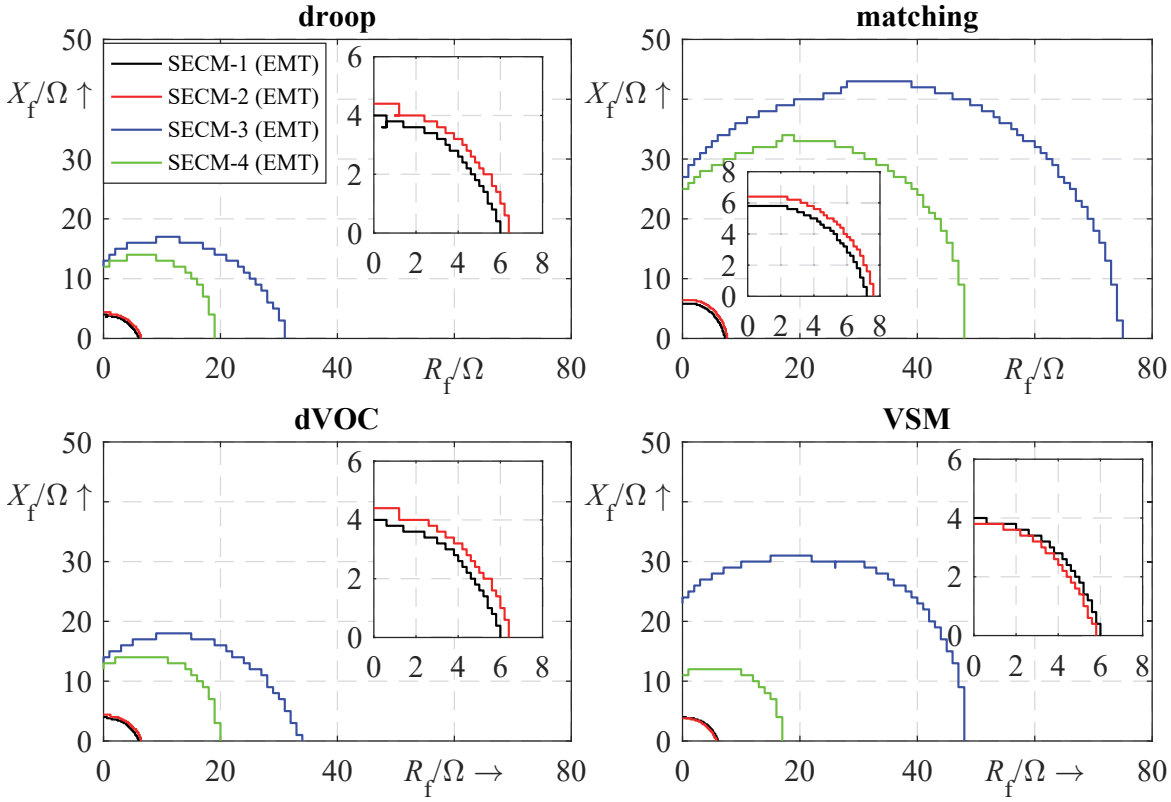

Figure 6.7: Short-term voltage stability limits for four GFM controls, four SECMs and pure constant current active power load ($p_{\mathrm{L,I}} = 1.0$, $|\Delta X_\mathrm{f}| = |\Delta R_\mathrm{f}| = 0.2\,\Omega$ for SECM-1 and SECM-2, $|\Delta X_\mathrm{f}| = |\Delta R_\mathrm{f}| = 1\,\Omega$ for SECM-3 and SECM-4)

iv) Impact of current axis prioritisation on short-term stability

As in the previous simulations only circular current limitation has been investigated, the next step is to examine the impact of q-axis and d-axis current prioritisation in the case of current limitation. Fig. 6.8 shows the stability regions in the case of q-axis and d-axis current prioritisation for a droop converter and varying SECM. In general, both current prioritisations lead to a larger unstable region. For the q-axis prioritisation, the main reason is that the converter injects more reactive power than active power and thus does not meet the active power required by the load. Therefore, the q-axis current prioritisation is not effective in the case of short circuits within this grid, which is also reflected in the SECMs where most of them are comparable according to their stability limit, except SECM-3. The unstable area for the d-axis current prioritisation is even larger compared to the q-axis. But the explanation is different from the previous one. In this case, the prioritisation is based on active power rather than reactive power, resulting in minimal support of the voltage magnitude. Thus, the voltage decreases more during the d-axis current prioritisation, leading to a less stable system. When comparing the SECM, the largest differences in stability limits are around the ordinate. Here SECM-3 and SECM-4 can stabilise the converter better than SECM-1 and SECM-2.

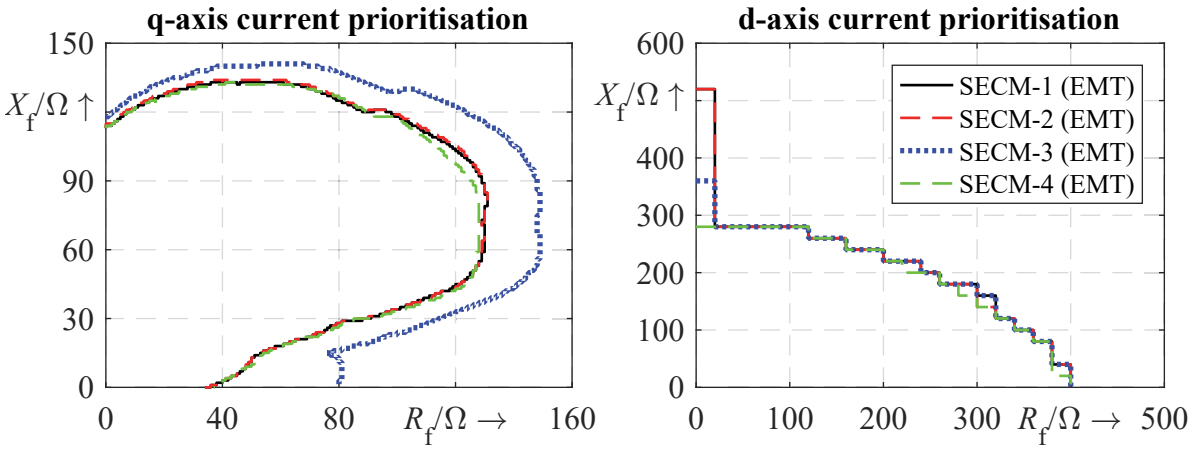

Figure 6.8: Short-term voltage stability limits of a droop converter with q-axis and d-axis current prioritisation for four SECMs and $p_{\mathrm{L,I}} = 1.0$ (q-axis: $|\Delta X_\mathrm{f}| = |\Delta R_\mathrm{f}| = 1\,\Omega$, d-axis: $|\Delta X_\mathrm{f}| = |\Delta R_\mathrm{f}| = 20\,\Omega$)

v) Trajectory sensitivity analyses of selected GFM control parameters

To conclude the short-term analysis of the GFM converters, a trajectory sensitivity calculation of the phasor droop converter with SECM-1 is performed. These sensitivities are used to determine approximate trajectories of the voltage $|\underline{v}_3|$. A positive parameter change of 100 % of the original parameter value is assumed. This means that the difference between the approximated and the original trajectory represents the relative sensitivity. As the results show, the droop parameter k_d has only a small impact on the voltage over the entire simulation time. Only during the fault k_d can increase the voltage magnitude, but only to a limited extent, since SECM-1 decelerates the angle θ. A damping effect on the post-fault voltage oscillations is obtained by increasing the voltage current control gain k_pv. On the other hand, increasing the DC voltage control gain k_dc amplifies these oscillations. Therefore, its value could also be reduced to have a similar effect as the gain k_pv. The maximum converter current i_cmax has a strong influence on the voltage during the fault if it were treated as a flexible parameter. However, the increase in voltage to almost 1.5 pu should be treated with caution as the linear sensitivities may overestimate its influence. Nevertheless, the sensitivities demonstrate that the magnitude of the short-circuit current is the main factor determining the voltage drop during the fault. In contrast, increasing the maximum DC current i_dcmax would amplify the voltage oscillations after the fault.

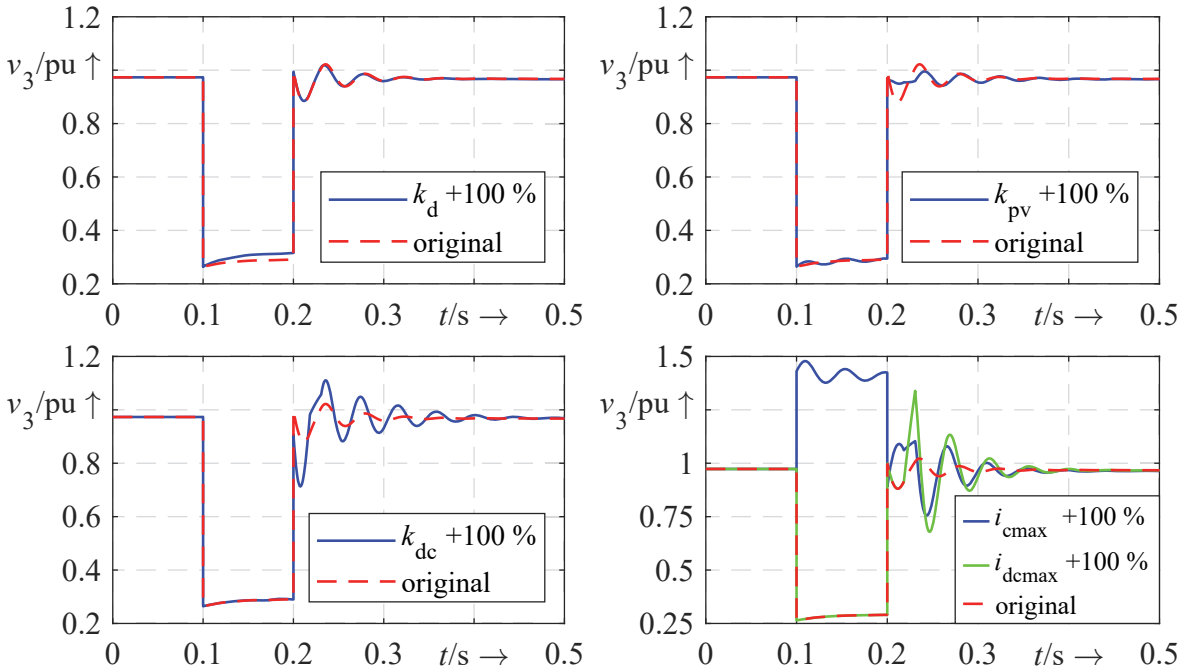

Figure 6.9: Approximated and original voltage trajectories of a droop converter with SECM-1 using selected trajectory sensitivities

In summary, the short-term voltage stability analyses of the GFM converters with current limitation and different SECMs show that there are small differences in the trajectories and stability regions between the EMT and phasor models. Therefore, the voltage dynamics and fundamental stability mechanisms are very similar. Regarding the GFM controls, there are no major differences between the droop, dVOC and VSM controls. Only the stability region of the matching control is significantly smaller in the scenarios performed. Since only fixed control parameters are used here, other parameters could lead to a different result for the GFM controls. However, even with optimised control parameters without SECM, it would probably not be possible to achieve as wide a stability range as with SECM. The proposed SECM-1 shows that it can at most increase the stability region for circular current limitation, but is very close to SECM-2. In the case of q-axis or d-axis current prioritisation, all SECMs lead to a comparable but significantly smaller stability region. Yet the reason is not the SECMs themselves, but rather the ineffectiveness of q- and d-axis current prioritisation in this grid. The trajectory sensitivity analysis indicates that the voltage during the fault can only be influenced mainly by increasing the maximum converter current. On the contrary, the control parameters could be optimised to dampen the post-fault voltage oscillations. However, the impact on other system variables and the stability of the control loop should also be considered when making such parameter changes.

6.3.2 Impact of power electronic loads

In this scenario, the impact of the EMT and phasor power electronic load models on short-term voltage stability is analysed. This is done by replacing a part of the aggregated load of the ANS by these models. Based on the actual simulation, different load shares are taken, where e.g. "PEL share = 30 %" means that 30 % of the total load is modelled by a power electronic load (PEL).

i) Comparison of voltage trajectories between EMT and phasor load model

Fig. 6.10 illustrates the simulation results for the EMT and phasor power electronic load models (PEL-1a). The comparison of the voltages shows differences in the initial voltages before the short circuit. This is because the steady-state reactive power consumption is capacitive for the phasor model, but inductive for the EMT model. This is due to the inductive phase shift of the EMT load current resulting from the high inductive grid impedance seen by the load. This is similar to the measurements made in the laboratory in case of high grid

impedances (see Section B.2.4). Other differences between the models arise particularly at the start and end of the fault. In the case of the phasor model, the voltage drops immediately when the fault occurs, as it is described by algebraic equations. Afterwards, a small voltage recovery can be observed due to the decreasing power consumption. However, this effect is negated by the subsequent power recovery. After the fault, the voltage jumps immediately but also drops again due to the charging of the capacitor and the resulting high power consumption. In the case of the EMT model, the calculation of the fundamental voltage also uses values from the previous cycle. This explains to some extent the delay in the voltage drop and rise at the beginning and after the fault. However, the comparison of active and reactive power also reveals differences in the magnitude of the power consumption and in the sign of the reactive power. It can be concluded that the active power of the EMT and phasor load models generally show to some extent similar dynamics, but mainly for the active power. The differences are greater for the reactive power, which is capacitive for the phasor model and inductive for the EMT model, which ultimately explains the voltage deviations.

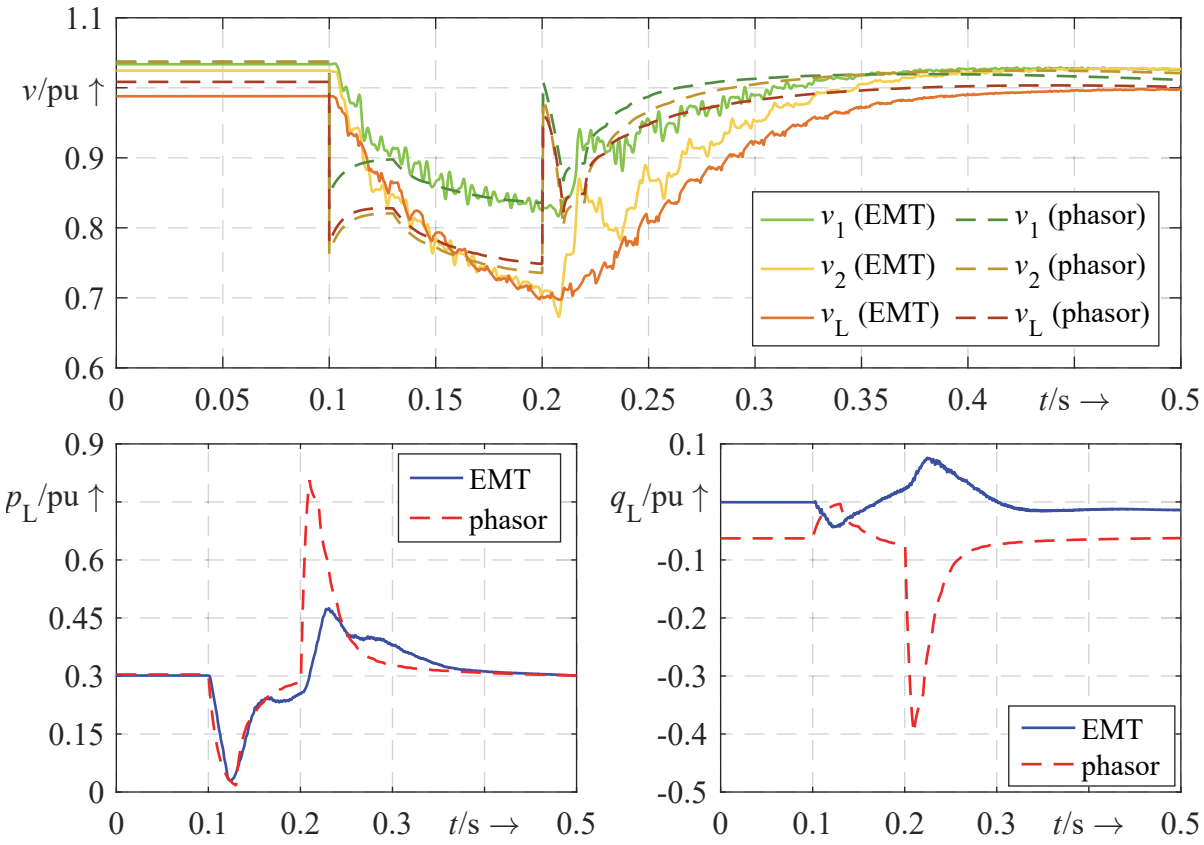

Figure 6.10: Comparison of voltage and load power dynamics between the EMT and phasor power electronic load model with a load share of 30 % and $\underline{Z}_f = 20 + j20\,\Omega$

ii) Impact of different power electronic loads on short-term stability

The next step is to analyse the different EMT models. PEL-1 to PEL-4 are used with different load shares to investigate their impact on short-term voltage stability. Fig. 6.11 displays the voltage trajectories, while Fig. 6.12 and Fig. 6.13 show the corresponding active and reactive power. For a power electronic load share of 30 % and 40 % all voltages remain within acceptable ranges. In addition, all loads reduce their power output during the fault and have a short period of higher power consumption after the fault is cleared. Load recovery is fastest for PEL1 and PEL-4, followed by PEL-3. For PEL-2, no load recovery can be observed during the fault, which helps to prevent the voltage from dropping significantly during this period. In addition, there is only a small overshoot in active and reactive power after the fault, compared to the other loads.

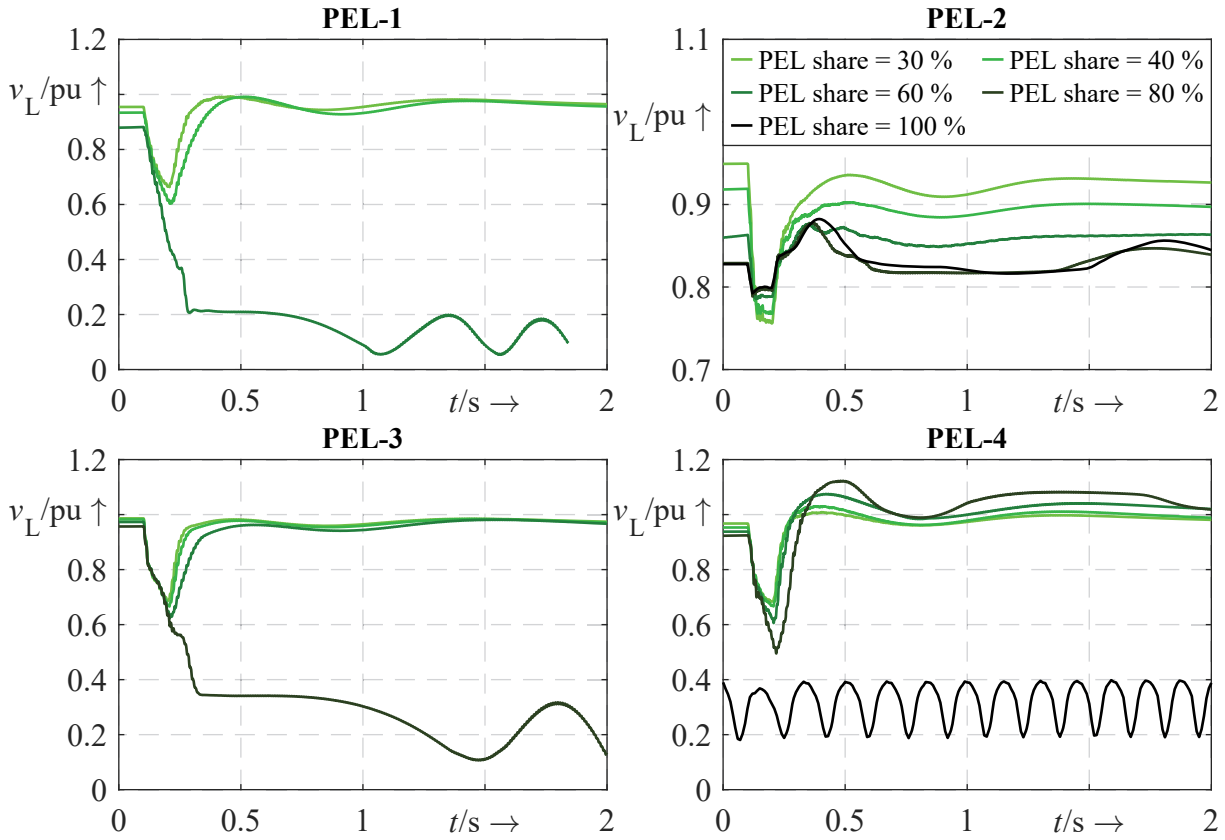

Figure 6.11: Load voltage trajectories of PEL-1 to PEL-4 for different load shares and $\underline{Z}_f = 20 + j20\,\Omega$ to analyse their impact on short-term voltage stability

Although PEL-2 has the highest inductive power consumption compared to all other loads, no instability is observed even for a load share of 100 %. However, as the load share increases, unsafe low steady-state voltages are present, which in reality could endanger the power system. In the case of PEL-1, it can be seen that a share of 60 % leads to short-term instability. This is mainly due to the recovery of its power consumption during the short circuit so that even after the fault has been cleared no equilibrium point is reached. Despite the overall very low reactive power consumption of PEL-3, the power system becomes unstable at a load share of 80 %. Like PEL-2, PEL-4 is also stable at higher load shares, but its voltages remain within safe operating ranges in steady-state conditions. One reason for this is that its reactive power consumption switches from inductive to capacitive, supporting the voltage after the fault. However, for a load share of 100 % the power system becomes unstable right at the start of the simulation.

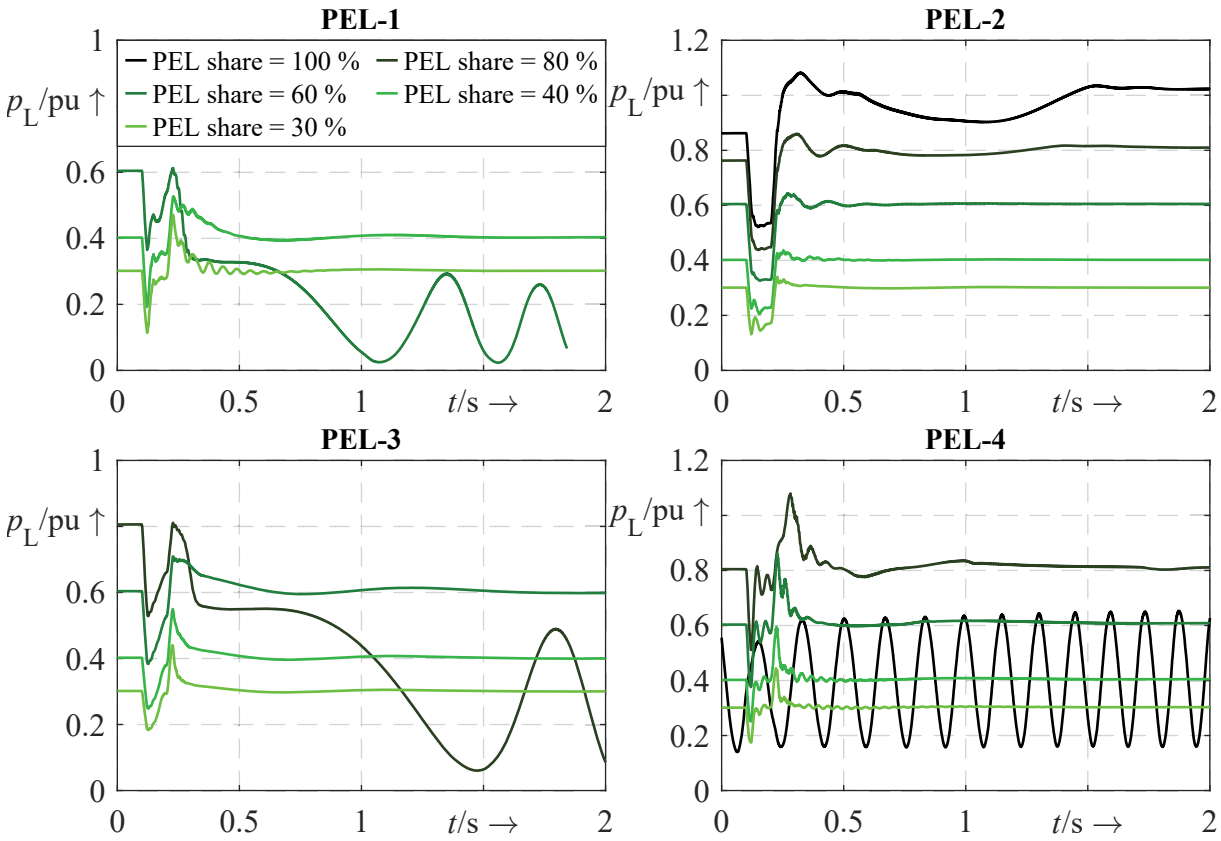

Figure 6.12: Active power trajectories of PEL-1 to PEL-4 for different load shares and $\underline{Z}_f = 20 + j20\,\Omega$ to analyse their impact on short-term voltage stability

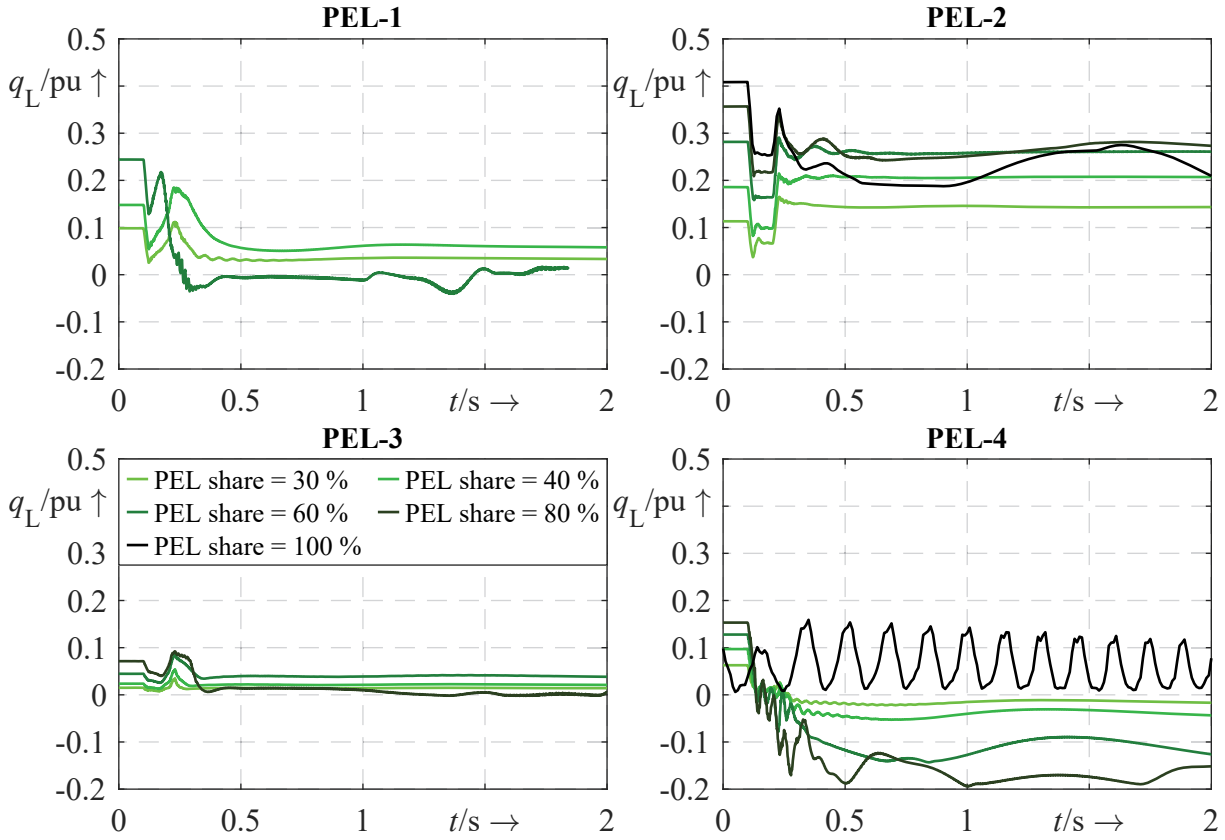

Figure 6.13: Reactive power trajectories of PEL-1 to PEL-4 for different load shares and $\underline{Z}_f = 20 + j20\,\Omega$ to analyse their impact on short-term voltage stability

Overall, the comparison of the four power electronic loads demonstrates that a high proportion of these loads can lead to short-term instability, but depends on the specific load. The biggest driver of instability is the power recovery during the fault, as it puts additional stress on the system. However, if this is not the case and power consumption is reduced, the short-term stability of the system greatly benefits from this. Steady-state voltages are also affected by the reactive power consumption of the load. In some cases, the power electronic loads even changed their reactive power consumption from inductive to reactive (PEL-1 and PEL-4). This also shows that the reactive power consumption of the load is highly dependent on the grid scenario, including faults and contingencies.

iii) Trajectory sensitivity analysis of PEL-1a parameters

To complete the analysis of power electronic loads in this subsection, a trajectory sensitivity analysis is performed for the PEL-1a load model. The corresponding original and approximated trajectories are shown in Fig. 6.14. If the capacitor c_{dc} is increased by 100 %,

it can be seen that the steady-state voltage $|\underline{v}_3|$ would decrease slightly due to the reduced capacitive reactive power. This is not intuitively clear as less reactive power is drawn despite the increased capacitance. A possible explanation could be that the switch-on and switch-off times are reduced due to the smoother rectified voltage. As a result, the period during which current is flowing into the load is also reduced and consists mainly of active power current. During the fault, the higher capacitance results in reduced active and reactive power consumption during power recovery, as it can supply the DC load for a longer period of time. Conversely, the higher value of the capacitor requires more energy after the fault has been cleared, significantly delaying voltage recovery, even though more capacitive reactive power is released. If the DC power p_{dc} is increased, it is obvious that the active power consumption will also increase. Here only a 33 % increase is chosen as the sensitivities for this parameter are quite high. The higher DC power also leads to higher reactive power consumption, probably due to longer switch-on and switch-off times, which could increase the reactive power part of the current. Furthermore, the power recovery during

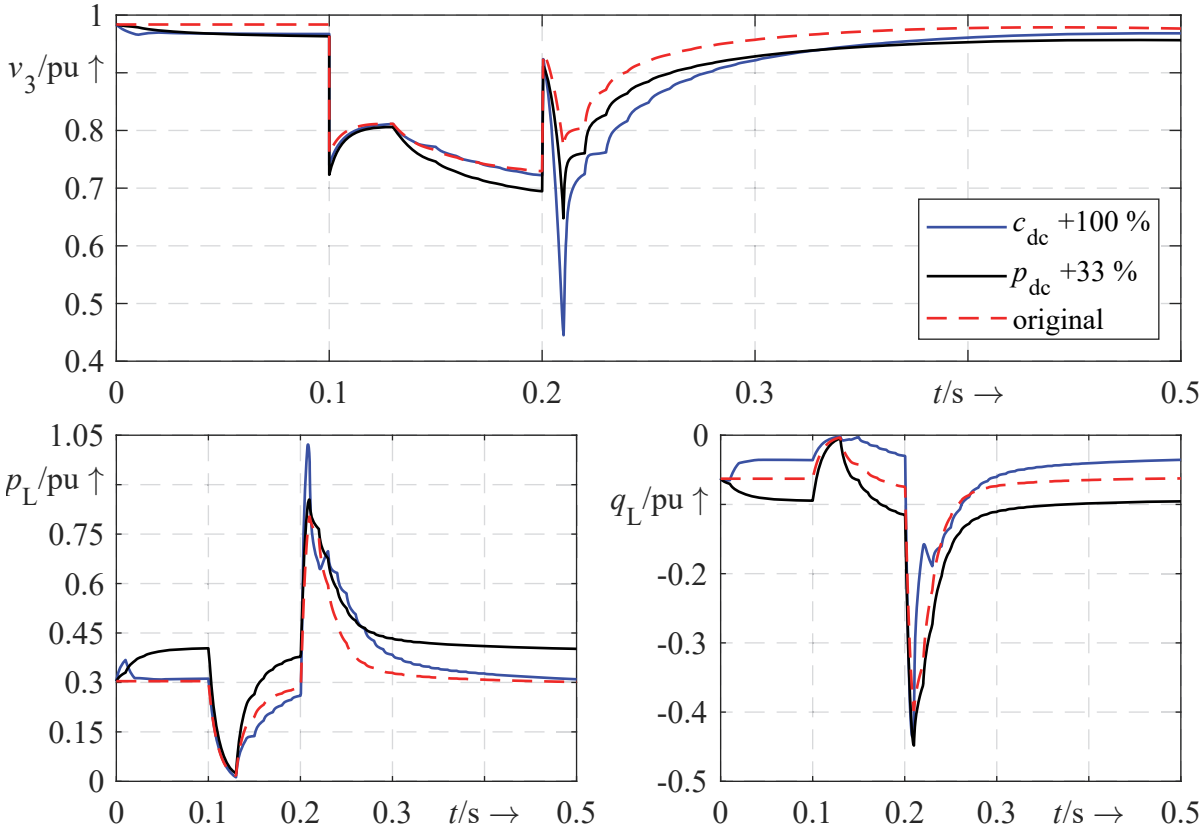

Figure 6.14: Approximated and original voltage and power trajectories of PEL-1a using the trajectory sensitivities of c_{dc} and p_{dc}

the fault is faster because the DC power p_{dc} has increased, but not the capacitor c_{dc}. This results in lower grid voltages during the fault. The delay in voltage recovery after the fault is not as pronounced as when the capacitance is increased because higher reactive power consumption is also observed.

It can be concluded that increasing the capacitor c_{dc} can delay the voltage recovery after the fault, due to the higher power consumption. Increasing the DC power p_{dc} always leads to lower voltages, although the capacitive reactive power is higher. At this point, however, it must be pointed out that the results of the trajectory sensitivity for PEL-1a must be considered with caution, as the previous EMT and phase model comparison had shown that the reactive power is different after all. The results may therefore apply to the model but do not necessarily reflect the true behaviour.

6.3.3 Mutual impact of grid-forming converters and power electronic loads

The last sub-section analyses the mutual impact of GFM converters and power electronic loads on short-term voltage stability. Here, mainly the impact of the different EMT load models on a droop converter is examined, because there were no major differences to the other GFM controls.

i) Impact of GFM converters and power electronic loads on short-term voltage stability

Next, the impact of the different power electronic loads with a load share of 15 % is examined in combination with a droop converter and SECM-1. As the results in Fig. 6.15 show, all load voltages are quite similar at the beginning of the simulation but drop to low and unsafe values after the fault has been cleared. Especially for PEL-1, PEL-3 and PEL-4 very low voltages result. The reason for this is that these loads try to recover their power consumption during the fault, which pushes the power system to an unsafe equilibrium point, which would be unstable in a real application. This can also be seen for PEL-4, which recovers its power the fastest, causing the voltage to drop the fastest. Unlike the other loads, PEL-2 does not recover power during the short circuit, resulting in much higher voltages throughout the simulation. Although it consumes the highest inductive reactive power at the beginning and end of the simulation.

Overall, the results indicate that the combination of reduced short-circuit current and fast power recovery is a serious problem for the short-term voltage stability of a power system.

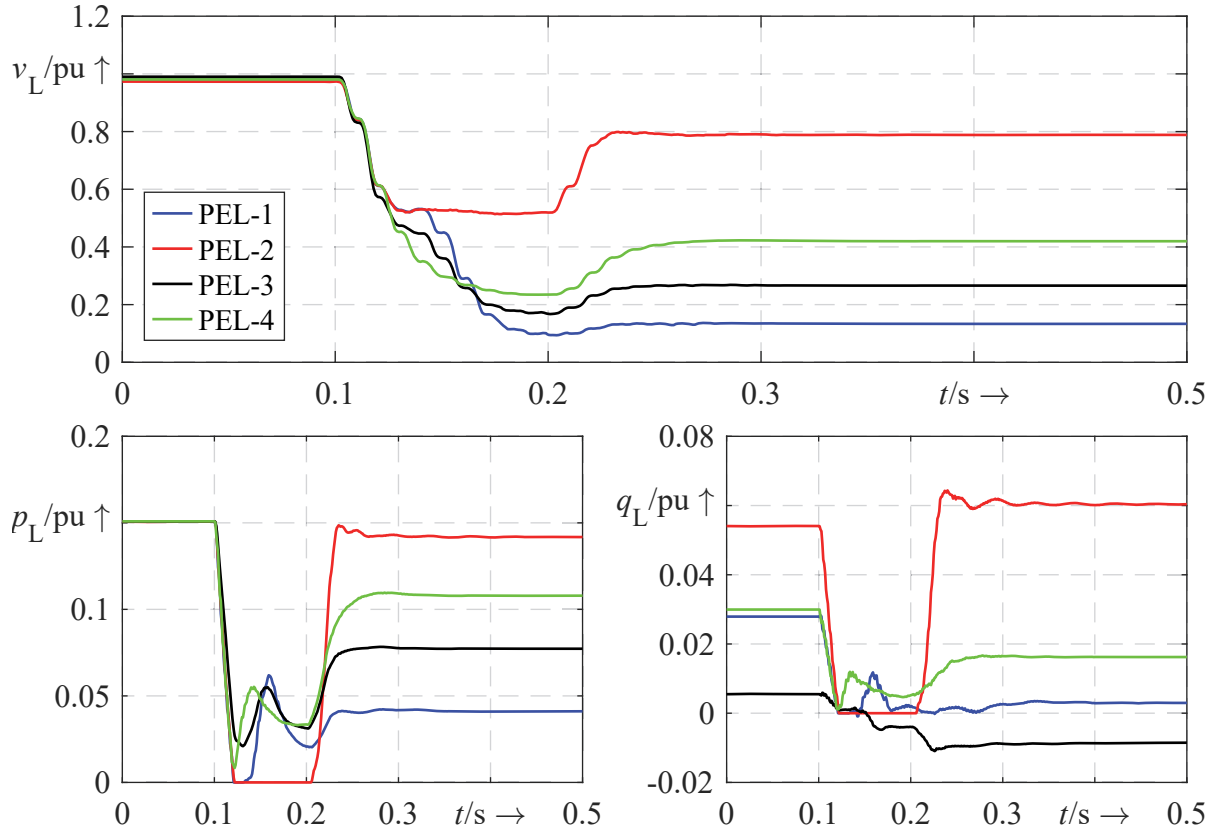

Figure 6.15: Load voltage and power trajectories for PEL-1 to PEL-4 with a load share of 15 % and a droop converter with SECM-1 and $\underline{Z}_f = 20 + j20\,\Omega$

The superimposed power control of the inverter plays only a minor role here, as the dynamics are largely determined by the current limitation mode. In the case of power electronic loads, however, the extent to which the power consumption drops in the event of a fault, and whether or not there is any recovery, is critical to the subsequent voltage recovery and therefore stability.

6.3.4 Summary and conclusion

In the preceding chapter the impact of different GFM control approaches and power electronic loads on short-term voltage stability is analysed. For this purpose, short circuits on a transmission line with subsequent disconnection of the line were regarded as faults. The concepts of stability region and associated limits were introduced to highlight the differences in stability between the GFM controls and SECM. This was done by sampling the inductive and resistive components of the short circuit impedance and evaluating the high and low-voltage fault ride-through requirements by time-domain simulations.

In this context, a general question was addressed on whether the models of GFM converters and power electronic loads need to be EMT or phasor models for accurate stability analysis. For the GFM converters, it was shown that the EMT and phasor models lead to almost the same stability region, with only small deviations. It could also be demonstrated that changing the load composition by 1 % has a greater influence on the stability region than changing from the EMT to the phasor model. This highlights the importance of accurate load modelling in the context of voltage stability. This can also be seen in the comparison between the EMT and phasor PEL-1a model. Here it can be clearly observed that there are large differences, especially for the reactive power. Due to this, deviations occur in the voltage trajectories during transients, but also at steady-state conditions. This leads to the conclusion that power electronic loads should be simulated as an EMT model if possible, while the phasor models for GFM converters also give similar results.

The general impact of GFM converters and power electronic loads can be summarised as follows. For GFM converters without SECM, the ANS is less stable in the short term due to the reduced short-circuit current. Among the GFM control approaches, the matching control is the least stable, while the droop, dVOC and VSM are quite similar. However, when a SECM is applied, the stability of all control approaches can be greatly increased. Here SECM-1 and SECM-2 could increase the stability the most, followed by SECM-4 and SECM-3. In the case of current axis prioritisation, it could be shown that q- and d-axis prioritisation leads to a smaller stability region compared to circular current limitation. However, this could change in a different grid and has to be analysed separately. For power electronic loads, the results show that the system is less stable with a higher share of these loads. The most significant influence on stability is the voltage at which the load disconnects from the grid, as this greatly reduces the load in the event of a fault. For this reason, the PEL-2 load does not cause instability even at a load share of 100 %, as it already disconnects at higher voltages than the other loads. The combined simulation of a GFM converter and a power electronic load showed that the combination of current limitation and power recovery during the fault is a serious threat to short-term voltage stability. This is true even for comparable small load shares and all types of power electronic loads. However, the type of GFM control has nearly no influence, as its dynamics are mainly determined by its current limitation mode.

Finally, trajectory sensitivities were calculated for the GFM control and the PEL-1a parameters. The results indicate that the maximum converter current i_{cmax} would have the greatest influence on the course of the voltage trajectories if it were treated as a parameter. In contrast, the droop gain k_{d} can slightly increase the voltage during the fault even though

SECM-1 is active. The simulation results also showed that increasing the outer voltage loop gain k_{pv} can dampen the post-fault voltage oscillations, while increasing the DC energy source model gain k_{dc} leads to amplified oscillations. However, k_{dc} could also be reduced to damp the oscillations. In the case of PEL-1a, the sensitivity analysis showed that a higher DC capacitor c_{dc} can delay the voltage recovery after the fault as the capacitor is charged more, resulting in a higher power consumption. Increasing the DC power p_{dc} always results in lower voltages, despite the higher capacitive reactive power. However, as the reactive power of the phasor PEL-1a model may not reflect the real behaviour of such a model, any statements about it must be taken with caution and further research is therefore required.

6.4 Analysis of long-term voltage stability

In the next subsection, the impact of GFM converters and power electronic loads on long-term voltage stability is analysed. Here the focus is on a slowly developing voltage collapse due to OLTC tap changes and possibly OEL activation by synchronous generators. As some of the previous simulations have shown that the grid is short-term unstable, in some scenarios the transmission line fails in this section without a previous short circuit. This means that it is more likely to be a failure of the protective tripping device than a damaged line.

6.4.1 Impact of grid-forming converters with current limitation

In the following, the impact of current limitation of GFM converters on long-term voltage stability is analysed. Parts of the subsequent results are based on the work in [SL1]. To demonstrate some of the dynamics of the GFM converter in the case of current limitation, its rated power is reduced by about 3 % (from 5300 MVA to 5142 MVA) in this section. The reason for this is that the ANS for a GFM converter is long-term stable at its original rated power, as the load voltage $\underline{v}_{\mathrm{L}}$ can be restored by a few taps of the OLTC to reach the deadband of the OLTC.

i) Comparison of voltage trajectories between EMT and phasor GFM model

Fig. 6.16 presents a time-domain comparison of a droop converter with and without the SECM-1 for the EMT and phasor models. Without SECM-1, it can be seen that the grid voltages collapse at the time when the converter reaches its current limit. This is because the converter can no longer feed in its active power, so its angle θ is constantly increasing and it is no longer synchronised with the grid. The EMT and phasor models generally show the same dynamics, but the voltage collapse occurs two seconds later in the phasor model. If SECM-1 is activated, the power system can be stabilised at the time of current limitation. However, the continuous tapping of the OLTC leads to continuously decreasing voltages until the maximum tapping position is reached. Comparing the EMT and the phasor model, basically the same long-term voltage dynamics occur. However, as time progresses, some differences in the voltage magnitude and time of tapping become more apparent. The differences in voltage amplitude can be explained by the fact that the EMT model of the transformer contains some small impedances due to additional internal switches to realise the tapping. In addition, the differences in the timing of the transformer tap change can be explained by the measured load voltage for the OLTC within the phasor model, which leaves the deadband of the OLTC later. In summary, this scenario demonstrates that a GFM converter can become unstable and induce voltage instability in the presence of current limitation, even at nearly nominal voltages. However, this unstable response can be avoided by the stabilising properties of SECM-1. In addition, the EMT and phasor models generally share the same long-term dynamics with minor deviations.

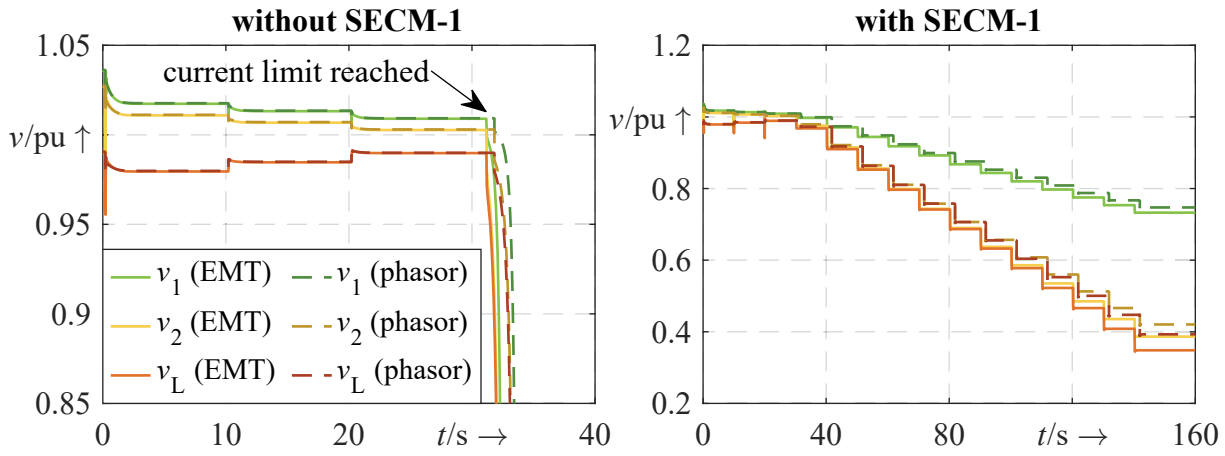

Figure 6.16: Comparison of long-term voltage dynamics between the EMT and phasor ANS model including a droop converter as well as activated and deactivated SECM-1

ii) Impact of GFM controls and SECMs on long-term stability

Next, the same scenario is presented but for all GFM control approaches and SECMs. All simulations are performed with the respective EMT models. Due to the reduced power rating of the converter and the resulting higher steady-state current, the current threshold i_{thr} for SECM-4 is increased to 0.95 compared to 0.9 in Section 6.3.1. As can be seen in Fig. 6.17 most SECMs can stabilise the GFM converters at the time of current limitation at $t \approx 30\,\mathrm{s}$, except for the VSM and SECM-3. Although SECM-3 and SECM-4 result in higher load voltages after current limitation (compared to SECM-1 and SECM-2), the power system voltages collapse fastest for all GFM controls (around $t \approx 60\,\mathrm{s}$ for SECM-3 and $t \approx 70\,\mathrm{s}$ for SECM-4). In the case of SECM-2, at the time of the current limitation, a chattering of the GFM voltage $\underline{v}_{\mathrm{G}}$ around the SECM-2 activation threshold of 0.9 pu occurs. The chattering stops after three additional tap changes, resulting in a voltage magnitude below the threshold. The chattering phenomenon can be explained by the dynamic phenomenon of hybrid systems described in Section 3.3.1. There is a sliding of the voltage

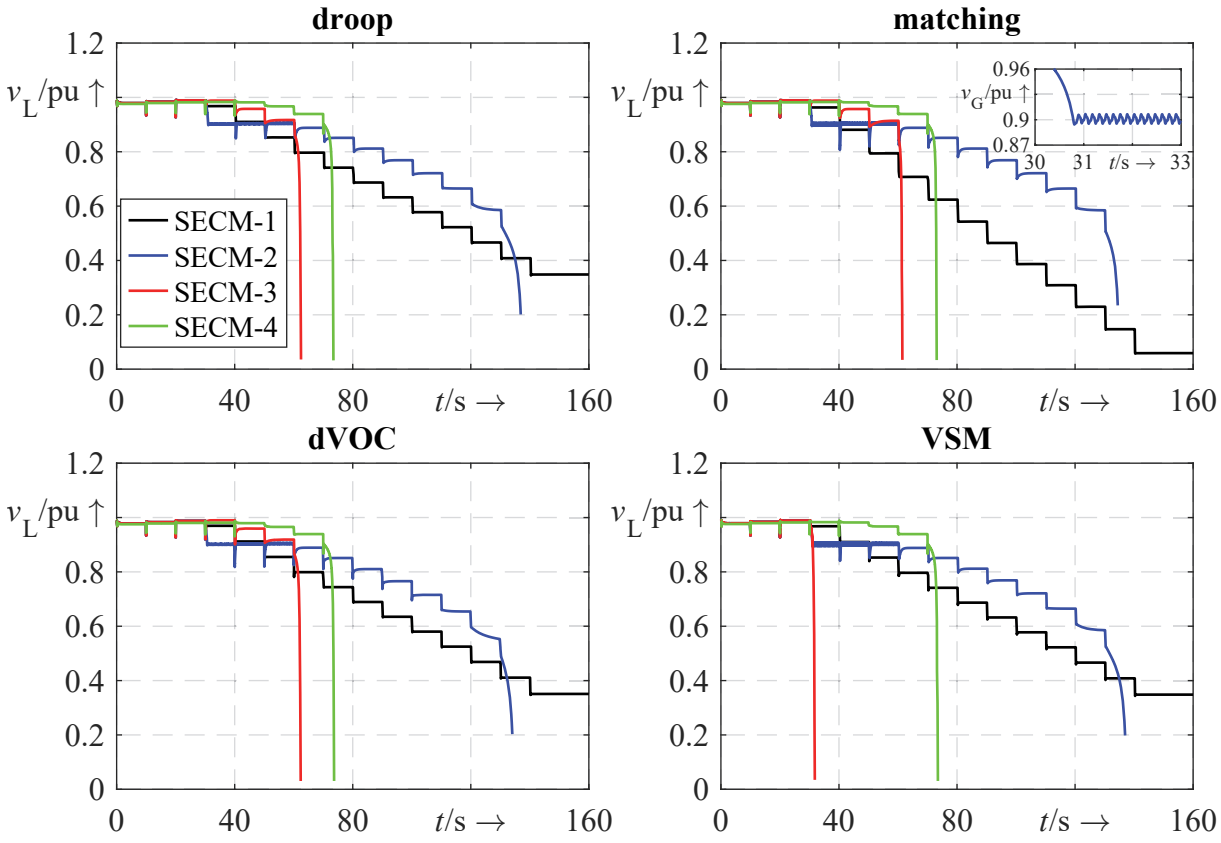

Figure 6.17: Comparison of load voltage trajectories for different GFM control approaches as well as different SECMs

trajectory along the activation threshold, where the vector fields of both subsystems point to the switching surface. The reason for this is that the system becomes unstable after current limitation and the voltage $\underline{v}_{\mathrm{G}}$ drops. But when the voltage $\underline{v}_{\mathrm{G}}$ reaches the threshold, SECM-2 is activated, stabilising the system and raising the voltage above 0.9 pu. However, this deactivates SECM-2 and the whole process starts again. Compared to SECM-3 and SECM-4, SECM-2 can stabilise the system for a longer period but also results in a voltage collapse around $t \approx 136\,\mathrm{s}$ for all GFM controls. In contrast, the proposed SECM-1 stabilises the converters for the entire simulation, even at extremely low voltages, until the OLTC has reached its final tap position. However, the voltage decreases more with each tap change during current limitation. It should be noted that the main function of a SECM is to keep the converter stable. It is not designed to compensate for other destabilising actions, such as the continuous tap changes of the OLTC.

In summary, the simulation results show that the SECM-1 can stabilise the converter also in the long term for all considered GFM control approaches. In contrast, the other SECMs lead to higher voltages and initially keep the converter stable, but ultimately leads to a voltage collapse.

iii) Trajectory sensitivity analysis of selected GFM control parameters

The next step is to perform a trajectory sensitivity analysis for a phasor droop converter with SECM-1. The resulting approximate voltage and power trajectories are shown in Fig. 6.18. Here only the approximate trajectories are shown where the sensitivities have a significant impact on the trajectory for a parameter change of at least 100 %, which is only the case for k_{d} and i_{cmax}. This shows that only a few parameters can influence the converter dynamics, especially during current limitation and SECM-1 activation. Note that the approximate trajectory for i_{cmax} is only done for a positive parameter change of 5 %, due to its high sensitivity. For k_{d} a parameter change of 100 % is assumed. As the results show, both positive parameter changes can increase the voltage, but increasing the maximum converter current has the highest sensitivity. Interestingly, although increasing the droop parameter k_{d} does not change the maximum power of the converter, it can increase the active and reactive power output.

iv) Comparison of approximated and perturbed trajectories

To verify this statement, a new simulation is performed with $k_{\mathrm{d}} = 2\pi\,\mathrm{pu}$, labelled *perturbed* as the parameter change can be interpreted as a perturbation. As the results from Fig. 6.19 demonstrate, the higher droop parameter can increase the active and reactive power output

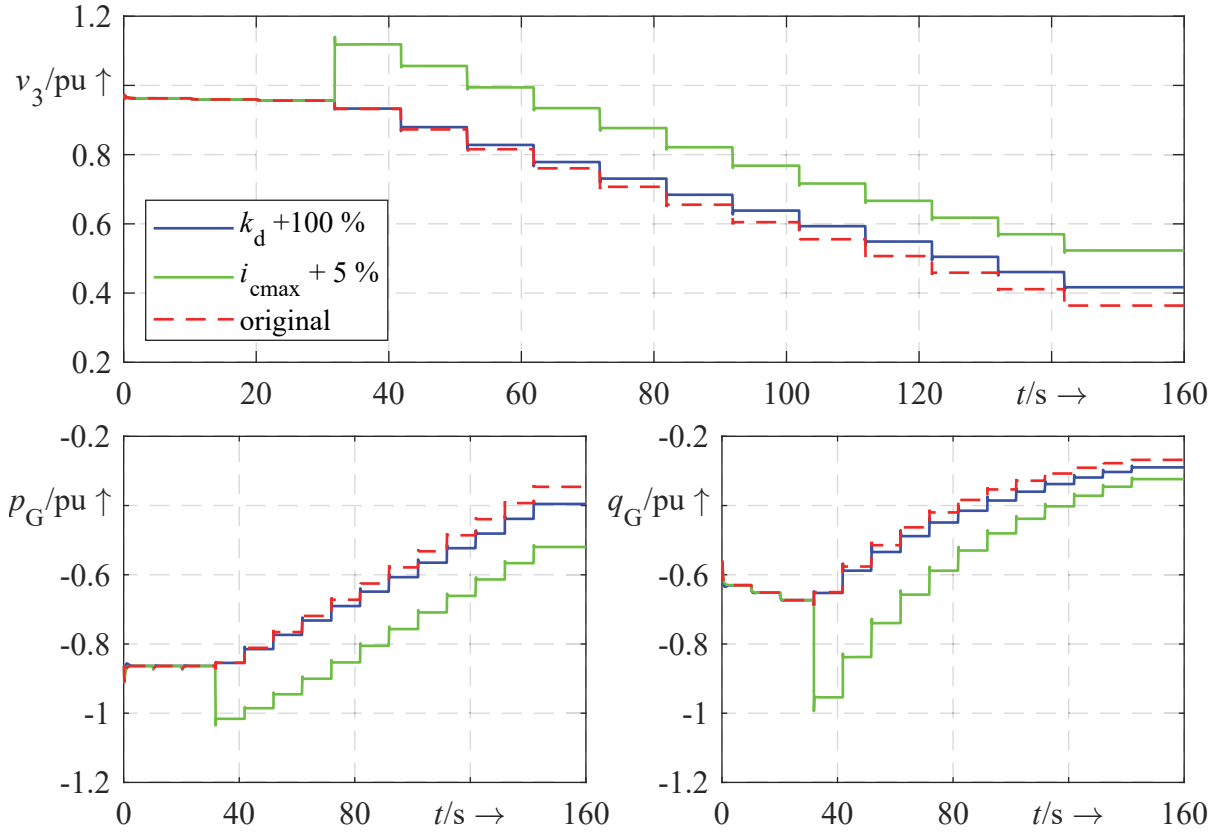

Figure 6.18: Approximated and original voltage and power trajectories of a droop converter with SECM-1 using the trajectory sensitivities of k_d and i_{cmax}

and hence the voltage. It is assumed that the higher droop parameter will result in a more beneficial power factor of the converter power injection, i.e. supporting the grid voltage more. It has already been shown in Section 6.3.1 that a complete prioritisation of active or reactive power is not beneficial in this grid. Therefore, a minimum proportion of active and reactive power is required. This result shows that trajectory sensitivity analysis can reveal such hidden optimisation potential.

Overall, the results of this section indicate that, on the one hand, EMT and phasor GFM models lead to approximately the same voltage dynamics. On the other hand, instability can occur when the converter reaches its current limit without additional control. It has been shown that the SECM-1 can protect the system from voltage collapse, but not from unsafe voltages as its main task is to stabilise the converter. The trajectory sensitivity analysis also showed that only two parameters of the GFM converter can significantly influence its long-term dynamics, whereby the maximum current is usually fixed. Furthermore, these sensitivities demonstrate that an increase in the droop parameter leads to a more beneficial power output of the converter, which can slightly increase the grid voltage.

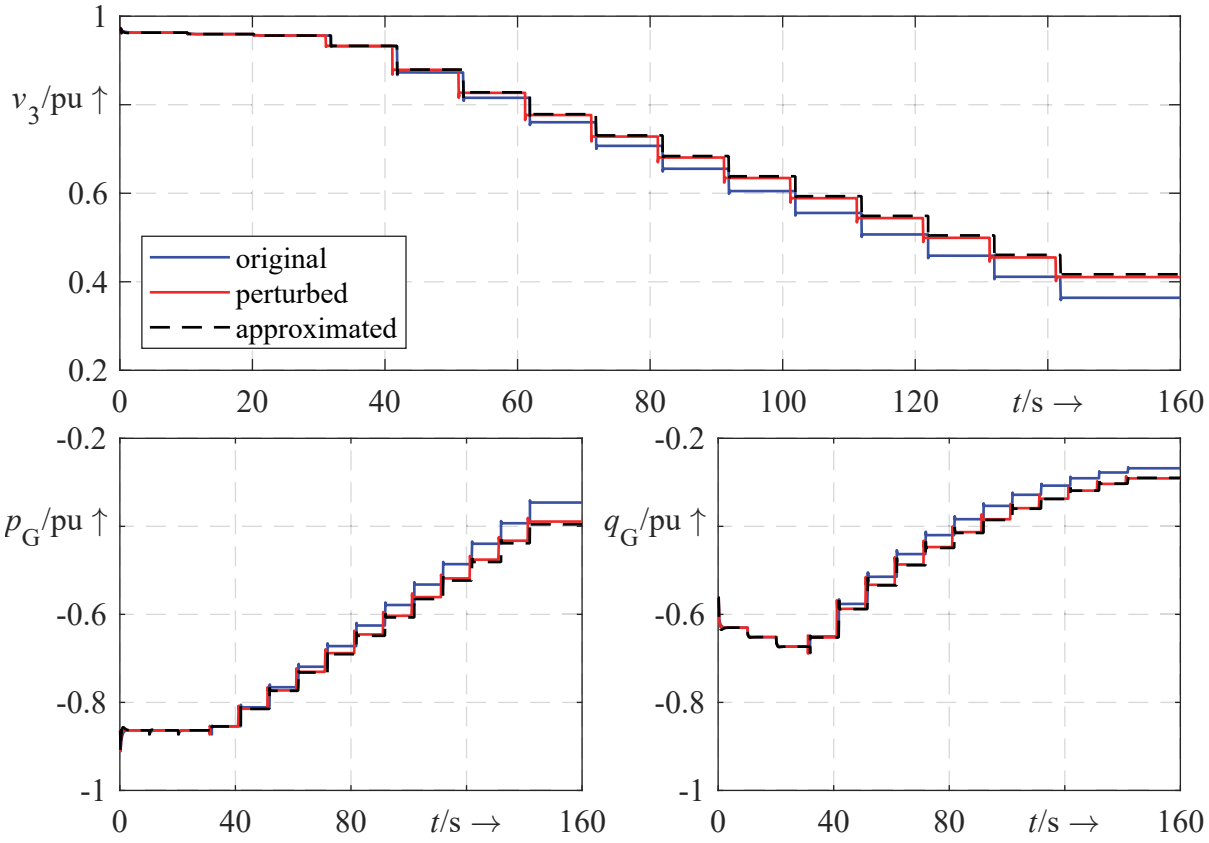

Figure 6.19: Comparison of the approximated voltage and power trajectories (k_d + 100 %) with the original and perturbed trajectories

6.4.2 Impact of power electronic loads

The measurement and simulation results in the previous chapter showed that power electronic loads do not consume constant active and reactive power during large disturbances. After such events, power consumption quickly returns to its original level. However, it is not clear how the different power electronic loads affect the long-term voltage stability.

i) Comparison of voltage trajectories between EMT and phasor load model

The comparison of the long-term voltage dynamics between the EMT and the phasor model is illustrated in Fig. 6.20. Since both systems are short-term stable (see Section 6.3.2), at $t = 0.1$ s a short circuit occurs with a fault impedance of $\underline{Z}_f = 20 + j20\,\Omega$ and a duration of 100 ms. As the results show, the voltages after fault clearance are lower for the EMT than for the phasor model. This is because the reactive power of the phasor PEL-1a model is capacitive, whereas that of the EMT model is inductive. As a result, the load voltage of the phasor model is within the deadband of the OLTC after the fault and no tap changes occur. In addition, as the excitation current of the synchronous generator remains below

its maximum value, there is no activation of the OEL. Thus the phasor model is stable in the long term. In contrast, the low voltages at the beginning of the EMT simulation lead to several tap changes that increase the load voltage. Due to these tap changes, the excitation current of the synchronous generator increases over time and leads to an activation of the OEL around $t \approx 62\,\mathrm{s}$. This results in an almost immediate voltage collapse of the system due to the lack of reactive power.

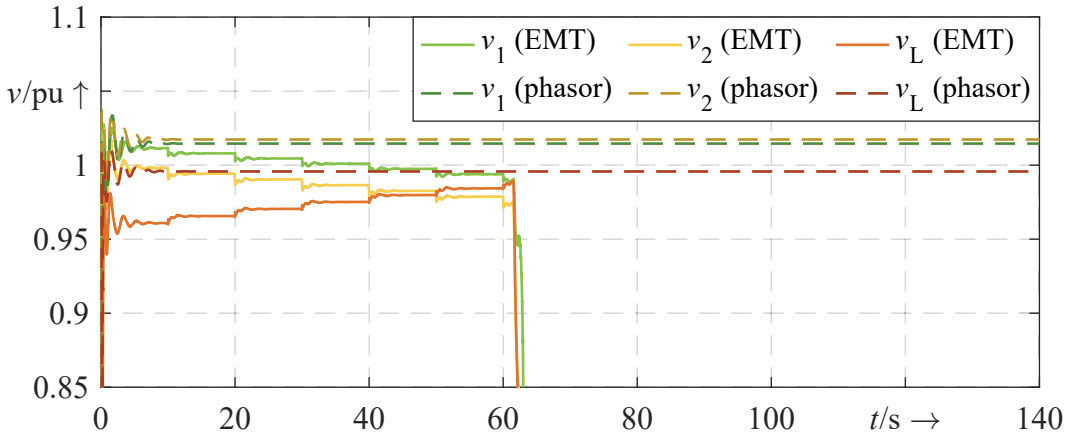

Figure 6.20: Comparison of long-term voltage dynamics between the EMT and phasor ANS model including a synchronous generator and PEL-1a with a load share of 30 % and $\underline{Z}_\mathrm{f} = 20 + j20\,\Omega$

In contrast to the previous sections, an additional comparison is now made to show how the EMT and phasor models perform when the steady-state reactive power of the power electronic load is compensated by the shunt reactance x_shunt. This is done by iteratively determining the steady-state reactive power consumption of PEL-1a at the start of the simulation and compensating for it with an appropriate inductor or capacitor for x_shunt. The simulation result is given in Fig. 6.21. Note that the reactive power q_L in this figure includes the reactive power of the compensation. Due to the compensation, the voltage trajectories of the EMT and phasor models are now much closer. Also, the activation of the OEL at about $t \approx 105\,\mathrm{s}$ now occurs almost at the same time. Greater differences arise after the OEL activation, as the EMT model becomes unstable almost immediately. As the reactive power trajectories show, the phasor load model is more capacitive after OEL activation, which could prevent the system from becoming unstable immediately. Fig. 6.21 also shows the short-term power dynamics to highlight that the reactive power response is very different during the short circuit.

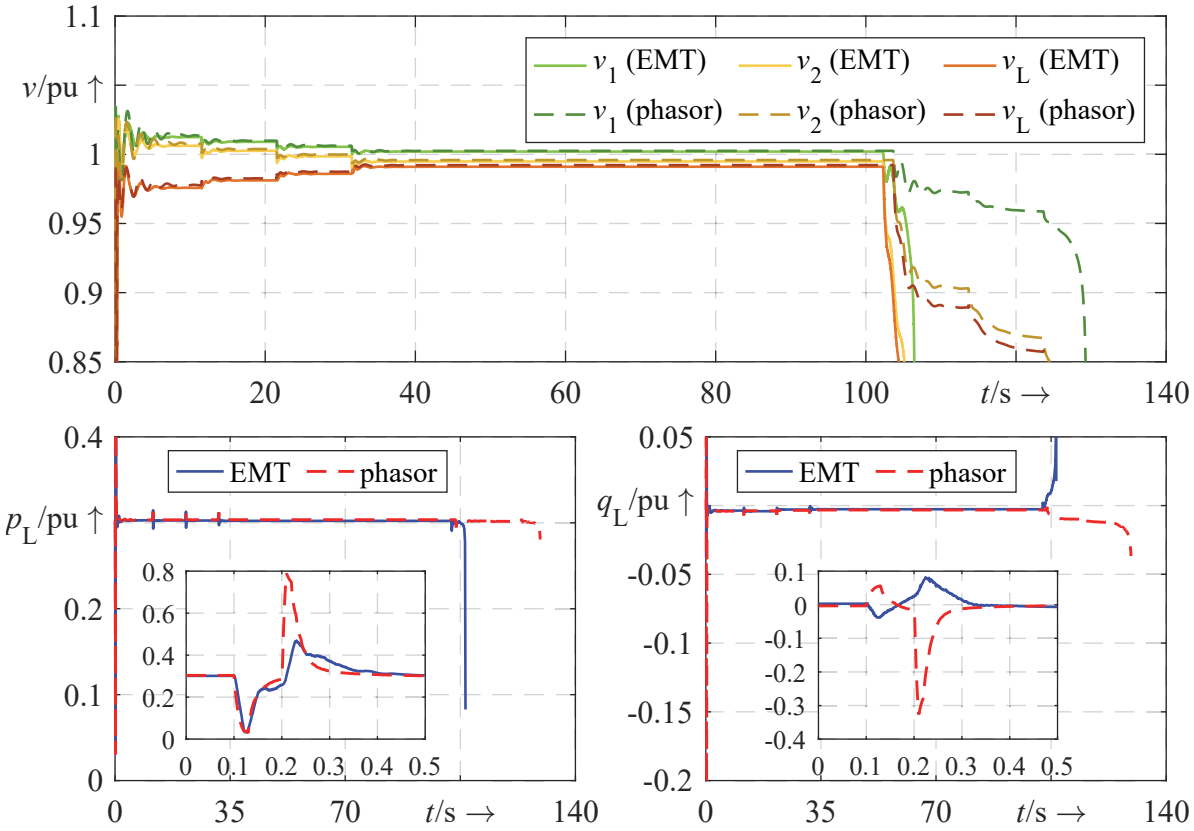

Figure 6.21: Comparison of long-term voltage and power dynamics between the EMT and phasor ANS model including a synchronous generator and PEL-1a with a load share of 30 %, but with compensated reactive power and $\underline{Z}_\mathrm{f} = 20 + j20\,\Omega$

In summary, both simulations demonstrate that the steady-state reactive power consumption of the power electronic load can have a large impact on the voltage evolution and the stability of the system. If the steady-state reactive power of the power electronic load is compensated in the EMT and phasor models, similar voltage trajectories are obtained. This emphasises that the reactive power consumption of the phasor load model does not reflect its EMT equivalent.

ii) Impact of different power electronic loads on long-term stability

In the next scenario, the impact on the long-term voltage stability of PEL-1 to PEL-4 with different load shares is investigated. The simulation results are presented in Fig. 6.22. For comparison, the simulation result without any power electronic load is also shown. The respective evolution of the active and reactive power consumption of the power electronic loads is shown in Fig. 6.23 and 6.24. The results show that increasing the power electronic load from PEL-1 to PEL-3 leads to a faster voltage collapse of the system. For PEL-4, a relatively high share of 30 % or 50 % is actually beneficial for the system, as shown in

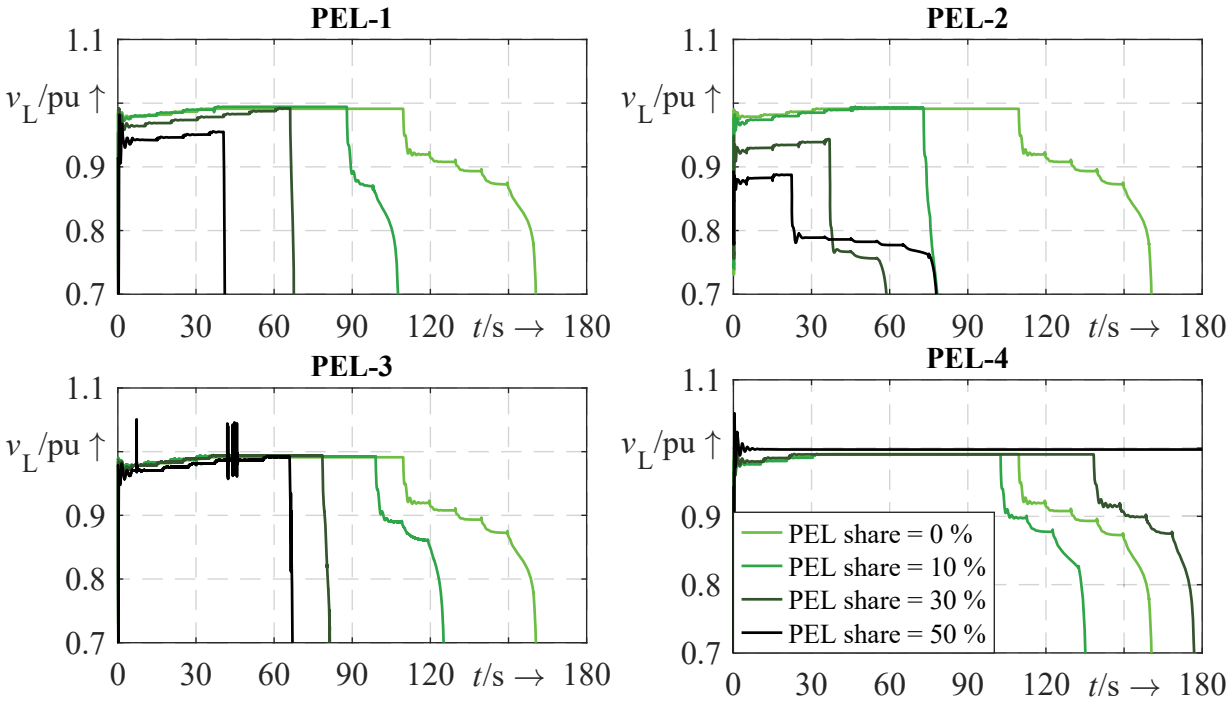

Figure 6.22: Load voltage trajectories of PEL-1 to PEL-4 for different load shares and $\underline{Z}_f = 20 + j20\,\Omega$ to analyse their impact on long-term voltage stability

Fig. 6.24, because its reactive power becomes increasingly capacitive. At a share of 50 % the system is long-term stable as the load voltage is within the deadband of the OLTC and no OEL activation occurs. On the other hand, a ratio of 10 % leads to a faster voltage collapse. As the reactive power consumption in this simulation is close to zero, the overall load is less voltage sensitive compared to the case with no power electronic load. For PEL-3 and a load share of 50 % there are some peaks in the voltage and power trajectories. This can be attributed to the fast switching of the a-PFC in combination with some snubber elements within the power electronic load circuit, resulting in small numerical errors. However, the results clearly show that a higher proportion of PEL-3 leads to a faster voltage collapse of the system. As can be seen from the active power consumed by the power electronic loads, it remains almost constant throughout the simulation (see Fig. 6.23). Only for PEL-2 is there a noticeable decrease in active power consumption. In this case, however, the voltage before collapse is also significantly lower than for the other loads. For reactive power, the long-term evolution is also largely independent of the voltage, but some variation due to the tap changes can be observed. Overall, the active and reactive power curves show that the power electronic loads behave mainly as constant power loads when voltage changes are small and within operational limits. Otherwise, their voltage dependence becomes more pronounced. Since the active power consumption of all loads is approximately the same, the long-term voltage stability is mainly influenced by their steady-state reactive power.

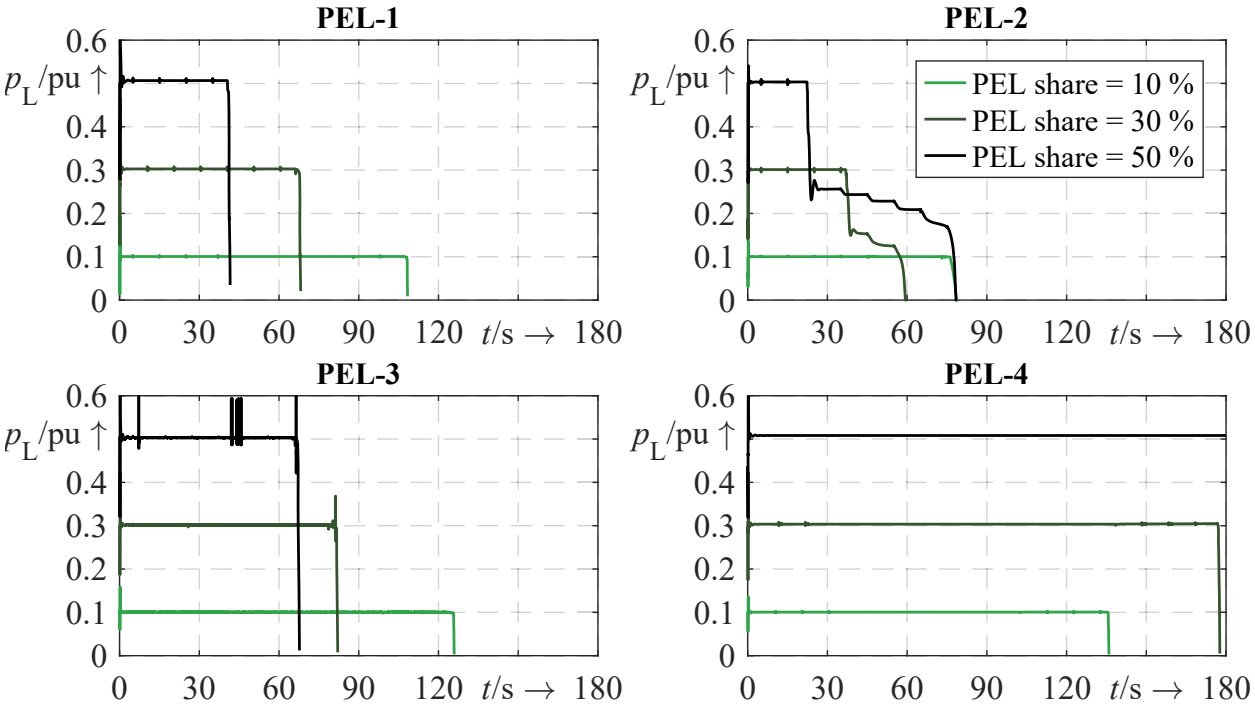

Figure 6.23: Active power trajectories of PEL-1 to PEL-4 for different load shares and $\underline{Z}_f = 20 + j20\,\Omega$ to analyse their impact on long-term voltage stability

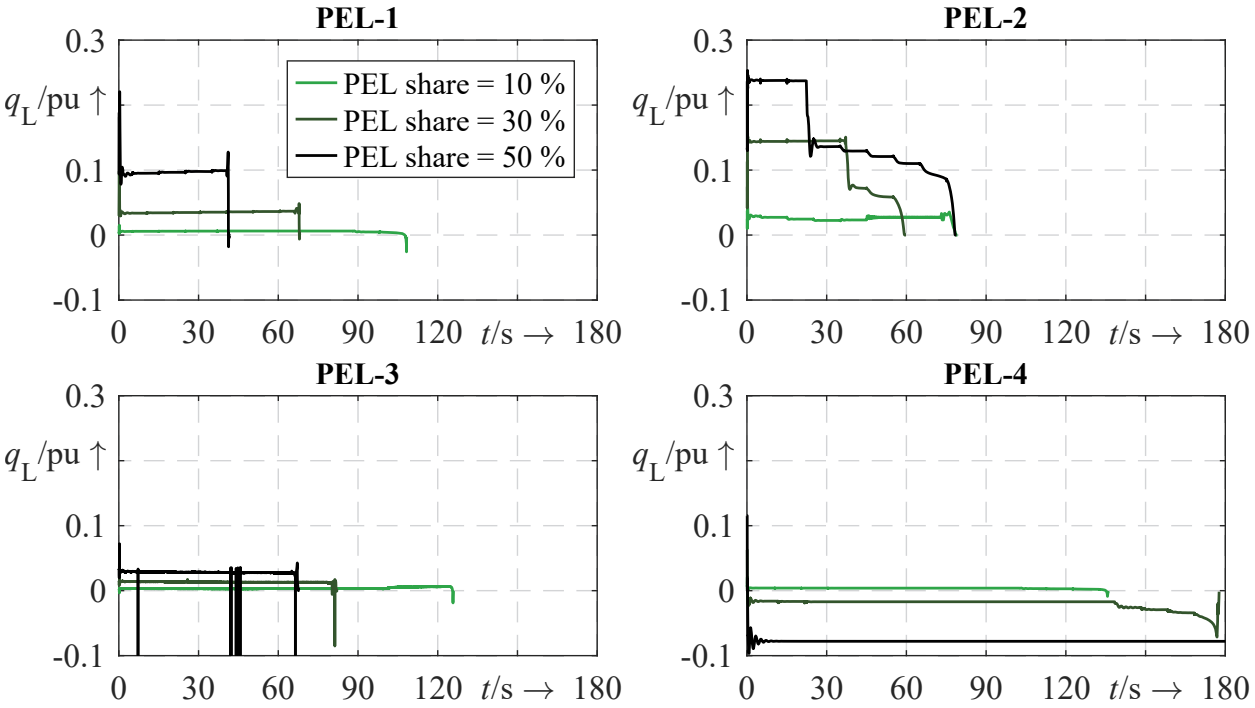

Figure 6.24: Reactive power trajectories of PEL-1 to PEL-4 for different load shares and $\underline{Z}_f = 20 + j20\,\Omega$ to analyse their impact on long-term voltage stability

iii) Trajectory sensitivity analyses of PEL-1a parameters

To calculate the trajectory sensitivities, the simulation results from Fig. 6.21 are taken. As in Section 6.3.2, the parameter sensitivities of the capacitor c_{dc} and the DC active power p_{dc} are used. The approximated trajectories are illustrated in Fig. 6.25. For a positive change in c_{dc} of 100 % it can be seen that the voltage v_3 would decrease due to the lower capacitive reactive power and slightly higher active power. There would also be a steeper voltage drop after activation of the OEL. In contrast, an increase of 50 % in p_{dc} would increase the voltage, although the total active power of the loads would be less voltage sensitive at a steady state. The voltage increase is due to the higher capacitive reactive power of the power electronic load as shown in Fig. 6.25. However, when the OEL is activated, an even steeper voltage drop can be observed compared to c_{dc}, due to the former mentioned voltage insensitive active power.

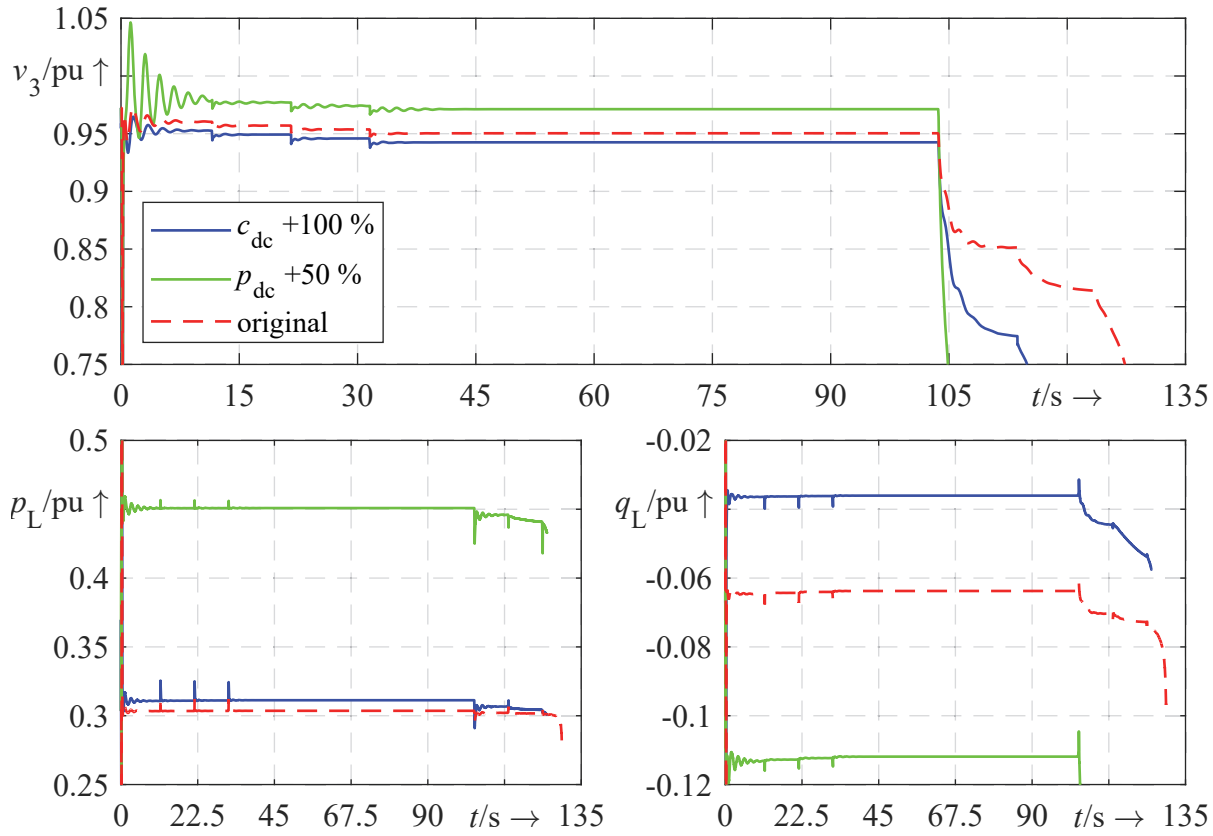

Figure 6.25: Evolution of approximated and original voltage and power trajectories of PEL-1a with a load share of 30 % using the trajectory sensitivities of c_{dc} and p_{dc}

iv) Comparison of approximated and perturbed trajectories

As it is counterintuitive that the voltage increases with an increase in active power, the approximated trajectory is compared with an actual new simulation. To do this, an additional simulation is carried out with $p_{dc} = 0.4\,\text{pu}$ and labelled as *perturbed*. The result is given in Fig. 6.26. For the active and reactive power, the overall agreement between the approximated and perturbed trajectories is quite high until the point of OEL activation. For the perturbed voltage trajectory, however, it can be seen that there is only one additional tap change at the beginning of the simulation and the system reaches a steady-state operating point. This shows that the first-order sensitivities can only approximate the trajectory over a small range. They are unable to detect that the voltage would reach the deadband of the OLTC. However, if an approximate trajectory of the load voltage v_L had been calculated, it would have been possible to see that the OLTC deadband would have been reached at $t = 15\,\text{s}$. It should also be noted that the sensitivities obtained in terms of reactive power should be treated with caution, as the previous simulations have shown that the reactive power of the phasor model may not reflect the reactive power of the EMT model.

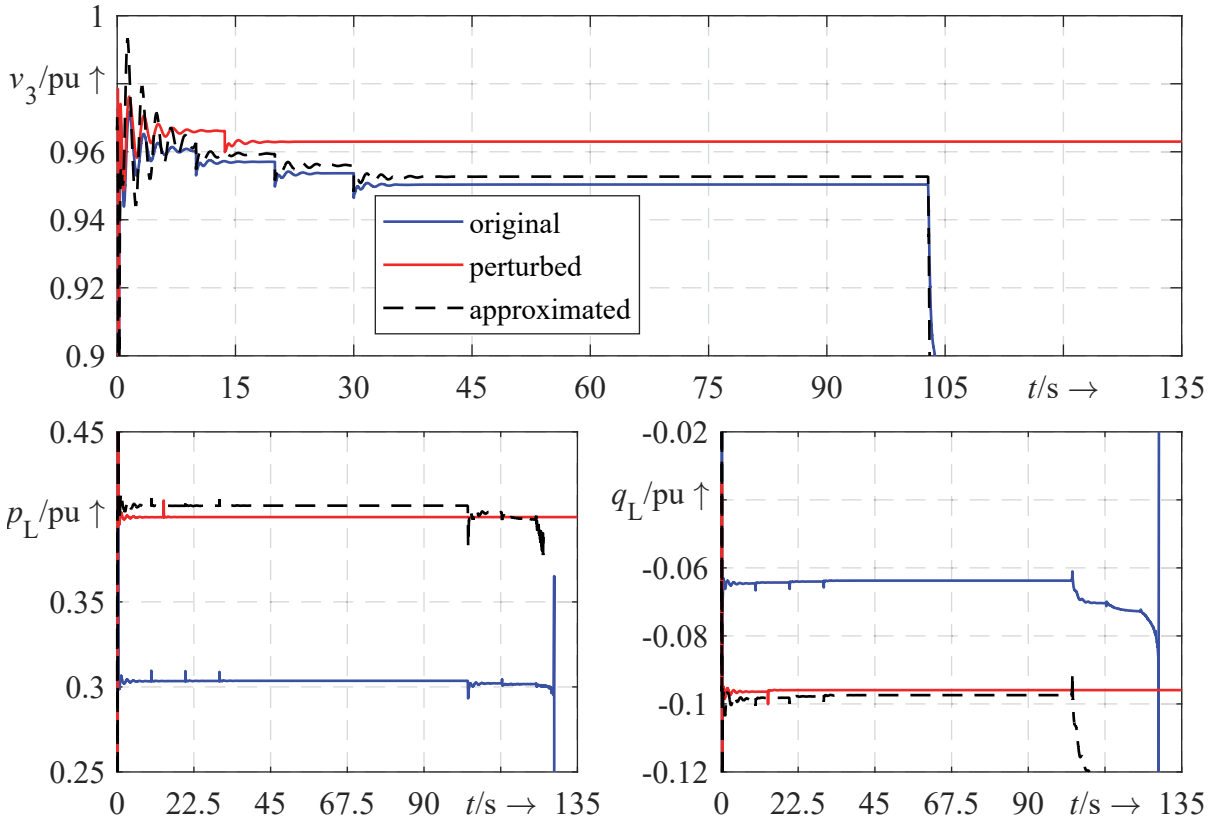

Figure 6.26: Comparison of the approximated voltage and power trajectories with the original and perturbed trajectories (p_{dc} + 33 %)

The simulation results in this section demonstrate that the steady-state reactive power consumption of the power electronic loads has a significant impact on long-term voltage stability. The analysis of the EMT power electronic loads showed that in most cases a higher load share leads to a less long-term voltage stable system. It has been shown that the reactive power of the phasor model does not reflect its EMT counterpart. If the reactive power is compensated, similar results are obtained.

6.4.3 Mutual impact of grid-forming converters and power electronic loads

In this section, the GFM converters and the power electronic loads are included together in the ANS. Their mutual influence on the long-term voltage stability is analysed. First, the impact of PEL-1 to PEL-4 on the long-term voltage dynamics is examined for a load share of 30 %. The results are only shown for the droop converter, as the results for the other GFM controllers are almost identical. Afterwards, the same scenario, but with a load share of 10 % is conducted.

i) Impact of GFM converters and power electronic loads on long-term voltage stability

Next, the impact of PEL-1 to PEL-4 with a load share of 30 % in combination with a droop converter and SECM-1 is investigated. The results are shown in Fig. 6.27. As is known from Section 6.3.3, the system is not stable in the short term in the event of a fault, even for lower power electronic load shares. Therefore, the transmission line trips without a preceding short circuit, which can be interpreted as a false triggering of the respective protection devices. As the results show, the system becomes unstable for PEL-1 and PEL-4 immediately after the line outage. The reason for this is probably that PEL-1 and PEL-4 want to restore their power too quickly after the line outage, forcing the system out of the stable region. However, the SECM-1 is able to stabilise the converter in such a way that there are no unbounded states or zero voltages. In the case of PEL-2, it can be seen that the voltages drop into an unsafe operating region, while in reality, additional countermeasures from protection equipment would be likely. Only for PEL-3, the voltages stay within an acceptable range after the line outage at first. However, the continuous tap changes of the OLTC lead to the current limitation of the converter at $t \approx 43\,\mathrm{s}$, which results directly in instability. Looking at the active power consumption, only PEL-3 is able to keep its active power at its rated value at first. One reason for the stability of the system in the case of PEL-3 is probably its very low reactive power consumption at the beginning of the simulation.

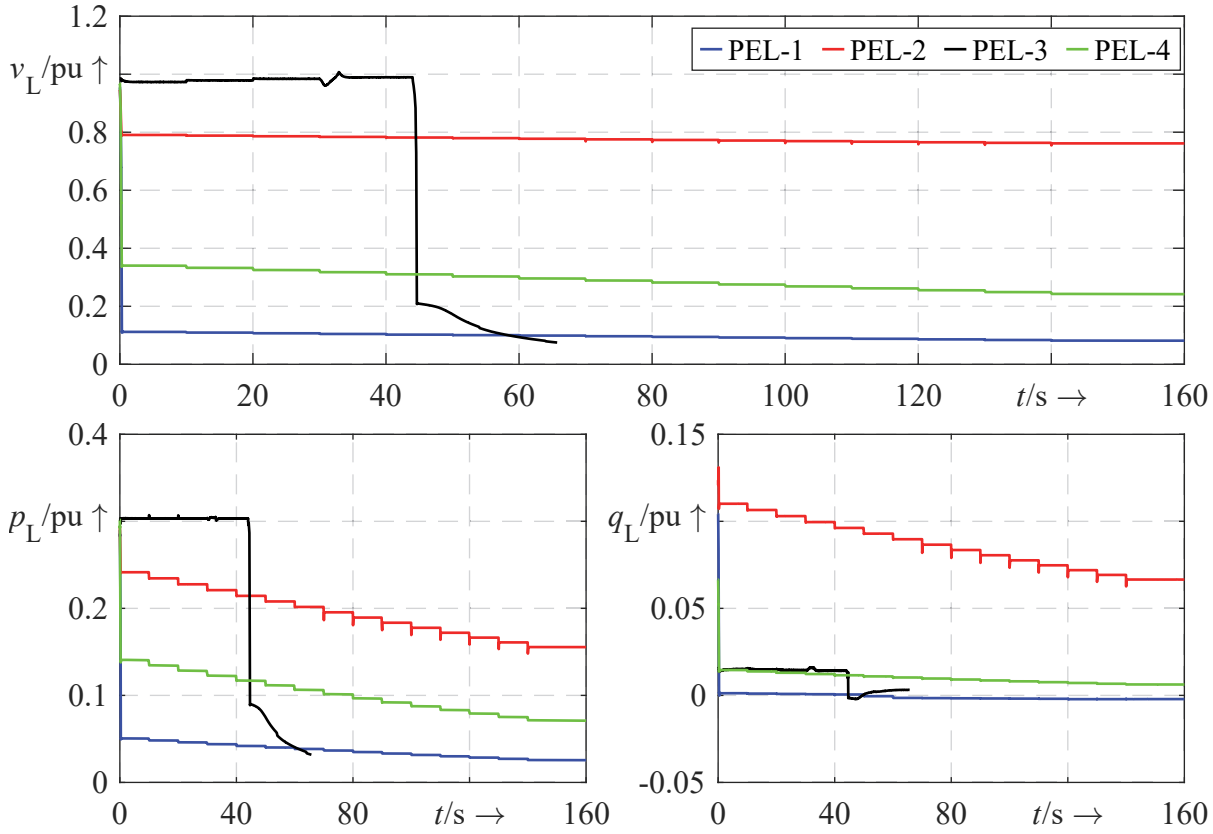

Figure 6.27: Load voltage and power trajectories of PEL-1 to PEL-4 with a load share of 30 % and a droop converter with SECM-1 to analyse their impact on long-term voltage stability

For PEL-1 and PEL-4, a drastic drop in their active and reactive power can be observed after the line outage. Although the active and reactive power consumption of PEL-2 is higher compared to all other loads, higher load voltages can be observed. This shows that the system has not yet reached the unstable region (lower part of the $P(V)$-curve).

In the next scenario, the load share of the power electronic loads is reduced to 10 % to relieve the system and thus observe some voltage dynamics before the current limitation of the GFM converters. By this, the differences regarding the GFM control approaches should be highlighted. The results are shown in Fig. 6.28. In general, it can be observed that PEL-2 does not lead immediately to a current limiting mode for all GFM controllers, but after approximately 35 s. For PEL-4 there are differences in the time for current limiting and therefore instability. For the matching and dVOC controls, the system becomes unstable immediately after the line outage. In the case of the droop and VSM control, the current limit is reached $t \approx 55$ s, but also leads to unsafe voltages. For PEL-1, a small delay until the current limitation can also be observed for the droop and VSM control, but this is negligible compared to the other power electronic loads. Only PEL-3 is stable for all

GFM controls, due to its initial low reactive power consumption. In general, the results show that the voltage drops at most when the current limit is reached. Although there are some differences between the GFM control approaches regarding the time at which the current limit is reached, their voltage dynamics up to that point are very similar. After the current limitation, there are no major differences as the dynamics are mainly determined by SECM-1. In summary, the results indicate that the time of current limitation is delayed due to the lower power electronic load share, but the voltage dynamics thereafter are very similar to the scenario before and are not greatly influenced by the GFM control approach (see Fig. 6.27).

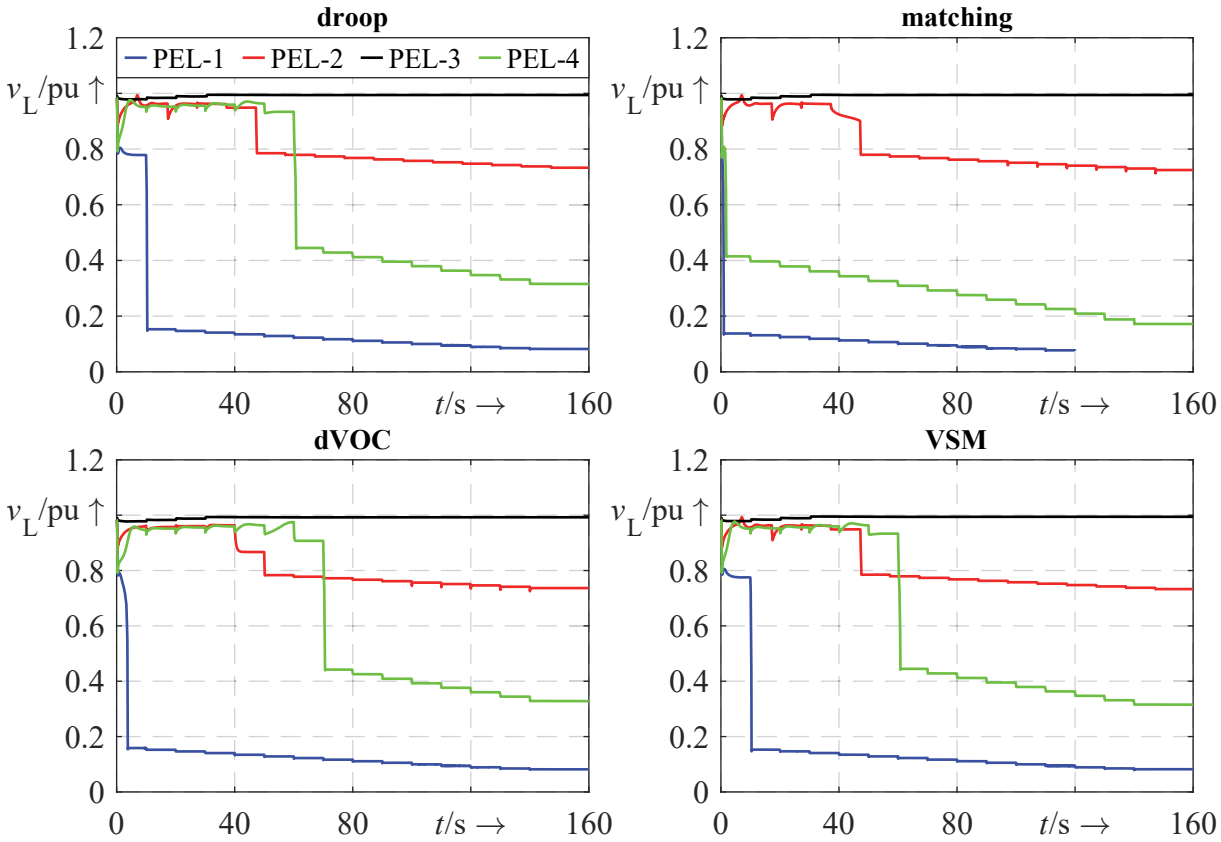

Figure 6.28: Load voltage trajectories of PEL-1 to PEL-4 with a load share of 10 % and four GFM converters with SECM-1 to analyse their impact on long-term voltage stability

Overall, the analyses of the long-term voltage stability for GFM converters and power electronic loads show that, even for small voltage changes, the current limitation dominates the stability of the system. Depending on the specific power electronic load, the current limit is reached quite quickly after some OLTC tap changes within the ANS, even for smaller

load shares. The SECM-1 is able to keep the GFM converters in a stabilised state, although it cannot prevent the system from entering unsafe operating regions. There are also no significant differences between the GFM control approaches, as the voltage dynamics before current limitation are small and are mainly determined by the SECM-1 afterwards.

6.4.4 Summary and conclusion

The previous sections have examined the impact of GFM converters and power electronic loads on long-term voltage stability. The focus has been on how these power electronic components react to slower voltage dynamics such as OLTC tap changes or OEL activations of synchronous generators.

The comparison between the EMT and phasor models of the GFM converter showed that there are no major deviations and the models have the main voltage dynamics, similar to the results in the short term. In contrast, the PEL-1a models again showed large differences between the EMT and phasor models. The main reason for this is the steady-state reactive power consumption, which is capacitive for the phasor and inductive for the EMT model. It can therefore be concluded that the phasor load model does not reflect the true reactive power response. In order to further investigate the similarities and differences between these two models, the initial steady-state reactive power consumption is compensated to obtain only their power transients and operating point shifts during the simulation. As a result, similar voltage trajectories are obtained, highlighting that the main differences are in reactive rather than active power. However, the simulations with compensated reactive power should only highlight the origin of the model differences and not reflect the true dynamics. Therefore, it is recommended to use only EMT models for power electronic loads or, if appropriate, only the active power of the phasor model.

When looking at the impact of GFM converters on long-term voltage stability, it can be concluded that induced current limitation by OLTC tap changes can lead to instability. The reason for this is that the converter cannot find a stable equilibrium because it cannot inject its power setpoint, and so its internal angle increases continuously, leading to a loss of synchronism. However, if a SECM is used, the initial instability at the time of current limitation can be avoided. Instability can be avoided entirely if SECM-1 is applied, or it can be delayed, where SECM-2 leads to the longest delay (but first chattering at the time of current limitation), followed by SECM-4 and SECM-3. In addition, the specific GFM control approach has only a marginal influence on the stability, as it is mainly determined

by the current limitation mode and thus the SECM. The simulations of the power electronic loads indicated that a higher load share leads to a faster activation of the OEL and thus to instability. However, in the case of PEL-4, a share of 30 % or more is actually beneficial for the grid, as its reactive power is capacitive and thus increases the voltage. At a share of 50 %, the system becomes stable in the long term. This again emphasises that the reactive power consumption of the power electronic load has a decisive influence on voltage stability. The combined simulation of GFM converter and power electronic loads showed that the current limitation of the former is the main driver of instability in such a scenario. This is the case even for small power electronic load shares of around 10 %. This underlines that the combination of current limitation and voltage insensitive loads can severely endanger long-term voltage stability.

To complete the analysis of long-term voltage stability, trajectory sensitivities were calculated for the GFM control and the PEL-1a parameters. Similar to the short circuit sensitivities, the maximum current i_{cmax} has the greatest influence on the voltage trajectory, highlighting its importance. The droop gain k_{d} can also increase the voltage in the long term, which was also confirmed by a new simulation. This shows that the trajectory sensitivity analysis can reveal some optimisation potential regarding the control parameters. However, if a control parameter is changed, the stability of the control loop and its influence on other state variables (e.g. frequency) should also be checked. As k_{d} and i_{cmax} have the highest sensitivity to the voltage, the results also show that the influence of the other control parameters on the voltage is low. One reason for this is that during current limitation and activated SECM-1, some parts of the outer and inner control loops are de facto deactivated. This could change if the sensitivities were not calculated in current limited mode. In the case of PEL-1a, an increase in the DC capacitor c_{dc} results in a lower grid voltage as the capacitive reactive power is reduced. Similarly, an increase in the DC power p_{dc} leads to higher voltages due to higher capacitive reactive power, although more active power is consumed. This shows that the voltage sensitivity of p_{dc} changes between the short and long term. However, as already mentioned, the sensitivities of the PEL-1a phasor model should be treated with caution and checked with its EMT equivalent.

7 Summary, conclusion and outlook

In the following chapter, a brief summary of the present thesis is given in Section 7.1. Furthermore, in Section 7.2 the results and findings obtained are summarised and reviewed based on the research questions and assumptions made. The chapter closes in Section 7.3 with an outlook of potential further research.

7.1 Summary

In the past, dynamic voltage stability assessment was mainly motivated by the interactions between conventional synchronous generators and OLTC at the transmission level and loads at the distribution level, such as directly connected induction motors. However, today's power systems are changing with the decommissioning of these generators and the installation of large HVDC converters, to transfer energy to remote load centres and to provide ancillary services such as virtual inertia, e.g. through GFM control. In addition, the load composition is changing due to a rapidly growing number of power electronic loads such as SMPS of consumer electronics, LEDs, charging stations for electric vehicles or variable speed induction motors. This leads to new dynamics in the power system and can endanger voltage stability. Therefore, the main research question within this thesis is how GFM converters and power electronic loads change voltage stability, either in the short or long term. To achieve this, Chapter 2 has reviewed voltage stability assessment methods that focus on power electronics-dominated power systems. The theory of voltage stability was also described and the current practice of power system modelling for voltage stability analysis was highlighted. In this context, it has been shown that the power electronic devices contain discrete dynamics, e.g. current limitation in the case of GFM converters or disconnection and fast power restoration during short circuits for power electronic loads. This motivated this work to orient the theoretical basis towards the theory of hybrid systems.

This has raised the question of the extent to which the theory of hybrid systems can support the modelling and analysis of voltage stability. Therefore, in Chapter 3, the applications of hybrid system theory to power systems in the current literature were first reviewed. Based on this, the most common formal modelling approaches for hybrid systems were described, including their unique hybrid dynamical phenomena. Emphasis has been placed on their

stability theory, which is fundamentally different from that of purely continuous systems. Moreover, the method of trajectory sensitivity for the analysis of non-linear power system models with such discontinuities was presented. However, this led to the next research question, which specific continuous and discrete dynamics are required for an accurate description of GFM converters and power electronic loads.

To answer this question, several state-of-the-art GFM control approaches were described in Chapter 4. One focus was the modelling of current limitation and how the converter can be stabilised in such a situation by applying SECMs. In this context, a self-developed parameter-free SECM (referred to as SECM-1) was presented, and it was mathematically shown that it can reach a stable equilibrium during current limitation for almost all GFM control approaches and dq-axis prioritisation. Finally, using the example of droop control and SECM-1, it was shown that only two discrete states and four switching conditions and reset events are required to model the GFM converter as a hybrid system.

For the power electronic loads, their general structure and power response to voltage drops were first shown in Chapter 5. An analytical phasor load model was then derived, as nothing comparable was found in the literature and used for later simulations. In addition, the power response of real power electronic loads was measured in the laboratory to derive accurate models for the EMT simulations. The chapter concluded how the phasor load model can be modelled through hybrid system theory by deriving the necessary discrete states as well as switching conditions and reset events. It was shown that the phasor power electronic load consists of five discrete states and that its events are mainly oriented to the evolution of a time-domain simulation.

Based on the models and findings from the previous chapters, comprehensive simulations were then carried out in Chapter 6 to analyse short- and long-term voltage stability. For this purpose, the ANS was first derived on the basis of the Nordic test system. It has been demonstrated that the ANS captures the main voltage dynamics of the Nordic test system, but due to its aggregated nature, it is much more computationally efficient to perform long EMT simulations with small step sizes and large sampling studies. Furthermore, within the ANS it is more convenient to replace the conventional generation or load with power electronic devices, which allows to achieve a high dominance of power electronics. In the next step, an overview of the scenario setup was given. It was determined that the short-term voltage stability is investigated before its long-term counterpart, as this also reflects the evolution after a disturbance. Also, the impact of GFM converters and power electronic loads on voltage stability was first examined separately before being combined. The focus

of the short-term voltage stability analysis was on large disturbances such as short circuits. In contrast, the long-term voltage stability analysis focused on the interaction between the power electronic devices and slower voltage dynamics such as OLTC tap changes and OEL activation. However, both stability analyses also included the impact of the current limitation of GFM converters as well as the stabilising effect of SECM. In addition, the disconnection and subsequent fast power restoration of the different power electronic loads in case of voltage fluctuations were investigated. Along with the simulations, the EMT and phasor models of the power electronic devices were compared and differences were highlighted. Finally, the analyses were complemented by trajectory sensitivity calculations to determine how a change in model or control parameters would influence the voltage evolution. This enabled the identification of the key parameters affecting voltage stability, which in turn enabled the final research question to be answered.

7.2 Conclusion

In the following, the main conclusions are outlined based on the results achieved within this thesis. This is done by summarising the key messages for each research question. In addition, the assumptions made within this thesis are discussed in order to better contextualise the results obtained.

1. How do grid-forming converters and power electronic loads influence short- and long-term voltage stability and associated dynamics?

In the case of GFM converters, the simulation results clearly demonstrate that the current limitation can quickly lead to instability both for short- and long-term voltage stability. The reason for this is that the converter tries to reach an active power setpoint, which is not possible due to the limited current. As a result, its internal transformation angle is continuously increased and the converter is no longer synchronised with the grid. To counteract this, SECMs have been introduced and have been shown to stabilise the converter in the short and long term. There were differences between the approaches, but the proposed SECM-1 showed the most stabilising effect. However, the dynamic response of all SECMs should be carefully evaluated in the case of other disturbances to analyse which SECMs is most suitable. Furthermore, no major differences between the GFM control approaches were found, as voltage (in-)stability in this thesis was mainly determined by the current limiting mode and the SECM applied. However, this could change if the converter is not

in a current limited mode, e.g. in case of small-signal stability. In addition, no detailed parameter study of the GFM control approaches was carried out, so potential differences could arise for other parameters.

The stability analysis of power electronic loads revealed that in general, a higher share of these loads destabilises the system, due to its less voltage-sensitive active power consumption. The main influence on short-term stability is the quasi-disconnection and the resulting reduced power consumption, which stabilises the system. However, their possible power recovery during the fault may cancel the previous relief and destabilise the system. It is therefore highly dependent on the voltage value at which the load disconnects and whether and how quickly it recovers its power. For the loads analysed in this work, these characteristics were highly dependent on the PFC technology. For long-term voltage stability, the steady-state reactive power consumption was identified as a key factor. In this context, structural changes (e.g. line outage) in the power system strongly affect the reactive power and can also change its sign. For example, the reactive power of PEL-4 changed from inductive to capacitive after the line outage, thus supporting the grid.

The combined simulation of GFM converters and power electronic loads reveals that the simultaneous occurrence of current limitation and fast load recovery can be a serious threat to short- and long-term voltage stability. Although the SECM-1 can stabilise the converter in such a case, it cannot protect the system from unsafe voltages. All in all, it can be concluded that the short-circuit power of a grid that is dominated by power electronic devices is one of the central quantities for ensuring stability.

2. How can hybrid system theory extend the modelling of dynamic power systems and support the assessment of voltage stability?

In general, hybrid system theory is needed to accurately model power systems with discontinuities, discrete dynamics and events. Otherwise, vital aspects would be missed for a proper stability analysis. This applies not only to voltage stability but to all types of stability. In particular, it should be considered as the modelling standard for large-signal stability assessment, as many models include discrete dynamics, e.g. limitations. The choice of the formal modelling approach depends on the discrete dynamics of the model. For this thesis, the DADS provided a sufficient modelling approach, which is based on the theory of switched systems. For more general modelling approaches, including jump phenomena of continuous states, the hybrid automata and the DAIS approach are promising. In general, all hybrid system modelling approaches can produce various hybrid dynamical phenomena that would otherwise not be observed in continuous systems. However, these

hybrid dynamic phenomena are highly dependent on the modelling approach and how the model is implemented in a simulation programme. Therefore, their appearance may simply be a modelling artefact. Nevertheless, it can indicate some problems that may occur in a real application.

The stability theory of hybrid systems shows that in the case of switched, non-linear DAE systems, formal stability analysis is extremely challenging. However, this is often the case when detailed power system models are used. Therefore, time-domain simulations with sampling studies are often required to explore the stability region of such models. In addition, other methods, such as reachability analysis or composition of hybrid automata, provide insight only up to a certain level of modelling, as they become challenging when dealing with large and complex systems. A promising method that supports the time-domain approach is trajectory sensitivity analysis. Here the sensitivity of the model parameters to the evolution of the states can be evaluated and approximated trajectories can be calculated. This can help to reduce the number of simulations as they can be calculated efficiently along the simulation, especially with automatic differentiation techniques. However, as the sensitivities are only a first-order approximation, they are only meaningful for small parameter changes. In [159] second-order sensitivities have been introduced, but these come at a higher computational cost.

In summary, hybrid system theory is necessary for accurate modelling of dynamic power systems, especially for large disturbances. It can help to understand how the continuous and discrete states interact. In addition, its specific implementation in a simulation programme is not trivial, which ultimately determines the dynamics. As the discrete dynamics increase the complexity of the system, their formal stability analysis is also more challenging and often not possible for detailed systems. However, some methods, such as trajectory sensitivity, support time-domain analysis even for detailed and complex systems.

3. How should grid-forming converters and power electronic loads be modelled and what are their main continuous and discrete dynamics?

For GFM converters it has been observed that current limitation and SECM are their main discrete dynamics. This requires only two discrete states if they are used efficiently. This is done by activating and deactivating parts of the equations. This also has additional advantages for the numerical solver. The continuous dynamics are mainly determined by the outer power synchronisation loop and the outer voltage control, as well as the inner voltage and current control, which are all necessary for large-disturbance analysis. The comparison between the EMT and phasor model showed that there are only minor differences and that

mainly the same dynamics occur. Greater differences might have resulted if the average model of the converter had been replaced by detailed power electronic switches. However, as voltage stability is about power balance at the fundamental frequency, it is questionable whether the increased complexity is justified. Therefore, for this thesis, it is concluded that for GFM converters, phasor models are sufficient for voltage stability analysis.

The discrete dynamics of the power electronic loads in this thesis are mainly determined by the uncontrolled bridge rectifier and the quasi-disconnection at low voltages. In the case of EMT models, their continuous dynamics result from the DC capacitor which energises the DC load during faults, as well as other passive devices such as inductances for passive PFC. Their interaction results in complex behaviour during short-circuits, represented by the sequence of disconnection, power recovery and inrush current at voltage recovery. The derived EMT models generally showed sufficient agreement with their laboratory measurements, although there are some deviations. As their modelling was mainly motivated to match the simulated power with the measured fundamental power, their use in harmonic studies should be carefully evaluated. In addition, as most of them represent single-phase loads, they had to be arranged in a Delta connection in order to use them in a three-phase system. Nevertheless, it has been shown that the PFC technique has a decisive influence and should therefore be taken into account when modelling these loads. The comparison between the EMT and phasor model of the power electronic load (here PEL-1a) demonstrated that there are major differences, especially for the reactive power. This is especially true when the load current is influenced by the grid impedance, resulting in non-sinusoidal voltages at the load. This effect was also observed by laboratory measurements. The hybrid system modelling approach of the phasor PEL-1a model showed that the discrete states are used to represent its internal dynamics. The calculated fundamental active and reactive power can be seen as instantaneous values. However, when the power is filtered by a first-order lag system, it was possible to achieve a closer match with the results of the EMT simulations. However, as the results show, for power electronic loads it is clearly recommended to use only EMT models, even for long-term voltage stability investigations.

4. What are the key parameters of grid-forming converters and power electronic loads that affect short- and long-term voltage stability and how could they be designed for a robust integration of these devices?

As previously discussed, the maximum converter current is one of the most important model parameters of GFM converters when analysing voltage stability under large disturbances. However, this parameter is directly related to the physical structure of the converter

and is therefore usually fixed. However, it could be considered at the design stage not only to match the power rating of the converter to the power rating of the energy source but to intentionally select a higher rating in order to improve the stability of the system. The provision of this capacity could then be paid for in the same way as the provision of capacity for frequency stability. In contrast, the trajectory sensitivities also revealed that the droop gain has some potential to increase the voltage in the short and long term. However, if this parameter is tuned, the stability of the control loop and the impact on other system variables such as frequency must be considered. In general, the sensitivity of most GFM control parameters on the voltage is low. The reason for this is that during large disturbances the current limitation mode and SECM-1 are active, which effectively deactivates large parts of the control. This results in a greatly reduced number of control parameters that can affect the voltage during current limitation. In addition, the SECM-1 is designed to have no parameters. Therefore there is no potential for optimisation. However, if another SECM is used, there may be some potential for parameter optimisation. In summary, this means that in case of large disturbances, the maximum converter current, which is a physical parameter, is the main parameter that determines voltage stability. However, there is still some potential for optimising the droop gain. In addition, if a parameter-dependent SECM or other GFM control approach is used, there may be other parameters that are important for voltage stability.

The phasor PEL-1a model was used to calculate the sensitivities for the power electronic load, which has only the DC capacitance and the DC power as parameters. It could be shown that a higher DC capacitance leads to a higher power consumption after the fault, which can delay voltage recovery. Similar to the maximum converter current, the DC power of a load is usually fixed. However, if treated as a parameter, a higher DC power will result in lower voltages during faults due to the increased power consumption. In the case of long-term voltage stability, a higher DC power was advantageous because it also increased the capacitive reactive power. However, it is questionable whether this would be observed in reality, as the results of the PEL-1 EMT model showed that a higher load share leads to a faster voltage collapse. It can also be concluded from the EMT models that the voltage value at which the loads disconnect is one of the most important parameters, although no sensitivities were calculated. In addition, the PFC technique also determines to a large extent the reactive power consumption. In summary, as the design of power electronic loads is usually motivated by harmonic legislation, explicit design recommendations are difficult. The main conclusion is that an early disconnection and a soft power restoration after the fault would greatly support the power system in case of large disturbances.

From a practical point of view, the results and findings of this thesis can be summarised as follows. For large-disturbance analyses of non-linear hybrid systems, the time-domain simulation is still the most suitable method to assess (voltage) stability. In addition, if no protection equipment is modelled, the operational constraints should be used as a stability threshold to stay within the confidence region of the model. As time-domain simulations can be computationally expensive, trajectory sensitivity analysis can help to reduce these costs for large parameter studies. When modelling GFM converters, it is highly recommended to include SECMs to stabilise these converters in case of large disturbances. It can also be concluded that phasor models of GFM converters are still valid in the case of symmetrical conditions. In contrast, when modelling power electronic loads, EMT models are recommended. However, recommending a universal power electronic load model is difficult as there are many different types. A composition of different load types could be a possible solution. If phasor simulations are performed, it may still be valid to use constant power loads for power electronic loads, as these can be interpreted as worst-case loads, especially during short circuits. Alternatively, only the active power part of the PEL-1a load can be modelled to take into account the power drop and its rapid recovery. All in all, it can be concluded that if all these recommendations are taken into account, more realistic results are likely to be obtained when assessing voltage stability in power electronics-dominated grids.

7.3 Outlook

The presented models and simulation results should only be considered as a starting point for analysing the impact of power electronics on short- and long-term voltage stability. Especially for power electronic loads, there is a huge potential to derive better load models by measuring the power response of more and different types. In addition, the derived ANS can be further developed to better incorporate the interactions between different power electronic devices. In the case of GFM converters, the field of SECM offers many research opportunities as the converter needs to be stabilised for a wide variety of disturbances. In particular, the following points have been identified as promising extensions to this work:

– As the generators and loads are aggregated in the ANS, no interactions between those units can be observed. Therefore, these units could either be split in parallel or distributed at each voltage level to analyse potential interactions.

- The impact of the SECMs should be evaluated also for other types of stability and disturbances so that they do not lead to undesirable behaviour in other situations.
- As no parameter variations were carried out for SECM-3 and SECM-4, it should be analysed if their stabilising effect could be increased by parameter optimisation.
- The proposed SECM-1 could also be based on sliding mode control (see e.g. [117]), for a smoother transition between normal operation and current limitation mode. As chattering was observed for SECM-2, sliding mode control could be a good solution to avoid this phenomenon.
- The measured loads represent only a small part of a large amount of different power electronic loads. Therefore other power electronic loads like charging stations or adjustable-speed-drive induction motors should be measured and modelled for stability studies.
- The parameters of the EMT load models were mainly selected to match the measurements. For general model parameters, more loads of these kinds should be measured so that the load models are not too specific.
- The derived EMT load models represent low voltage loads, it should be investigated how they can be aggregated to represent a more general power electronic load that can be used at the transmission system level.
- For the phasor PEL-1a model, the reactive power part could be omitted and only the filtered active power is used. By this, only the active power part of a load would be modelled as a power electronic load, which can be sufficient in some situations. In general, more research should be done to incorporate the dynamics of power electronic loads into phasor simulations, as they are normally more computationally efficient.
- Since only the phasor model was explicitly modelled as a DADS, the EMT load models should also be modelled in this way to analyse their hybrid system properties.

Bibliography

[1] T. Cutsem and C. Vournas, *Voltage Stability of Electric Power Systems*. Springer New York, NY, March 1998, ISBN: 978-0-7923-8139-6. DOI: 10.1007/978-0-387-75536-6.

[2] I. Dobson and H. D. Chiang, 'Towards a theory of voltage collapse in electric power systems,' *Systems and Control Letters*, vol. 13, no. 3, pp. 253–262, 1989, ISSN: 01676911. DOI: 10.1016/0167-6911(89)90072-8.

[3] X. Wang, M. G. Taul, H. Wu, Y. Liao, F. Blaabjerg and L. Harnefors, 'Grid-synchronization stability of converter-based resources—an overview,' *IEEE Open Journal of Industry Applications*, vol. 1, pp. 115–134, 2020. DOI: 10.1109/OJIA.2020.3020392.

[4] M. H. Roos, P. H. Nguyen, J. Morren and J. G. Slootweg, 'Modeling and Experimental Validation of Power Electronic Loads and DERs for Microgrid Islanding Simulations,' *IEEE Transactions on Power Systems*, vol. 35, no. 3, pp. 2279–2288, 2020, ISSN: 15580679. DOI: 10.1109/TPWRS.2019.2953757.

[5] J. Lunze and F. Lamnabhi-Lagarrigue, *Handbook of Hybrid Systems Control*. Cambridge University Press, 2009, ISBN: 9780511807930. DOI: 10.1017/CBO9780511807930.

[6] N. Hatziargyriou, J. Milanovic, C. Rahmann, V. Ajjarapu, C. Canizares, I. Erlich, D. Hill, I. Hiskens, I. Kamwa, B. Pal, P. Pourbeik, J. Sanchez-Gasca, A. Stankovic, T. Van Cutsem, V. Vittal and C. Vournas, 'Definition and classification of power system stability – revisited & extended,' *IEEE Transactions on Power Systems*, vol. 36, no. 4, pp. 3271–3281, 2021. DOI: 10.1109/TPWRS.2020.3041774.

[7] V. A. Lacerda, E. P. Araujo, M. Cheah-Mañe and O. Gomis-Bellmunt, 'Phasor modeling approaches and simulation guidelines of voltage-source converters in grid-integration studies,' *IEEE Access*, vol. 10, pp. 51 826–51 838, 2022. DOI: 10.1109/ACCESS.2022.3174958.

[8] G. De Carne, M. Langwasser, M. Ndreko, R. Bachmann, R. W. De Doncker, R. Dimitrovski, B. J. Mortimer, A. Neufeld, F. Rojas and M. Liserre, 'Which Deepness Class Is Suited for Modeling Power Electronics?: A Guide for Choosing the Right Model for Grid-Integration Studies,' *IEEE Industrial Electronics Magazine*, vol. 13, no. 2, pp. 41–55, 2019, ISSN: 19410115. DOI: 10.1109/MIE.2019.2909799.

[9] K. Praprost and K. Loparo, 'A stability theory for constrained dynamic systems with applications to electric power systems,' *IEEE Transactions on Automatic Control*, vol. 41, no. 11, pp. 1605–1617, 1996. DOI: 10.1109/9.543998.

[10] M. Paolone, T. Gaunt, X. Guillaud, M. Liserre, S. Meliopoulos, A. Monti, T. Van Cutsem, V. Vittal and C. Vournas, 'Fundamentals of power systems modelling in the presence of converter-interfaced generation,' *Electric Power Systems Research*, vol. 189, December 2020, ISSN: 03787796. DOI: 10.1016/j.epsr.2020.106811.

[11] Forum Netztechnik / Netzbetrieb im VDE, *VDE-AR-N 4130 - Technical requirements for the connection and operation of customer installations to the extra high voltage network (TAR extra high voltage)*, November 2018.

[12] P. Kundur, J. Paserba, V. Ajjarapu, G. Andersson, A. Bose, C. Canizares, N. Hatziargyriou, D. Hill, A. Stankovic, C. Taylor, T. Van Cutsem and V. Vittal, 'Definition and classification of power system stability ieee/cigre joint task force on stability terms and definitions,' *IEEE Transactions on Power Systems*, vol. 19, no. 3, pp. 1387–1401, 2004. DOI: 10.1109/TPWRS.2004.825981.

[13] Power System Dynamic Performance Committee, 'Stability definitions and characterization of dynamic behavior in systems with high penetration of power electronic interfaced technologies,' *IEEE PES Technical Report PES-TR77*, April 2020.

[14] C. Vournas, P. Sauer and M. Pai, 'Relationships between voltage and angle stability of power systems,' *International Journal of Electrical Power & Energy Systems*, vol. 18, no. 8, pp. 493–500, November 1996, ISSN: 01420615. DOI: 10.1016/0142-0615(96)00009-9.

[15] Power System Dynamic Performance Committee, 'Voltage stability assessment: Concepts, practices and tools,' *IEEE PES Technical Report PES-TR9*, August 2002.

[16] R. Seydel, *Practical Bifurcation and Stability Analysis* (Interdisciplinary Applied Mathematics). Springer New York, 2010, ISBN: 978-1-4419-1739-3. DOI: 10.1007/978-1-4419-1740-9.

[17] C. Rehtanz, *Einsatz eines SMES zur Verbesserung der Spannungsstabilität Elektrischer Energieübertragungssysteme*, Fortschritt-Berichte VDI / Verein Deutscher Ingenieure Reihe 21 Elektrotechnik. Düsseldorf: VDI-Verlag, 1998, ISBN: 9783183239214.

[18] H.-D. Chiang, I. Dobson, R. Thomas, J. Thorp and L. Fekih-Ahmed, 'On voltage collapse in electric power systems,' *IEEE Transactions on Power Systems*, vol. 5, no. 2, pp. 601–611, May 1990, ISSN: 08858950. DOI: 10.1109/59.54571.

[19] I. Dobson and L. Lu, 'Voltage collapse precipitated by the immediate change in stability when generator reactive power limits are encountered,' *IEEE Transactions on Circuits and Systems I: Fundamental Theory and Applications*, vol. 39, no. 9, pp. 762–766, 1992, ISSN: 10577122. DOI: 10.1109/81.250167.

[20] I. Dobson, 'The irrelevance of electric power system dynamics for the loading margin to voltage collapse and its sensitivities,' *Nonlinear Theory and Its Applications, IEICE*, vol. 2, no. 3, pp. 263–280, 2011, ISSN: 2185-4106. DOI: 10.1587/nolta.2.263.

[21] K. Kim, H. Schattler, V. Venkatasubramanian, J. Zaborszky and P. Hirsch, 'Methods for calculating oscillations in large power systems,' *IEEE Transactions on Power Systems*, vol. 12, no. 4, pp. 1639–1648, 1997, ISSN: 08858950. DOI: 10.1109/59.627870.

[22] W. Zhu, R. Mohler, R. Spee, W. Mittelstadt and D. Maratukulam, 'Hopf bifurcations in a SMIB power system with SSR,' *IEEE Transactions on Power Systems*, vol. 11, no. 3, pp. 1579–1584, 1996, ISSN: 08858950. DOI: 10.1109/59.535700.

[23] I. Dobson, F. Alvarado and C. DeMarco, 'Sensitivity of hopf bifurcations to power system parameters,' in *Proceedings of the 31st IEEE Conference on Decision and Control*, 1992, 2928–2933 vol.3. DOI: 10.1109/CDC.1992.371275.

[24] W. D. Rosehart and C. A. Cañizares, 'Bifurcation analysis of various power system models,' *International Journal of Electrical Power and Energy Systems*, vol. 21, no. 3, pp. 171–182, 1999, ISSN: 01420615. DOI: 10.1016/s0142-0615(98)00037-4.

[25] M. Watanabe, Y. Mitani and K. Tsuji, 'Evaluation of a power system stable region based on Hopf bifurcation theory,' *Electrical Engineering in Japan (English translation of Denki Gakkai Ronbunshi)*, vol. 142, no. 1, pp. 16–24, 2003, ISSN: 04247760. DOI: 10.1002/eej.10104.

[26] V. Ajjarapu and B. Lee, 'Bifurcation theory and its application to nonlinear dynamical phenomena in an electrical power system,' *IEEE Transactions on Power Systems*, vol. 7, no. 1, pp. 424–431, February 1992. DOI: 10.1109/59.141738.

[27] CIGRE C4/C2.58/IEEE Joint Working Group, 'Evaluation of voltage stability assessment methodologies intransmission systems,' *IEEE PES Technical Report PES-TR109*, May 2023.

[28] A. Boričić, J. L. R. Torres and M. Popov, 'Comprehensive Review of Short-Term Voltage Stability Evaluation Methods in Modern Power Systems,' *Energies*, vol. 14, no. 14, p. 4076, Jul. 2021. DOI: 10.3390/en14144076.

[29] Forum Netztechnik / Netzbetrieb im VDE, *VDE-AR-N 4131 -Technical requirements for grid connection of high voltage direct current systems and direct current-connected power park modules (TAR HVDC)*, March 2019.

[30] Forum Netztechnik / Netzbetrieb im VDE, *VDE-AR-N 4120 -Technical requirements for the connection and operation of customer installations to the high voltage network (TAR high voltage)*, November 2018.

[31] Forum Netztechnik / Netzbetrieb im VDE, *VDE-AR-N 4110 -Technical requirements for the connection and operation of customer installations to the medium voltage network (TAR medium voltage)*, Sep. 2023.

[32] North American Electric Reliability Corporation (NERC). 'TPRC-024-3 —Frequency and Voltage Protection Settings for Generating Resources.' (), [Online]. Available: https://www.nerc.com/pa/Stand/Reliability%20Standards/PRC-024-3.pdf (visited on 11th March 2024).

[33] Réseau de Transport d'Electricité, S.A. (RTE). 'Documentation Technique de Référence. Chapitre 8 – Trames types. Article 8.24 – Cahier des charges des capacités constructives pour un système HVDC.' (), [Online]. Available: https://www.services-rte.com/files/live//sites/services-rte/files/documentsLibrary/Article%208.24%20-%20Cahier%20des%20charges%20des%20capacit%C3%A9s%20constructives%20pour%20un%20syst%C3%A8me%20HVDC_fr (visited on 11th March 2024).

[34] National Grid Electricity System Operator. 'The Grid Code.' (October 2022), [Online]. Available: https://www.nationalgrideso.com/document/162271/download (visited on 11th March 2024).

[35] H. Kantz, 'A robust method to estimate the maximal Lyapunov exponent of a time series,' *Physics Letters A*, vol. 185, no. 1, pp. 77–87, 1994, ISSN: 03759601. DOI: 10.1016/0375-9601(94)90991-1.

[36] K. Yoon, D. Choi, S. H. Lee and J. W. Park, 'Optimal Placement Algorithm of Multiple DGs Based on Model-Free Lyapunov Exponent Estimation,' *IEEE Access*, vol. 8, pp. 135 416–135 425, 2020, ISSN: 21693536. DOI: 10.1109/ACCESS.2020.3011162.

[37] A. Wolf, J. B. Swift, H. L. Swinney and J. A. Vastano, 'Determining Lyapunov exponents from a time series,' *Physica D: Nonlinear Phenomena*, vol. 16, no. 3, pp. 285–317, Jul. 1985, ISSN: 01672789. DOI: 10.1016/0167-2789(85)90011-9.

[38] M. T. Rosenstein, J. J. Collins and C. J. De Luca, 'A practical method for calculating largest Lyapunov exponents from small data sets,' *Physica D: Nonlinear Phenomena*, vol. 65, no. 1-2, pp. 117–134, 1993, ISSN: 01672789. DOI: 10.1016/0167-2789(93)90009-P.

[39] G. Datseris and U. Parlitz, *Nonlinear Dynamics* (Undergraduate Lecture Notes in Physics). Springer Cham, 2022, ISBN: 978-3-030-91031-0. DOI: 10.1007/978-3-030-91032-7.

[40] S. Dasgupta, M. Paramasivam, U. Vaidya and V. Ajjarapu, 'Real-time monitoring of short-term voltage stability using PMU data,' *IEEE Transactions on Power Systems*, vol. 28, no. 4, pp. 3702–3711, 2013, ISSN: 08858950. DOI: 10.1109/TPWRS.2013.2258946.

[41] D. P. Wadduwage, C. Q. Wu and U. D. Annakkage, 'Power system transient stability analysis via the concept of Lyapunov Exponents,' *Electric Power Systems Research*, vol. 104, pp. 183–192, 2013, ISSN: 03787796. DOI: 10.1016/j.epsr.2013.06.011.

[42] A. Reddy, K. Ekmen, V. Ajjarapu and U. Vaidya, 'Pmu based real-time short term voltage stability monitoring — analysis and implementation on a real-time test bed,' in *2014 North American Power Symposium (NAPS)*, 2014, pp. 1–6. DOI: 10.1109/NAPS.2014.6965485.

[43] P. Banerjee, S. C. Srivastava and K. N. Srivastava, 'A lyapunov exponent based method for online transient stability assessment,' in *2014 Eighteenth National Power Systems Conference (NPSC)*, 2014, pp. 1–6. DOI: 10.1109/NPSC.2014.7103871.

[44] S. Wildenhues, J. L. Rueda and I. Erlich, 'Optimal Allocation and Sizing of Dynamic Var Sources Using Heuristic Optimization,' *IEEE Transactions on Power Systems*, vol. 30, no. 5, pp. 2538–2546, 2015, ISSN: 08858950. DOI: 10.1109/TPWRS.2014.2361153.

[45] G. Lammert, K. Yamashita, L. D. P. Ospina, H. Renner, S. M. Villanueva, P. Pourbeik, F. E. Ciausiu and M. Braun, 'International industry practice on modelling and dynamic performance of inverter based generation in power system studies,' *CIGRE Science & Engineering*, vol. 8, no. 1, pp. 25–37, 2017, ISSN: 2426-1335.

[46] L. D. P. Ospina and T. Van Cutsem, 'Emergency Support of Transmission Voltages by Active Distribution Networks: A Non-Intrusive Scheme,' *IEEE Transactions on Power Systems*, vol. 36, no. 5, pp. 3887–3896, 2021. DOI: 10.1109/TPWRS.2020.3027949.

[47] P. Aristidou, G. Valverde and T. Van Cutsem, 'Contribution of Distribution Network Control to Voltage Stability: A Case Study,' *IEEE Transactions on Smart Grid*, vol. 8, no. 1, pp. 106–116, January 2017, ISSN: 1949-3053. DOI: 10.1109/TSG.2015.2474815.

[48] L. Robitzky, U. Hager and C. Rehtanz, 'Modelling of Active Distribution Networks and its Impact on the Performance of Emergency Controls,' *2018 Power Systems Computation Conference (PSCC)*, Jun. 2018. DOI: 10.23919/PSCC.2018.8443004.

[49] C. Taylor, *Power System Voltage Stability* (The EPRI Power System Engineering Series). McGraw-Hill Inc., 1994, ISBN: 0070631840.

[50] V. Ajjarapu and C. Christy, 'The continuation power flow: A tool for steady state voltage stability analysis,' *IEEE Transactions on Power Systems*, vol. 7, no. 1, pp. 416–423, 1992, ISSN: 15580679. DOI: 10.1109/59.141737.

[51] N. Yorino, H. Q. Li and H. Sasaki, 'A predictor/corrector scheme for obtaining Q-limit points for power flow studies,' *IEEE Transactions on Power Systems*, vol. 20, no. 1, pp. 130–137, 2005. DOI: 10.1109/TPWRS.2004.831696.

[52] X. P. Zhang, P. Ju and E. Handschin, 'Continuation three-phase power flow: A tool for voltage stability analysis of unbalanced three-phase power systems,' *IEEE Transactions on Power Systems*, vol. 20, no. 3, pp. 1320–1329, 2005. DOI: 10.1109/TPWRS.2005.851950.

[53] J.-P. Heckel and C. Becker, 'Investigation of the voltage stability in the integrated energy system of northern germany,' in *NEIS 2020; Conference on Sustainable Energy Supply and Energy Storage Systems*, Hamburg, Germany, 2020, pp. 1–6.

[54] J. Modarresi, E. Gholipour and A. Khodabakhshian, 'A comprehensive review of the voltage stability indices,' *Renewable and Sustainable Energy Reviews*, vol. 63, 2016. DOI: 10.1016/j.rser.2016.05.010.

[55] M. S. S. Danish, T. Senjyu, S. M. S. Danish, N. R. Sabory, K. Narayanan and P. Mandal, 'A recap of voltage stability indices in the past three decades,' *Energies*, vol. 12, no. 8, 2019. DOI: 10.3390/en12081544.

[56] A. R. R. Matavalam, S. M. H. Rizvi, A. K. Srivastava and V. Ajjarapu, 'Critical Comparative Analysis of Measurement Based Centralized Online Voltage Stability Indices,' *IEEE Transactions on Power Systems*, vol. 37, no. 6, pp. 4618–4629, 2022. DOI: 10.1109/TPWRS.2022.3145466.

[57] C. Vournas and T. Van Cutsem, 'Local Identification of Voltage Emergency Situations,' *IEEE Transactions on Power Systems*, vol. 23, no. 3, pp. 1239–1248, August 2008. DOI: 10.1109/TPWRS.2008.926425.

[58] C. D. Vournas, C. Lambrou and P. Mandoulidis, 'Voltage Stability Monitoring From a Transmission Bus PMU,' *IEEE Transactions on Power Systems*, vol. 32, no. 4, pp. 3266–3274, Jul. 2017. DOI: 10.1109/TPWRS.2016.2629495.

[59] T. Weckesser, L. Papangelis, C. D. Vournas and T. Van Cutsem, 'Local identification of voltage instability from load tap changer response,' *Sustainable Energy, Grids and Networks*, vol. 9, pp. 95–103, March 2017. DOI: 10.1016/j.segan.2017.01.001.

[60] L. Robitzky, T. Weckesser, U. Häger, C. Rehtanz and T. V. Van Cutsem, 'Agent-based identification and control of voltage emergency situations,' *IET Generation, Transmission and Distribution*, vol. 12, no. 6, pp. 1446–1454, 2018. DOI: 10.1049/iet-gtd.2017.1167.

[61] L. Robitzky, D. G. Mayorga, C. Kittl, C. Strunck, S. C. Mueller, U. Haeger, J. Myrzik and C. Rehtanz, 'Impact of active distribution networks on voltage stability of electric power systems,' *2017 IREP Symposium Bulk Power System Dynamics and Control*, 2017.

[62] L. David Pabon Ospina, A. Felipe Correa, M. Valov, G. Lammert and D. Premm, 'Impact of plant level voltage control of large-scale inverter based generators on long-term voltage stability,' *2018 Power Systems Computation Conference (PSCC)*, 2018. DOI: 10.23919/PSCC.2018.8442740.

[63] B. C. Karatas, M. Sarkar, H. Jóhannsson, A. H. Nielsen and P. E. Sørensen, 'Voltage stability assessment accounting for current-limited converters,' *Electric Power Systems Research*, vol. 189, December 2020, ISSN: 03787796. DOI: 10.1016/j.epsr.2020.106772.

[64] Western Electricity Coordinating Council. 'Solar Photovoltaic Power Plant Modeling and Validation Guideline.' (2019), [Online]. Available: https://www.wecc.org/Reliability/Solar%20PV%20Plant%20Modeling%20and%20Validation%20Guidline.pdf (visited on 11th March 2024).

[65] Western Electricity Coordinating Council, *Wecc wind power plant dynamic modeling guide*, 2014. [Online]. Available: https://www.wecc.org/Reliability/WECC%20Wind%20Plant%20Dynamic%20Modeling%20Guidelines.pdf (visited on 13th January 2023).

[66] S. Stankovic, T. Van Cutsem and L. Soder, 'Fault-Current Injection Strategies of Inverter-Based Generation for Fast Voltage Recovery,' *IEEE Transactions on Power Systems*, vol. 37, no. 2, pp. 1543–1553, 2022, ISSN: 15580679. DOI: 10.1109/TPWRS.2021.3108064.

[67] K. Kawabe and K. Tanaka, 'Impact of Dynamic Behavior of Photovoltaic Power Generation Systems on Short-Term Voltage Stability,' *IEEE Transactions on Power Systems*, vol. 30, no. 6, pp. 3416–3424, 2015, ISSN: 08858950. DOI: 10.1109/TPWRS.2015.2390649.

[68] A. Boricic, J. L. Rueda Torres and M. Popov, 'Impact of modelling assumptions on the voltage stability assessment of active distribution grids,' in *2020 IEEE PES Innovative Smart Grid Technologies Europe (ISGT-Europe)*, 2020, pp. 1040–1044. DOI: 10.1109/ISGT-Europe47291.2020.9248764.

[69] G. Lammert, D. Premm, L. D. P. Ospina, J. C. Boemer, M. Braun and T. Van Cutsem, 'Control of Photovoltaic Systems for Enhanced Short-Term Voltage Stability and Recovery,' *IEEE Transactions on Energy Conversion*, vol. 34, no. 1, pp. 243–254, March 2019, ISSN: 0885-8969. DOI: 10.1109/TEC.2018.2875303.

[70] M. Islam, M. Nadarajah and M. J. Hossain, 'Short-Term Voltage Stability Enhancement in Residential Grid with High Penetration of Rooftop PV Units,' *IEEE Transactions on Sustainable Energy*, vol. 10, no. 4, pp. 2211–2222, 2019, ISSN: 19493037. DOI: 10.1109/TSTE.2018.2883453.

[71] M. Islam, M. Nadarajah and M. J. Hossain, 'A Grid-Support Strategy with PV Units to Boost Short-Term Voltage Stability under Asymmetrical Faults,' *IEEE Transactions on Power Systems*, vol. 35, no. 2, pp. 1120–1131, 2020, ISSN: 15580679. DOI: 10.1109/TPWRS.2019.2942094.

[72] L. Steinhäuser, M. Coumont, S. Weck and J. Hanson, 'Comparison of RMS and EMT models of converter-interfaced distributed generation units regarding analysis of short-term voltage stability,' in *NEIS 2019 - Conference on Sustainable Energy Supply and Energy Storage Systems*, 2019, pp. 31–36, ISBN: 978-3-8007-5152-5.

[73] S. F. Zarei, H. Mokhtari, M. A. Ghasemi and F. Blaabjerg, 'Reinforcing Fault Ride through Capability of Grid Forming Voltage Source Converters Using an Enhanced Voltage Control Scheme,' *IEEE Transactions on Power Delivery*, vol. 34, no. 5, pp. 1827–1842, 2019, ISSN: 19374208. DOI: 10.1109/TPWRD.2018.2844082.

[74] J. Song, M. Cheah-Mane, E. Prieto-Araujo and O. Gomis-Bellmunt, 'Short-Circuit Analysis of AC Distribution Systems Dominated by Voltage Source Converters Considering Converter Limitations,' *IEEE Transactions on Smart Grid*, vol. 13, no. 5, pp. 3867–3878, 2022, ISSN: 19493061. DOI: 10.1109/TSG.2021.3102011.

[75] R. Rosso, S. Engelken and M. Liserre, 'Current limitation strategy for grid-forming converters under symmetrical and asymmetrical grid faults,' in *2020 IEEE Energy Conversion Congress and Exposition (ECCE)*, 2020, pp. 3746–3753. DOI: 10.1109/ECCE44975.2020.9236314.

[76] M. G. Taul, X. Wang, P. Davari and F. Blaabjerg, 'Current Limiting Control with Enhanced Dynamics of Grid-Forming Converters during Fault Conditions,' *IEEE Journal of Emerging and Selected Topics in Power Electronics*, vol. 8, no. 2, pp. 1062–1073, 2020, ISSN: 21686785. DOI: 10.1109/JESTPE.2019.2931477.

[77] D. Pan, X. Wang, F. Liu and R. Shi, 'Transient Stability of Voltage-Source Converters with Grid-Forming Control: A Design-Oriented Study,' *IEEE Journal of Emerging and Selected Topics in Power Electronics*, vol. 8, no. 2, pp. 1019–1033, 2020, ISSN: 21686785. DOI: 10.1109/JESTPE.2019.2946310.

[78] L. Huang, H. Xin, Z. Wang, L. Zhang, K. Wu and J. Hu, 'Transient Stability Analysis and Control Design of Droop-Controlled Voltage Source Converters Considering Current Limitation,' *IEEE Transactions on Smart Grid*, vol. 10, no. 1, pp. 578–591, 2019, ISSN: 19493053. DOI: 10.1109/TSG.2017.2749259.

[79] T. Qoria, F. Gruson, F. Colas, G. Denis, T. Prevost and X. Guillaud, 'Critical Clearing Time Determination and Enhancement of Grid-Forming Converters Embedding Virtual Impedance as Current Limitation Algorithm,' *IEEE Journal of Emerging and Selected Topics in Power Electronics*, vol. 8, no. 2, pp. 1050–1061, 2020, ISSN: 21686785. DOI: 10.1109/JESTPE.2019.2959085.

[80] X. He, S. Pan and H. Geng, 'Transient Stability of Hybrid Power Systems Dominated by Different Types of Grid-Forming Devices,' *IEEE Transactions on Energy Conversion*, vol. 37, no. 2, pp. 868–879, 2022, ISSN: 15580059. DOI: 10.1109/TEC.2021.3113399.

[81] A. Tayyebi, D. Grob, A. Anta, F. Kupzog and F. Dorfler, 'Frequency Stability of Synchronous Machines and Grid-Forming Power Converters,' *IEEE Journal of Emerging and Selected Topics in Power Electronics*, vol. 8, no. 2, pp. 1004–1018, 2020, ISSN: 21686785. DOI: 10.1109/JESTPE.2020.2966524.

[82] C. Li, Y. Yang, N. Mijatovic and T. Dragicevic, 'Frequency Stability Assessment of Grid-Forming VSG in Framework of MPME with Feedforward Decoupling Control Strategy,' *IEEE Transactions on Industrial Electronics*, vol. 69, no. 7, pp. 6903–6913, 2022, ISSN: 15579948. DOI: 10.1109/TIE.2021.3099236.

[83] S. Samanta and N. R. Chaudhuri, 'Stability Analysis of Grid-Forming Converters Under DC-Side Current Limitation in Primary Frequency Response Regime,' *IEEE Transactions on Power Systems*, vol. 37, no. 4, pp. 3077–3091, 2022, ISSN: 15580679. DOI: 10.1109/TPWRS.2021.3130226.

[84] M. Coumont, B. Braun and J. Hanson, 'Influence of grid-forming inverter control on short-term voltage stability in distribution grids,' in *18th Wind Integration Workshop*, 2019, ISBN: 978-3-9820080-5-9.

[85] M. Herrmann and L. Hofmann, 'Ensuring Short-term Voltage Stability in Extensive Grids With High Power Electronic Penetration by Applying Grid Forming Controls,' in *2020 International Conference on Smart Grids and Energy Systems (SGES)*, November 2020, pp. 24–29, ISBN: 978-1-7281-8550-7. DOI: 10.1109/SGES51519.2020.00012.

[86] C. Eckel, J. C. Kamma and C. Becker, 'Converter-driven small signal stability and interaction analysis for grid-following converters using emt and phasor simulations,' in *22nd Wind and Solar Integration Workshop (WIW 2023)*, Sep. 2023, pp. 339–346. DOI: 10.1049/icp.2023.2757.

[87] S. Stock, D. Babazadeh, P. Hund and C. Becker, 'Reinforcement learning based coordination of virtual inertia provision from inverter-dominated distribution grids,' in *2023 IEEE 32nd International Symposium on Industrial Electronics (ISIE)*, 2023, pp. 1–6. DOI: 10.1109/ISIE51358.2023.10228065.

[88] P. Hund, S. Stock, D. Babazadeh and C. Becker, 'Modelling the influence of virtual inertia in distribution systems on frequency stability,' in *IEEE Power and Energy Student Summit 2022 and Power Electronics Student Summit*, Kassel, Germany, November 2022.

[89] J. V. Milanović, K. Yamashita, S. Martínez Villanueva, S. Ž. Djokić and L. M. Korunović, 'International industry practice on power system load modeling,' *IEEE Transactions on Power Systems*, vol. 28, no. 3, pp. 3038–3046, 2013, ISSN: 08858950. DOI: 10.1109/TPWRS.2012.2231969.

[90] A. Arif, Z. Wang, J. Wang, B. Mather, H. Bashualdo and D. Zhao, 'Load Modeling—A Review,' *IEEE Transactions on Smart Grid*, vol. 9, no. 6, pp. 5986–5999, November 2018, ISSN: 1949-3053. DOI: 10.1109/TSG.2017.2700436.

[91] P. Kundur, *Power System Stability and Control* (The EPRI Power System Engineering Series). McGraw-Hill Inc., 1994, ISBN: 978-0070359581.

[92] C. Cresswell, 'Steady state load models for power system analysis,' Ph.D. dissertation, The University of Edinburgh, 2013. [Online]. Available: https://era.ed.ac.uk/handle/1842/3846 (visited on 11th March 2024).

[93] J.-P. Heckel, T. Steffen and C. Becker, 'Voltage stability risks caused by dynamic interactions in integrated energy systems,' in *CIGRE 2022 Paris Session*, Paris, France, Sep. 2022.

[94] M. Rylander, W. M. K. Grady, A. Arapostathis and E. J. Powers, 'Power electronic transient load model for use in stability studies of electric power grids,' *IEEE Transactions on Power Systems*, vol. 25, no. 2, pp. 914–921, 2010, ISSN: 08858950. DOI: 10.1109/TPWRS.2009.2032351.

[95] C. Cresswell, S. Djokic and S. Munshi, 'Analytical modeling of adjustable speed drive load for power system studies,' in *2007 IEEE Lausanne Power Tech*, 2007, pp. 1899–1904. DOI: 10.1109/PCT.2007.4538607.

[96] C. Cresswell and S. Djokic, 'Representation of directly connected and drive-controlled induction motors. part 1: Single-phase load models,' in *2008 18th International Conference on Electrical Machines*, Sep. 2008. DOI: 10.1109/ICELMACH.2008.4800118.

[97] C. Cresswell and S. Djokic, 'Representation of directly connected and drive-controlled induction motors. Part 2: Three-phase load models,' in *2008 18th International Conference on Electrical Machines*, Sep. 2008. DOI: 10.1109/ICELMACH.2008.4800119.

[98] A. Emadi, 'Modeling of Power Electronic Loads in AC Distribution Systems Using the Generalized State-Space Averaging Method,' *IEEE Transactions on Industrial Electronics*, vol. 51, no. 5, pp. 992–1000, October 2004, ISSN: 0278-0046. DOI: 10.1109/TIE.2004.834950.

[99] A. J. Collin, S. Z. Djokic, J. Drapela, Z. Guo, R. Langella, A. Testa and N. R. Watson, 'Analysis of Approaches for Modeling the Low Frequency Emission of LED Lamps,' *Energies*, vol. 13, no. 7, p. 1571, March 2020, ISSN: 1996-1073. DOI: 10.3390/en13071571.

[100] A. J. Collin, S. Z. Djokic, H. F. Thomas and J. Meyer, 'Modelling of electric vehicle chargers for power system analysis,' in *11th International Conference on Electrical Power Quality and Utilisation*, vol. 21, November 2011. DOI: 10.1109/EPQU.2011.6128816.

[101] A. Collin, J. Acosta, B. Hayes and S. Djokic, 'Component-based aggregate load models for combined power flow and harmonic analysis,' in *7th Mediterranean Conference and Exhibition on Power Generation, Transmission, Distribution and Energy Conversion (MedPower 2010)*, vol. 2010, IET, 2010, pp. 171–171, ISBN: 978 1 84919 319 1. DOI: 10.1049/cp.2010.0901.

[102] D. Ramasubramanian and V. Vittal, 'Positive sequence induction motor speed control drive model for time-domain simulations,' *IET Generation, Transmission & Distribution*, vol. 11, no. 7, pp. 1809–1819, May 2017, ISSN: 1751-8687. DOI: 10.1049/iet-gtd.2016.1682.

[103] North American Electric Reliability Corporation, *Technical reference document - dynamic load modeling*, 2016. [Online]. Available: https://www.nerc.com/comm/PC/LoadModelingTaskForceDL/Dynamic%20Load%20Modeling%20Tech%20Ref%202016-11-14%20-%20FINAL.PDF (visited on 3rd November 2024).

[104] I. Hiskens and M. Pai, 'Hybrid systems view of power system modelling,' in *2000 IEEE International Symposium on Circuits and Systems (ISCAS)*, vol. 2, 2000, 228–231 vol.2. DOI: 10.1109/ISCAS.2000.856300.

[105] V. Donde and I. Hiskens, 'Dynamic performance assessment: Grazing and related phenomena,' *IEEE Transactions on Power Systems*, vol. 20, no. 4, pp. 1967–1975, 2005. DOI: 10.1109/TPWRS.2005.856990.

[106] M. F. Mejia and S. C. Leirens, 'Hybrid differential algebraic equations approach for modeling interconnected power systems,' in *2009 6th International Conference on Electrical Engineering, Computing Science and Automatic Control (CCE)*, 2009. DOI: 10.1109/ICEEE.2009.5393397.

[107] W. Al-Rousan, C. Wang and F. Lin, 'A discrete-event system approach for modeling and mitigating power system cascading failures,' *IEEE Transactions on Control Systems Technology*, vol. 30, no. 6, pp. 2547–2560, 2022. DOI: 10.1109/TCST.2022.3154153.

[108] Y. Zhou, P. Zhang and M. Yue, 'Reachable dynamics of networked microgrids with large disturbances,' *IEEE Transactions on Power Systems*, vol. 36, no. 3, pp. 2416–2427, 2021. DOI: 10.1109/TPWRS.2020.3034886.

[109] I. Hiskens and M. Pai, 'Trajectory sensitivity analysis of hybrid systems,' *IEEE Transactions on Circuits and Systems I: Fundamental Theory and Applications*, vol. 47, no. 2, pp. 204–220, 2000. DOI: 10.1109/81.828574.

[110] I. A. Hiskens, 'Power system modeling for inverse problems,' *IEEE Transactions on Circuits and Systems I: Regular Papers*, vol. 51, no. 3, pp. 539–551, 2004. DOI: 10.1109/TCSI.2004.823654.

[111] I. Hiskens and J. Alseddiqui, 'Sensitivity, approximation, and uncertainty in power system dynamic simulation,' *IEEE Transactions on Power Systems*, vol. 21, no. 4, pp. 1808–1820, 2006. DOI: 10.1109/TPWRS.2006.882460.

[112] V. Donde and I. A. Hiskens, 'Analysis of tap-induced oscillations observed in an electrical distribution system,' *IEEE Transactions on Power Systems*, vol. 22, no. 4, pp. 1881–1887, 2007. DOI: 10.1109/TPWRS.2007.907349.

[113] S. Echalih, A. Abouloifa, I. Lachkar, A. E. Aroudi, Z. Hekss, F. Giri and M. S. Al-Numay, 'A cascaded controller for a grid-tied photovoltaic system with three-phase half-bridge interleaved buck shunt active power filter: Hybrid control strategy and fuzzy logic approach,' *IEEE Journal on Emerging and Selected Topics in Circuits and Systems*, vol. 12, no. 1, pp. 320–330, 2022. DOI: 10.1109/JETCAS.2022.3152535.

[114] I. Jaramillo-Cajica and J. Schiffer, 'A dwell-time approach for grid-aware operation of a distributed generator in an islanded dc microgrid,' in *2022 European Control Conference (ECC)*, 2022, pp. 1079–1084. DOI: 10.23919/ECC55457.2022.9838354.

[115] O. A. Beg, T. T. Johnson and A. Davoudi, 'Detection of false-data injection attacks in cyber-physical dc microgrids,' *IEEE Transactions on Industrial Informatics*, vol. 13, no. 5, pp. 2693–2703, 2017. DOI: 10.1109/TII.2017.2656905.

[116] C. J. Javaid, A. Allahham, D. Giaouris, S. Blake and P. Taylor, 'Modelling of a virtual power plant using hybrid automata,' *The Journal of Engineering*, vol. 2019, pp. 3918–3922, 17 2019. DOI: 10.1049/joe.2018.8161.

[117] M. A. A. Murad and F. Milano, 'Chattering-free modelling and simulation of power systems with inclusion of filippov theory,' *Electric Power Systems Research*, vol. 189, 2020, ISSN: 0378-7796. DOI: 10.1016/j.epsr.2020.106727.

[118] I. A. Hiskens, 'Trajectory deadlock in power system models,' in *2011 IEEE International Symposium of Circuits and Systems (ISCAS)*, 2011, pp. 2721–2724. DOI: 10.1109/ISCAS.2011.5938167.

[119] J. Haack, A. Narayan, A. Patil, M. Klaes, M. Braun, S. Lehnhoff, H. de Meer and C. Rehtanz, 'A hybrid model for analysing disturbance propagation in cyber–physical energy systems,' *Electric Power Systems Research*, vol. 212, p. 108 356, 2022, ISSN: 0378-7796. DOI: 10.1016/j.epsr.2022.108356.

[120] H. K. Khalil, *Nonlinear Systems*. Prentice Hall, 2002, ISBN: 9780130673893.

[121] H. Lin and P. J. Antsaklis, *Hybrid Dynamical Systems An Introduction to Control and Verification*. now Publishers Inc., 2014, ISBN: 978-1-60198-784-6. DOI: 10.1561/2600000001.

[122] R. Goebel, R. G. Sanfelice and A. R. Teel, *Hybrid Dynamical Systems Modeling, Stability, and Robustness*. Princeton University Press, March 2012, ISBN: 9781400842636. DOI: 10.1515/9781400842636.

[123] D. Liberzon, *Switched Systems: Stability Analysis and Control Synthesis*. [Online]. Available: http://liberzon.csl.illinois.edu/teaching/Liberzon-LectureNotes.pdf (visited on 11th March 2024), Lecture Notes for HYCON-EECI Graduate School on Control.

[124] A. van der Schaft and H. Schumacher, *An introduction to hybrid dynamical systems* (Lecture Notes in Control and Information Sciences). Springer London, 2000, ISBN: 978-1-85233-233-4. DOI: 10.1007/BFb0109998.

[125] A. Abate, A. D'Innocenzo, G. Pola, M. D. Di Benedetto and S. Sastry, 'The Concept of Deadlock and Livelock in Hybrid Control Systems,' in *Hybrid Systems: Computation and Control (HSCC 2007)*, vol. 4416, 2007, pp. 628–632. DOI: 10.1007/978-3-540-71493-4_48.

[126] D. Liberzon and S. Trenn, 'Switched nonlinear differential algebraic equations: Solution theory, Lyapunov functions, and stability,' *Automatica*, vol. 48, no. 5, pp. 954–963, 2012. DOI: 10.1016/j.automatica.2012.02.041.

[127] P. Kunkel and V. Mehrmann, *Differential-Algebraic Equations*. EMS Press, February 2006, ISBN: 978-3-03719-017-3. DOI: 10.4171/017.

[128] D. Liberzon and S. Trenn, 'On stability of linear switched differential algebraic equations,' in *Proceedings of the 48h IEEE Conference on Decision and Control (CDC) held jointly with 2009 28th Chinese Control Conference*, 2009, pp. 2156–2161. DOI: 10.1109/CDC.2009.5400076.

[129] J. Daafouz, S. Tarbouriech and M. Sigalotti, *Hybrid Systems with Constraints*. John Wiley & Sons, Inc., May 2013, ISBN: 9781118639856. DOI: 10.1002/9781118639856.

[130] A. D. Domínguez-García and S. Trenn, 'Detection of impulsive effects in switched daes with applications to power electronics reliability analysis,' in *49th IEEE Conference on Decision and Control (CDC)*, 2010, pp. 5662–5667. DOI: 10.1109/CDC.2010.5717011.

[131] Y. Chen and S. Trenn, 'On impulse-free solutions and stability of switched nonlinear differential–algebraic equations,' *Automatica*, vol. 156, p. 111 208, 2023, ISSN: 0005-1098. DOI: 10.1016/j.automatica.2023.111208.

[132] D. B. Rathnayake, M. Akrami, C. Phurailatpam, S. P. Me, S. Hadavi, G. Jayasinghe, S. Zabihi and B. Bahrani, 'Grid Forming Inverter Modeling, Control, and Applications,' *IEEE Access*, vol. 9, pp. 114 781–114 807, 2021, ISSN: 2169-3536. DOI: 10.1109/ACCESS.2021.3104617.

[133] R. Rosso, 'Stability analysis of converter control strategies for power electronics-dominated power systems,' Ph.D. dissertation, Christian-Albrechts-Universitat zu Kiel, 2020. [Online]. Available: https://macau.uni-kiel.de/receive/macau_mods_00001684 (visited on 11th March 2024).

[134] S. Debnath, J. Qin, B. Bahrani, M. Saeedifard and P. Barbosa, 'Operation, control, and applications of the modular multilevel converter: A review,' *IEEE Transactions on Power Electronics*, vol. 30, no. 1, pp. 37–53, 2015. DOI: 10.1109/TPEL.2014.2309937.

[135] National Grid Electricity System Operator. 'Great Britain Grid Forming Best Practice Guide.' (April 2023), [Online]. Available: https://www.nationalgrideso.com/document/278491/download (visited on 11th March 2024).

[136] R. Rosso, X. Wang, M. Liserre, X. Lu and S. Engelken, 'Grid-Forming Converters: Control Approaches, Grid-Synchronization, and Future Trends—A Review,' *IEEE Open Journal of Industry Applications*, vol. 2, pp. 93–109, 2021. DOI: 10.1109/OJIA.2021.3074028.

[137] S. Henninger and J. Jaeger, 'Advanced classification of converter control concepts for integration in electrical power systems,' *International Journal of Electrical Power & Energy Systems*, vol. 123, 2020. DOI: 10.1016/j.ijepes.2020.106210.

[138] S. D'Arco and J. A. Suul, 'Equivalence of Virtual Synchronous Machines and Frequency-Droops for Converter-Based MicroGrids,' *IEEE Transactions on Smart Grid*, vol. 5, no. 1, pp. 394–395, January 2014, ISSN: 1949-3053. DOI: 10.1109/TSG.2013.2288000.

[139] T. Qoria, F. Gruson, F. Colas, X. Kestelyn and X. Guillaud, 'Current limiting algorithms and transient stability analysis of grid-forming vscs,' *Electric Power Systems Research*, vol. 189, p. 106 726, 2020, ISSN: 0378-7796. DOI: 10.1016/j.epsr.2020.106726.

[140] B. Fan and X. Wang, 'Equivalent circuit model of grid-forming converters with circular current limiter for transient stability analysis,' *IEEE Transactions on Power Systems*, vol. 37, no. 4, pp. 3141–3144, 2022. DOI: 10.1109/TPWRS.2022.3173160.

[141] N. Wiese, D. Duckwitz, M. Nuschke, Y. Zhang and M. Braun, 'Fault operation of grid-forming converters with focus on system stability,' in *11th Solar & Storage Power System Integration Workshop (SIW 2021)*, 2021, pp. 65–70. DOI: 10.1049/icp.2021.2485.

[142] V. Mehrmann and L. Scholz, 'Hybrid systems of differential-algebraic equations - analysis and numerical solution,' *Journal of Process Control*, vol. 19, pp. 1218–1228, Sep. 2009. DOI: 10.1016/j.jprocont.2009.05.002.

[143] A. J. Collin, 'Advanced load modelling for power system studies,' Ph.D. dissertation, The University of Edinburgh, 2013. [Online]. Available: https://era.ed.ac.uk/handle/1842/8890 (visited on 11th March 2024).

[144] T. Wohlfahrt, C. Waniek, J. M. Myrzik, J. Meyer and P. Schegner, 'Design recommendations for future household devices concerning their high frequency emission in the range between 2 khz and 150 khz,' in *2017 IEEE PES Innovative Smart Grid Technologies Conference Europe (ISGT-Europe)*, 2017. DOI: 10.1109/ISGTEurope.2017.8260259.

[145] A. Kaknevicius and A. Hoover, *Managing inrush current - application report slva670a*, May 2015. [Online]. Available: https://www.ti.com/lit/an/slva670a/slva670a.pdf (visited on 11th March 2024).

[146] C. Waniek, T. Wohlfahrt, J. M. Myrzik, J. Meyer and P. Schegner, 'Topology identification of electronic mass-market equipment for estimation of lifetime reduction by hf disturbances above 2 khz,' *2017 IEEE Manchester PowerTech*, DOI: 10.1109/PTC.2017.7981207.

[147] CIGRE WG C4.605, 'Modelling and Aggregation of Loads in Flexible Power Networks,' *Technical Brochure No. 566*, February 2014.

[148] C. E. Cresswell and S. Ž. Djokić, 'The analysis of the occurrence of high inrush currents in dc power supplies,' in *4th IET International Conference on Power Electronics, Machines and Drives (PEMD 2008)*, 2008, pp. 441–445, ISBN: 9780863419003. DOI: 10.1049/cp:20080560.

[149] B. L. van der Waerden, *Algebra I*. Springer Berlin Heidelberg, 1993, ISBN: 978-3-642-85528-3. DOI: 10.1007/978-3-642-85527-6.

[150] Texas Instruments, *UCC28180 programmable frequency, continuous conduction mode (CCM), boost power factor correction (PFC) controller*, Jul. 2016. [Online]. Available: https://www.ti.com/lit/ds/symlink/ucc28180.pdf?ts=1646734144903 (visited on 11th March 2024).

[151] G. Tulay, I. Iskender and H. Erdem, 'Optimal tuning of a boost pfc converter pi controller using heuristic optimization methods,' *International Transactions on Electrical Energy Systems*, vol. 27, no. 12, 2017. DOI: 10.1002/etep.2458.

[152] G. Rojas-Dueñas, J.-R. Riba and M. Moreno-Eguilaz, 'Parameter estimation of a single-phase boost pfc converter with emi filter based on an optimization algorithm,' *Electronics*, vol. 10, no. 11, 2021. DOI: 10.3390/electronics10111231.

[153] T. Van Cutsem, M. Glavic, W. Rosehart, C. Canizares, M. Kanatas, L. Lima, F. Milano, L. Papangelis, R. A. Ramos, J. A. d. Santos, B. Tamimi, G. Taranto and C. Vournas, 'Test systems for voltage stability studies,' *IEEE Transactions on Power Systems*, vol. 35, no. 5, pp. 4078–4087, 2020. DOI: 10.1109/TPWRS.2020.2976834.

[154] Z. Ali, N. Christofides, L. Hadjidemetriou, E. Kyriakides, Y. Yang and F. Blaabjerg, 'Three-phase phase-locked loop synchronization algorithms for grid-connected renewable energy systems: A review,' *Renewable and Sustainable Energy Reviews*, vol. 90, pp. 434–452, 2018, ISSN: 1364-0321. DOI: 10.1016/j.rser.2018.03.086.

[155] A. Plietzsch, R. Kogler, S. Auer, J. Merino, A. Gil-de-Muro, J. Liße, C. Vogel and F. Hellmann, 'Powerdynamics.jl—an experimentally validated open-source package for the dynamical analysis of power grids,' *SoftwareX*, vol. 17, 2022, ISSN: 2352-7110. DOI: 10.1016/j.softx.2021.100861.

[156] C. Rackauckas and Q. Nie, 'Differentialequations.jl–a performant and feature-rich ecosystem for solving differential equations in julia,' *Journal of Open Research Software*, vol. 5, no. 1, p. 15, 2017. DOI: 10.5334/jors.151.

[157] The MathWorks Inc., *Matlab version: 9.11.0 (r2021b)*, Natick, Massachusetts, United States, 2021. [Online]. Available: https://www.mathworks.com.

[158] Y. Ma, V. Dixit, M. J. Innes, X. Guo and C. Rackauckas, 'A comparison of automatic differentiation and continuous sensitivity analysis for derivatives of differential equation solutions,' in *2021 IEEE High Performance Extreme Computing Conference (HPEC)*, 2021, pp. 1–9. DOI: 10.1109/HPEC49654.2021.9622796.

[159] S. Geng and I. A. Hiskens, 'Second-order trajectory sensitivity analysis of hybrid systems,' *IEEE Transactions on Circuits and Systems I: Regular Papers*, vol. 66, no. 5, pp. 1922–1934, 2019. DOI: 10.1109/TCSI.2019.2903196.

[160] IEC 61000-3-2:2018, *Electromagnetic compatibility (emc) - part 3-2: Limits - limits for harmonic current emissions (equipment input current ≤ 16 a per phase)*, February 2018.

[161] Infineon Technology AG, *PFC boost converter design guide - 1200 W design example*, February 2014. [Online]. Available: https://www.infineon.com/dgdl/InfineonApplicationNote_PFCCCMBoostConverterDesignGuide-AN-v02_00-EN.pdf?fileId=5546d4624a56eed8014a62c75a923b05 (visited on 11th March 2024).

[162] ON Semiconductor, *Power factor correction (PFC) handbook - choosing the right power factor controller solution*, April 2014. [Online]. Available: https://www.onsemi.com/pub/Collateral/HBD853-D.PDF (visited on 11th March 2024).

[163] IEC 61000-3-12:2011, *Electromagnetic compatibility (emc) - part 3-12: Limits - limits for harmonic currents produced by equipment connected to public low-voltage systems with input current > 16 a and ≤ 75 a per phase*, December 2011.

[164] IEC 61800-3:2017, *Adjustable speed electrical power drive systems - part 3: Emc requirements and specific test methods*, March 2017.

Journal publications

[SL1] S. Liemann and C. Rehtanz, 'Voltage stability analysis of grid-forming converters with current limitation,' *Electric Power Systems Research*, vol. –, 2024, Accepted for the Power System Computation Conference (PSCC) 2024.

[SL2] S. Liemann, M. Greve, S. Ohrem, M. Lindners, T. Noll and C. Rehtanz, 'Investigation on the suitability of equivalent models of subtransmission level for security analyses at transmission level,' *Electric Power Systems Research*, vol. 189, December 2020. DOI: 10.1016/j.epsr.2020.106712, Presented at the Power System Computation Conference (PSCC) 2020.

[SL3] S. Liemann, T. Hennig, L. Robitzky, M. Finkelmann and C. Rehtanz, 'Analysis of the stability and dynamic responses of converter-based generation in case of system splits,' *IET Generation, Transmission & Distribution*, vol. 13, no. 16, pp. 3696–3703, August 2019. DOI: 10.1049/iet-gtd.2018.6763.

Conference publications

[SL4] S. Liemann and C. Rehtanz, 'Power response and modelling aspects of power electronic loads in case of voltage drops,' in *2022 IREP Symposium Bulk Power System Dynamics and Control*, Banff, Canada, Jul. 2022. [Online]. Available: https://arxiv.org/abs/2207.03965 (visited on 11th March 2024).

[SL5] S. Liemann and C. Rehtanz, 'Dynamic power electronic load model for transient stability analyses,' in *2021 IEEE Madrid PowerTech*, Madrid, Spain, Jul. 2021. DOI: 10.1109/PowerTech46648.2021.9494756.

[SL6] S. Liemann, L. Strenge, P. Schultz, H. Hinners, J. Porst, M. Sarstedt and F. Hellmann, 'Probabilistic stability assessment for dynamic active distribution grids,' in *2021 IEEE Madrid PowerTech*, Madrid, Spain, Jul. 2021. DOI: 10.1109/PowerTech46648.2021.9494855.

[SL7] S. Liemann, L. Robitzky and C. Rehtanz, 'Einfluss eines variierenden anteils leistungselektronischer erzeugung in spannungskritischen situationen im übertragungsnetz,' in *International ETG-Congress 2019*, Esslingen, May 2019.

[SL8] S. Liemann, L. Robitzky and C. Rehtanz, 'Impact of varying shares of distributed energy resources on voltage stability in electric power ystems,' in *2019 IEEE Milan PowerTech*, Milan, Italy, Jun. 2019. DOI: 10.1109/PTC.2019.8810761.

[SL9] D. M. Gonzalez, L. Robitzky, S. Liemann, U. Häger, J. Myrzik and C. Rehtanz, 'Distribution network control scheme for power flow regulation at the interconnection point between transmission and distribution system,' in *2016 IEEE Innovative Smart Grid Technologies - Asia (ISGT-Asia)*, 2016, pp. 23–28. DOI: 10.1109/ISGT-Asia.2016.7796355.

Supervised Master and Bachelor Theses

[T1] P. Hauska, 'Auswirkungen einer anhebung des offshore-seitigen ac-spannungslevels bei zukünftigen offshore-netzanschlüssen,' Master's thesis, TU Dortmund University, November 2022, In cooperation with Dr. Michael Steglich from Amprion GmbH in Dortmund.

[T2] D. M. Robin, 'Untersuchung des einflusses der strombegrenzung von netzbildenden umrichtern auf die langzeit-spannungsstabilität,' Master's thesis, TU Dortmund University, Jun. 2021.

[T3] S. Elsner, 'Modellierung generischer leistungslektronischer lasten für spannungsstabilitätsanalysen,' Bachelor's thesis, TU Dortmund University, Jul. 2020.

[T4] L. O. Nießen, 'Analyse der funktionsfähigkeit von virtual inertia in einem elektroenergiesystem mit abnehmender schwungmasse,' Bachelor's thesis, TU Dortmund University, January 2020.

[T5] P. S. Schorn, 'Ausnutzung der spannungsabhängigkeit von lasten zur entlastung von übertragungsnetzen in spannungskritischen situationen,' Bachelor's thesis, TU Dortmund University, Jul. 2020.

[T6] D. Baier, 'Numerische methoden zur stabilitätsbestimmung in elektrischen netzen und implementierung in verschiedenen simulationsumgebungen,' Master's thesis, TU Dortmund University, October 2019, In cooperation with Dr. Frank Hellmann from PIK in Potsdam.

[T7] M. Ludwigs, 'Methoden zur online-bewertung der transienten stabilität,' Master's thesis, TU Dortmund University, April 2019, In cooperation with Dr. Andreas Kubis from PSI Software AG in Dortmund.

List of acronyms

ANS aggregated Nordic system

AVR automatic voltage regulator

CPF continuation power flow

DADS differential-algebraic-discrete system

DAE differential-algebraic equation

DAIS differential-algebraic impulsive switched system

dVOC dispatchable virtual oscillator control

EMI electromagnetic interference

EMT electromagnetic transient

GFL grid-following

GFM grid-forming

HVDC high-voltage direct current

HVRT high voltage ride-through

ICT information and communication technology

LED light-emitting diode

LVRT low voltage ride-through

ODE ordinary differential equation

OEL over excitation limitation

OLTC on-load tap changer

PCC point of common coupling

PFC power factor correction

PLL phase-locked loop

PMU phase measurement unit

PV photovoltaic

PWA piecewise affine

RAW running average window

RMS root mean square

SECM stability-enhancing control method

SMPS switch-mode power supplies

TVI trajectory violation integral

VSI voltage stability index

VSM virtual synchronous machine

Symbols

General notation rules are as follows.

- Scalar functions, variables and parameters express in pu are in lower case fonts, e.g. p, q, v.
- Upper case fonts indicate scalar variables and parameters expressed in absolute values, e.g. P [MW].
- Function and variable vectors are in lower case, bold face fonts, e.g. $\mathbf{x}$, $\mathbf{f}$
- Matrices are in upper case, bold fonts, e.g $\mathbf{A}$.
- Underlined values like $\underline{V}$ indicates complex values.
- A superscript T indicates transpose, e.g. $\mathbf{x}^{\mathrm{T}}$.
- Time derivates appear with a dot, e.g. $\dot{x}$.

$\mathbf{A}$	square matrix
a	Fourier component
b	Fourier component
c, C	capacitance or capacitor
$\mathbf{d}$	distance
D	damping or duty cycle
$\mathbf{E}$	square matrix
$\mathbf{f}$	function of differential equations
f	frequency or function
$\mathbf{g}$	function of algebraic equations
$\mathbf{H}$	Tuple of hybrid automaton
$\mathbf{h}, h$	reset function
$\mathbf{I}$	identity matrix
i, I	current
$Init$	set of initial states
Inv	set of invariants
$\mathbf{J}$	Jacobian matrix
J	inertia
l, L	inductance or inductor

$\mathbf{M}$	Monodromy matrix
m	control parameter of VSM (mutual impedance)
$\mathbf{P}$	square and positive definite matrix
$\mathbf{p}$	vector of parameters
PF	power factor
p, P	active power
$\mathbf{Q}$	square and positive definite matrix
q, Q	reactive power or discrete state (only case)
r, R	resistance
S	short-circuit power
s	switching condition
t, T	time or period of time
u	input to a system
v, V	voltage
$\mathbf{x}$	continuous state vector
x, X	reactance or parameter sensitivity
$\mathbf{y}$	algebraic state vector
z, Z	impedance
α	exponent of load voltage sensitivity or control parameter of dVOC
β	control parameter of dVOC
γ	parameter
δ	distance for Lyapunov exponent
ϵ	parameter
η	control parameter of dVOC or efficiency
Θ	transition relation or angle
λ	eigenvalue
Λ	Lyapunov exponent
Π	consistency projector
σ	switching signal
τ	junction time
φ	phase angle or ODE solution
ω	angular frequency
Ω	consistency space
∇	nabla operator (gradient)
$\Re$	real part
$\Im$	imaginary part

$\mathcal{G}$	guard condition
$\mathcal{R}$	reset map
$\mathcal{S}$	switching surface

Indices, subscripts and superscripts

It should be noted that some of the indices listed below are also used together, e.g. i_{cdref} is the reference value of the d-axis current of the converte.

-	time instant before event
+	time instant after event
0	enumeration index or equilibrium
1	enumeration index
2	enumeration index
AC	alternating current
abc	related to phase a,b and c
aggr	aggregated
appr	approximated
base	base value
c	related to converter or capacitance
C	related to capacitance
D	related to diode
dc, DC	direct current
d	related to droop, d-axis component or diode
dq	related to d-component
droop	related to droop
f	related to frequency, fault or AC filter
fd	field
fault	fault
flt	filter
G	related to Generator
g, grid	related to grid

H	hopf bifurcation
hold	hold-up time
IL	current of inductance (trajectory sensitivity)
i	integral gain
is	current saturation
i, m, k, l	counting variables
load	load
L	related to inductance or Load
lim	limited
m	modulation or related to matching control
max	maximum
min	minimum
meas	measurement
mod	modulo
N	number of elements
nom	nominal
off	switch-off
on	switch-on
P	related to active power
PCC	point of commom coupling
p	proportional gain
pu	in per unit
q	related to q-component
R	related to resistance
r, rated	rated (e.g. apparent power)
ref	reference
ripple	ripple
SNB	saddle-node bifurcation
s	stable or switching frequency
shunt	shunt
sim	simulation
sum	sum
sys	system
$T/2$	half a period
thr	threshold
trip	trip

u	unstable
VR	rectified voltage (trajectory sensitivity)
v	voltage
x	partial derivates to x
$\overline{\mathbf{x}}$	partial derivates to $\overline{\mathbf{x}}$
$\overline{\mathbf{x}}_0$	partial derivates to $\overline{\mathbf{x}}_0$
y	partial derivates to y
z	related to impedance
Δ	distance
θ	synchronous reference frame to angle θ
Σ	sum
τ	at junction time or time constant

A Additional information about the modelling of GFM converters

In this appendix, additional information about the modelling of GFM converters is given. At first, in Section A.1, the model (AC filter, DC energy source model) and control parameters of the four GFM controls and SECMs are given. Afterwards, the complete DADS description of the droop-based GFM converter is presented in Section A.2. This is followed by an eigenvalue analysis of this system in Section A.3.

A.1 Parameters of GFM controls and SECM

Table A1: Model parameters of GFM converter, AC Filter and DC energy source model (partly taken from [81])

Parameter	Value
S_{rated}	5300 MVA
P_{ref}	4440 MW
v_{ref}	1.0 pu
i_{cmax}	1.0 pu
i_{dcmax}	1.2 pu
r_{dc}	20 pu
c_{dc}	0.096 pu
T_{dc}	0.05 s
k_{dc}	100 pu
r_{f}	0.0005 pu
x_{lf}	0.031416 pu
x_{cf}	5.305165 pu

Table A2: Control parameters of inner voltage and current control (taken from [81])

k_{pv}	k_{iv}	k_{pi}	k_{ii}
0.52 pu	1.161022 pu	0.738891 pu	1.19 pu

Table A3: Control parameters of the four power synchronisation and outer voltage control loops (taken from [81])

	k_d	ω_f	k_p	k_i		
droop	π pu	$10\pi \frac{1}{\mathrm{s}}$	0.5 pu	0.001 pu		
	k_m	k_p	k_i			
matching	100π pu	0.5 pu	0.001 pu			
	η	ω_f	α	ϵ		
dVOC	π pu	$10\pi \frac{1}{\mathrm{s}}$	66666.666 pu	10^{-9} pu		
	D	J	ω_f	k_p	k_i	m_fd
VSM	100 pu	2 pu	$10\pi \frac{1}{\mathrm{s}}$	0.5 pu	0.001 pu	1.0 pu

Table A4: Parameters of SECM-3 and SECM-4 (taken from [78] and [81])

Parameter	Value
k_q	5 pu
i_thr	0.92 pu
γ	$2.3 \frac{p_\mathrm{base}}{i_\mathrm{base}}$ pu
p_base	4440 MW
i_base	$\frac{5300\mathrm{MVA}}{15\mathrm{kV}\sqrt{3}}$

A.2 DADS model of droop-based GFM converter in an islanded microgrid

Next, a complete description of the GFM converter from Section 4.5 as DADS is given. Differential equations are marked with □, algebraic equations with ■ and auxiliary equations are marked with (aux.). For every discrete state, a trivial differential equation with $\dot{q} = 0$ is inserted. Their corresponding switching conditions and reset functions are marked with △. Variables with the superscript $\Delta\theta$ indicate that they are orientated at the local dq-reference frame of the converter. The differential, algebraic and discrete states as well as parameters are given by

$$\dot{\mathbf{x}} = \frac{\mathrm{d}}{\mathrm{d}t}\begin{bmatrix} x_{\mathrm{id}} \\ x_{\mathrm{iq}} \\ x_{\mathrm{vd}} \\ x_{\mathrm{vq}} \\ x_{\mathrm{vdroop}} \\ p_{\mathrm{f}} \\ \Delta\theta \\ \Delta v_{\mathrm{dc}} \\ \Delta p_{\mathrm{cf}} \\ \Delta i_{\mathrm{dcref}\tau} \end{bmatrix}, \quad \mathbf{y} = \begin{bmatrix} v_{\mathrm{d}} \\ v_{\mathrm{q}} \\ v_{\mathrm{cd}} \\ v_{\mathrm{cq}} \\ i_{\mathrm{cdlim}} \\ i_{\mathrm{cqlim}} \\ p_{\mathrm{ref}} \\ i_{\mathrm{dcref}} \end{bmatrix}, \quad \mathbf{p} = \begin{bmatrix} r_{\mathrm{f}} \\ x_{\mathrm{lf}} \\ x_{\mathrm{cf}} \\ r_{\mathrm{load}} \\ x_{\mathrm{load}} \\ c_{\mathrm{dc}} \\ r_{\mathrm{dc}} \\ T_{\mathrm{dc}} \\ k_{\mathrm{ii}} \\ k_{\mathrm{ip}} \\ k_{\mathrm{vi}} \\ k_{\mathrm{vp}} \\ p_{\mathrm{ref0}} \\ v_{\mathrm{dcref}} \\ i_{\mathrm{cmax}} \\ k_{\mathrm{vidroop}} \\ k_{\mathrm{vpdroop}} \\ \omega_{\mathrm{f}} \\ k_{\mathrm{d}} \\ v_{\mathrm{ref}} \\ i_{\mathrm{dcmax}} \\ k_{\mathrm{dc}} \end{bmatrix}, \quad \dot{\mathbf{q}} = \frac{\mathrm{d}}{\mathrm{d}t}\begin{bmatrix} q_{\mathrm{imax}} \\ q_{\mathrm{idcmax}} \end{bmatrix} = \mathbf{0}. \tag{A.1}$$

The network equations are given by

$$0 = v_\mathrm{d} - v_\mathrm{cd} + r_\mathrm{f}\left(\underbrace{\frac{v_\mathrm{d}}{r_\mathrm{load}} + \frac{v_\mathrm{q}}{x_\mathrm{load}}}_{i_\mathrm{d}} \underbrace{-\frac{v_\mathrm{q}}{x_\mathrm{cf}}}_{i_\mathrm{cfd}}\right) - x_\mathrm{f}\left(\underbrace{\frac{v_\mathrm{q}}{r_\mathrm{load}} - \frac{v_\mathrm{d}}{x_\mathrm{load}}}_{i_\mathrm{q}} \underbrace{+\frac{v_\mathrm{d}}{x_\mathrm{cf}}}_{i_\mathrm{cfq}}\right), \quad \blacksquare \tag{A.2a}$$

$$0 = v_\mathrm{q} - v_\mathrm{cq} + x_\mathrm{lf}\left(\frac{v_\mathrm{d}}{r_\mathrm{load}} + \frac{v_\mathrm{q}}{x_\mathrm{load}} - \frac{v_\mathrm{q}}{x_\mathrm{cf}}\right) + r_\mathrm{f}\left(\frac{v_\mathrm{q}}{r_\mathrm{load}} - \frac{v_\mathrm{d}}{x_\mathrm{load}} + \frac{v_\mathrm{d}}{x_\mathrm{cf}}\right). \quad \blacksquare \tag{A.2b}$$

Coupling between DC and AC voltage

$$0 = v_\mathrm{cd} - v_\mathrm{cdm}\frac{1.0 + \Delta v_\mathrm{dc}}{v_\mathrm{dcref}} \quad \blacksquare, \tag{A.3a}$$

$$0 = v_\mathrm{cq} - v_\mathrm{cqm}\frac{1.0 + \Delta v_\mathrm{dc}}{v_\mathrm{dcref}}. \quad \blacksquare \tag{A.3b}$$

Back transformation to global dq reference frame

$$\begin{aligned} v_\mathrm{cdm} &= v_\mathrm{cdm}^{\Delta\theta} \cdot \cos(\Delta\theta) - v_\mathrm{cqm}^{\Delta\theta} \cdot \sin(\Delta\theta), \quad \text{(aux.)} \\ v_\mathrm{cqm} &= v_\mathrm{cqm}^{\Delta\theta} \cdot \cos(\Delta\theta) + v_\mathrm{cdm}^{\Delta\theta} \cdot \sin(\Delta\theta). \quad \text{(aux.)} \end{aligned} \tag{A.4}$$

The current control is given by

$$\begin{aligned} v_\mathrm{cdm}^{\Delta\theta} &= v_\mathrm{d}^{\Delta\theta} + x_\mathrm{id} + (i_\mathrm{cdlim} - i_\mathrm{cd}^{\Delta\theta})k_\mathrm{ip} - i_\mathrm{cq}^{\Delta\theta}x_\mathrm{lf}, \quad \text{(aux.)} \\ v_\mathrm{cqm}^{\Delta\theta} &= v_\mathrm{q}^{\Delta\theta} + x_\mathrm{iq} + (i_\mathrm{cqlim} - i_\mathrm{cq}^{\Delta\theta})k_\mathrm{ip} + i_\mathrm{cd}^{\Delta\theta}x_\mathrm{lf}, \quad \text{(aux.)} \end{aligned} \tag{A.5}$$

$$\begin{aligned} \dot{x}_\mathrm{id} &= (i_\mathrm{cdlim} - i_\mathrm{cd}^{\Delta\theta})k_\mathrm{ii}, \quad \square \\ \dot{x}_\mathrm{iq} &= (i_\mathrm{cqlim} - i_\mathrm{cq}^{\Delta\theta})k_\mathrm{ii}. \quad \square \end{aligned} \tag{A.6}$$

The switching conditions and reset functions of the current limitation are implemented by

$$\dot{q}_\mathrm{imax} = 0, \quad \square \tag{A.7}$$

$$q_\mathrm{imax}^{+} = h_\mathrm{qimax,1}(\overline{\mathbf{x}}^{-}, \mathbf{y}^{-}) = 1, \qquad s_\mathrm{imax,1}(\overline{\mathbf{x}}, \mathbf{y}) = |\underline{i}_\mathrm{cdqref}| - i_\mathrm{cmax} - k \cdot q_\mathrm{imax} \geq 0, \quad \triangle \tag{A.8}$$

$$q_\mathrm{imax}^{+} = h_\mathrm{qimax,0}(\overline{\mathbf{x}}^{-}, \mathbf{y}^{-}) = 0, \qquad s_\mathrm{imax,0}(\overline{\mathbf{x}}, \mathbf{y}) = (|\underline{i}_\mathrm{cdqref}| - i_\mathrm{cmax}) \cdot q_\mathrm{imax} < 0, \quad \triangle \tag{A.9}$$

whereas the algebraic equations are given by

$$0 = i_{\mathrm{cdlim}} - \left((1 - q_{\mathrm{imax}}) i_{\mathrm{cdref}} + q_{\mathrm{imax}} \frac{i_{\mathrm{cdref}} i_{\mathrm{cmax}}}{\sqrt{i_{\mathrm{cdref}}^2 + i_{\mathrm{cqref}}^2}} \right), \quad \blacksquare \tag{A.10}$$

$$0 = i_{\mathrm{cqlim}} - \left((1 - q_{\mathrm{imax}}) i_{\mathrm{cqref}} + q_{\mathrm{imax}} \frac{i_{\mathrm{cqref}} i_{\mathrm{cmax}}}{\sqrt{i_{\mathrm{cdref}}^2 + i_{\mathrm{cqref}}^2}} \right). \quad \blacksquare \tag{A.11}$$

The inner voltage control is

$$\begin{aligned} i_{\mathrm{cdref}} &= i_{\mathrm{d}}^{\Delta\theta} + x_{\mathrm{vd}} + (v_{\mathrm{dref}} - v_{\mathrm{d}}^{\Delta\theta}) k_{\mathrm{vp}} - \frac{v_{\mathrm{q}}^{\Delta\theta}}{x_{\mathrm{cf}}}, \quad \text{(aux.)} \\ i_{\mathrm{cqref}} &= i_{\mathrm{q}}^{\Delta\theta} + x_{\mathrm{vq}} + (v_{\mathrm{qref}} - v_{\mathrm{q}}^{\Delta\theta}) k_{\mathrm{vp}} + \frac{v_{\mathrm{d}}^{\Delta\theta}}{x_{\mathrm{cf}}}. \quad \text{(aux.)} \end{aligned} \tag{A.12}$$

The inner voltage control with anti-windup is

$$\begin{aligned} \dot{x}_{\mathrm{vd}} &= (v_{\mathrm{dref}} - v_{\mathrm{d}}^{\Delta\theta}) k_{\mathrm{iv}} (1 - q_{\mathrm{imax}}), \quad \square \\ \dot{x}_{\mathrm{vq}} &= (\underbrace{v_{\mathrm{qref}}}_{=0} - v_{\mathrm{q}}^{\Delta\theta}) k_{\mathrm{iv}} (1 - q_{\mathrm{imax}}). \quad \square \end{aligned} \tag{A.13}$$

The outer loop voltage control with anti-windup is

$$v_{\mathrm{dref}} = x_{\mathrm{vdroop}} + k_{\mathrm{vpdroop}} \left(v_{\mathrm{ref}} - \underbrace{\sqrt{\left(v_{\mathrm{d}}^{\Delta\theta}\right)^2 + \left(v_{\mathrm{d}}^{\Delta\theta}\right)^2}}_{v_{\mathrm{meas}}^{\Delta\theta}} \right), \quad \text{(aux.)} \tag{A.14}$$

$$\dot{x}_{\mathrm{vdroop}} = k_{\mathrm{vidroop}} \left(v_{\mathrm{ref}} - \sqrt{\left(v_{\mathrm{d}}^{\Delta\theta}\right)^2 + \left(v_{\mathrm{d}}^{\Delta\theta}\right)^2} \right) (1 - q_{\mathrm{imax}}). \quad \square \tag{A.15}$$

The power synchronisation loop (droop control) is given by

$$\Delta\dot{\theta} = (p_{\mathrm{ref}} - p_{\mathrm{f}}) k_{\mathrm{d}}, \quad \square \tag{A.16}$$

with

$$\begin{aligned}\dot{p}_\mathrm{f} &= (p_\mathrm{meas}^{\Delta\theta} - p_\mathrm{f})\omega_\mathrm{f} \\ &= \left(v_\mathrm{d}^{\Delta\theta} i_\mathrm{d}^{\Delta\theta} + v_\mathrm{q}^{\Delta\theta} i_\mathrm{q}^{\Delta\theta} - p_\mathrm{f}\right)\omega_\mathrm{f}. \quad \square\end{aligned} \tag{A.17}$$

The adaption of the power reference by SECM-1 is given by

$$0 = p_\mathrm{ref} - \left((1 - q_\mathrm{imax})p_\mathrm{ref0} + q_\mathrm{imax}\left(i_\mathrm{cdlim} v_\mathrm{d}^{\Delta\theta} + i_\mathrm{cqlim} v_\mathrm{q}^{\Delta\theta}\right)\right). \quad \blacksquare \tag{A.18}$$

The DC circuit and energy model is modelled by

$$\dot{\Delta v}_\mathrm{dc} = \frac{1}{c_\mathrm{dc}}\left(i_\mathrm{dcref} - \frac{1.0 + \Delta v_\mathrm{dc}}{r_\mathrm{dc}} - \underbrace{\frac{v_\mathrm{cd} i_\mathrm{cd} + v_\mathrm{cq} i_\mathrm{cq}}{1.0 + \Delta v_\mathrm{dc}}}_{i_\mathrm{dc}}\right), \quad \square \tag{A.19}$$

whereas the switching condition and reset function of the DC current limitation are given by

$$\dot{q}_\mathrm{idcmax} = 0, \quad \square \tag{A.20}$$

$$q_\mathrm{idcmax}^{+} = h_\mathrm{qidcmax,1}(\overline{\mathbf{x}}^{-}, \mathbf{y}^{-}) = 1, \quad s_\mathrm{idcmax,1}(\overline{\mathbf{x}}, \mathbf{y}) = |\underline{i}_{\mathrm{dcref}\tau}| - i_\mathrm{dcmax} - k q_\mathrm{idcmax}, \geq 0, \triangle \tag{A.21}$$

$$q_\mathrm{idcmax}^{+} = h_\mathrm{qidcmax,0}(\overline{\mathbf{x}}^{-}, \mathbf{y}^{-}) = 0, \quad s_\mathrm{idcmax,0}(\overline{\mathbf{x}}, \mathbf{y}) = (|\underline{i}_{\mathrm{dcref}\tau}| - i_\mathrm{dcmax}) \cdot q_\mathrm{idcmax} < 0. \triangle \tag{A.22}$$

This is followed by the algebraic equation for the DC reference current

$$0 = i_\mathrm{dcref} - \left((1 - q_\mathrm{idcmax}) i_{\mathrm{dcref}\tau} + q_\mathrm{idcmax} \mathrm{sgn}(i_{\mathrm{dcref}\tau}) i_\mathrm{dcmax}\right), \quad \blacksquare \tag{A.23}$$

and its delay

$$\dot{i}_{\mathrm{dcref}\tau} = \frac{i_\mathrm{dcref0} - i_{\mathrm{dcref}\tau}}{T_\mathrm{DC}}. \quad \square \tag{A.24}$$

In general, the DC reference current is given by

$$i_\mathrm{dcref0} = \frac{p_\mathrm{ref}}{v_\mathrm{dcref}} - \Delta v_\mathrm{dc} k_\mathrm{dc} + \frac{1.0 + \Delta v_\mathrm{dc}}{r_\mathrm{dc}} + \frac{\Delta p_\mathrm{cf}}{v_\mathrm{dcref}}. \quad \text{(aux.)} \tag{A.25}$$

The power difference between the converter and PCC is determined by

$$\Delta \dot{p}_{\mathrm{cf}} = (\Delta p_{\mathrm{c}} - \Delta p_{\mathrm{cf}})\omega_{\mathrm{f}}, \tag{A.26}$$

with

$$\Delta p_{\mathrm{c}} = v_{\mathrm{cd}}^{\Delta\theta} i_{\mathrm{cd}}^{\Delta\theta} + v_{\mathrm{cq}}^{\Delta\theta} i_{\mathrm{cq}}^{\Delta\theta} - \left(v_{\mathrm{d}}^{\Delta\theta} i_{\mathrm{d}}^{\Delta\theta} + v_{\mathrm{q}}^{\Delta\theta} i_{\mathrm{q}}^{\Delta\theta}\right). \quad \text{(aux.)} \tag{A.27}$$

The voltage v_{d}, v_{q}, v_{cd}, v_{cq} as well as the currents i_{d}, i_{q}, i_{cd}, $_{\mathrm{cq}}$ are transformed into a local dq-coordinate system by the droop angle $\Delta\theta$

$$v_{\mathrm{d}}^{\Delta\theta} = v_{\mathrm{d}} \cdot \cos(\Delta\theta) + v_{\mathrm{q}} \cdot \sin(\Delta\theta), \quad \text{(aux.)} \tag{A.28}$$

$$v_{\mathrm{q}}^{\Delta\theta} = v_{\mathrm{q}} \cdot \cos(\Delta\theta) - v_{\mathrm{d}} \cdot \sin(\Delta\theta), \quad \text{(aux.)} \tag{A.29}$$

$$i_{\mathrm{d}}^{\Delta\theta} = \frac{v_{\mathrm{d}}^{\Delta\theta}}{r_{\mathrm{load}}} + \frac{v_{\mathrm{q}}^{\Delta\theta}}{x_{\mathrm{load}}}, \quad \text{(aux.)} \tag{A.30}$$

$$i_{\mathrm{q}}^{\Delta\theta} = \frac{v_{\mathrm{q}}^{\Delta\theta}}{r_{\mathrm{load}}} - \frac{v_{\mathrm{d}}^{\Delta\theta}}{x_{\mathrm{load}}}, \quad \text{(aux.)} \tag{A.31}$$

$$i_{\mathrm{cfd}}^{\Delta\theta} = \frac{v_{\mathrm{q}}^{\Delta\theta}}{x_{\mathrm{cf}}}, \quad \text{(aux.)} \tag{A.32}$$

$$i_{\mathrm{cfq}}^{\Delta\theta} = -\frac{v_{\mathrm{d}}^{\Delta\theta}}{x_{\mathrm{cf}}}, \quad \text{(aux.)} \tag{A.33}$$

$$i_{\mathrm{cd}}^{\Delta\theta} = i_{\mathrm{cd}}^{\Delta\theta} - i_{\mathrm{cfd}}^{\Delta\theta}, \quad \text{(aux.)} \tag{A.34}$$

$$i_{\mathrm{cq}}^{\Delta\theta} = i_{\mathrm{cq}}^{\Delta\theta} - i_{\mathrm{cfq}}^{\Delta\theta}. \quad \text{(aux.)} \tag{A.35}$$

A.3 Eigenvalue analysis of DADS model with SECM-1

To calculate the eigenvalues $\lambda_i = \sigma_i + \mathrm{j}\omega_i$, the steady-state values from the simulation in Section 4.5 at $t = 0\,\mathrm{s}$ and at $t = 4\,\mathrm{s}$ are taken. The results in Fig. A1 show that all eigenvalues remain in the left half-plane, revealing that the GFM converter is stabilised by SECM-1. The main difference is that under current limiting some eigenvalues become zero. This means that the system does not have a unique equilibrium point, but an equilibrium subspace [120]. This means for this grid that for example for $\Delta\theta \neq 0$ and $\Delta\dot{\theta} = 0$ other steady-state frequency deviations could be present for such an equilibrium.

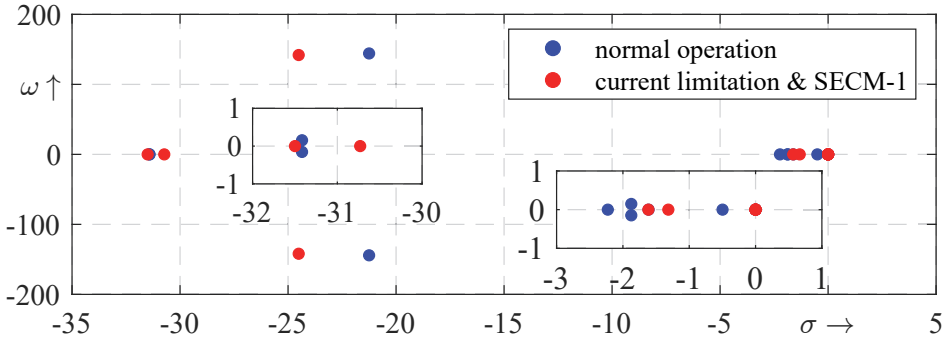

Figure A1: DADS eigenvalues under normal and current limitation conditions

Table A5: List of the DADS eigenvalues with and without current limitation

Eigenvalue	Corresponding state	without AC current lim.	with AC current lim.
λ_1	x_{id}	-31.417 - j0.15439	-31.5
λ_2	x_{iq}	-31.417 + j0.15439	-30.73
λ_3	x_{vd}	-21.249 - j144.2	-24.508 - j141.94
λ_4	x_{vq}	-21.249 + j144.2	-24.508 + j141.94
λ_5	x_{vdroop}	-2.2275	-1.616
λ_6	p_{f}	-1.8738 - j0.14723	-1.3154
λ_7	$\Delta\theta$	-1.8438 + j0.14723	0
λ_8	Δv_{dc}	-1.6133	0
λ_9	$\Delta i_{\mathrm{dcref}\tau}$	-0.4978	0
λ_{10}	Δp_{cf}	0	0
λ_{11}	q_{imax}	0	0
λ_{12}	q_{idcmax}	0	0

B Additional information about the modelling of power electronic loads

In this appendix, additional information about the measurement and modelling of power electronic loads from Chapter 5 is given. First, additional information about the phasor load model is given in Section B.1. Second, in Section B.2 additional information about the laboratory setup, the EMT load models as well as some extra measurements are presented.

B.1 Inclusion of the phasor power electronic load model into transient stability programs

First, the inclusion of the phasor power electronic load model into transient stability programs is outlined. Afterwards, in Section B.1.1 the function to calculate the switch-on time for the phasor load model with Cardano's formula is presented.

Next, a general inclusion of the phasor power electronic load model into a time-domain simulation, based on the flowchart given in Fig. B1, is presented. The implementation starts with an iterative procedure between the power flow of the grid and the initialisation of the power electronic load model, due to its voltage-dependent power consumption. At the beginning of each iteration of the time-domain simulation, t_{mod} is calculated over the *modulo* function of the current simulation t_{sim} and the duration of a half-cycle $T/2$. With t_{mod} it is thus possible to determine the current point in time of the half-wave. Here, it is assumed that this 'fictional' half-wave (due to the phasor simulation) also starts at the beginning of the simulation. Next, t_{sum} is formed, which represents the sum of its last value $t_{\mathrm{sum}-1}$ and the deviation between the current time step t_{sim} and last time step $t_{\mathrm{sim}-1}$. Through t_{sum} it can be determined if the accumulation of the last time steps is greater than $T/2$ and thus if a new half-wave has started or not.

In general, the implementation can be divided into two parts. In part one it is first checked, if a new half-wave has started or not. If a new half-wave has started, the declined capacitance voltage $v_{\mathrm{off},T/2}$ at the beginning of this half-wave is calculated (cf. (5.12)). Here, it is distinguished whether in the half-wave before the capacitance voltage coincided with the

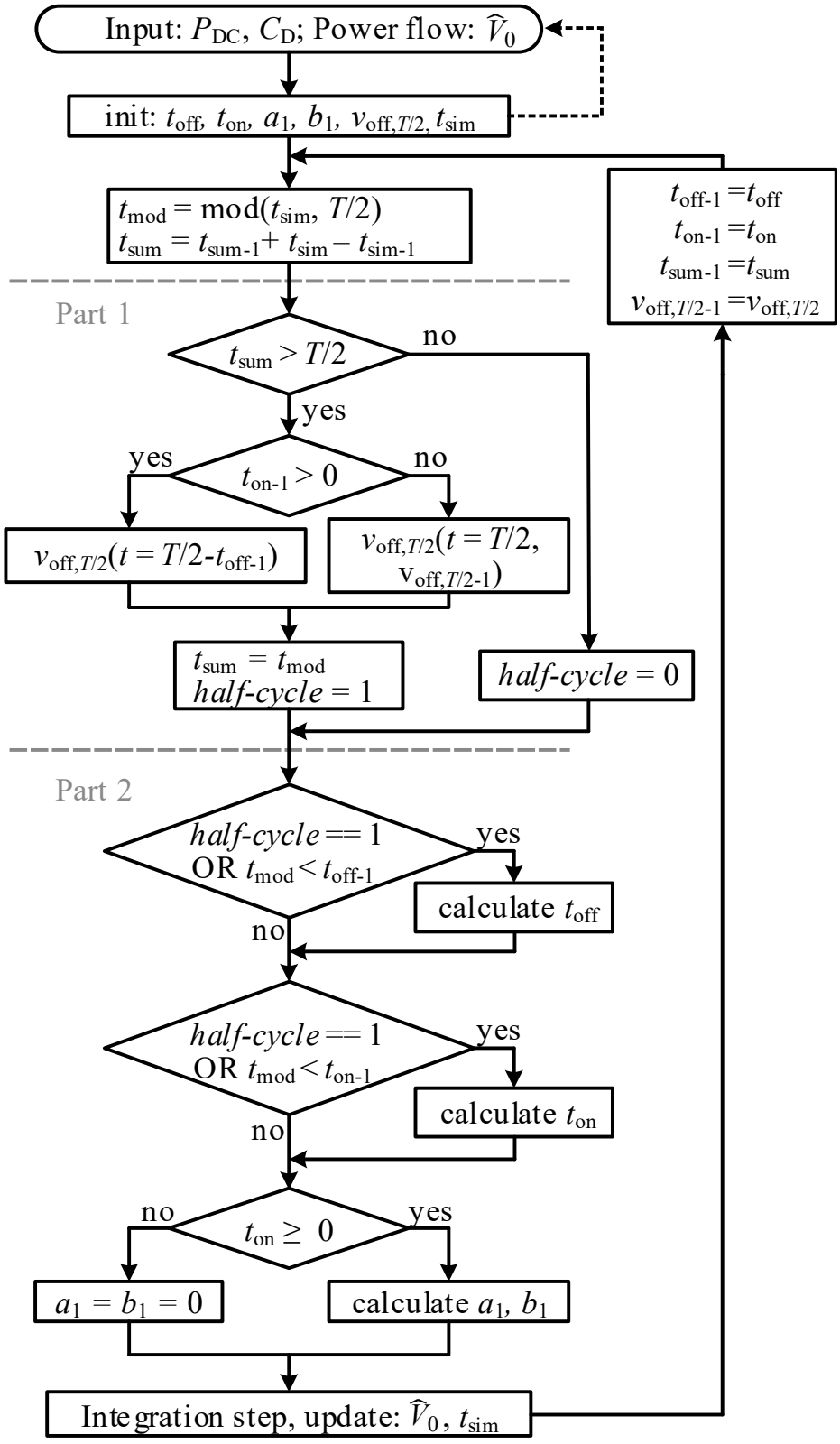

Figure B1: Flowchart of the PE load model for the inclusion in transient stability simulations

grid voltage or not, which is checked by the previous switch-on time $t_{\mathrm{on}-1}$. If no coincidence has occurred before, $v_{\mathrm{off},T/2}$ has to be calculated over a complete half-wave with its previous value $v_{\mathrm{off},T/2-1}$, as it has decreased much more (cf. Fig. 5.3 at $t = 0.05\,\mathrm{s}$ or $0.06\,\mathrm{s}$). In this part also the flag *half-cycle* is set to pass on the information of a new half-wave, since t_{sum} is previously reset. In the second part, t_{on} and t_{off} are calculated on the basis of the current voltage $\hat{U}_0$ and $v_{\mathrm{off},T/2}$ from part one. Here, t_{on} and t_{off} are always calculated if a new half-wave has started. They are also recalculated during the half-cycle if the current point in time t_{mod} is before their occurrence. To determine if they have already occurred, their value from the last time step is used. For example, if t_{mod} is currently between $t_{\mathrm{on}-1}$ and $t_{\mathrm{off}-1}$, only t_{off} is recalculated, because $t_{\mathrm{on}-1}$ was already before (cf. Fig. 5.3 for $t_{\mathrm{mod}} = 4\,\mathrm{ms}$ at $t = 0.014\,\mathrm{s}$). In the case that no coincidence happened before, $t_{\mathrm{on}-1}$ is negative. In the end, the RMS values of the current are calculated and given to the simulation program. After the integration step, the grid voltage $\hat{U}_0$ and the simulation time are updated. Furthermore the calculated values of $t_{\mathrm{on}}, t_{\mathrm{off}}, t_{\mathrm{sum}}$ and $v_{\mathrm{off},T/2}$ from the current iteration are taken into the subsequent iteration as previous elements $t_{\mathrm{on}-1}, t_{\mathrm{off}-1}, t_{\mathrm{sum}-1}$ and $v_{\mathrm{off},T/2-1}$.

B.1.1 Function for calculating the switch-on time with Cardano's formula

First, a comparison between the approximated squared sine function and the original function is presented, which is needed for calculating the switch-on time t_{on}. As can be seen in Fig. B2, the approximated function matches the original function inside the region of interest very well. In addition, as x_4 is negative, the approximation function goes negative after $\pi/2$, which is preferred to determine if the rectified voltage hits the grid voltage.

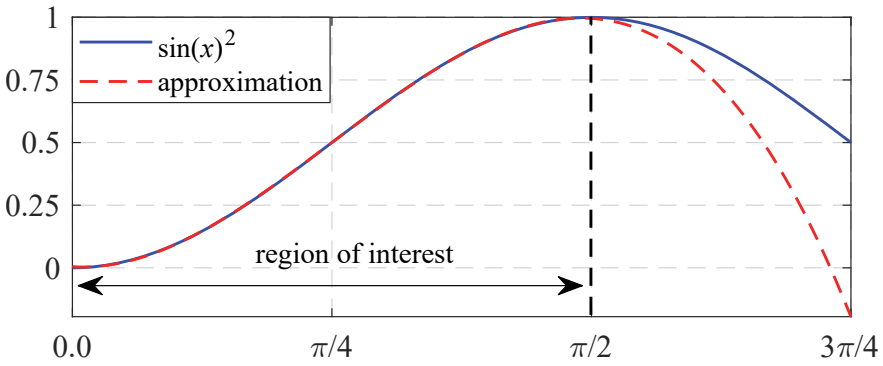

Figure B2: Comparison between the squared sine function and its approximation function

The following Julia code is for realising the function f_{ton} including Cardano's formulas from section 5.4. Different to Fig.5.12, here also p_{dc} and c_{dc} are taken as an input. However, as these are constant parameters, they do not change during a simulation. Yet, they could change between the simulations, which is why they are included here as inputs. In addition, note that for the case where *delta* is less or greater than zero, an additional if-statement is included to avoid solutions greater than 5 ms, which would imply a switch-on after the voltage peak.

```
function fon(V0,voffT2,Pdc,Cdc)
    x1 = 0.004517042542168
    x2 = -0.084973441092720
    x3 =  1.367157627046003
    x4 = -0.580239811988436
    w = 100*pi
    A = V0^2*w^3*x4
    B = V0^2*w^2*x3
    C = V0^2*w*x2 + 2*Pdc/Cdc
    D = V0^2*x1 - voffT2^2

    # Cardano's formula
    p = (9*A*C-3*B^2)./(9*A^2)
    q = (2*B^3 -9*A*B*C + 27*D*A^2)./(27*A^3)
    delta = (q/2)^2 +  (p/3)^3

    ton = -1.0
    if delta > 0
        u = Complex(-q/2+sqrt(delta))^(1/3)
        v = Complex(-q/2-sqrt(delta))^(1/3)
        x1 = u+v- B/(3*A)
        ton = real(x1)
        if ton > 0.005
            ton = -1.0
        end
    elseif delta == 0 && p == 0
        x2 = - B/(3*A)
        ton = real(x2)
    elseif delta == 0 && p != 0
        x1 = 3*q/p- B/(3*A)
        x23 = -3*q/(2*p)- B/(3*A)
```

```
        ton = real(x23)
    elseif delta < 0
        tmp = 1/3.0*acos(-q/2.0*sqrt(-27.0/(p.^3)))
        x1 = -sqrt(-4/3*p).*cos(tmp+pi/3) - B/(3*A)
        x2 =  sqrt(-4/3*p).*cos(tmp)      - B./(3*A)
        x3 = -sqrt(-4/3*p).*cos(tmp-pi/3) - B./(3*A)
        ton =  real(x1)
        if ton > 0.005
            ton = -1.0
        end
    end
    return ton
end
```

B.2 Laboratory: Load data and additional measurements

This section provides additional information on the power electronic loads and laboratory equipment. First, the load and transformer data which have been used in the laboratory are given in Section B.2.1. Second, in Section B.2.2, an example is given of the distorted voltage of the power amplifiers during current limitation. This is followed by the determination of grid impedance values for power response measurements in Section B.2.3. The corresponding measurement results are given in Section B.2.4. In Section B.2.5 the measured impact of the EMI filter on power response is shown. In the end, a detailed description of the general component design of power electronic loads is given in Section B.2.6.

B.2.1 Load and transformer data

Table B1: Technical data of the measured power electronic loads

Label	# Phases	PFC	P_{dc} (W)	measured cos(φ)	V_{dc} (V)
PEL-1	1	none	60	0.967 (cap.)	29.4
PEL-2	1	passive	230	0.937 (ind.)	12
PEL-3	1	active	360	0.996 (cap.)	390
PEL-4	3	passive	3000	0.989 (ind.)	300

Table B2: Electrical parameters of the laboratory transformers

	1+2 Winding resistance	1+2 Leakage inductance	Iron resistance	Primary inductance
B (1ph)	0.311 Ω	0.472 mH	225.11 Ω	1.29 H
	a: 0.082 Ω	a: 0.221 mH	a: 192.39 Ω	L1: 1.25 H
C (3ph)	b: 0.079 Ω	b: 0.226 mH	b: 532.39 Ω	L2: 2.45 H
	c: 0.080 Ω	c: 0.223 mH	c: 203.09 Ω	L3: 1.27 H

Table B3: Electrical and base values of the power electronic EMT models (note that v_{trip} is based on the peak voltage of v_{base}. *Minimal value of load resistance R_{dc} is set to 65% of base impedance)

Label	x_{Cdc}	x_{Ld}	v_{trip}	V_{base}	P_{dc}
PEL-1	0.058 pu	-	0.0 pu	230 V	60 W
PEL-2	0.06 pu	0.034 pu	0.65 pu	230 V	230 W
PEL-3	0.1 pu	0.0007 pu	0.1 pu	230 V	360 W
PEL-4	0.361 pu	0.01247 pu	0.0 pu *	230 V	3000 W

Table B4: Electrical values of the phasor and EMT PEL-1a model

Label	c_{dc}	x_{Ld}	v_{trip}
PEL-1a	$\frac{1}{0.036 \cdot 100\pi} \approx 0.088$ pu	-	0.0 pu

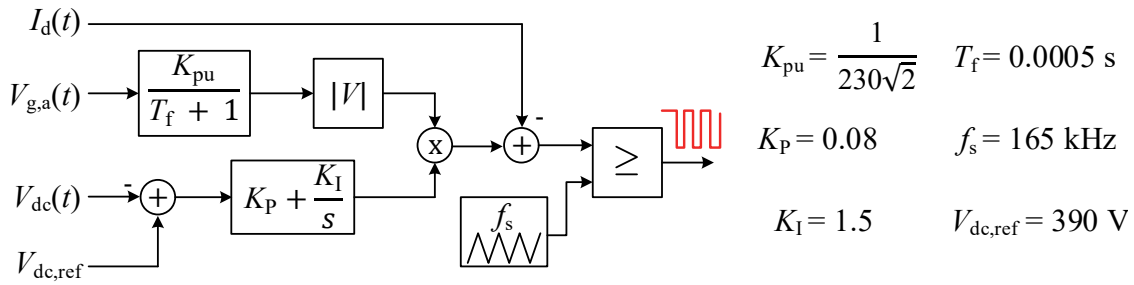

Figure B3: Controller of boost converter for active PFC of PEL-3

B.2.2 Distortion of power amplifier voltage due to current limitation

Fig. B4 shows an example of the distorted voltage of the power amplifiers, due to their internal current limitation. As can be seen, the voltage distortion of the three-phase load PEL-4 is much more severe than that of PEL-2. The reason is that PEL-2 would only slightly violate the current limitation value, whereas PEL-4 would lead to much higher currents. This also explains the more significant deviation of the PEL-4 model from its measurements.

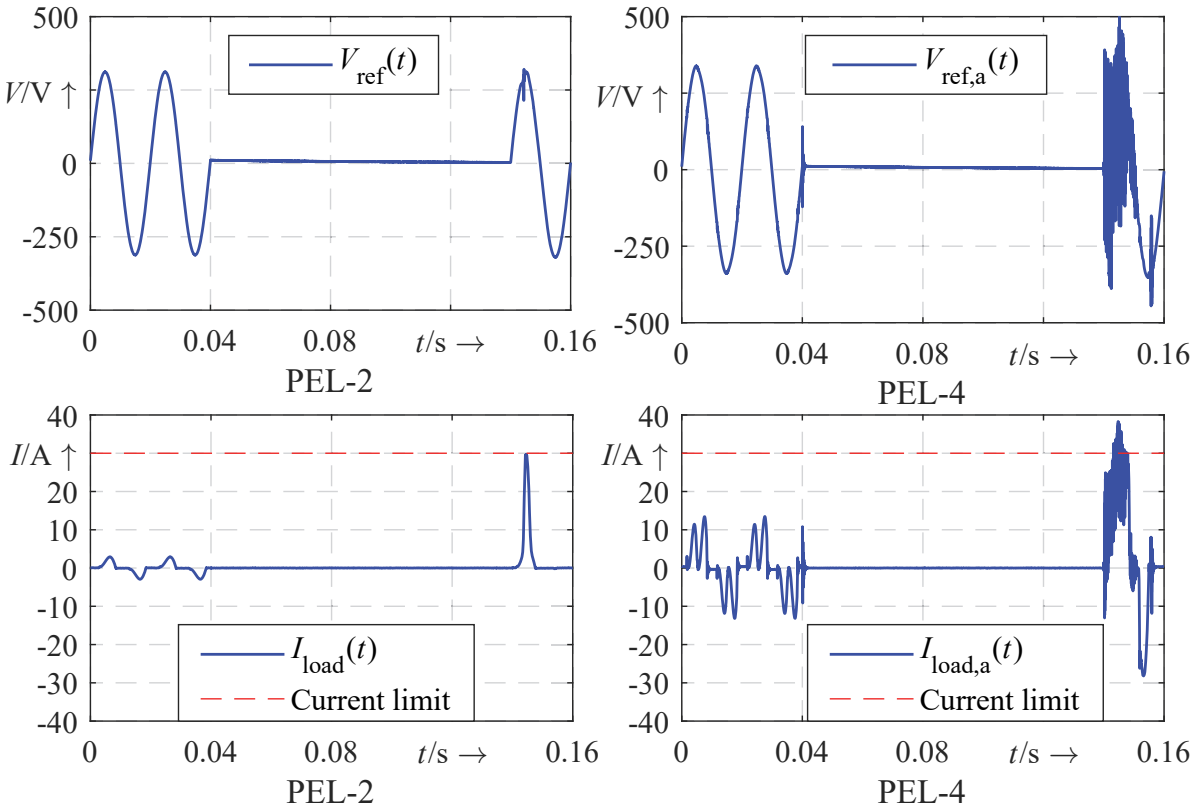

Figure B4: Examples of measured distorted power amplifier voltage due to internal current limitation after $\Delta v = 1.0$ pu

B.2.3 Determination of grid impedance values for power response measurements

This section describes how to determine the values of the laboratory grid impedances in order to measure their impact on the power response of the loads. The values of the grid resistance R_{grid} and grid inductance $X_{\text{L,grid}}$ are chosen according to two objectives. The first objective is that the approximate voltage drop from the source to the load should be around 10 % at steady-state so that the loads operate at their lower voltage band. Therefore, a rated grid impedance z_{grid} of 0.1 pu is needed, which can be expressed as follows

$$z_{\text{grid}} = \frac{Z_{\text{grid}}}{Z_{\text{base}}} = \frac{Z_{\text{grid}}}{\frac{V_{\text{base}}^2}{P_{\text{r}}}} = 0.1\,\text{pu}. \tag{B.1}$$

The second objective is that the ratio between inductance and resistance shall reflect the conditions that are usual in low-voltage grids. Here, a value around 0.4 is chosen. Therefore, this second condition has to be met

$$\frac{X_{\text{L,grid}}}{R_{\text{grid}}} = 0.4. \tag{B.2}$$

These equations can be coupled by calculating the magnitude of the grid impedance Z_{grid}

$$Z_{\text{grid}} = \sqrt{X_{\text{L,grid}}^2 + R_{\text{grid}}^2}. \tag{B.3}$$

By inserting (B.2) and (B.3) in (B.1), the corresponding values for resistance and inductance of each power electronic load can be calculated. Tab. B5 shows the actual values that are used for the measurements. Overall, the real values are close enough to the targeted values. It has to be noted that for PEL-4 no sufficient grid impedances are available at the laboratory, due to the high current requirements. For this reason, the measurements in the next section are carried out for PEL-1 to PEL-3 only.

Table B5: Grid impedance values for each power electronic load

Label	R_{grid}	L_{grid}	$X_{\text{L,grid}}$	z_{grid}	$\frac{X_{\text{L,grid}}}{R_{\text{grid}}}$
PEL-1	81.4 Ω	107.73 mH	33.84 Ω	0.100 pu	0.416
PEL-2	22.8 Ω	29.71 mH	9.33 Ω	0.107 pu	0.409
PEL-3	14.4 Ω	20.81 mH	6.54 Ω	0.108 pu	0.454

B.2.4 Impact of high grid impedance on power response

The impact of a high grid impedance on the power response of the power electronic loads is analysed in the following. The background to this is that in voltage-critical situations, high power often flows from a generation centre to a load centre, with heavily loaded lines in between. As a result, a high voltage drop occurs across these lines, resulting in a reduced voltage at the load side. From the point of view of the load, this can also be seen as a high grid impedance between load and generation. A detailed description of how the grid impedances are selected for each load is given in the previous section.

Fig. B5 displays the comparison of the active and reactive power behaviour between the measurements without (which are the previous measurements) and with the grid impedance marked by a (g). The legend entries for PEL-1 are also valid for PEL-3, whereas for PEL-2 only the legend for the simulation with the grid impedance of PEL-1 is used As can be seen from the measurements, the grid impedance has a strong influence on all power responses. Furthermore, the current limit of the power amplifier is never reached in all measurements with the grid impedance, as the grid inductance limits the rising current. A major change is seen in the greatly reduced power consumption during voltage recovery. This is partly because the inrush current is limited, but also because there is a large voltage drop across the grid impedance, reducing the voltage at the load. Looking at PEL-1, the reactive power changes from capacitive to inductive for almost the entire time. This includes its steady-state reactive power consumption. This can be explained by the fact that the current now has a significantly larger phase shift due to the relatively large grid inductance. However, this is not the case for the reactive power of PEL-3, which is more capacitive. One reason for this could be that in this case the grid inductance only serves as a larger storage for the active PFC controller. For active power, however, the pre- and post-fault values are always at rated power for all loads. In the case of PEL-1 for $\Delta v = 0.8\,\mathrm{pu}$ and $\Delta v = 1.0\,\mathrm{pu}$, the load disconnects after voltage recovery but reconnects after one second, which is not shown here. It can also be observed that the loads are more often unable to recover their active power during the fault or disconnect earlier. This is probably due to the DC/DC converters reaching their limits earlier due to the lower voltages. It can be concluded that the high power consumption during voltage recovery is significantly reduced and that power recovery during the fault is not as frequent as before. These measurements also reveal that reactive power in particular is dependent on the grid impedance, even at a steady state. In addition, the grid impedance can be characterised not only by the voltage drop it causes but also by its inductance dynamics and the resulting current phase shift. If

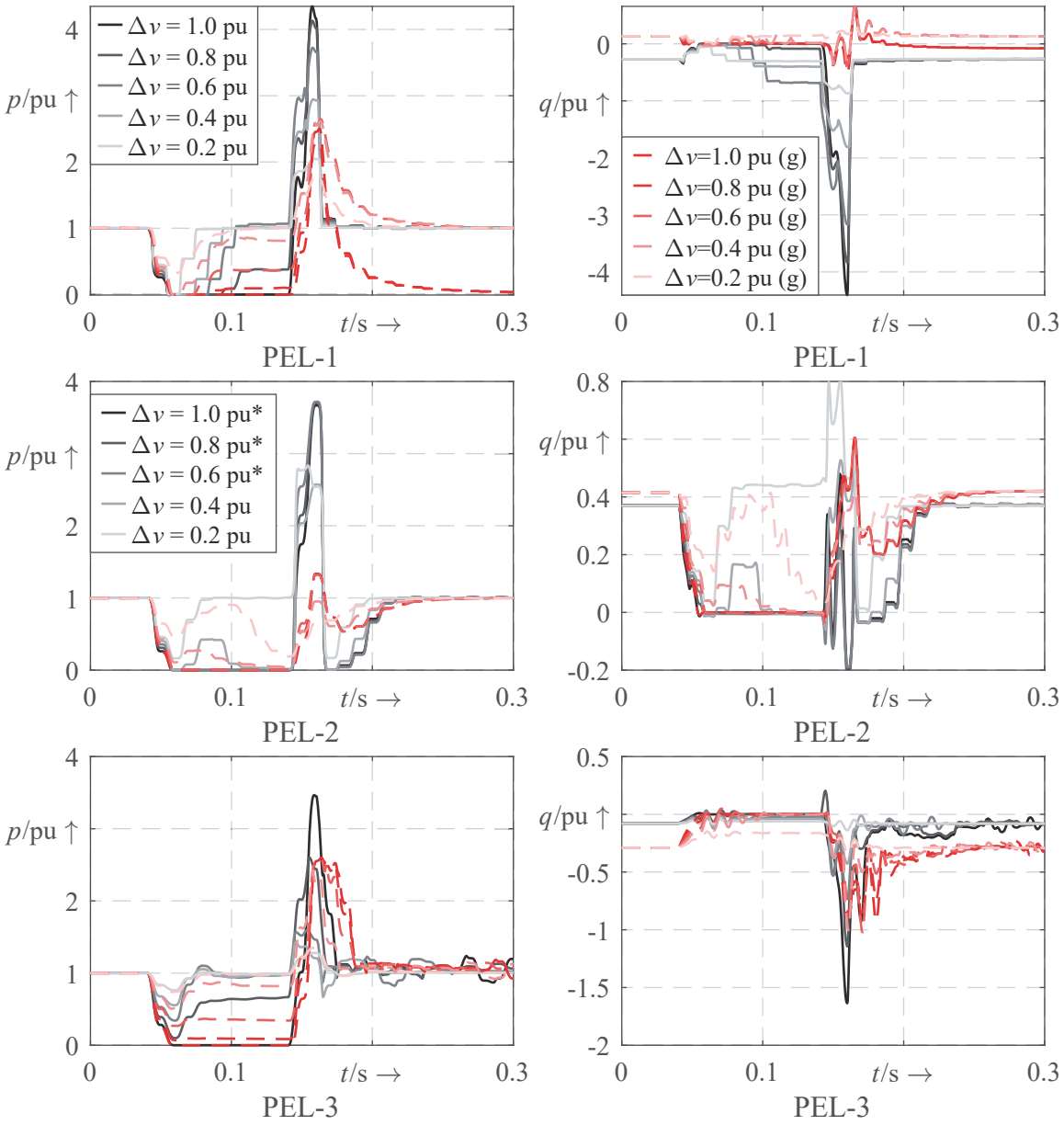

Figure B5: Comparison between the measured active and reactive power response for no and high grid impedance (measurements with grid impedance are marked with a (g))

the characteristics of the power electronic loads were dominated only by the voltage magnitudes, similar characteristics should have been observed from the earlier measurements. Since the observations made here show dynamics faster than the fundamental frequency, and the interactions between the system impedance and the load can only be adequately described by the differential equations of inductances and capacitances, it is concluded that EMT models should be used for these loads.

In addition to the grid impedance, the effect of the EMI filter on the power response is also analysed. The results can be found in the next section.

B.2.5 Impact of EMI filter on power response

Next, the impact of the grid side EMI filter of the power electronic load on the power response is analysed. For this, an additional measurement is carried out where the EMI filter of PEL-3 is unsoldered. Generally, the EMI filter shall attenuate high-frequency noise which is emitted by the load, but also to protect the load from high grid harmonics [144]. The filter circuit is illustrated in Fig. B6, where the inductance is a common mode choke. Fig. B6 also shows the power response of PEL-3 with and without the EMI filter. As the results indicate, the filter has nearly no influence on the fundamental active component. For reactive power, only small differences can be seen. For example, the steady-state reactive power consumption decreases from 26.5 VAr (cap.) to 12.5 VAr (cap.), which results in a higher power factor from 0.997 to 0.999. As can be seen by these numbers, the impact of the filter is almost negligible. In addition, the reactive power evolution during and after the voltage drop is slightly different, but the influence is also small. For this reason, it can be concluded that the EMI filter has a negligible impact on the fundamental power response and can therefore be neglected for modelling, although this leads to small errors within the reactive power.

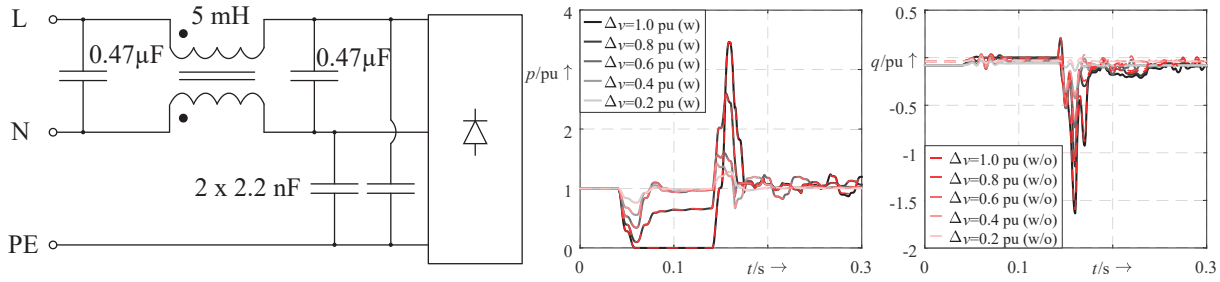

Figure B6: EMI filter design and comparison of measured active and reactive power response for PEL-3 with (w) and without (w/o) EMI filter (own illustration, EMI filter circuit based on [144])

B.2.6 Component design of power electronic loads

For most SMPS loads, the design of the smoothing capacity C_{dc} depends on the rated power, the voltage input range and the hold-up time. The following equation can be used

to calculate the needed capacitance [92]

$$C_{\mathrm{dc}} = \frac{2 \cdot P_{\mathrm{r}} \cdot t_{\mathrm{hold}}}{\eta \cdot (V_{\mathrm{nom}}^2 - V_{\mathrm{min}}^2)}. \tag{B.4}$$

Here, the time t_{hold} is the hold-up time and describes how long the capacitance can supply the load, in case of an undesired disconnection from the grid. A typical value is 23 ms which is also the main criterion in sizing this capacitance [92]. The parameter η is the efficiency of the load, V_{nom} is the nominal phase to ground RMS voltage and V_{min} is the minimum input voltage at which normal operation shall be possible for the load. Fig. B7 shows typical values of C_{dc} depending on the rated power P_{r} with $t_{\mathrm{hold}} = 23\,\mathrm{ms}$, $\eta = 95\,\%$, $V_{\mathrm{nom}} = 230\,\mathrm{V}$ and $V_{\mathrm{min}} = 150\,\mathrm{V}$ (values taken from [92]). If these values are related by V_{nom} and P_{r}, a per unit impedance x_{Cd} for C_{dc} can be calculated

$$x_{\mathrm{Cd}} = \frac{1}{C_{\mathrm{dc}} \cdot 2\pi \cdot 50\,\mathrm{Hz}} \cdot \frac{P_{\mathrm{r}}}{V_{\mathrm{nom}}^2} \approx 0.036\,\mathrm{pu}. \tag{B.5}$$

With this value, the capacitance C_{dc} can be calculated for a different base power and base voltage, e.g. for a specific load.

Similarly, a per unit value can be calculated for the filtering induction L_{d}, which is here for passive PFC. The aim of the inductor L_{d} is to reduce the load current harmonics. Therefore, its sizing aims to meet the harmonic limits for class D devices of the IEC norm 61000-3-2 [160]. Here, class D devices range from 75 W to 600 W. As the harmonic limits depend on the rated power of the device, a per unit value for L_{d} is also possible. In [92] the following per unit impedance x_{Ld} has been determined for which the harmonic class D limits are met

$$x_{\mathrm{Ld}} = 2\pi \cdot 50\,\mathrm{Hz} \cdot L_{\mathrm{d}} \cdot \frac{P_{\mathrm{r}}}{V_{\mathrm{nom}}^2} \approx 0.03\,\mathrm{pu}. \tag{B.6}$$

Values of L_{d} meeting this requirements are also presented in Fig. B7 as a function of the rated power. As for loads smaller than 75 W no harmonic limits are specified, there is also no need for a filtering inductance and thus no PFC.

For active PFC, the sizing of L_{d} is a bit different since its primary function is now to work as temporary storage of the current $I_{\mathrm{d}}(t)$ of the boost converter. In the following, the dimensioning process is made using the example of the design of load PEL-3 [150] and is, therefore, consistent with the modelling of this circuit. It should be noted here that other manufacturers may design the active PFC slightly differently, depending on the underlying design goals, e.g. continuous or discontinuous current mode [161, 162]. Here,

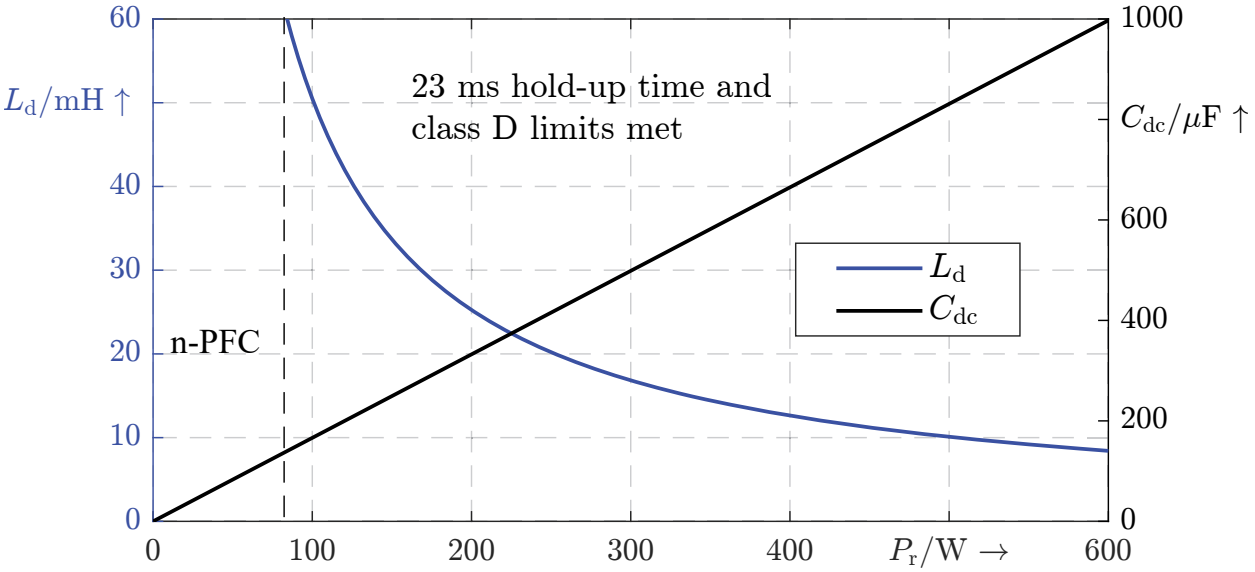

Figure B7: Sizing of smoothing capacitance C_{dc} to meet 23 ms hold-up time and filter inductance L_d to meet class D limits (own representation, based on [92])

the inductance L_d can be calculated by the following equation [150]

$$L_d \geq \frac{V_{nom} \cdot D(1-D)}{I_{ripple} \cdot f_s}. \tag{B.7}$$

In the above equation, D is the duty cycle (which is assumed here as 0.5 for the worst case), I_{ripple} the ripple current and f_s the switching frequency. The inequality of the equation means that L_d should be at least as high as the right-hand side of the equation. The current ripple can be estimated by the following formula, where it is assumed that it is around 40 % of the maximum RMS input current

$$I_{ripple} = 0.4 \cdot \frac{\sqrt{2} \cdot P_r}{\eta \cdot V_{g,min} \cdot PF}. \tag{B.8}$$

To calculate the current ripple, values for the efficiency η, the minimum RMS input voltage $V_{g,min}$ and the power factor PF have to be specified. As these values are design parameters for the active PFC, no further information can be given here. However, in [150] actual values for these parameters for PEL-3 are provided. The switching frequency f_s is also assumed there. For active PFC, the calculation of C_{dc} is the same as in (B.4). To model the active PFC stage or boost converter, an additional switch and one or two diodes are necessary (see Fig. 5.10).

To realise the active PFC, the MOSFET has to be controlled regarding two control targets [151] (see Fig. B3). First, the voltage $V_{dc}(t)$ is regulated to the reference value $V_{dc,ref}$ over a PI-controller. This reference is higher than the peak grid voltage, as a boost converter stage is used. Second, the current $I_d(t)$ is controlled in a way that it should take on the temporal course of the grid voltage. As a result, the load current and grid voltage are in phase and thus the power factor decreases to a small value. In some applications, additional current control can also be used [151], but is omitted here, due to simplicity. Besides, an additional first-order lag is used to filter high harmonics of the measured grid voltage. Note that the time constant should not be too large in order to avoid a phase shift to the grid voltage. The gain K_{pu} is set according to the reciprocal peak value of the grid voltage $\hat{V}_g$.

For three-phase passive PFC loads, the sizing of the capacitance C_{dc} and inductance L_d is different, compared to single-phase passive PFC devices. On the one hand, the rectified voltage $V_d(t)$ is larger by a factor of $\sqrt{3}$ and the capacitor C_{dc} is charged more often per period. On the other hand, the harmonic limits for three-phase loads can vary greatly, depending on their application. In IEC 61000-3-2 symmetrical three-phase loads with a rated current per phase smaller than 16 A are class A devices, if they do not belong to another class [160]. For phase currents greater 16 A and lower 75 A, IEC norm 61000-3-12 has to be applied [163]. If the load is an adjustable speed drive and does not belong to IEC 61000-3-2 or IEC 61000-3-12, the harmonic limits are specified by IEC norm 61800-3 [164]. However, if the three-phase load is used as 'professional equipment' with a rated power greater than 1 kW no specific harmonic limits are specified [160]. Here, PEL-4 falls into this last category, as this DC power supply is mostly used in a laboratory environment. This assumption is supported by the fact that measurements from PEL-4 show that under normal conditions the current contains harmonics from the 5^{th} and 7^{th} order which are 2.5 times higher than the respective harmonic limits (cf. Fig. B4 of PEL-4 before $t = 0.04$). Therefore, the PEL-4 inductance has not to be selected to meet these limits and the device can be classified as professional equipment. It can be concluded that for three-phase loads the sizing of L_d and C_{dc} are individual and must be considered per device. For that reason, no further specifications can be made here. For those who are interested to know how the sizing is done for adjustable speed drive loads, the reader is referred to [148] and [96].

C Parameters of the aggregated Nordic system

Table C1: Technical data of ANS (partly based on [153])

Parameter	Value
S_{base}	8000 MVA
V_{base}	400 kV
$\lvert\underline{v}_0\rvert$	1.05427507825 pu
$\underline{z}_{\text{g}}$	0.0757040985049529 + j0.8622967163531461 pu
$x_{\text{L,aggregated}}$	j0.874274 pu
$r_{\text{aggregated}}$	0.15701275 pu
$x_{\text{C/2,aggregated}}$	16.331917372392102 pu
$x_{\text{L,original}}$	4.0 pu
r_{original}	0.48 pu
$x_{\text{C/2,original}}$	66.73161833378876 pu
Q_{C1}	-600 MVAr
Q_{C2}	-850 MVAr
P_{L}	7580 MW
Q_{L}	2243.7 MVAr
k_{P}(PLL)	92 pu
k_{I}(PLL)	4255.3 pu

Table C2: Technical data of transformers within ANS (partly based on [153])

Name	S_{base}	V_{HV}	V_{LV}	u_{k}	R/X
T1	8000 MVA	1.05·400 kV	130 kV	0.12 pu	0
T2	5300 MVA	1.05·130 kV	15 kV	0.15 pu	0
T3	8000 MVA	130 kV	20 kV	0.11 pu	0

Table C3: Technical data of OLTC (T3) within the ANS (taken from [153])

min. tap	max. tap	initial tap	Δv	v_{ref}	deadband	τ
0	20	6	0.01 pu	1.0 pu	±0.01 pu	10 s

Table C4: Technical data of synchronous generator within ANS (taken from [153])

Parameter	Value
S_{base}	5300 MVA
P_{ref}	4440 MVA
H	6 s
D	0
x_{l}	0.15 pu
r_{a}	0 pu
x_{d}	2.2 pu
x_{q}	2.0 pu
x'_{d}	0.3 pu
x'_{q}	0.4 pu
x''_{d}	0.2 pu
x''_{q}	0.2 pu
T'_{d0}	7 s
T'_{q0}	1.5 s
T''_{d0}	0.05 s
T''_{q0}	0.05 s
S_{10}	0.1 pu
S_{12}	0.3 pu
K_{is}	0 pu

Table C5: Control parameters of automatic voltage regulator (AVR) and power system stabiliser (PSS) (mostly based on the values of generator G6 in [153])

Parameter	Value
$i_{\text{fd,lim}}$	3.0618 pu
v_{ref}	1.0 pu
L_1	-20 pu
L_2	5 pu
G_1	120 pu
G_2	10 pu
T_{a}	5.0 s
T_{b}	12.5 s
f	0 pu
r	1 pu
C	0.1 pu
T_1	0.22 s
T_2	0.012 s
T_{w}	15 s
k_{p}	75 pu